

On the effects of surface texturing on turbulent flow and its impact on the early-stage of bio-fouling settlement

Amin Peyvasteh Nejad, M.Sc. B.Eng

Supervised by Dr. Yan Delaure



A thesis presented for the degree of Doctor of Philosophy

SCHOOL OF MECHANICAL &
MANUFACTURING ENGINEERING
DUBLIN CITY UNIVERSITY

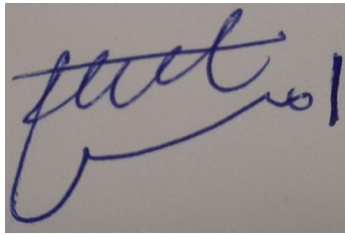
October 2023

Dedication

To my Mum and Dad for giving me their endless love and support.

Declaration

I, Amin Peyvasteh Nejad hereby certify that this material, which I now submit for assessment on the program of study leading to the award of PhD, is entirely my work, and that I have exercised reasonable care to ensure that the work is original, and does not to best of my knowledge breach any law of copyright, and has not been taken from works of others save and to the extent that such work has been cited and acknowledged within the text of my work.

A handwritten signature in blue ink, appearing to read 'amin peyvasteh nejad', written on a light-colored background.

Signed: _____ ID No.20210037, Date: October 10th, 2023

Acknowledgements

I would like to express my gratitude to Dr. Yan Delaure, my supervisor, for his valuable feedback and constructive criticisms over the past three years and half.

Contents

1	Introduction	20
1.1	Background	20
1.2	Research objectives	22
1.3	Thesis outline	24
2	Literature review	25
2.1	Fouling species and formation	27
2.2	Bio-mimetic of marine species	29
2.2.1	Marine mammals and fishes	29
2.2.2	Molluscs	30
2.2.3	Bio-mimetic campaign	30
2.2.4	Hydro-dynamical effect on fouling settlement	35
2.2.5	Bio-fouling impact on tidal turbines	36
2.3	Review of turbulent Flow problem over roughened surfaces	39
2.3.1	Roughened surface effect on the velocity profile of a turbulent flow	39
2.3.2	Roughness function estimation	42
2.3.3	Equivalent sand grain roughness (k_s^+)	45
2.3.4	Riblet effect	48
2.4	High-fidelity numerical simulation of roughened flow over the past twenty years	50
2.4.1	Regular geometries	50
2.4.2	Irregular geometries	60
2.5	Summary and the contribution to the state of the art	63
3	Turbulence modeling and the finite volume method	64
3.1	Turbulence modeling	64
3.1.1	SGS models	68
3.2	Finite volume method	70
3.2.1	Solution domain discretization	70
3.2.2	Semi-discretised equations	70
3.2.3	Spatial and temporal discretizational schemes	71
3.2.4	Navier-stokes solver	79
3.3	Summary and Conclusion	81
4	Numerical set-ups	82
4.1	Fully developed turbulent channel flow with smooth walls	82
4.1.1	Mesh generation	84
4.1.2	Discretization schemes	86

4.1.3	Boundary conditions	86
4.1.4	Solver algorithm	87
4.2	Fully developed turbulent channel Flow with roughened walls	87
4.2.1	Boundary conditions	92
4.2.2	Discretization schemes and solver algorithm	92
4.3	Fully developed turbulent channel flow with one-side textured wall and attached organism	92
4.3.1	The candidate bio-organism geometry	92
4.3.2	Texture with the organism meshes	94
4.3.3	Boundary conditions	94
4.3.4	Discretization schemes and solver algorithm	96
4.4	Simulation campaign and computational resources	96
4.5	Summary and Conclusion	98
5	LES solver validation on a smooth wall channel	99
5.1	LES solutions on a smooth wall channel at $Re_\tau = 395$ (methodology validation)	99
5.1.1	Mean velocity profiles	100
5.1.2	Reynolds stress tensor (turbulence fluctuations)	101
5.1.3	Turbulent vortical structures	103
5.2	Summary and Discussion	106
6	LES results for the three stream-wise elongated textures at four different locations on and within textures	107
6.1	Mean wall shear stress within and on textures	107
6.2	Turbulent shear stresses within textures	109
6.3	Second to fourth order of statistics in four various regions	112
6.3.1	Second order statistics	112
6.3.2	Higher-order statistics	116
6.4	Discussion and Conclusions	124
7	Dispersive stress versus Reynolds stresses and its implication for bio-fouling prevention	127
7.1	Turbulent stresses in a textured Wall	127
7.2	Spatially averaged stresses within and above textures	128
7.2.1	Spatially averaged Reynolds and dispersive stresses	129
7.2.2	Quadrant analysis and spatial average of higher order statistics of turbulent fluctuations	134
7.2.3	Distribution of Reynolds and Dispersive stresses within textures	139
7.3	Discussion and Conclusions	149
8	Hydro-dynamical forces acting on a simplified organism model positioned on and within $\lambda_p = 0.457$ ($S^+ = 80$) stream-wise texture	150
8.1	Time histories of forces acting on the organism	151
8.2	Dispersive and Reynolds shear stresses impact on the exerted forces .	158
8.3	Discussion and Conclusions	162
9	Overall thesis discussion	163

10 Conclusion and future works	165
10.1 Future work	169
A Celik LES Index Quality	170
B Definition of the Statistical Quantities	173
B.1 Temporal averaging	173
B.2 Spatial averaging	174
B.3 Higher order of statistics	174
C Definition of Quadrant Analysis Variables and Higher Order Statis- tics in OpenFOAM	176

List of Figures

1.1	Image of Microridges from the growth rings of the brill fish, <i>Scophthalmus rhombus</i> [13].	22
1.2	A simplified model of the candidate texture.	23
2.1	Micro-foulers, [top left]: diatoms, [bottom left]: bacteria, [bottom right]: <i>Ulva</i> zoospores, [top right]: <i>Balanus Amphitrite</i> cyprid larva (about 300-500 μm) [14].	25
2.2	Macro-foulers, [top images]: macro-algae, [bottom left]: <i>Balanus amphitrite</i> , [bottom middle]: serpulid worm, [bottom right]: a ship hull which is highly affected by fouling [14].	26
2.3	Schematic simplistic view of the bio-fouling formation process on an immersed solid surface [5].	28
2.4	[Left] Morphology of skin patterns on the <i>Globicephala melas</i> , [Right] replicated sample produced by polyelectrolyte self-assembly [28].	29
2.5	[Left] and [right] Images: Denticles on the spinner shark skin [25], middle image: replicated skin patterns on (Polydimethylsiloxane elastomer) PDMS _e [33].	30
2.6	Topographical variations on Molluscs skins [25].	30
2.7	Degrees of bio-fouling retention of critical surface tension of substratum [44].	32
2.8	Correlations of eight different <i>Ulva</i> and <i>C.marina</i> growth settlement cases, including new parameter on PDMS _e and hydrogel surface [5], [46].	33
2.9	[Left]: The mapped image of spore settlement on Sharklet AF TM . [Right]: the mapped image of spore settlement on recessed Sharklet AF TM (higher density area indicate preferential settlement locations) [5].	34
2.10	Bio-fouling in a cross-flow turbine which was deployed for a long run application [3].	37

2.11	Bio-fouling formed over the Magallanes turbine blades after one-year deployment in Orkney. [Left] Surface near the root of the blade and in the lee. [Right] Surface towards the tip of the blade [17].	38
2.12	Moddy diagram [93].	41
2.13	Mean stream-wise velocity comparison of different sets of roughness with smooth wall based on wall units [96].	42
2.14	Velocity deficit profiles by [96].	43
2.15	Turbulent velocity profile over roughness surface [98].	44
2.16	Roughness function for several transitionally rough surfaces, as a function of the Reynolds number based on the fully rough equivalent sand roughness. Uniform sand [91]; ▽, uniform packed spheres [102]; ▲, triangular riblets [8]; ..., galvanized iron; —, tar-coated cast iron; -.-, wrought-iron [92];	45
2.17	Frontal and plan area per unit wall-parallel area [105].	46
2.18	Roughness length against frontal solidity [100].	47
2.19	Different scale pattern grow on different sharks [117].	49
2.20	A closer look at surface patterns grow on shark skin (Great white shark [117]).	50
2.21	Drag reduction against triangular riblet with 60-degree tip angle [116].	51
2.22	Geometry of a turbulent channel flow with two-dimensional ribs [121].	51
2.23	Roughness types with their respective velocity profiles.(a): d-type, (b): semi-k-type and (c): k-type [127].	52
2.24	High-resolution flow over k-type roughness [86].	53
2.25	Photographs from urban-like morphologies [133].	55
2.26	Egg-pattern roughness [136].	56
2.27	Schematic of a channel flow with one side fully covered with hemispheres [139].	57
2.28	The pipe with internal sinusoidal roughness geometry [140].	57
2.29	Aligned and staggered arrays of rectangular prism used in [143]. . . .	58
2.30	Scalloped shape used as riblet profile to cover the bottom wall [147]. .	59
2.31	(a) clip from the layout of the channel flow. (b) random roughness profiles are generated in a stream-wise direction. [148].	60
2.32	Six out of seventeen realistic roughness topologies produced and used in work of [151].	61
2.33	Open channel with pebble layer roughness [156].	62
3.1	Leonardo Davinchi famous sketch of water falling into a pool [159]. .	65
3.2	Different angles of a turbulent boundary layer formed on a smooth surface [159].	66

3.3	Instantaneous u_x and filtered velocity $\overline{u_x}$ [159].	67
3.4	A typical control Volume [165].	71
3.5	Conservative fluxes on CVs surfaces [164].	72
3.6	Linear interpolation between two straddling cell [165].	74
3.7	Mesh non-orthogonality [165].	75
3.8	Flowchart of Pimple algorithm [170].	81
4.1	Computational domain used in smooth wall channel flow.	83
4.2	Computational mesh used in smooth wall channel flow. (a): coarse mesh, (b): medium mesh, (c): fine mesh.	85
4.3	Image of Microridges from the growth rings of the brill fish, <i>Scophthalmus rhombus</i> [13].	88
4.4	A simplified model of the candidate texture.	89
4.5	Five textures used in simulations: stream-wise textures separated by gaps (a) $S^+ = 10$, (b) $S^+ = 20$, (c) $S^+ = 40$, and (d) $S^+ = 80$ spacing, and span-wise textures with $S^+ = 80$	90
4.6	Image of a marine organism belonging to <i>Nitzschia</i> family taken from [178].	93
4.7	(a) The oval cylinder shape representing <i>Nitzschia</i> suggested by [179], (b) The stadium cylinder shape used in the present work to represent the <i>Nitzschia</i>	93
4.8	Illustration of the locations where the organism is placed [175].	94
4.9	Surface meshes used on and around the organism.	95
4.10	Overview of related geometry and mesh textures: (A) Organism placed at the texture crest, (B) Organism placed in the texture stream-wise gap, (C) Organism placed in the texture span-wise gap, (D) Organism placed at a smooth wall.	95
5.1	Comparison of the normalised stream-wise velocity profile predicted by mesh refinements with the LES turbulence model against DNS results from [180]. The plots are scaled against the wall distance, (a) in outer and (b) in inner units.	100
5.2	Comparison of the normalized stream-wise resolved Reynolds stress profile predicted by the successive mesh refinements with the LES turbulence model against DNS results from (citemoser1999direct. The plots are scaled against the wall distance, (a) in outer and (b) in inner units.	102

5.3	Comparison of the normalized normal-to-wall resolved Reynolds stress profile predicted by the successive mesh refinements with the LES turbulence model against DNS results from [180]. The plots are scaled against the wall distance, (a) in outer and (b) in inner units.	102
5.4	Comparison of the normalized span-wise resolved Reynolds stress profile predicted by the successive mesh refinements with the LES turbulence model against DNS results from [180]. The plots are scaled against the wall distance, (a) in outer and (b) in inner units.	102
5.5	Comparison of the normalized resolved shear stress Reynolds stress profile predicted by the successive mesh refinements with the LES turbulence model against DNS results from [180]. The plots are scaled against the wall distance, (a) in outer and (b) in inner units.	103
5.6	Hair-pin vortex shape [159].	104
5.7	Vorticity countours at different y^+ normal to wall.	105
5.8	Stream-wise vortexes next to wall (hair-pin legs).	106
6.1	Mean wall shear stress on distinctive surfaces of rectangular cubes. . .	108
6.2	Contours of the normalized turbulent shear stress $\overline{\tau_{tot}}$ at $y^+ = 12$ or $y/l_y = 0.3$ for (a) Smooth wall , (b) $S^+ = 10$, (c) $S^+ = 40$ and (d) $S^+ = 80$	110
6.3	Contours of the normalized turbulent shear stress $\overline{\tau_{tot}}$ at $y^+ = 35$ or $y/l_y = 0.9$ for (a) Smooth wall, (b) $S^+ = 10$, (c) $S^+ = 40$ and (d) $S^+ = 80$	111
6.4	Contours of \overline{uv} (Left Column), \overline{vw} (middle column Column) and \overline{uw} (right column Column) stresses over the section plane centred over the textures.((a) $S^+ = 10$, (b) $S^+ = 40$, (c) $S^+ = 80$)). The cross-section shown is in the plane perpendicular to the stream-wise direction and contains the prism centroid.	112
6.5	Vortical structures illustration with $Q=0.05$	113
6.6	Illustration of the sampling wall normal lines A, B, C and D.	114
6.7	Comparison of uv^+ profiles at locations (a): A, (b): B, (c): C and (d): D against y^+ for three different textures.	115
6.8	Comparison of wall-normal profiles of Q_2 as a measure of the strength of ejection events against y^+ at locations (a): A, (b): B, (c): C and (d): D for three different textures.	117
6.9	Comparison of wall-normal profiles of Q_4 as a measure of the strength of ejection events against y^+ at locations (a): A, (b): B, (c): C and (d): D for three different textures.	117

6.10	Comparison of wall-normal profiles of Q_2 and Q_4 against y^+ at locations (a): A, (b): B, (c): C and (d): D for three different textures.	118
6.11	Comparison of $(uuu)^+$ profiles at locations (a): A, (b): B, (c): C and (d): D against y^+ for three different textures.	119
6.12	Comparison of $(vvv)^+$ profiles at locations (a): A, (b): B, (c): C and (d): D against y^+ for three different textures.	120
6.13	Comparison of $(uuv)^+$ profiles at locations (a): A, (b): B, (c): C and (d): D against y^+ for three different textures.	121
6.14	Comparison of $(uvv)^+$ profiles at locations (a): A, (b): B, (c): C and (d): D against y^+ for three different textures.	122
6.15	Comparison of S_u profiles at locations (a): A, (b): B, (c): C and (d): D against y^+ for three different textures.	123
6.16	Comparison of F_u profiles at locations (a): A, (b): B, (c): C and (d): D against y^+ for three different textures.	124
7.1	L_x , L_z , a and b lengths used in plan area density [134].	129
7.2	Spatially averaged Reynolds stresses for the textured surface plotted against the scaled wall distance $y^+ - \epsilon^+$ compared with smooth wall DNS results [174]. (a): scaled stream-wise Reynolds stresses, (b): scaled normal to wall Reynolds stresses, (c): scaled span-wise Reynolds stresses, (d): scaled Reynolds shear stress.	132
7.3	Spatially averaged dispersive stresses for the textured surface plotted against the scaled wall distance $y^+ - \epsilon^+$ compared with smooth wall DNS results [174]. (a): scaled stream-wise dispersive stresses, (b): scaled normal to wall dispersive stresses, (c): scaled span-wise dispersive stresses, (d): scaled dispersive shear stress.	133
7.4	Normalized total stresses for the textured wall plotted against the scaled wall distance $y^+ - \epsilon^+$ compared with smooth wall DNS results [174]. (a): scaled total stream-wise stresses, (b): scaled total normal to wall stresses, (c): scaled total span-wise stresses, (d): scaled total turbulent shear stress.	134
7.5	Comparison of spatially averaged Reynolds and dispersive shear stresses diagrams of $\lambda_p = 0.457$ textures drawn against $(y^+ - \epsilon^+)$	135
7.6	Comparison of the ratio of different Q_i on the total Q_t drawn against $y^+ - \epsilon^+$. (a): upward interaction(Q_1/Q_t), (b): ejection (Q_2/Q_t), (c): downward interaction(Q_3/Q_t) and (d): sweep (Q_4/Q_t).	136
7.7	Profiles of (a) Q_2 (ejection) and (b) Q_4 (sweep) against $y^+ - \epsilon^+$	136

7.8	Comparison of the triple correlation profiles against $y^+ - \epsilon^+$ for flow over textured surfaces and the equivalent smooth surface for (a): $\langle \overline{uuu} \rangle^+$, (b): $\langle \overline{vvv} \rangle^+$, (c): $\langle \overline{uuv} \rangle^+$ and (d): $\langle \overline{uvv} \rangle^+$	137
7.9	Comparison of the triple quadruple correlation profiles against $y^+ - \epsilon^+$ for flow over textured surfaces and the equivalent smooth surface for (a): Skewness, and (b): Flatness.	138
7.10	Contours of stream-wise Reynolds stress (\overline{uu}), at the height of $y^+ = 10$, above the bottom wall. (a): $\lambda_p = 0.88$, (b): $\lambda_p = 0.77$, (c): $\lambda_p = 0.64$, (d): $\lambda_p = 0.457$ stream-wise, (e): $\lambda_p = 0.457$ span-wise. . .	140
7.11	Contours of stream-wise Reynolds stress (\overline{uu}), at the height of $y^+ = 30$ above, the bottom wall. (a): $\lambda_p = 0.88$, (b): $\lambda_p = 0.77$, (c): $\lambda_p = 0.64$, (d): $\lambda_p = 0.457$ stream-wise, (e): $\lambda_p = 0.457$ span-wise. . .	141
7.12	Contours of stream-wise dispersive stress ($\tilde{u}\tilde{u}$), at the height of $y^+ = 10$, above the bottom wall. (a): $\lambda_p = 0.88$, (b): $\lambda_p = 0.77$, (c): $\lambda_p = 0.64$, (d): $\lambda_p = 0.457$ stream-wise, (e): $\lambda_p = 0.457$ span-wise. . .	141
7.13	Contours of stream-wise dispersive stress ($\tilde{u}\tilde{u}$), at the height of $y^+ = 10$, above the bottom wall. (a): $\lambda_p = 0.88$, (b): $\lambda_p = 0.77$, (c): $\lambda_p = 0.64$, (d): $\lambda_p = 0.457$ stream-wise, (e): $\lambda_p = 0.457$ span-wise. . .	142
7.14	Contours of normal-to-wall Reynolds stress (\overline{vv}), at the height of $y^+ = 10$, above the bottom wall. (a): $\lambda_p = 0.88$, (b): $\lambda_p = 0.77$, (c): $\lambda_p = 0.64$, (d): $\lambda_p = 0.457$ stream-wise, (e): $\lambda_p = 0.457$ span-wise. . .	142
7.15	Contours of normal-to-wall Reynolds stress (\overline{vv}), at a height of $y^+ = 30$, above the bottom wall. (a): $\lambda_p = 0.88$, (b): $\lambda_p = 0.77$, (c): $\lambda_p = 0.64$, (d): $\lambda_p = 0.457$ stream-wise, (e): $\lambda_p = 0.457$ span-wise. . .	143
7.16	Contours of normal-to-wall dispersive stress ($\tilde{v}\tilde{v}$), at the height of $y^+ = 10$, above the bottom wall. (a): $\lambda_p = 0.88$, (b): $\lambda_p = 0.77$, (c): $\lambda_p = 0.64$, (d): $\lambda_p = 0.457$ stream-wise, (e): $\lambda_p = 0.457$ span-wise. . .	143
7.17	Contours of normal-to-wall dispersive stress ($\tilde{v}\tilde{v}$), at the height of $y^+ = 30$, above the bottom wall. (a): $\lambda_p = 0.88$, (b): $\lambda_p = 0.77$, (c): $\lambda_p = 0.64$, (d): $\lambda_p = 0.457$ stream-wise, (e): $\lambda_p = 0.457$ span-wise. . .	144
7.18	Contours of span-wise Reynolds stress (\overline{ww}), at the height of $y^+ = 10$, above the bottom wall. (a): $\lambda_p = 0.88$, (b): $\lambda_p = 0.77$, (c): $\lambda_p = 0.64$, (d): $\lambda_p = 0.457$ stream-wise, (e): $\lambda_p = 0.457$ span-wise.	144
7.19	Contours of span-wise Reynolds stress (\overline{ww}), at the height of $y^+ = 30$, above the bottom wall. (a): $\lambda_p = 0.88$, (b): $\lambda_p = 0.77$, (c): $\lambda_p = 0.64$, (d): $\lambda_p = 0.457$ stream-wise, (e): $\lambda_p = 0.457$ span-wise.	145
7.20	Contours of span-wise dispersive stress ($\tilde{w}\tilde{w}$), at the height of $y^+ = 10$, above the bottom wall. (a): $\lambda_p = 0.88$, (b): $\lambda_p = 0.77$, (c): $\lambda_p = 0.64$, (d): $\lambda_p = 0.457$ stream-wise, (e): $\lambda_p = 0.457$ span-wise.	145

7.21	Contours of span-wise dispersive stress ($\tilde{w}\tilde{w}$), at the height of $y^+ = 30$, above the bottom wall. (a): $\lambda_p = 0.88$, (b): $\lambda_p = 0.77$, (c): $\lambda_p = 0.64$, (d): $\lambda_p = 0.457$ stream-wise, (e): $\lambda_p = 0.457$ span-wise.	146
7.22	Contours of stream-wise Reynolds shear stress (\overline{uv}), at the height of $y^+ = 10$, above the bottom wall. (a): $\lambda_p = 0.88$, (b): $\lambda_p = 0.77$, (c): $\lambda_p = 0.64$, (d): $\lambda_p = 0.457$ stream-wise, (e): $\lambda_p = 0.457$ span-wise. . .	147
7.23	Contours of stream-wise Reynolds shear stress (\overline{uv}), at the height of $y^+ = 30$, above the bottom wall. (a): $\lambda_p = 0.88$, (b): $\lambda_p = 0.77$, (c): $\lambda_p = 0.64$, (d): $\lambda_p = 0.457$ stream-wise, (e): $\lambda_p = 0.457$ span-wise. . .	147
7.24	Contours of stream-wise dispersive shear stress ($\tilde{u}\tilde{v}$), at the height of $y^+ = 10$, above the bottom wall. (a): $\lambda_p = 0.88$, (b): $\lambda_p = 0.77$, (c): $\lambda_p = 0.64$, (d): $\lambda_p = 0.457$ stream-wise, (e): $\lambda_p = 0.457$ span-wise. . .	148
7.25	Contours of stream-wise dispersive shear stress ($\tilde{u}\tilde{v}$), at the height of $y^+ = 30$, above the bottom wall. (a): $\lambda_p = 0.88$, (b): $\lambda_p = 0.77$, (c): $\lambda_p = 0.64$, (d): $\lambda_p = 0.457$ stream-wise, (e): $\lambda_p = 0.457$ span-wise. . .	148
8.1	The time-history of hydrodynamic forces exerted on the organism model in the stream-wise direction.	152
8.2	The time-history of hydrodynamic forces exerted on the organism model in the normal-to-wall direction.	153
8.3	The time-history of hydrodynamic forces exerted on the organism model in the span-wise direction.	154
8.4	Contours of the stream-wise Reynolds and dispersive shear stresses around the organism model positioned at location A. (a): Reynolds shear stress at $y^+ = 2$, (b): Reynolds shear stress at $y^+ = 4$, (c): dispersive shear stress at $y^+ = 2$, (d): dispersive shear stress at $y^+ = 4$.	155
8.5	Contours of the stream-wise Reynolds and dispersive shear stresses around organism model positioned at location B. (a): Reynolds shear stress at $y^+ = 2$, (b): Reynolds shear stress at $y^+ = 4$, (c): dispersive shear stress at $y^+ = 2$, (d) dispersive shear stress at $y^+ = 4$	156
8.6	Contours of the stream-wise Reynolds and dispersive shear stresses around organism model positioned on C location. (a): Reynolds shear stress at $y^+ = 2$, (b): Reynolds shear stress at $y^+ = 4$, (c): dispersive shear stress at $y^+ = 2$, (d) dispersive shear stress at $y^+ = 4$	156
8.7	The time-history of total hydrodynamic forces exerted on the organism model.	159
8.8	Forces applied to the organism at B and C locations within the texture, (a): stream-wise force (F_x/F_{ref}), (b): normal-to-wall force (F_y/F_{ref}), (c): span-wise force (F_z/F_{ref}).	160

8.9	Forces applied to the organism at A and C locations, (a): stream-wise force (F_x/F_{ref}), (b): normal-to-wall force (F_y/F_{ref}), (c): span-wise force (F_z/F_{ref}).	161
A.1	LESIQ for $\lambda_p = 0.88$, [Left]: Stream-wise view, [Right]: Span-wise view.	171
A.2	LESIQ for $\lambda_p = 0.77$, [Left]: Stream-wise view, [Right]: Span-wise view.	171
A.3	LESIQ for $\lambda_p = 0.64$, [Left]: Stream-wise view, [Right]: Span-wise view.	171
A.4	LESIQ for $\lambda_p = 0.457$, [Left]: Stream-wise view, [Right]: Span-wise view.	171
A.5	LESIQ for $\lambda_p = 0.457$, [Left]: Stream-wise view, [Right]: Span-wise view.	172

List of Tables

4.1	Geometrical parameters and physical properties of the smooth wall fully developed turbulent channel flow at $Re_\tau = 395$	84
4.2	The mesh properties employed to evaluate the LES methodology in a smooth channel flow at $Re_\tau = 395$	85
4.3	Mesh characteristics used for the different textures at $Re_\tau = 395$. . .	91
4.4	Number of mesh nodes used for the $\lambda_p = 0.457$ stream-wise texture with the organism placed at different locations.	96
4.5	Characteristics of carried out simulations.	97
7.1	Plan area densities of the studied textures and their corresponding S^+ .	130
7.2	Zero-plane displacement calculated for each texture.	130
8.1	Mean hydrodynamic forces acting on the organism in different directions.	152
8.2	Intensity of the hydrodynamic forces acting on the organism in different directions.	153
8.3	Pressure and viscous drag ratio acting on the organism.	157
8.4	Total hydrodynamic forces acting on the organism in different cases. .	158

List of abbreviations

LES Large Eddy Simulation

DNS Direct Numerical Simulation

AF Anti Fouling

ES Effective Slope

EPS Extracellular Polymeric Substances

On the effects of surface texturing on turbulent flow and its impact on the early-stage of bio-fouling settlement

Amin Peyvasteh Nejad

Abstract

Bio-fouling formation and growth can significantly alter the surfaces of most structures, systems, or equipment designed to operate in the marine environment. Many effective anti-fouling solutions have been developed over the years, but in the past, these have mainly relied on paints or coatings designed to leach biocides. Environmental concerns and regulatory changes have prompted research into alternative, non-toxic anti-fouling solutions. Bio-inspired micro-scale surface modifications have gained popularity as an anti-fouling solution. Surface textures typically rely on roughness ridges arranged in arrays with spacings smaller than the dimensions of fouling species to prevent organisms from forming secure attachments to the substrate. Although this has proven effective at limiting bio-fouling settlement under static conditions, below a certain spacing, narrow gaps can also be expected to prevent hydrodynamic stresses from reaching initial settlement sites on surfaces. This work attempts to examine how the size of texture gaps affects the turbulent flow above and within textures, with the implication of disrupting the early stage of fouling settlement, which could result in minimizing fouling settlement.

This research has relied on high-fidelity Large Eddy Simulations to model turbulent flow within and above five sets of bio-inspired texture models. The spacing scales were chosen to mimic spacing gaps observed on the growth rings of the brill fish *Scophthalmus rhombus*. Local and high-order turbulent correlations ranging from second to fourth order have been used to analyse the turbulent stresses forming within and above textures. Furthermore, A bio-fouling organism model placed at three locations within and above a candidate texture was used to assess the impact of the textures on hydrodynamic forces acting on the organism. The arrangement of textures was observed to significantly affect turbulent flow by altering the distribution of Reynolds and dispersive stress within them, potentially leading to the disruption of fouling settlements. Furthermore, the analysis of hydrodynamically exerted forces on the organism at various locations of candidate textures showed that areas with elevated dispersive stress intensity, particularly at the rear side of textures, could lead to a 60% stream-wise force acting on the organism. Moreover,

additional examination revealed that dispersive stresses primarily influence mean hydrodynamic forces, whereas the role of Reynolds stresses is to adjust the fluctuations in forces acting on an organism. This shows the importance of the textures arrangements to minimize biofouling settlements by maximizing the hydrodynamic forces exerted on organisms.

Chapter 1

Introduction

1.1 Background

The growth and accumulation of marine organisms on submerged surfaces have a significant and often negative impact on marine systems. On ships, it increases the surface roughness of the hull, which impacts drag and manoeuvrability and contributes to higher fuel consumption and greenhouse gas emissions [1]. It has been estimated that the shipping industry incurs billions of dollars in expenses annually [2]. Similarly, it is known to affect rotary devices, such as marine turbines, designed to harness the energy from ocean tide currents. Relatively limited operational experience beyond more than a year makes it difficult to project the performance of existing designs throughout their intended lifespan, but it has been estimated that biofouling can cause a significant loss of performance and an impact on reliability. A key source of uncertainty is related to the degradation of materials caused by biofouling [3]. Other effects include increases in the weight and thickness of active components, along with corrosion and other surface modifications caused by mechanical and chemical interactions. These changes have implications for the system's structural integrity and hydrodynamic efficiency [4]. In the past, a conventional approach to preventing bio-fouling settlement involved employing chemical coatings, which have proven to be harmful to ecosystems. Ecological concerns and legislative changes have led to the search for alternative, more ecologically sound solutions. Research into alternative approaches has been inspired by nature. The effectiveness of these solutions appears to be achieved by combining physical, chemical and stimuli-responsive strategies [5]. The research presented in this thesis focuses only on physical aspects to help better understand the impact of hydrodynamic stresses experienced by fouling organisms at the early stage of their settlement.

The research will consider smooth and modified surfaces flow designed to replicate certain patterns observed over the skin of marine creatures such as sharks, dolphins,

and crabs. This approach is termed "bio-mimicry" in the existing literature [5]. Several instances of successful bio-mimicry outlined in the literature have demonstrated their efficacy in reducing the occurrence of fouling. A notable illustration is the Sharklet AFTM, a well-known case of bio-mimicry that resulted in an 86% reduction in settlements of *Ulva* spores. A common characteristic of these developed patterns on marine organism skin is the arrangement of physical protrusions in varying spacing sizes across all directions. According to the literature, these spacing sizes are smaller than the dimensions of certain common fouling species, which prevents organisms from infiltrating and establishing colonies within the gaps (Attachment Point Theory [6], [7]). These ridges could potentially be beneficial by inducing drag reduction under turbulent conditions (referred to as the riblet effect [8], [9]) but the opposite effect is also possible depending on the geometry and, in particular, the size of the gap between the ridges. Increasing the gap allows turbulent flow structures to penetrate within the gaps, which also has implications for stress distributions and flow interaction with early-stage micro-fouling settlement and growth. Wider gaps may increase stress locally, but regions of relative shelter can develop similarly. This can significantly impact biofouling development and growth, which ultimately can add significant weight and alter surface roughness, with implications hydrodynamic performance of tidal turbine blades. This interplay between turbulent flow and surface roughness is still poorly understood in turbulent flow.

The majority of investigations in this field have focused on experimental studies conducted within a laminar flow regime or under conditions where water remains motionless on the surface [10]–[12] (static condition). Limited research has attempted to characterize how turbulent flow may affect micro-organisms settling on submerged surfaces as found over ship hulls or tidal turbine blades. Fluctuations in turbulent flow can lead to changes in flow structures that develop in proximity to surfaces. This phenomenon can lead to significant alterations in the forces exerted on fouling organisms' surfaces at the early settlement stage.

To study the impact of micro-textures on the over-lying flow, a numerical high-fidelity turbulence approach based on a Large Eddy Simulation model with no wall treatment was implemented on a series of simplified models of bio-inspired textures with different spacing in the stream-wise and span-wise directions. The candidate textures selected for the research are inspired by the rings grown on brill fish *Scophthalmus rhombus* (see Fig. 1.1) and consist of rectangular prisms aligned with the stream-wise and span-wise directions (see Fig. 1.2). They have been found in a parallel study ([13]) to hinder biofouling settlement and development under static immersion conditions, but the impact of flow when applied to moving surfaces remained to be characterized.

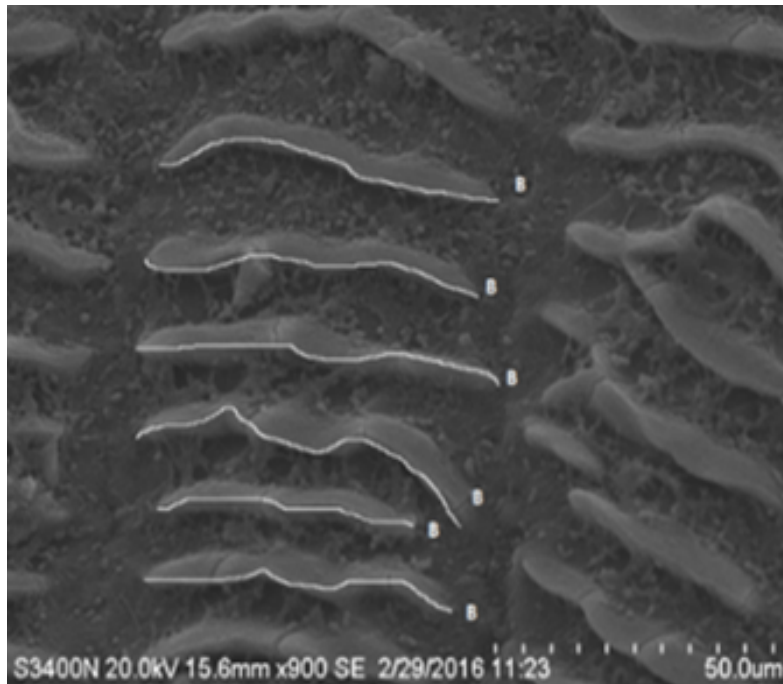


Figure 1.1: Image of Microridges from the growth rings of the brill fish, *Scophthalmus rhombus* [13].

1.2 Research objectives

Research has verified that the influence of bio-inspired texture significantly relies on the size of organisms; organisms surpassing texture sizes exhibited fewer attachment points (attachment point theory [6]). Consequently, larger organisms tended to exhibit reduced adherence to surfaces. Additionally, it has been established that lateral spacing less than 15 ($S^+ \leq 15$) can induce a riblet effect, diminishing wall shear stress on texture surfaces. Therefore, the primary objective of this study is to numerically explore the effects of bio-inspired surface textures with lateral spacings both smaller and larger than $S^+ = 15$ ($S^+ = 20, 40, 80$) on turbulent flow and their implications in disrupting early-stage bio-fouling organisms. In this study, the texture with a gap size of $S^+ = 10$ mimics the effect of the brill fish skin patterns. Therefore, specific goals are outlined in different chapters of this thesis. Initially, considering that bio-fouling is a localized phenomenon, the research focused on examining the local turbulence effects. This involves simulating the turbulent flow over the surface textures to assess turbulence statistics, ranging from second to fourth-order magnitudes, and understanding their potential implications for settling organisms. The study focuses initially on a narrow spacing of $S^+ = 10$ which has been found from previous lab-based studies to disrupt the settlement of marine diatoms, and at which the riblet effect can be expected to reduce drag, with a view to comparing it with larger sizes ($S^+ = 20, 40, 80$). The gap size is expressed here in

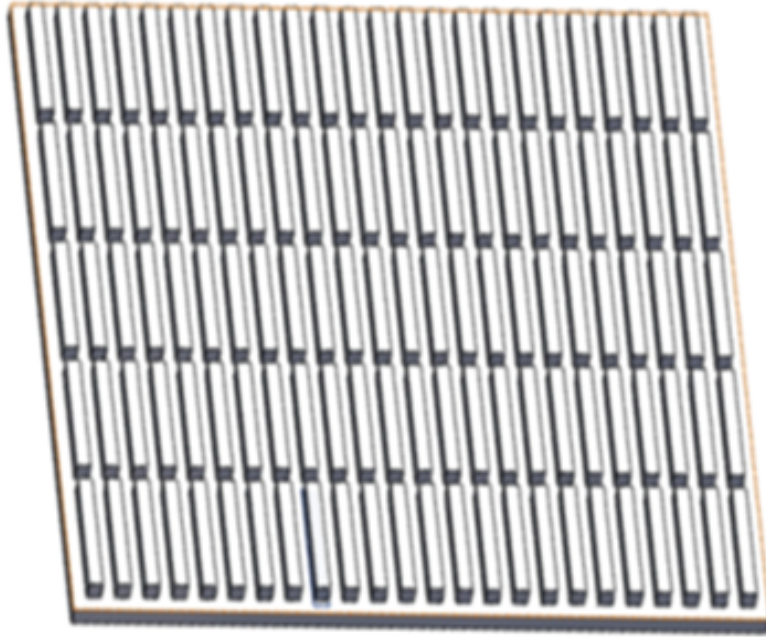


Figure 1.2: A simplified model of the candidate texture.

no-dimensional wall units. The aim is to characterize how the gap size can enhance turbulent stresses that settling organisms are exposed to at the initial stage of attachment.

The second objective is to determine the importance of spatial variability on both stress concentration and stress generation. Four specific locations within and above the textures have been selected to study local turbulent statistics. Most previous research on roughness analysis has focused on spatially averaged variables, so local effects such as stress sheltering are still poorly understood. In contrast to scenarios involving smooth walls, the mean velocity within and above textures changes over space, resulting in additional stresses that are solely dependent on spatial coordinates. Identification of regions prone to this type of stress can help optimize texture designs with the aim of disrupting early-stage fouling settlement.

The final aim of the research is to study hydrodynamic forces acting on a settled organism with a texture based on the spacing $S^+ = 80$ that has been shown to demonstrate better performance in generating turbulent activity. A simplified model of an organism is positioned at four locations within and above the texture, and the transient hydrodynamic forces acting on the organism are studied. To the best of the author's knowledge, no prior attempts have been made to quantify the forces acting on an organism in turbulent flow.

1.3 Thesis outline

The remainder of the thesis is organized as follows:

- Chapter 2 is divided into two sections. The initial section examines the existing literature on bio-fouling and bio-mimicry for the design of anti-fouling surface modifications. The second part provides an overview of research conducted on turbulent flow over roughened surfaces.
- Chapter 3 examines the fundamental equations governing a high-fidelity Large Eddy Simulation (LES) and the finite volume method.
- Chapter 4 presents the numerical configuration adopted for all simulation cases, including the initial validation, the study of textured surfaces, and the interaction between the turbulence generated by the textures and the organism. This includes mesh generation, selected numerical methodologies, and defined boundary conditions for each scenario.
- Chapter 5 presents the validation of the LES methodology using fully developed flow simulations over smooth channel walls.
- Chapter 6 discusses the turbulent flow characteristics of local flow for the tested surface textures.
- Chapter 7 compares the dispersive and Reynolds stresses and discusses their importance in terms of their potential impact on early-stage bio-fouling settlement.
- Chapter 8 studies the hydrodynamic forces acting on a simplified organism model positioned within and above the texture for the case based on the $S^+ = 80$ gap between textures aligned with the stream-wise direction.
- Chapter 9 provides an overview of the key discoveries from this study pertaining to anti-fouling. Furthermore, suggestions for potential future research work are suggested.

Chapter 2

Literature review

The process of undesired buildup of marine organisms on submerged surfaces is called bio-fouling. Bio-fouling is a common occurrence on the surfaces of marine species and most man-made structures and is notorious for its detrimental effects. It is customary to categorize bio-foulers based on their sizes: micro-foulers (e.g., bacterial and diatomic biofilms) as shown in Fig. 2.1, and macrofoulers (e.g., barnacles, mussels, tubeworms, etc.) as shown in Fig. 2.2. Both types can co-exist on a fouled surface.



Figure 2.1: Micro-foulers, [top left]: diatoms, [bottom left]: bacteria, [bottom right]: *Ulva* zoospores, [top right]: *Balanus Amphitrite* cyprid larva (about 300-500 μm) [14].

The following paragraphs provide an overview of the negative impacts of bio-fouling formation on our daily lives.

As highlighted by the World International Maritime Organization (IMO), naval trade plays a vital role in global trade. Almost 90% of all global trade is conducted through maritime shipment. However, this reliance on shipping has signif-

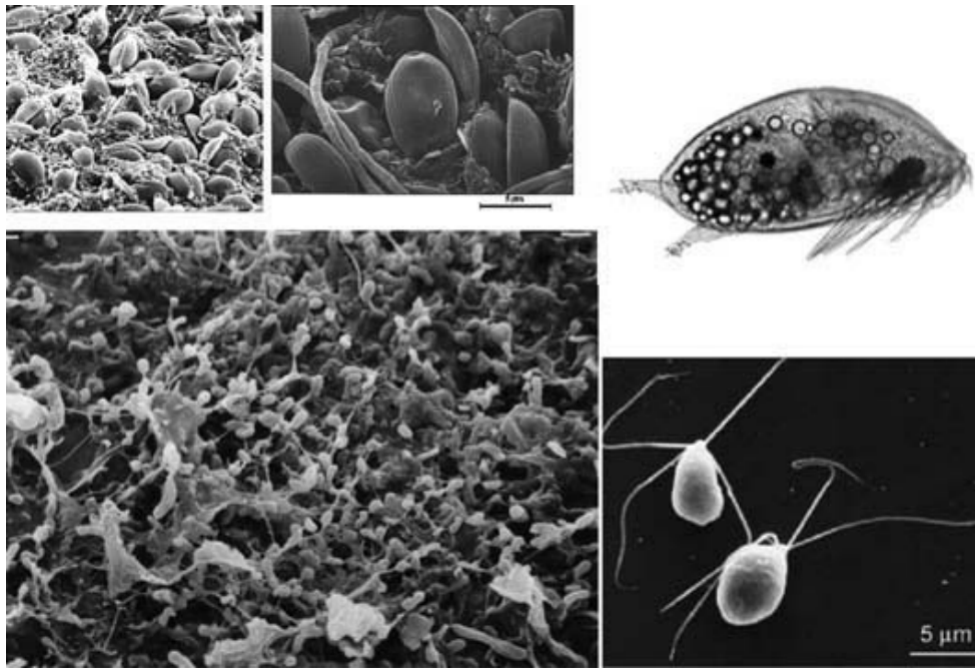


Figure 2.2: Macro-foulers, [top images]: macro-algae, [bottom left]: *Balanus amphitrite*, [bottom middle]: serpulid worm, [bottom right]: a ship hull which is highly affected by fouling [14].

icant consequences in terms of the substantial amount of fossil fuel consumption. The accumulation of bio-fouling on vessels leads to increased hull roughness and hydrodynamic drag, ultimately impairing important vessel performance parameters such as speed and vessel manoeuvrability. These issues result in higher fuel consumption and increased production of greenhouse gases [1], [2].

According to [2], a ship with extensive fouling coverage on its hull, may experience up to a 70% reduction in power compared to a clean hull. Even thin layers of fouling, such as diatoms, cause a loss of 10-16% of generated power. The economic impact of fouling-related problems is also substantial. The annual budget of the US Navy for dealing with fouling-related issues is estimated to be \$ 180-260 million, despite the fact that its fleet represents less than 1% of the global fleet [2].

The presence of fouling, attached to the naval vessel surfaces poses a threat to local ecosystem environments as well. Due to the widespread nature of naval vessels and their relatively high speed, they carry non-indigenous species, which can introduce invasive marine creatures to new locations, thereby harming local species. Research conducted in Osaka port, Japan, revealed that out of the 22 attached barnacles found on two inter-continental ships, 14 were non-indigenous, and four were sighted for the first time in Japan [15].

Bio-fouling is a major obstacle, ahead of marine power generation systems. The Marine Renewable Energy (MRE) sector is projected to reach a global value of £ 76

billion by 2050 [16]. However, in the EU, the total operational production capacity from tidal energy sources was only 12 MW in 2020, significantly falling short of the target of achieving a total combined ocean energy production capacity of 2.25 GW [17]. Despite the ongoing challenges, the 27 EU countries have maintained ambitious goals to make tidal energy cost competitive by 2030, with a target capacity of 15.7 GW by 2050. The slow pace of development in the industry can be attributed to various challenges. In this regard, a tidal turbine serves as a means to generate marine renewable energy. Tidal turbines are complex dynamic structures designed for long-term deployments. A relative lack of operational experience extending beyond a few years makes it challenging to project design performance over the design lifetime. One significant uncertainty factor is material degradation from bio-fouling [3]. It can rapidly cause considerable alteration to the hydrodynamic characteristics of immersed structures in general. The impact on marine renewable equipment is significant and a persistent challenge [18]. Effects range from increases in the weight and thickness of active parts, corrosion and other surface alterations by mechanical and chemical actions with implications for the system's structural integrity and hydrodynamic performance [4].

2.1 Fouling species and formation

Bio-fouling organisms exhibit remarkable diversity. According to estimates, there are over 1,700 species comprising more than 4,000 organisms responsible for bio-fouling [19]. Biofouling is categorized into microfouling, involving biofilm formation and bacterial adhesion, and macrofouling, which pertains to the attachment of larger organisms. Organisms are further classified into hard- or soft-fouling types based on distinct chemistry and biology that influence their settlement-prevention mechanisms. Calcareous (hard) fouling organisms encompass barnacles, encrusting bryozoans, mollusks, polychaete and other tube worms, and zebra mussels. Non-calcareous (soft) fouling organisms include seaweed, hydroids, algae [20]. Bio-fouling growth dynamics are strongly dependent on environmental growth conditions. Factors such as salinity and water temperature, solar radiation intensity, etc., play essential roles in fouling growth. Therefore, various contributing factors make the design of anti-fouling coatings challenging [21].

Upon getting immersed in water, every solid wall will immediately be covered by a microscopic layer of dissolved organic compounds made of substances such as polysaccharides and proteins. This thin layer is called the conditioning layer, and bio-fouling is established on these layers in less than 24 hours. The conditioning layer increases the probability of marine bacteria settlement [22]. The third stage usually occurs less than one week after colonization, and colonizers such as fungi

start to settle on the conditioning layer. Invertebrate larvae usually settle in the last stage of formation. Green macro-alga *Ulva* is a macro-fouler frequently seen on ship hull surfaces. It develops its presence on a colony surface by releasing self-propelled (motile) species (zoospores), which cultivate plants on the colony surface. *Ulva*, invertebrates larvae (barnacle *Balanus amphitrite*), and tube worm *Hydroides elegans* have been used to model the settlement of bio-fouling [23], [24]. It should be noted that the mentioned sequence of the bio-fouling formation process offers a very simplistic scenario of fouling settlement, which could be very complex in reality [5], [14]. Fig. 2.3 shows a simplified representation of the formation of bio-fouling on a free-fouling surface when submerged in the ocean based on the duration of immersion of the wall in the water.

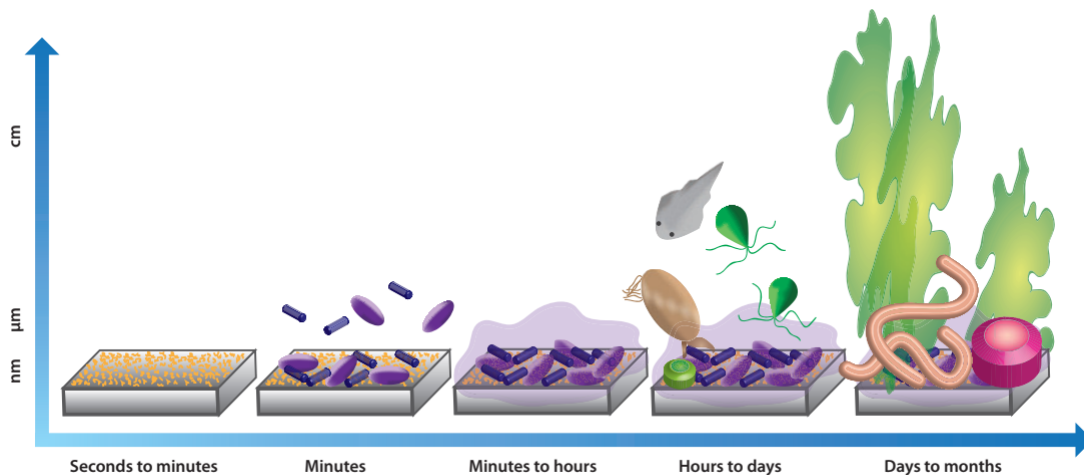


Figure 2.3: Schematic simplistic view of the bio-fouling formation process on an immersed solid surface [5].

Generally speaking, the three nature-based strategies (bio-inspired) adopted, to help combat bio-fouling and minimize its adverse effects are classified as physical, stimuli-responsive and chemical approaches [5]. This thesis is devoted to the first (physical approach), and the rest is outside the scope of this thesis. The physical approach often known as bio-mimicry, replicates grown texture patterns inspired by marine animal skins that have evolved to limit bio-fouling [25]. Bio-mimetics is an environmentally friendly way to avoid traditional anti-fouling methods, such as bio-cidal paints and fouling-releasing coating, which could harm the ecosystem due to their toxicity. The following section presents two well-documented examples of successful bio-mimetics.

2.2 Bio-mimetic of marine species

2.2.1 Marine mammals and fishes

High manoeuvrability and fast speed are certain attributes of marine mammal species such as dolphins, whales and fish such as sharks. They all share textured skins, which helps them prevent bio-fouling and reduce drags [26], [27]. For example, the pilot whale *Globicephala melas* skin surface comprises a $2\ \mu\text{m}$ ridge pattern combined with $0.2\ \mu\text{m}$ circular pores in diameter [27]. A replicated sample of *G. melas* skin showed minimum settlements of spores of *Ulva* [28].

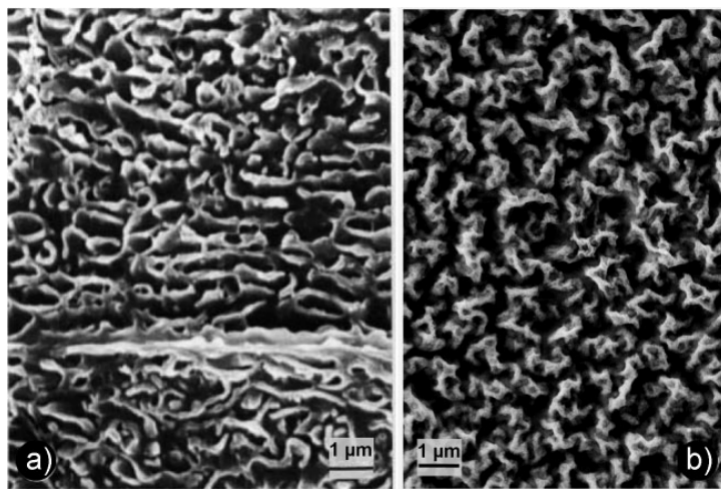


Figure 2.4: [Left] Morphology of skin patterns on the *Globicephala melas*, [Right] replicated sample produced by polyelectrolyte self-assembly [28].

Another example is the patterns that grow on shark skin and shark skin has also shown high efficiency in combating bio-fouling. The skin surface comprises placoid scales or dermal denticles (Fig. 2.5). Fig. 2.5 [Left] and [Right] show arrays of dermal denticles on a shark skin surface. The diamond-shaped dermal denticles are accompanied by longitudinal riblets [9], [29] and the shark skin patterns are also known to have the ability to reduce exerted drag, allowing them to be fast swimmers. The first replicated sample of shark skin was introduced in 2006 as Sharklet AFTM. It was produced on (Polydimethylsiloxane elastomer) PDMS_e and has been shown to reduce *Ulva* spores settlements [9]. Sharklet AFTM consists of $2\ \mu\text{m}$ spaced and $2\ \mu\text{m}$ width longitudinal rectangular ribs with 4, 8, 12, and $16\ \mu\text{m}$ lengths protruding $3\ \mu\text{m}$ normal to the wall. These patterns form diamond-shaped arrays spread all over the skin. The replicated pattern showed an *Ulva* settlement reduction of 86%. Also, it proved its effectiveness in reducing other types of bio-fouling such as diatoms *Navicula incerta*, cyprids of *B. Amphitrite*, etc. [30]–[32].

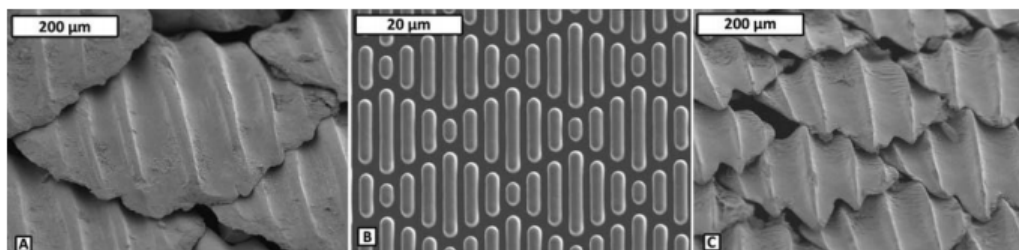


Figure 2.5: [Left] and [right] Images: Denticles on the spinner shark skin [25], middle image: replicated skin patterns on (Polydimethylsiloxane elastomer) PDMS [33].

2.2.2 Molluscs

Similar to shark skin and marine mammals, most Molluscs surfaces are fouling-resistant. However, some Molluscs species can become heavily fouled despite their anti-fouling strategies. A comparison between those species has provided a chance to compare distinctive features in terms of their anti-fouling performance. It is observed that various morphologies have been developed on Molluscs species, varying from micro to macro scales (Fig. 2.6). In this regard, two different fouling-resistance bivalve surface patterns were chosen and replicated. Four species of fouling diatoms of various sizes were tested on sinusoidal ripple features placed 2mm and 4mm apart. It was observed that all diatom species settled in high numbers on the ripples with spacings larger than cell sizes; thus, reducing the ripple spacing led to less fouling settlement. This fact highlighted the importance of allowing multiple attachment points for anti-fouling organisms to securely attach to a surface ([6], [7]).

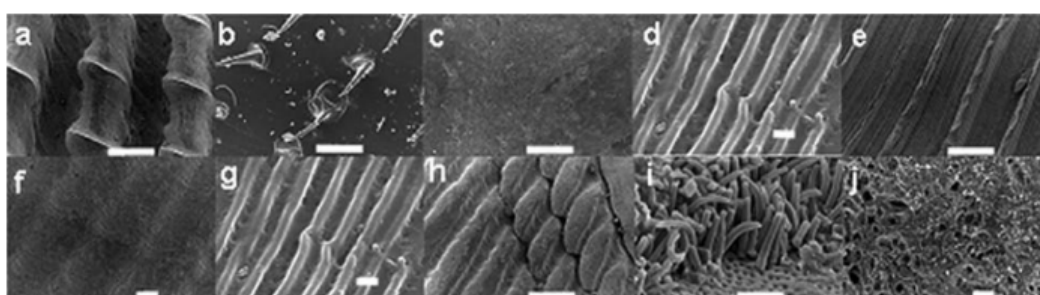


Figure 2.6: Topographical variations on Molluscs skins [25].

2.2.3 Bio-mimetic campaign

Since the advent of marine navigation, marine organism accumulation on the vessel surfaces has been a constant problem that has heavily affected vessel performance and structural integrity. In the past, traditional methods have been widely used to

combat the harmful effect of fouling [14]. These have often been relying on toxic substances that leach and threaten the environment. The main breakthrough in the anti-fouling (AF) industry occurred in the past 30 years by studying marine species. Some bio-inspired methods have attempted to mimic surface textures naturally grown and evolved by marine species to overcome the destructive effects of bio-fouling on their bodies. Innovative technologies made this feasible by reproducing texture patterns at micro and nano scales. The following presents a brief history of the past 20 years of ongoing research on AF topics. In the past twenty years, extensive efforts have been made to replace tin and copper or chemical-based paints with more environment-friendly methods. According to literature, some motile organisms, such as invertebrate larvae and algae, are actively searching for suitable surfaces. Other non-motile organisms, such as marine diatoms, secrete conditioning substances to attach to surfaces. Understanding the correlation between the physical features of the colonized surfaces would serve better AF surface design. A significant body of research has been dedicated to the physical properties of anti-fouling, including micro-textures and their effect on macro-biofouling organisms [34]–[36]. Investigations revealed that although the deterrence effect on the bio-fouling settlement was promising, the result has tended to be time-dependent (faded after a while) and species-based [37], [38]. Research confirmed that the micro-textures effect is highly dependent on the size of organisms, and organisms larger than texture sizes had fewer attachment points (attachment point theory [6]) and, as a result, tended to adhere to surfaces less. According to attachment point theory, the tendency to attach to a surface diminishes with organisms which are larger in scale than the surface roughness sizes. In contrast, smaller organisms increase their attachment tendency by exploiting micro-refuges, which provide shelter from hydrodynamic stresses [34], [39]. The attachment point theory was tested on barnacle cyprids and spores [34]–[36], [40]. It was also tested on four different diatoms ranging from 1-14 μm sizes [7]. In this case, the textures were replicated from a bivalve surface of various sizes. Results verified that the attachment point was also applicable in diatom fouling control.

Investigations have revealed that the energy of adhesion is a crucial factor determining the likelihood of bio-fouling attachment to surfaces [31], [41]. Adhesion energy is required to displace a solid-water contact and allow contact between the biological substance with the substrate. Topology and chemistry of the attachment surface are two critical factors in modulating this energy [42], [43]. Changes to the substrate material can be a highly effective way to avoid or at least minimise fouling. In this regard, [44] provided a correlation between fouling retention and critical surface tension of substrates. According to this Baer curve (see Fig. 2.7), minimum fouling occurs in the range of 20-30 mN/m and above 60 mN/m of critical surface tensions.

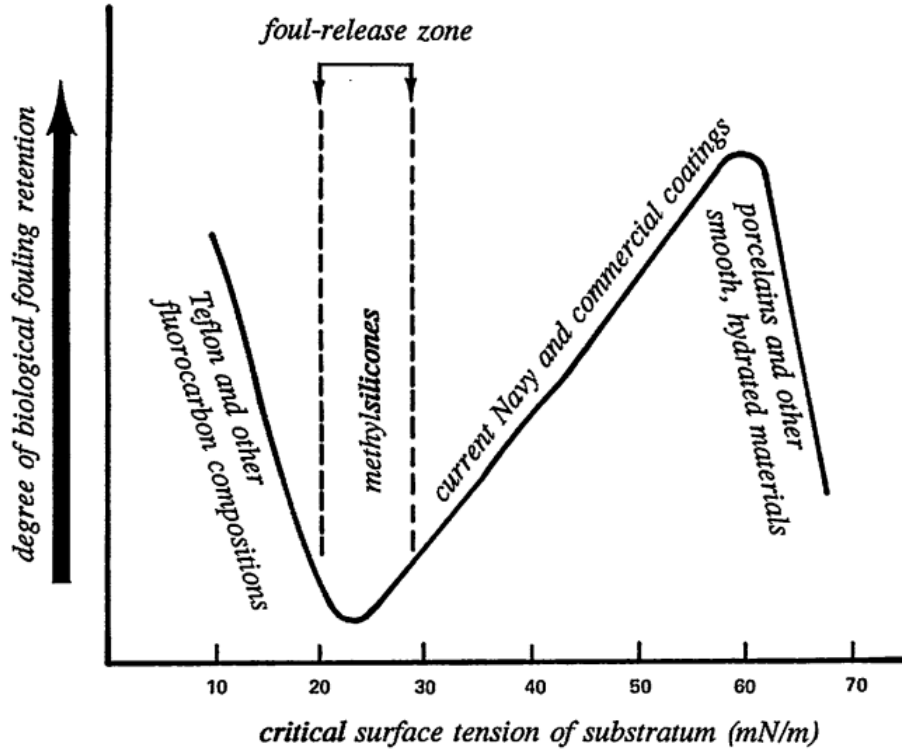


Figure 2.7: Degrees of bio-fouling retention of critical surface tension of substratum [44].

[30] suggested the first mathematical model relating *Ulva* spores settlement with topological and geometrical surface roughness features. They found an indirect relation between the Engineered Roughness Index (ERI) and spore settlement. The ERI definition includes all topological features in terms of roughness (size, geometry and special arrangement):

$$ERI = \frac{r \times d_f}{f_D} \quad (2.1)$$

where r , d_f and f denote Wenzel's roughness factor, depressed surface fraction and degree of relative motion of bio-organism to the depressed surface, respectively [45]. It was reported that a correlation of $R^2 = 0.69$ exists between mean spore density settlements and four investigated roughness with their respective ERI. Sharklet AFTM showed a 77% reduction in *Ulva* spore settlement with $ERI = 9.5$. [41] suggested a predictive model that related *Ulva* spore settlement to modified roughness based on their ERI roughness factor. The newly arrived model was tested on poly (dimethylsiloxane) elastomer (PDMSe) and successfully showed a correlation factor with spore settlement density ($R^2 = 0.88$). Further refinements were necessary to the definition of the ERI index theory to extend its applicability to organisms other than *Ulva* [31]. The definition was adapted to include the Reynolds number to describe organism species' physical size and motility. The updated formula also incorporates the attachment surface energy, to suit materials other than PDMSe

[46]. Eq. (2.2) incorporates these recent refinements:

$$\ln\left(\frac{A}{A_0}\right) = Re \frac{\gamma}{\gamma_0} \left(\frac{rn}{1 - \phi_s}\right) \quad (2.2)$$

where Re is the Reynolds number of flow around the organism, A and A_0 , respectively, are the density of settling organisms on the updated roughness and smooth wall (both roughness and smooth surface share the same chemistry), γ and γ_0 account for surface energy of the new roughened surface and smooth standard PDMS surface, respectively, n is equal to different feature patterns on new roughness topology, r is Wenzels's roughness ratio, and $1 - \phi_s$ is the depressed surface fraction extracted from the Cassie-Baxter wetting model [45], [47]. Fig. (2.8) plots the correlation of this attachment model for 8 cases of *Ulva* spore and marine bacteria *Cobetia marina* on two different PDMS and hydrogel base.

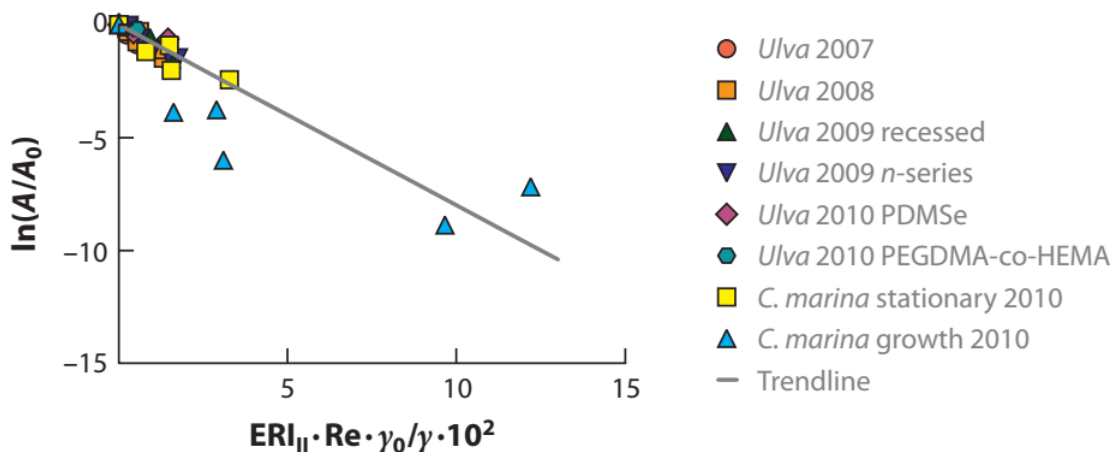


Figure 2.8: Correlations of eight different *Ulva* and *C.marina* growth settlement cases, including new parameter on PDMS and hydrogel surface [5], [46].

Anti-fouling roughness design based on mathematical modelling has proven to be a successful method to develop a surface capable of decreasing fouling settlement. However, it did not contribute to fully fouling-free surfaces. Therefore, a mapping method was introduced to identify the preferential and inhibitory locations regarding micro-roughness bio-fouling density settlement [5](Fig. (2.9)).

In this method, images of *Ulva* spore settlement on modified roughness were processed by locating the centroid of *Ulva* species and plotting their location on an attachment map to show the settlement density (Fig 2.9). This method is also beneficial in studying the time dependency of the settlement of the organism on smooth and roughened PDMS surfaces [48]. [48], exposed a single pack of multiple spores to 4h mapping. It showed that Sharklet AFTM could inhibit single spores from con-

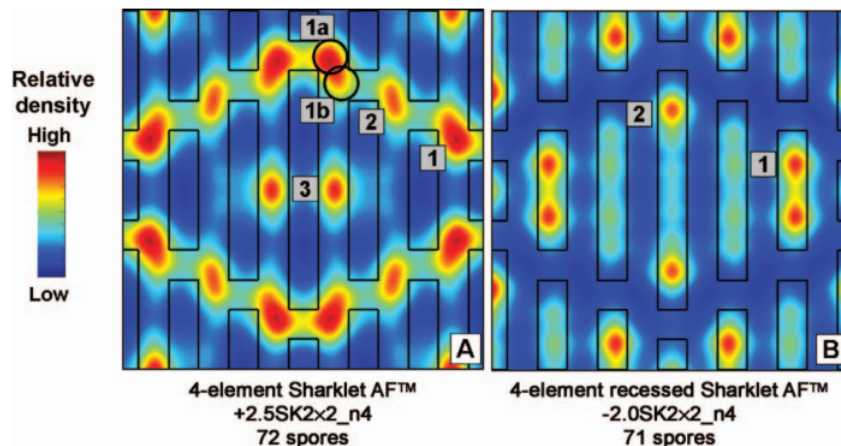


Figure 2.9: [Left]: The mapped image of spore settlement on Sharklet AF™ . [Right]: the mapped image of spore settlement on recessed Sharklet AF™ (higher density area indicate preferential settlement locations) [5].

necting with neighboring spores. Specifying the preferential location of organism settlement by this mapping technique proved a useful method to support the design of new AF roughness [49].

Various other methods have been proposed to limit bio-fouling formation and growth to reduce its adverse effects. The ideal solution limits settlement but incorporates foul release properties [30]. Physiological and stimuli-response strategies may achieve this without using toxic bio-cidal coatings ([5]). Bio-mimetic studies have inspired surface modification strategies targeting cells over sizes ranging from $1 \mu m$ to $100 \mu m$ simultaneously [21]. Hierarchical and ordered micro- and nano-scale surface topographies are particularly effective against the adhesion of micro-organisms and can be modified to produce hydrophobic or hydrophilic surfaces to enhance anti-fouling properties further[50]. Topographies larger than cells can protect against hydrodynamic shear, encouraging irreversible cell attachment and subsequent biofilm growth [10]. At the same time, sheltering from flow-induced stresses can also have detrimental effects on biofilm formation or growth by hindering the transport of cells sufficiently close to the substrate (that is, less than $50 nm$) to initiate the first stage of attachment [12] or also by limiting the supply of nutrients to the biofilm from the bulk fluid which both has a detrimental effect on biofouling growth [51]. The study of cell attachment in groves is useful in this regard. The displacement of the cells in the laminar flow depends on the shape of the cells and whether they are motile. Although non-motile cells can approach the substratum under the effect of Brownian motion coupled with shear-induced rotation [52], the low incidence of attachment at the bottom of confined laminar cavities formed in the micro-groves as observed in [11], indicates that laminar shear layers can act like an effective barrier

to non-motile cells or inert particles.

2.2.4 Hydro-dynamical effect on fouling settlement

Bodies exposed to any flow stream will experience hydrodynamic forces. These forces tend to drag and lift bodies in the stream-wise direction and perpendicular to it, respectively:

$$D = 0.5\rho SC_D U^2 \quad (2.3)$$

$$L = 0.5\rho SC_L U^2 \quad (2.4)$$

In the above equations, ρ is the fluid velocity, S is the projected area of the body normal to flow, and C_D and C_L are drag and lift coefficients, respectively, and U is the free stream velocity. In a turbulent flow, shear stresses divide into two distinct forces: viscous forces and Reynolds stress forces. Unlike laminar flow, the boundary layer divides into three different regions based on the nature of the layers. The first layer next to the wall is the viscous sublayer, where viscous stresses dominate. The buffer layer, in which Reynolds and viscous stress are equally important, is the next and final, inertial layer in which Reynolds stresses dominate [53]. Turbulent flow makes the velocity gradient in the boundary layer steeper adjacent to the wall compared to laminar flow, leading to higher viscous stress on walls.

Meanwhile, velocity fluctuations generate Reynolds stresses, which increase stresses acting on particles and organisms as they approach walls. Turbulence creates sweeping and ejections, which are responsible for turbulence production, which exert additional stresses on the organisms. Sweeping eddies describe turbulence events which bring higher momentum flow from the upper layer toward the slower flow close to the wall. Ejections refer to flow with lower momentum near walls which burst into the upper layer. The frequency of occurrence of this phenomenon increases as the flow velocity increases along with instantaneous Reynolds shear stresses. These turbulent effects combine to increase the disruptive effects of flow on settling organisms [54]–[56].

Experiments have confirmed that bio-fouling settlements are affected by flow motion [56]–[58]. While a steep velocity gradient close to surfaces can help to transport organisms that tumble towards surfaces, they can also help wash off the same organisms due to local stresses [59]. Some studies in flumes and pipes have shown that high velocity or turbulence activity close to the surface enhances the growth and settlement of some fouling species while decreasing other types [60]–[62]. It has also been shown that the flow over fouling organisms can affect their mortality [63]. Much of the published investigations have focused on whether fouling species passively transport through flowing water or are actively involved in surface selection

[64]. Some Larvae do actively search for the best spot to settle after landing and could reject a surface to continue swimming in search of a more suitable surface [65]–[68]. The process of bio-fouling settlement is a multifaceted issue that depends on different factors such as fouling settlement behaviour (swimming, crawling on the surface, etc.) and the transport process that delivers species to the surface of an immersed wall.

Most of the flow’s apparent effect on organisms relates to the stress it induces. Above a “critical hydrodynamic stress”, cell detachment is observed. The values reported in the literature [52], vary depending on surfaces and organisms and include 2.7 ∓ 1.1 Pa with *S. epidermidis* HBH276 bacteria on silicone rubber and 0.2 ∓ 0.1 Pa when the substratum was coated with polyethylene oxide. It is generally less than 2-3 Pa for larvae and bacteria immersed for one hour and up to 2000-3000 Pa for one-month-old diatoms [69]. This can be contrasted with the much higher stresses of the order of 1 MPa, which are needed to detach much older settled macro-foulers or the stresses of the order of 300-700 Pa expected over tidal turbine blades at nominal conditions. There is also evidence that mean stresses alone are insufficient to explain the detachment of settle organisms, which can be exposed to large spatial and temporal stress variations due to turbulent fluctuations. There is, however, very limited published information on the variability of turbulent statistics over textured surfaces. Most research on turbulent flow over micro-typographies has focused on drag reduction and reported that turbulent statistics are mostly averaged over space [8], [9]. Furthermore, The relevant flow Reynolds numbers are much higher than typical values reported in cell adhesion studies over micro-textured surfaces. The study of larvae transport through the shear layer [11], attachment onto the micro-grooved surface [10], *Escherichia coli* adhesion on nano-composite coatings [12] or bacterial adhesion on substratum with transverse micro-channels [70], were all performed under laminar flow conditions with Reynold’s number of 0.62 to 3.11, 51 and 5.5 respectively.

2.2.5 Bio-fouling impact on tidal turbines

Bio-fouling formation can affect the hydrodynamic performances of marine energy converters such as tidal turbines (Figs. 2.10, 2.11). Tidal turbines are designed to convert the kinetic energy of the tidal current into power. They are usually installed in rivers or tidal currents for energy extraction.

While heavy bio-fouling can be observed on parts of marine turbines after long-term deployment, both hydrodynamic stresses on moving surfaces and the anti-fouling coating have proved to be effective in bio-fouling reduction. However, anti-fouling coatings can be toxic and performance can vary, motivating further research [71].



Figure 2.10: Bio-fouling in a cross-flow turbine which was deployed for a long run application [3].

The fouling effect on the airfoil performance was experimentally investigated in [72]. In this work, the attached barnacles modelled using extruded plastic cones. At a fixed angle of attack, fouling increases led to a lift-to-drag ratio peaks decline and reduced blade power by almost 70% and at least 20 %. Another experimental study by [73], revealed the detrimental effect of fouled blade surfaces on their performance. It was shown that applying contact cement on the blade surface of an axial turbine to simulate the effect of fouling on the surface of blades resulted in a 20% thrust and performance reduction. Two-dimensional simulation on an axial turbine showed that barnacle settlement changes the vorticity field around blades, leading to reduced performance [74]. The study also highlighted the importance of using realistic shapes of organisms for accurate results. The authors also noted that the turbulence models and high mesh resolution are significant factors in a numerical simulation of flow around bio-fouling. Therefore, high-fidelity modelling is necessary for the study of bio-fouling through simulations. An experimental study by [75], assessed a cross-flow turbine performance over a range of Reynolds numbers with roughened and smooth blades. They reported that maximum torque in turbines with roughened blades happened at a lower tip-speed ratio than in smooth blades. The turbine performance was shown to decrease from the peak as the Reynolds number was increased beyond a critical value [76].



Figure 2.11: Bio-fouling formed over the Magallanes turbine blades after one-year deployment in Orkney. [Left] Surface near the root of the blade and in the lee. [Right] Surface towards the tip of the blade [17].

In the state of the art, CFD simulation has become a common tool in predicting bio-fouling effects in naval architecture. The fouling effect has generally been modelled using wall functions to represent bio-fouling as an added roughness [77]. A relatively large number of CFD simulations have been carried out to study the penalty incurred by fouling on ships and turbine blades [78]–[81].

2.3 Review of turbulent Flow problem over roughened surfaces

With the beginning of the turbulence research, most attention has been paid to turbulent flow over smooth walls. The study of flow over roughened surfaces adds complexity to the flow simulations but has attracted more attention in the recent past. Increasing the Reynolds number leads to finer viscous length scales, making the roughness height larger than the viscous layer scale. This can have a significant impact on the overlying turbulent flow. Industrial problems such as the interaction of flow over turbo-machinery blades [82], [83], heat exchangers [84], atmospheric flows over canopies or urban structures, flow over a bio-fouled marine vehicle are all considered as flow over roughened surfaces. Ignoring the roughness effect could ultimately lead to a significant error in close wall calculation.

The main reason for the slower progress of research in roughened surfaces lies in two difficulties inherent to turbulent flow [85], which are linked to their high turbulent intensity and the heterogeneity of the flow. High turbulent intensity close to rough surfaces introduces errors in experimental measurements, whereas the heterogeneous nature of the flow creates additional variability that necessitates statistical manipulation.

The advent of higher computational power has prompted increased simulation-based studies of turbulent flow over rough surfaces. In this case, the main challenge is the extremely large computational cost needed to capture all turbulent scales or their effect accurately, considering the increased time needed to reach steady flow features. The multiple time and spatial scales of turbulent flow features require that scales ranging from the smallest viscous scales to the integral scale are captured or modelled accurately. While less accurate turbulence models, such as Reynolds Averaged Navier Stokes (RANS) models, have been adopted to resolve flow around simple geometries, their lower accuracy means that they are not capable of resolving the flow in close to the roughness [86], [87]. A high-fidelity turbulence simulation can overcome experimental difficulties. Large Eddy Simulation (LES) and Direct Numerical Simulation (DNS) approaches were adopted for this purpose, namely, to resolve the flow around more complex and irregular geometries. Research toward more realistic roughness shape simulations is current and active.

2.3.1 Roughened surface effect on the velocity profile of a turbulent flow

Turbulent boundary layers over smooth walls consist of inner and outer layers. Flow is highly influenced by viscosity in the inner layer, which spans $0 < y/\delta < 0.1$ where

y and δ are the normal distance to the wall and boundary layer thickness, respectively. The relevant length scale in the inner layer is $\delta_v = \nu/u_\tau$ where ν is the fluid kinematic viscosity, and u_τ is the friction velocity defined as $\sqrt{\tau/\rho}$, where τ is the total drag applied on the surface and ρ is the fluid density. In the outer layer spanning $0.3 < y/\delta < 1$, the only relevant length scale is δ and the flow is dominated by inertial forces. Between the two layers is a buffer range $0.1 < y/\delta < 0.3$ called the logarithmic layer, where both length scales are relevant [88]. There is no clear evidence of the relative importance of the inner and outer layers in the dynamics of smooth wall flow, but it is generally believed that there is an interaction between both that governs the dynamic flow close to the surface [89]. Adding roughness to surfaces will introduce more length scales depending on the roughness topology. Their characterisation is crucial to understanding the flow dynamics adjacent to the wall. Length scales, such as roughness element length scales in the stream-wise, span-wise and wall-normal directions, would not be sufficient to give an accurate account of the flow around roughness [90]. This fact has compounded efforts to develop a unified model for the effect of roughness.

One of the main goals of a roughness flow model is to estimate the increase in skin friction compared to a smooth wall. Nikuradse[91], measured the pressure drop in a pipe coated with uniform sand-grain roughness for the first time. He detailed his data and experiment and paved the way for further investigations into roughness flow prediction. His work was extended by [92], [93] which led to graphical and commercial charts (moody chart), used by engineers. The moody chart was based on a bulk Reynolds number, friction factor, pipe diameter d and equivalent sand roughness height k_s , which is the same roughness height as defined in the experiments by the Nikuradse which produced the same skin friction. Its drawbacks relate to two problems: firstly since k_s is not a real physical parameter, an equivalent sand roughness must be defined for any roughness type. Secondly, any small flaw regarding manufacturing, corrosion, fouling, etc., could alter the skin friction.

Since skin friction is affected by different roughness geometries, it would be suitable to introduce a parameter that allows comparison between various roughness shapes. Hama[94] and Clauser[95] observed that roughness on a smooth wall would result in a downward shift in the logarithmic layer of mean velocity, indicative of an increased momentum deficit by roughness. These authors coined this effect as roughness function ΔU^+ as shown in Fig. 2.13. Since the mean velocity profile remains unchanged in the outer layer and logarithmic region, they proposed Eq. (2.5) for the velocity profile of a roughened surface where κ is the Von Karman constant, and B is the smooth wall intercept ($B \sim 5.1 - 5.4$) [88].

$$U^+ = \frac{1}{\kappa} \text{Ln}(y^+) + B - \Delta U^+ \quad (2.5)$$

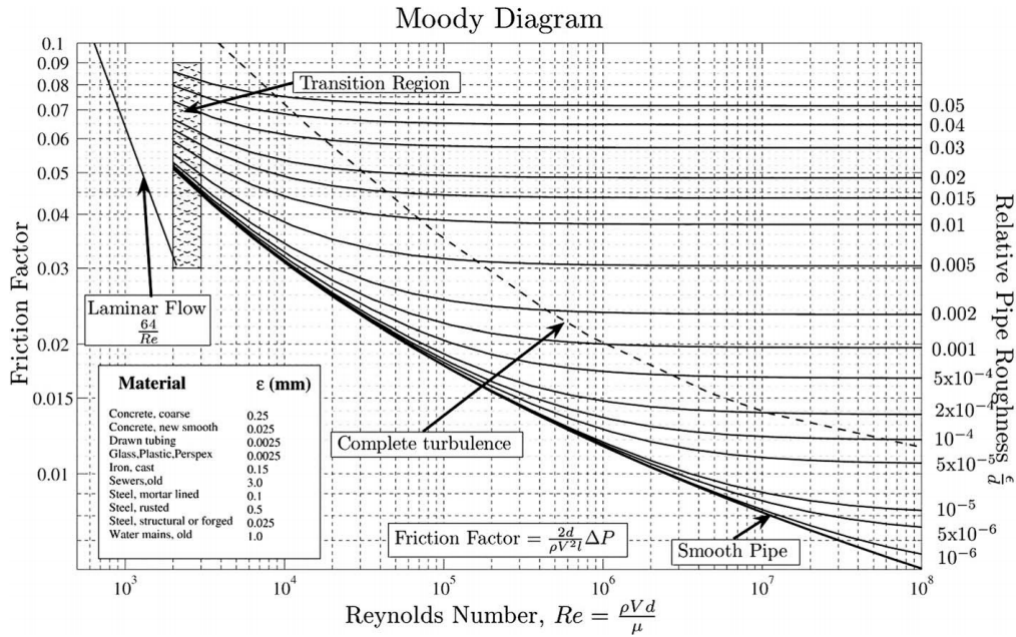


Figure 2.12: Moddy diagram [93].

Fig 2.13 compares a smooth wall mean velocity profile with profiles for various roughness scales based on inner wall units. As can be seen, roughness surfaces have not altered the fundamental shape of the velocity profile in the overlap (logarithmic layer) and outer layer of the boundary layer compared to the smooth wall. This is known as the Townsend wall similarity law [97]. Wall similarity law is more apparent if the velocity profile is shown in the velocity-deficit form $U_e^+ - U^+$ where U_e^+ is scaled by the velocity at the middle of the channel. Fig. 2.14 shows a velocity-deficit comparison between a smooth wall case and a series of honed pipe roughness protruding at different heights [96]. The similarity law can be noticed through most of the boundary layers. For $y/\delta > 0.05$, an excellent collapse of roughness data can be seen on the smooth velocity profile.

The similarity law plays a crucial role in roughness flow applications. It has practical implications for engineering applications. Most commercial computational Fluid Dynamics (CFD) codes rely on the roughness function concept to model the wall effect. Townsend similarity hypothesis states that turbulent motions become independent of roughness presence at a sufficiently high Reynolds number up to a specific height from the roughness tip. This specific height is called the roughness sub-layer [85]. This is a highly turbulent anisotropic layer in which roughness length scales are significant in the layer. The thickness layer spans $2h$ to $5h$ (h is the maximum roughness height), where, normal to wall distance is calculated from the crest plane of roughness. Fig 2.15 shows different velocity profile layers formed close to a roughened surface.

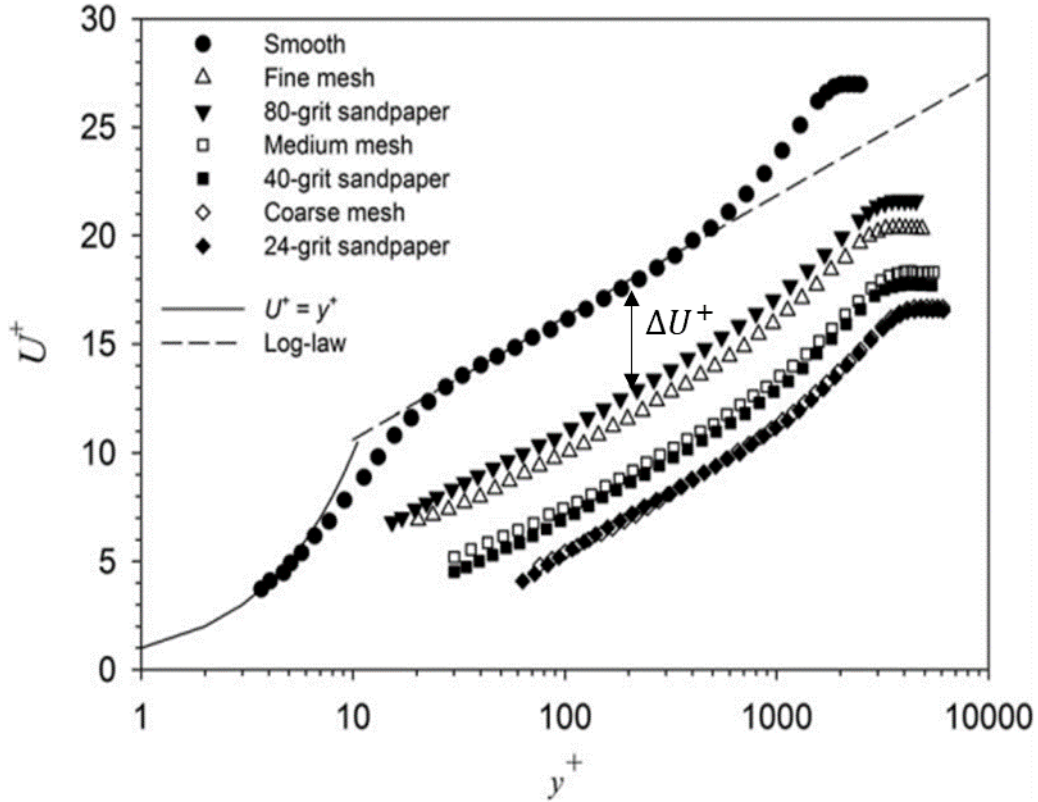


Figure 2.13: Mean stream-wise velocity comparison of different sets of roughness with smooth wall based on wall units [96].

2.3.2 Roughness function estimation

The logarithmic layer velocity is usually formulated in two different approaches, engineering [99] and meteorological [100]. In this regard, Eq. (2.5) could be recast into Eq. (2.6):

$$\frac{U^+(y)}{u_\tau} = \frac{1}{\kappa} \ln(y^+) + B_0 - \frac{\Delta U^+(h^+, L_i^+)}{u_\tau} \quad (2.6)$$

Eq. (2.6) is commonly known as the engineering form of the logarithmic layers, in which u_τ is the friction velocity defined based on pressure (form) and friction drag acting upon the roughness topology. Comparing Eq. (2.5) and (2.6), the roughness function is presented in scaled form as $\Delta U^+ = \frac{\Delta U^+(h^+, L_i^+)}{u_\tau}$ which is dependent on roughness geometrical length scale and friction velocity. This dependency has classified roughness flows into three distinct regimes: smooth, transitionally rough and fully rough. Those different regimes are normally shown against equivalent sand roughness height $k_s^+ = \kappa u_\tau / \nu$ of the Nikuradse experiment.

According to Nikuradse's experiment, $0 < k_s^+ < 5$ is a smooth region in which the roughened wall is dynamically smooth and cannot create any downward shift in the

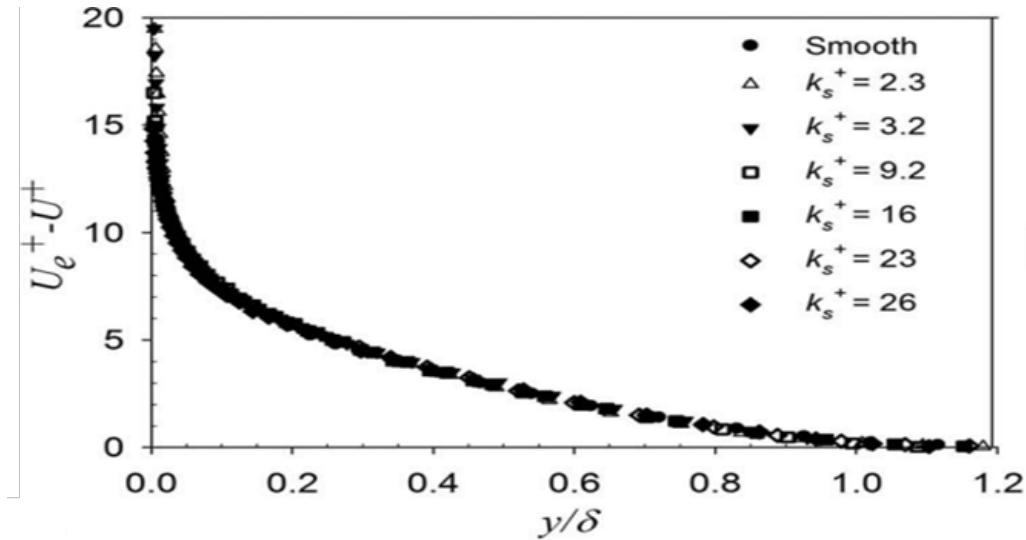


Figure 2.14: Velocity deficit profiles by [96].

logarithmic profile. For $k_s^+ > 70$, the Reynolds number effect on the roughness function becomes insignificant and the roughness length scale plays a crucial role. The roughness function shows linear dependency with equivalent sand grain roughness variation. The buffer zone, $5 < k_s^+ < 70$, is a transitionally rough regime in which flow is under equal influence from both the Reynolds number and roughness length scales (pressure forces). Fig. 2.16 shows different roughness function trends observed in rough transitional regimes reported by numerous researchers [101]. The riblet behaviour of roughened surfaces, which induces drag reduction and that has been observed in marine species (sharks and dolphins) belongs to this range [8], [9]. Due to the lower complexity and frequent occurrence of the fully rough regime in practical engineering applications, most roughened surface research was initiated and developed based on this range. Roughened flow is often seen in meteorological and urban-like applications. This analysis required an alternative approach in the logarithmic profile called the meteorological approach:

$$\frac{U(y)}{u_\tau} = \frac{1}{\kappa} \text{Ln}\left(\frac{y}{y_0}\right) = \frac{1}{\kappa} \text{Ln}\left(\frac{y-d}{y_0}\right) \quad (2.7)$$

In Eq. (2.7), y_0 is the roughness length, used as an alternative to the roughness function in engineering applications. Another parameter worth mentioning is d , which represents zero plane displacement due to the roughness effect. According to [103], [104], d is the mean height of momentum absorption by the roughness. Mathematically, d is the centroid of hydrodynamical forces acting on roughness. Instead of searching for roughness function dependencies, in the meteorological approach, the main goal is to find the roughness length relationship with geometrical features of roughness, which are not the roughness height. Frontal solidity and

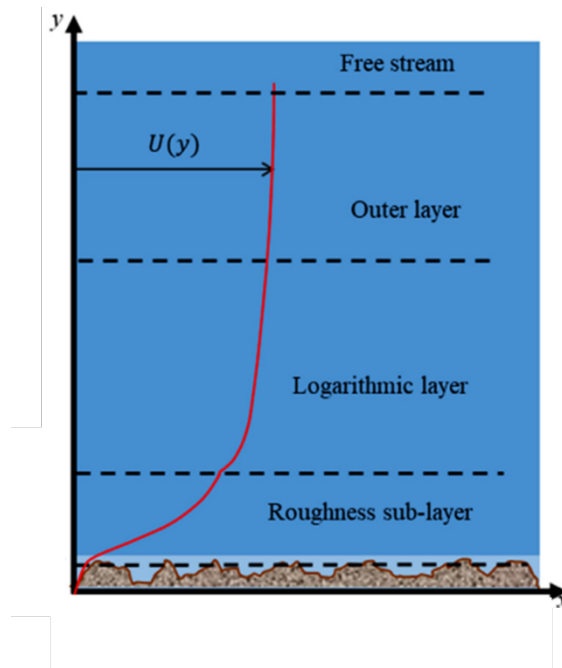


Figure 2.15: Turbulent velocity profile over roughness surface [98].

plan solidity(plan area density), defined as the ratio of frontal and plan area per unit wall-parallel area, respectively, have been used for that purpose [105]. Several experiments were conducted to determine the relationship between solidity and roughness length.

[106] were amongst the first who sought this relationship. They showed that y_0/d increases with increasing λ to a certain value λ_{max} , and declines beyond this value, where y_0 stands for the roughness length, d for roughness height and λ is frontal solidity. They attributed this decline to the mutual sheltering of roughness elements [100]. They found that λ_{max} is dependent on the roughness shapes. Also, a linear correlation exists between the frontal solidity and y_0/d for $\lambda < \lambda_{max}$ (Fig. 2.18) where z_0 accounts for the roughness length instead of y_0 in the original work. According to [101], for $\lambda_{max} \leq 0.15$ the roughness is sparsely distributed, in which case increasing the frontal solidity results in a roughness length increase, while for $\lambda_{max} \geq 0.15$ (dense distribution), increasing the solidity reduces the roughness length. [107], conducted several experiments in the fully rough regime, including cones, spheres, etc. He aimed to find a relationship that enables skin friction prediction in other Reynolds numbers. To this end, he used k/r_h as a geometric parameter to characterize flow where k is the roughness height and r_h is the hydraulic radius of the plate on the roughness. He found that the surface resistance is not only dependent on the k/r_h but also the roughness density (frontal solidity) S/S_f where S_f is the projected area of roughness surfaces on the normal plane to mainstream flow, and S is the total area of the plane that roughness elements are installed. He also defined

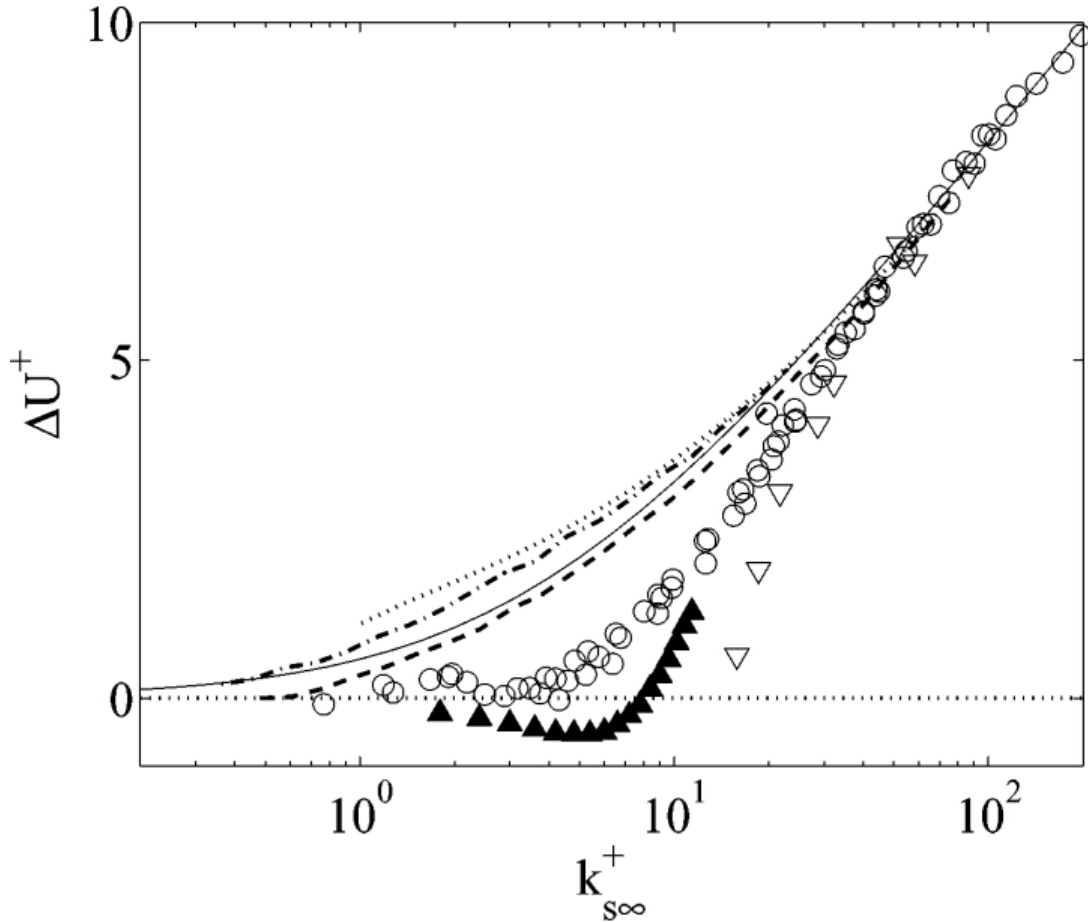


Figure 2.16: Roughness function for several transitionally rough surfaces, as a function of the Reynolds number based on the fully rough equivalent sand roughness. Uniform sand [91]; ∇ , uniform packed spheres [102]; \blacktriangle , triangular riblets [8]; ..., galvanized iron; —, tar-coated cast iron; -.-, wrought-iron [92];.

the skin friction for roughness elements as:

$$C_f = \frac{2W_r}{\rho u_k^2 S_f} \quad (2.8)$$

where $W_r = W - W_g$ is the force acting on the elements, W is the total resistance of the roughened surface, W_g is the resistance force occurring by a smooth wall between roughness elements, and u_k is the flow velocity at the tip of roughness elements. His results showed that C_f is independent of S/S_f for small values of solidity (roughness density) and decreases with higher values.

2.3.3 Equivalent sand grain roughness (k_s^+)

Equivalent sand grain roughness, k_s^+ , has become a universal parameter in the roughness literature. Many researchers have tried finding a universal formula correlating roughness function and k_s^+ . It has been widely known that within the fully rough

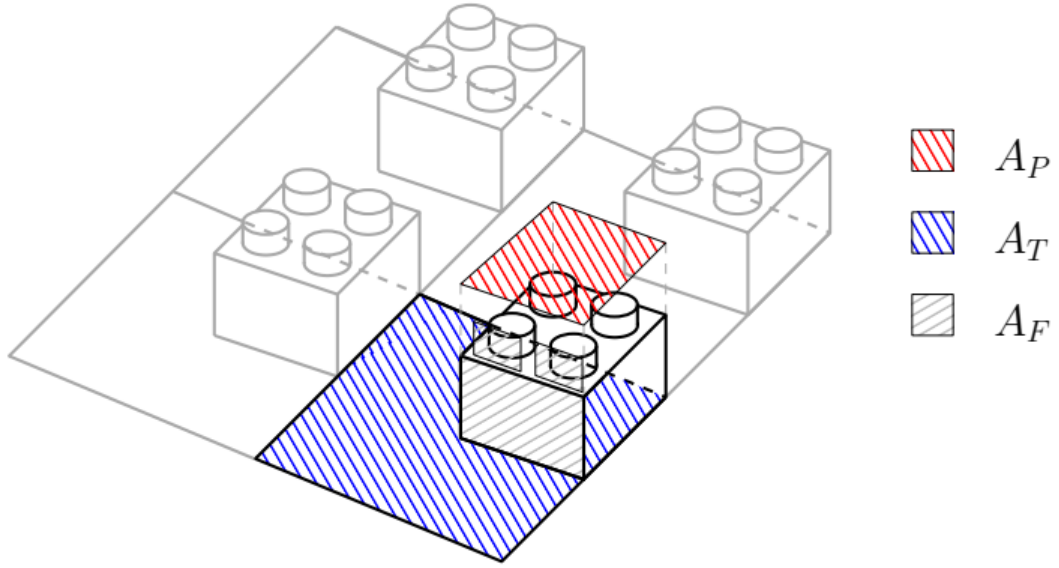


Figure 2.17: Frontal and plan area per unit wall-parallel area [105].

regime, the roughness function empirically correlates with k_s^+ through Eq. (2.9):

$$\Delta U^+ = \frac{1}{k} \ln(k_s^+) - 3 \quad (2.9)$$

It must be noted that k_s^+ is not a prior known parameter and should be calculated through experiments, then, the extracted k_s^+ is matched into some standard curves, such as the Colbrook interpolation formula [101], given by:

$$\Delta U^+ = \frac{1}{k} \ln(1 + 2.6k_s^+) \quad (2.10)$$

[108], [109], proposed some correlations based on 2D roughness. [110] and [111], conducted a study to determine whether geometric parameters correlate with the roughness density. They used the Schlichting experimental database [107] for their analysis. Their new roughness density incorporated a new ratio that did not exist in Schlichting's roughness density.

$$\Lambda_s = \frac{S}{S_f} \left(\frac{A_f}{A_s} \right)^{-1.6} \quad (2.11)$$

They proposed their two-dimensional roughness as:

$$\frac{k_{s,eq}}{k} = \begin{cases} 0.003215\Lambda_s^{4.99} & 1.4 \leq \Lambda_s \leq 7.8 \\ 8 & 4.89 \leq \Lambda_s \leq 100 \\ 151.71\Lambda_s^{-1.3376} & 13.25 \leq \Lambda_s \leq 100 \end{cases} \quad (2.12)$$

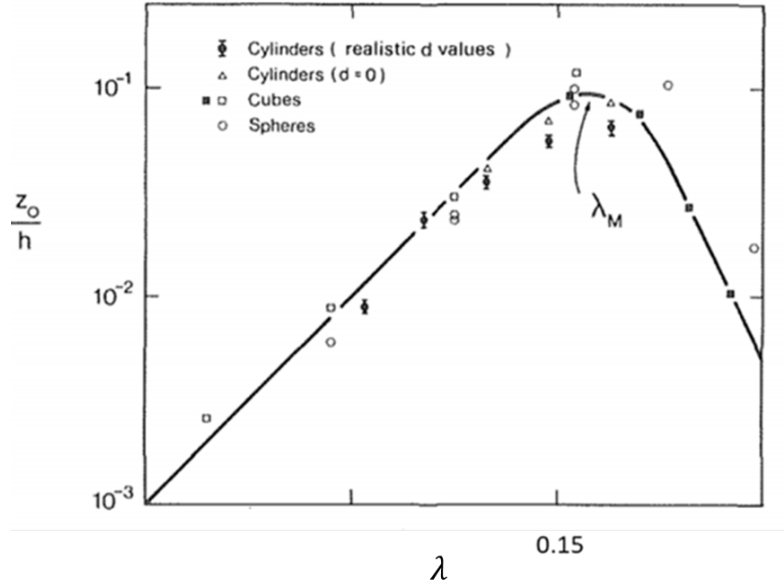


Figure 2.18: Roughness length against frontal solidity [100].

And 3D roughness as:

$$\frac{k_{s,eq}}{k} = 0.003215\Lambda_s^{4.99} \quad 16 \leq \Lambda_s \leq 200 \quad (2.13)$$

In the above formulas, A_f is the frontal area of a single roughness and A_s which is the wetted area of a single roughness.

[112] proposed a new correlation based on data from [111]. For three-dimensional irregular roughness, they replaced A_f/A_s ratio in Λ_s with S_f/S and S_w is the total wetted area of total roughness elements. The updated version of the correlation based on [110] work is:

$$\frac{k_{s,eq}}{k} = \begin{cases} 1.538 \times 10^{-5}\Lambda_s^{5.683} & \Lambda_s \leq 7.842 \\ 1.802\Lambda_s^{0.0303} & 7.842 \leq \Lambda_s \leq 28.12 \\ 255.5\Lambda_s^{-1.454} & 28.12 \leq \Lambda_s \end{cases} \quad (2.14)$$

[113], proposed a correlation for various geometrical shapes. They adopted their roughness density parameter from [114]:

$$\Lambda_k = \lambda_k \frac{k}{S_m} \quad (2.15)$$

S_m is stream-wise roughness length and λ_k is the ratio of total surface area to total frontal area to stream-wise flow. The correlation formula was presented as:

$$C = \begin{cases} 10.65 \log_{10}(\lambda_k(\frac{k}{b_m})^{0.87} \times (\frac{A_f}{A_w})^{0.44} - 7.59) & \Lambda_s \leq 6 \\ -5.75 \log_{10}(\lambda_k(\frac{k}{b_m})^{0.55} \times (\frac{A_f}{A_w})^{1.38} + 5.78) & \Lambda_s \leq 6 \end{cases} \quad (2.16)$$

[115] considered the feasibility of a correlation between roughness function and geometrical features of roughness surface. He found that the root-mean-square of roughness height and skewness and kurtosis of roughness profile probability density function has a role in the roughness characterization. Other geometrical parameters such as peak-to-trough roughness height, mean surface elevation, and effective slope can also be important in determining roughness function. In this regard, the effective slope distinguishes between wavy roughness and regular roughened surface. Roughness with ES (Effective Slop) value less than 0.35 is known as wavy roughness. Effective slop is defined as Eq. (2.17) where L is the sampling length, r is the roughness amplitude, and x is the stream-wise direction.

$$ES = \frac{1}{L} \int \left| \frac{\partial r}{\partial x} \right| dx \quad (2.17)$$

[90] reviewed previous works on predicting surface frictional drag on rough surfaces. They mentioned that since most of the former skin friction correlations were established on regular roughness, they cannot estimate general irregular roughness. Therefore, they proposed a new correlation based on roughness profile statistics. Their proposed correlation for equivalent roughness was:

$$k_{s,eq} \approx 4.43 k_{rms} (1 + s_k)^{1.37} \quad (2.18)$$

k_{rms} is the root mean square of roughness heights, and s_k is the skewness of surface elevation probability density function.

2.3.4 Riblet effect

The roughness effect is well known for its resistance effect on the overlying turbulent flow. However, the roughness, known as riblet, can behave as a resistance reducer under special circumstances. riblet is an array of tiny roughness, normally protruding into the flow and aligned with the flow direction [116]. riblet patterns are frequently seen on the surface skin of marine species such as sharks. This feature enables them to reduce drag and move with high manoeuvrability in the water. Fig. 2.19 and Fig. 2.20 illustrate a common pattern that grows on different shark species.

The riblet effect is shown in Fig. 2.16 with \blacktriangle symbols. For $k_s^+ < 10$, it is apparent that using some geometrical shapes, such as triangular geometries, as a roughness can result in roughness function reduction, which classifies riblets as a transitionally

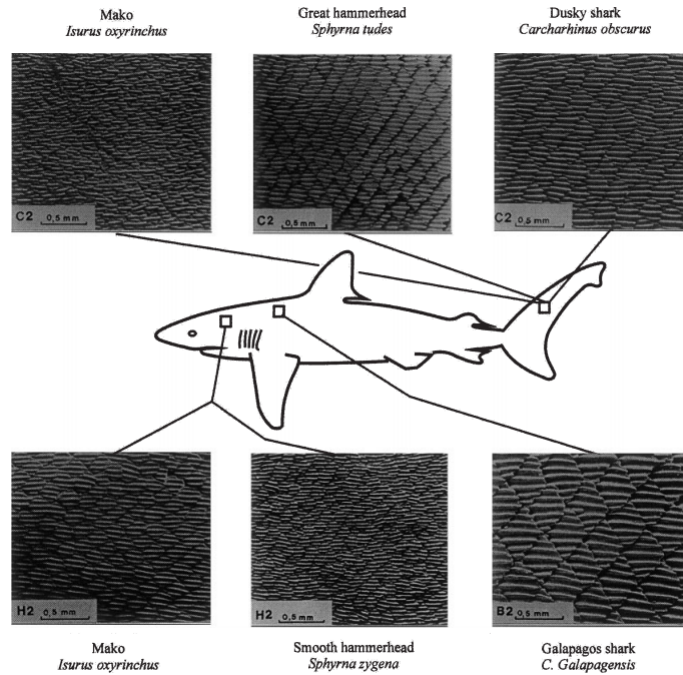


Figure 2.19: Different scale pattern grow on different sharks [117].

rough regime. Due to riblet drag reduction attributes, riblets became an exciting research topic. Different riblets of very different shapes were tested into wind tunnels, which reduced skin friction by up to 10% compared to smooth walls [116]. Drag reduction has been interpreted as resulting from the prevention of stream-wise vortex by limiting span-wise spacing between riblets. According to experiments by [118] and [119], which proved the existence of low-speed streaks that form close to walls and calculated their length scales, the riblets hamper the penetration of the streaks close to a wall, as a result, the viscous layer grows in thickness, which leads to a decrease in the velocity gradient at the wall [9] which can reduce skin friction. [120], has done numerous experiments on different shapes in which a maximum drag reduction of 7-8% was achieved for lateral spacing of approximately $S^+ = 15$. To improve experimentation on riblets, water tunnels were replaced by oil flow. [8] used an oil tunnel to conduct several tests on blade-shaped and trapezoidal-groove riblets, proposing trapezoidal-groove as a better alternative from a manufacturing point of view. It is worth mentioning that the drag reduction that can be achieved is highly dependent on the geometrical shape of roughness. Fig. 2.21 shows the amount of drag reduction against lateral scaled spacing value for a triangular shape with a 60-degree tip angle. [116] proposed lateral surface within riblets elements as a better alternative.

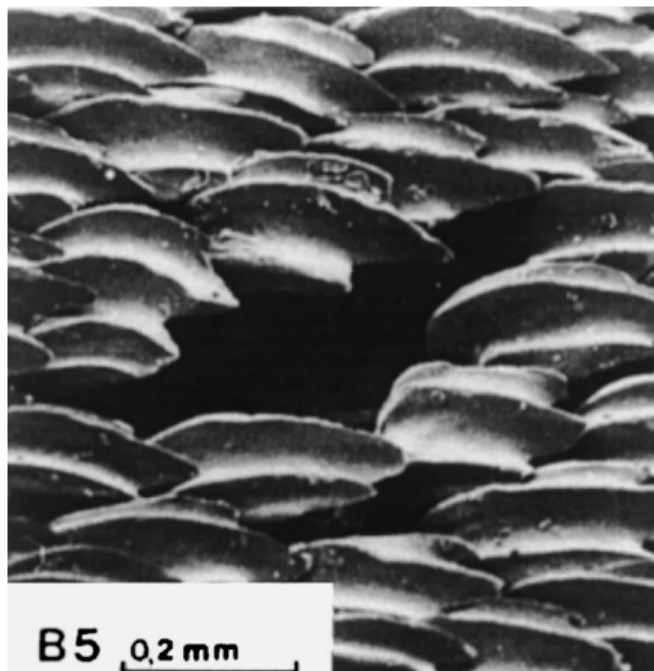


Figure 2.20: A closer look at surface patterns grow on shark skin (Great white shark [117]).

2.4 High-fidelity numerical simulation of roughened flow over the past twenty years

With the advent of super-computing since 1970, several industrial turbulence models have been proposed to tackle turbulent flow problems. In the final years of the 90s, CFD found its way into turbulent flow problems with roughened surfaces. A significant amount of computational resources was needed to properly resolve turbulent flow scales around an array of roughness. Therefore, studies focused initially on two-dimensional geometries using two equations RANS models. More complex turbulence models and geometries were studied as computational resources gained power. Applying DNS and LES turbulence approaches on irregular roughness turbulent flow helped to gain insight into flow features within and over roughness, which was not always possible by experiments due to errors inherent to flow measurements. This section summarizes turbulent flow simulation progress with two and three-dimensional geometries over the past thirty years.

2.4.1 Regular geometries

Two-dimensional rib geometry is one of the most common geometrical shapes used in experimental tunnels for roughness flow research (Fig. 2.22).

Experimental methods suffer from the inherent drawback of low resolution [122];

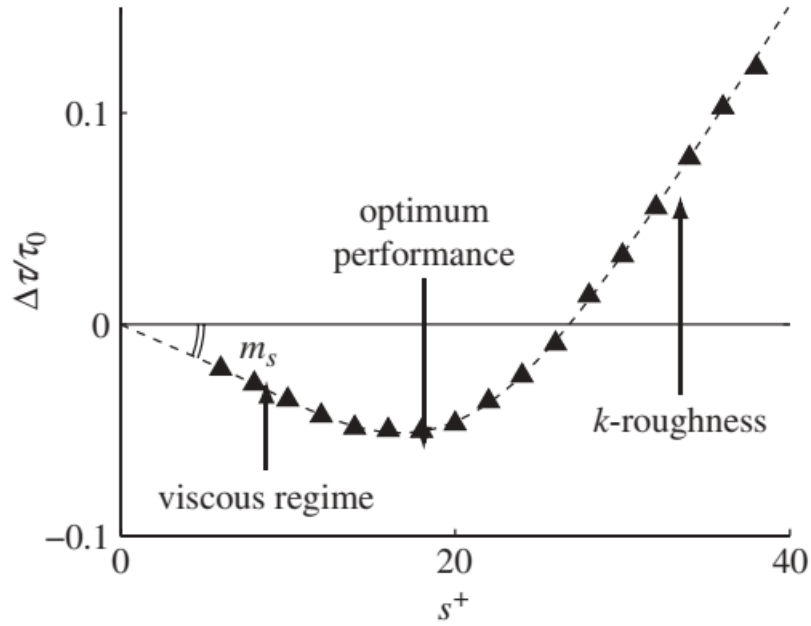


Figure 2.21: Drag reduction against triangular riblet with 60-degree tip angle [116].

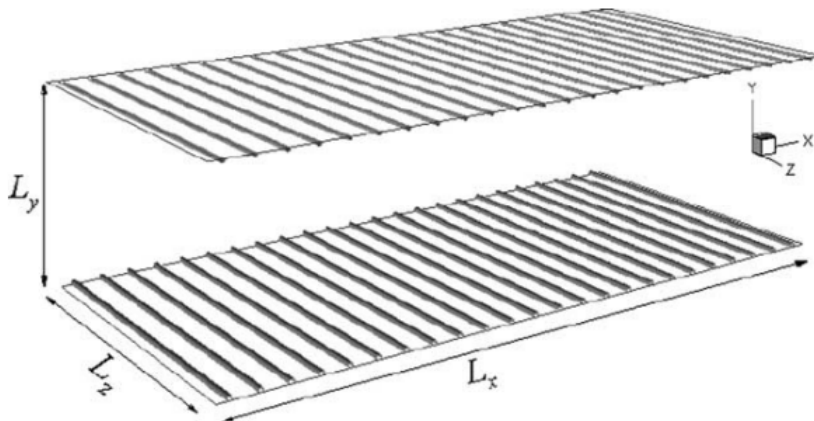


Figure 2.22: Geometry of a turbulent channel flow with two-dimensional ribs [121].

so high-fidelity numerical methods appear as an attractive alternative. Researchers started relying on DNS and LES simulations of two-dimensional ribs to enhance insight over roughened flow.

DNS simulations were performed on two-dimensional transverse ribs [123]. The results were in good agreement with Townsend's similarity of walls. Also, it was found that 2D ribs slightly modified the hairpin vortices.

DNS simulations were carried out on 2D transverse ribs with a broad range of w/k where w is the pitch distance of mounted ribs, and k stands for ribs height [124]. It was found that for $w/k = 7$, the form drag (pressure drag) achieved its maximum value, coinciding with the minimum skin friction value. Their visualization of flow structures on the roughened wall verified [125] observations that stream-wise struc-

tures are shorter than over smooth walls. Also, their result was consistent with [126] findings over a mesh roughness, which showed that two-point correlations become shorter while span-wise correlations are larger. [121] used a DNS approach in a transitionally rough regime and observed different flow patterns in the cavity between two consecutive ribs. In this case, Instead of a single vortex, two counter-rotating flows started filling in the gaps. Roughness is well-known for inducing a downward shift in the velocity profile (roughness function) when compared to a smooth wall. Historically, in 2D span-wise ribs (Fig. 2.23) roughness features have been classified based on their geometrical configurations. This was made by defining the ratio between the distance of two consecutive stream-wise roughness elements (w) over the height (k) of roughness. Usually, a roughness for $w/k \leq 1$ is considered as a d-type roughness, while sometimes this ratio has been extended to 3 [99], [127].

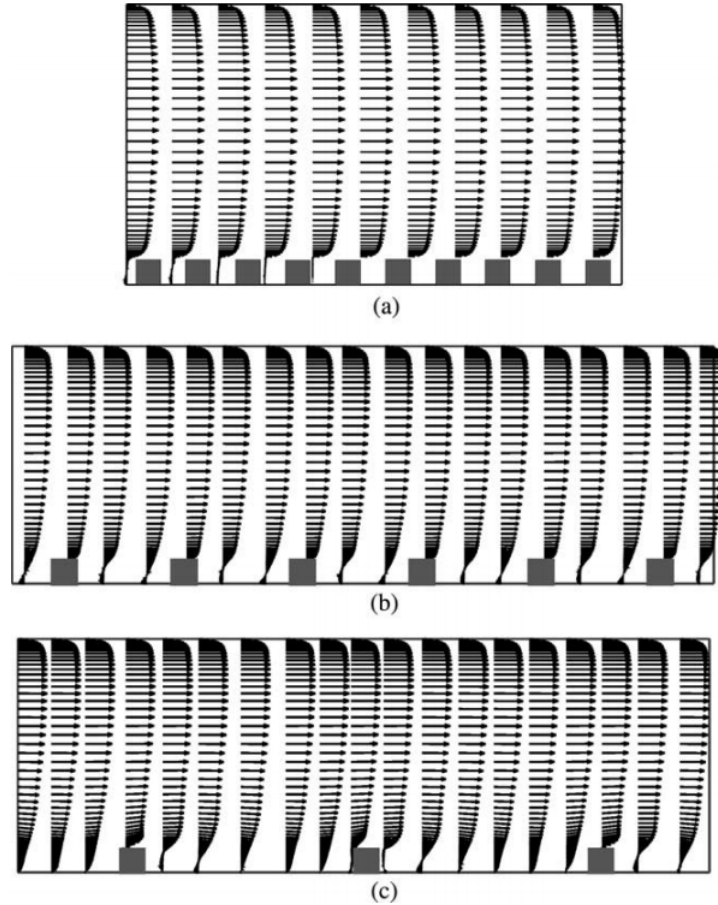


Figure 2.23: Roughness types with their respective velocity profiles.(a): d-type, (b): semi-k-type and (c): k-type [127].

For a k-type roughness, a correlation exists between the roughness function and k^+ (Eq. (2.19)):

$$\Delta U^+ = \frac{1}{k} \text{Ln}(k^+) + C \quad (2.19)$$

Where C is dependent on density function and roughness nature[99].

This correlation could not be found for the d-type case. On the other hand, [99] proposed a similar correlation for d-type roughness, which does not depend on roughness height and is a function of channel height or pipe diameter(Eq. (2.20)):

$$\Delta U^+ = \frac{1}{k} \text{Ln}(d^+) + B \quad (2.20)$$

B is a function of the roughness density and the nature of roughness.

It was perceived that the significant difference in the behaviour of these two types of roughness originates from vortexes that shed from cavities to the overlying flow. Unlike k-type roughness, it was envisaged that the d-type roughness could not shed vortexes toward the overlying flow. It was shown by [128] and [129] that this is not the case, and occasional shedding occurs with lower intensity. According to [129], the most important factor that distinguishes a k-type from a d-type is the distribution of pressure (form drag) and wall shear stress (friction drag) around the roughness element. This agrees with how k-type and d-type roughness behave at different Reynolds numbers. They carried out a series of DNS simulations over a broad range of w/k and found that while the skin friction drag is the dominant force in d-type roughness, form (pressure) drag plays a crucial role in k-type. Although their results verified the k-type (Eq. (2.19)), the proposed d-type formula, Eq.(2.20), failed to collapse the numerical data in [129]. [86] performed a DNS high-resolution simulation with over 70 million computational cells on a k-type roughness (Fig (2.24)). In his work, regions with high turbulent kinetic energy were found close to the roughness (roughness sub-layer), which were not found in the (equilibrium layer) logarithmic layer. They also showed that the turbulent RANS models perform poorly near rough surfaces. Turbulent structures play a crucial role in characterizing turbulent flow

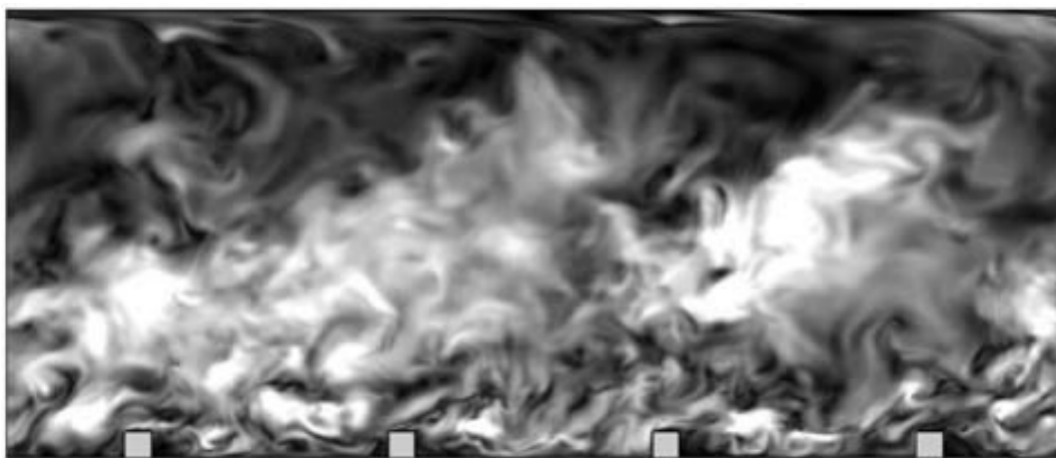


Figure 2.24: High-resolution flow over k-type roughness [86].

next to the walls. Roughness has an undeniable role in modifying these structures.

In this regard, most research attention has focused on the roughness impact on the turbulent statistics and structures of the flow.

[130] compared the budget of Reynolds stress of fully turbulent flow over arrays of transverse circular and square roughness with pitch-to-height ratios of 4 and 8. It was shown that the velocity pressure gradient term corrects the energy budget to be more isotropic. They mentioned that turbulent convection is an important factor brought by overlying flow to the cavity between roughness and being dissipated. [131], considered the interaction of overlying flow with wall boundary conditions by applying slip conditions to smooth walls. It revealed that drag reduction and roughness effects are achievable by using slip wall condition of walls in separate stream-wise and normal-to-wall directions.

Furthermore, span-wise slip condition contributed to no significant change similar to unperturbed channels. This implied that the roughness effect could be replicated only by applying slip boundary conditions in a normal-to-wall direction. This gave [132] the idea of using normal-to-wall Reynolds stress instead of roughness topology to characterize the roughness function. They showed that the roughness function is correlated with normal to-wall Reynolds stress at the gap between crest planes. The suggestion of using normal-to-wall Reynolds stress rather than the geometrical roughness shape proved impractical in d-type roughness.

Along with the simulation advancements in 2D transverse geometries and the necessity to analyze turbulent flow over urban-like structures (Fig. (2.25)), researchers turn their attention to more realistic three-dimensional shapes.

[134] used LES simulations to investigate an array of cubes in a fully developed turbulent flow. Their results were in good agreement with experimental results. They showed that the dispersive momentum fluxes were quite large between cubes and reduced when they got further from cubes in the normal direction. Also, they confirmed the existence of a conventional flow regime between roughness reported by prior researchers and the formation of elongated vortical streaks above cubes, identical to turbulent structures over smooth surfaces. [135] conducted DNS simulations on two and three-dimensional roughness with small consecutive separation. Since, for this type of roughness (d-type), the roughness function is weakly correlated with the roughness geometry, they confirmed that the correlation exists between the roughness function and mean root square (RMS) of normal to wall velocity at the roughness crest plane within gaps between roughness crests. This was shown before in their related work [132] on the two-dimensional longitudinal and transversal bars. They also showed that three-dimensional roughness affects the overlying flow more than two-dimensional roughness.

[87] conducted numerous LES and RANS simulations of urban-like shapes at various Reynolds numbers. They compared turbulent statistical results from DNS at

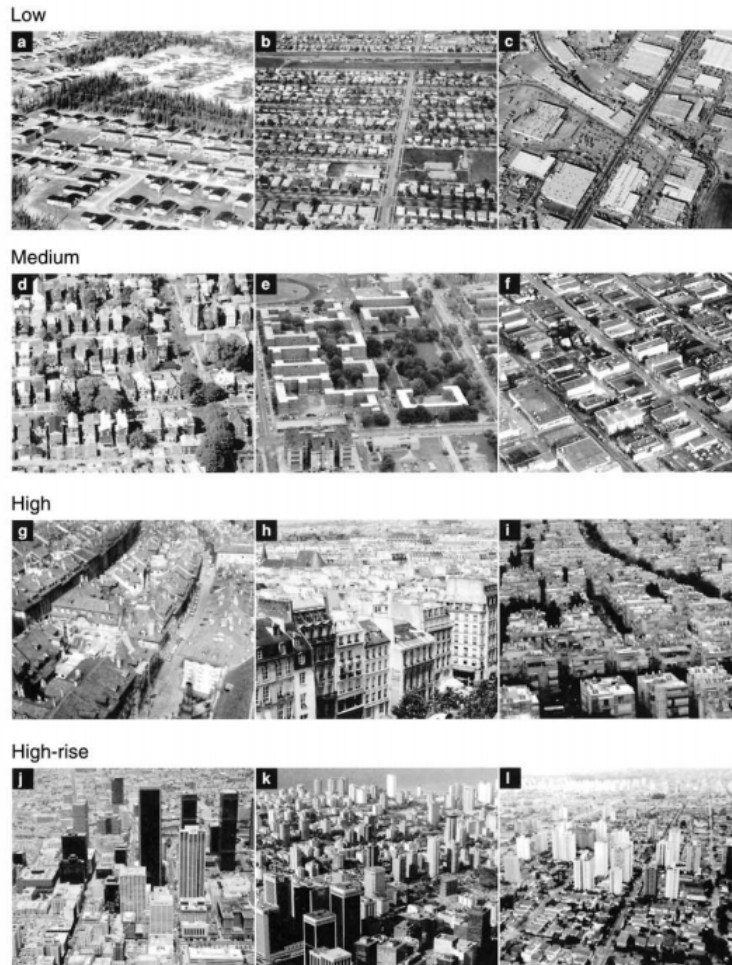


Figure 2.25: Photographs from urban-like morphologies [133].

Reynolds number $Re = 5000$ and LES at $Re = 5 \times 10^4$ and $Re = 5 \times 10^6$. They showed the results were almost identical except for fine scales close to the walls. Also, the inertial sub-range of the calculated turbulent kinetic energy spectrum diagram was wider in their urban-like obstacle flow. By this, they concluded that unlike smooth wall or blunt obstacle cases, urban-like flows are affected by large scales more than small ones, making LES models an efficient choice capable of producing results similar to DNS. Last but not least, they suggested that by using a smaller computational domain (in order of 4-16 times larger than roughness heights), there would be no significant change in the turbulence statistics up to the height of $3.5h$ measured from the crest plane where h is roughness height. This could not be applied to a smooth surface due to long low and high-speed streaks.

[136] were among the first who performed a DNS simulation on a non-conventional geometrical topography. They used an egg-carton pattern as a roughness texture, mounted on one side of a channel flow. Their aim was more to investigate roughness impact on the outer boundary layer. To this end, they compared the results of three roughness cases of $h^+ = 5.4, 10.8, 21.6$ for $Re_\tau = 400$ with a smooth wall. They ob-

served that although the velocity fluctuations in the inner layer were intensified by the roughness effect, no significant changes were observed in the outer layer's vorticity fluctuations. Their assessment of roughness length scales suggests that span-wise length scales are more important than stream-wise lengths regarding their impact on the outer boundary layer, while neither is significant in velocity profile variations.

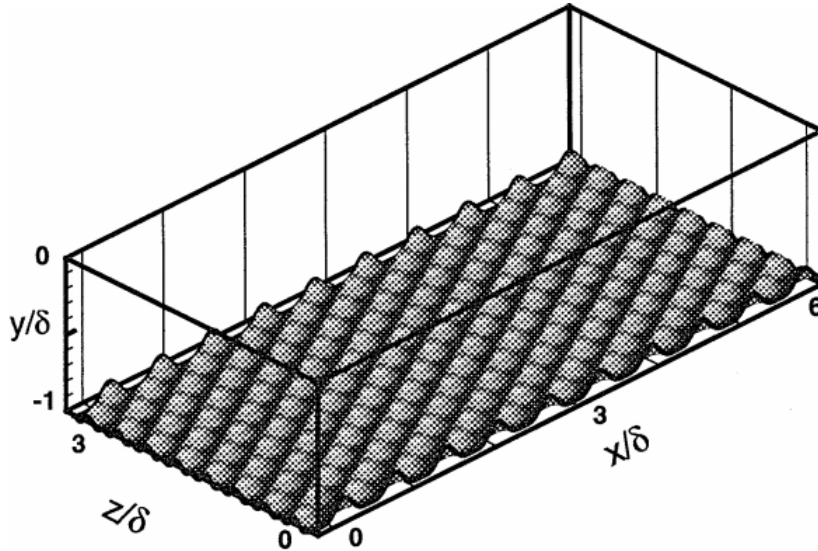


Figure 2.26: Egg-pattern roughness [136].

[137] presented DNS simulations of staggered arrays of cubes in a fully rough regime. To have an interpretation of flow within cubes, they applied spatial averaging over the results. [138], used the DNS method to simulate staggered arrays of cubes with a plan area density range from 0.04 to 0.25. They identified a plan area density of 0.15 to be the one that sustains the maximum surface drag. Also, they discussed over overflow dependency of von-karman constant κ in their cases. [139] performed DNS and LES simulations on a fully turbulent channel covered with hemispherical roughness at $Re_\tau = 180, 400$, simulating situations where bubbles attached to the surface of boilers (Fig. 2.27). They studied two different roughness heights $k^+ = 10, 20$ with a height ratio to spacing ranging from 2 to 6. Their simulations showed that, close to roughness, while there is no significant variation in normal to wall fluctuations, there is a decrease and increase in stream-wise and span-wise fluctuations, respectively. Their results indicate that similar turbulent structures on smooth wall forms on the hemispherical roughness surface but with a height shift equal to roughness height k^+ .

[140] implemented the first body-conforming mesh on DNS in a three-dimensional pipe with sinusoidal roughness (Fig. 2.28) at $Re_\tau = 180, 360, 540$. They used different roughness wavelengths and heights independent from each other and found that the average roughness height k_a^+ effect on the roughness function is more important

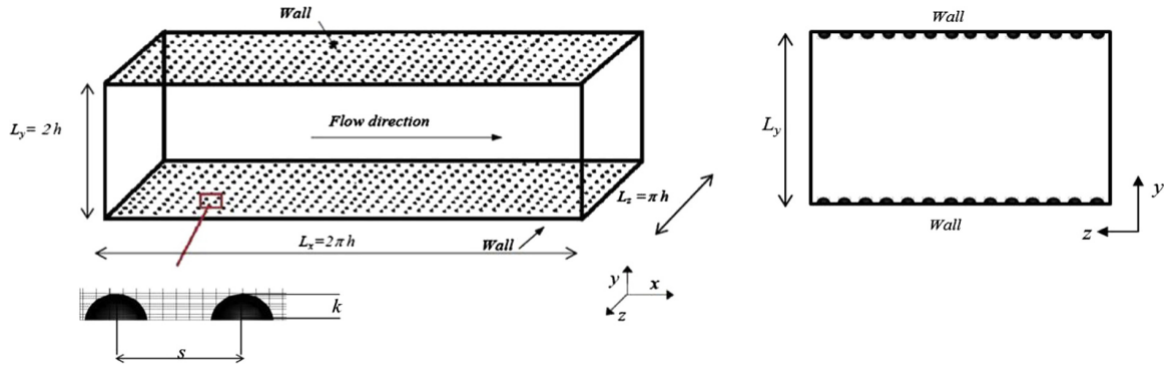


Figure 2.27: Schematic of a channel flow with one side fully covered with hemispheres [139].

than the roughness wavelength. They have also studied the effect of the effective slope (ES) on the roughness function and showed that by increasing the roughness height, ES would increase, which leads to a roughness function increase. They also calculated the virtual origin of roughness by three different momentum absorption methods [103], locations where velocity reaches zero and wall shear stress method (collapsing total shear stress outside roughness layer), respectively. The shear stress method yielded more accurate turbulence statistics than the other two methods.

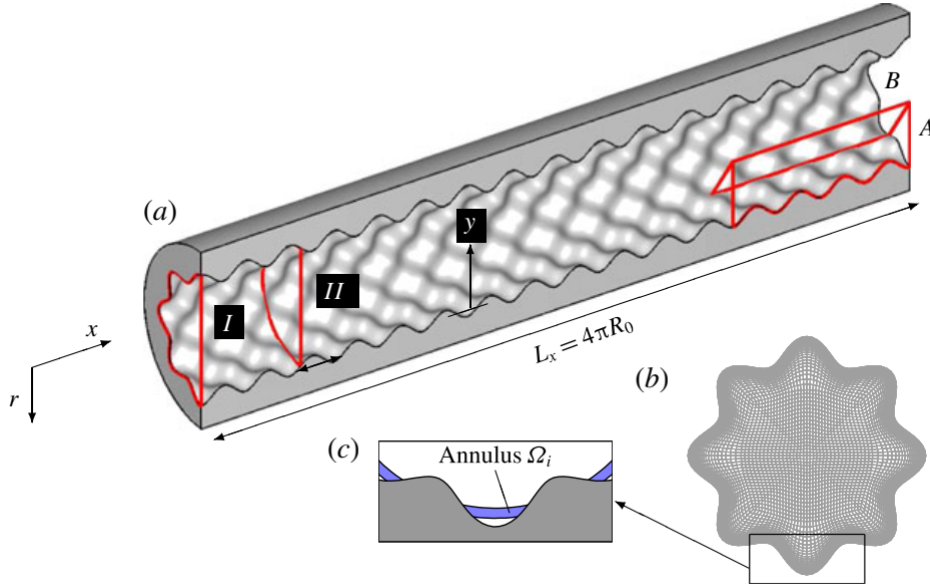


Figure 2.28: The pipe with internal sinusoidal roughness geometry [140].

[141] performed a series of LES simulations over arrays of rectangular prism elements with different geometrical features. They aimed to confirm the exponential shape of the mean velocity profile (as found previously by [142] that forms between two consecutive elements. They used the general velocity profiles to introduce an analytical model for predicting exerted drag by the turbulent flow on rectangular prism

elements. To this end, the Karman–Pohlhausen integral approach was employed using the proposed gap velocity profile and assuming a shape function. [143] used the LES model to examine a half-channel flow covered with aligned and staggered arrays of rectangular prisms (Fig. 2.29). They showed that aligned cubes in prisms with high aspect ratios show an initial increase in friction velocity and roughness length until they reach a plateau. Further increase in the aspect ratio did lead to further change. However, these staggered prism results indicate a continuous increase in both u_τ and the roughness length for the surface cover density studied.

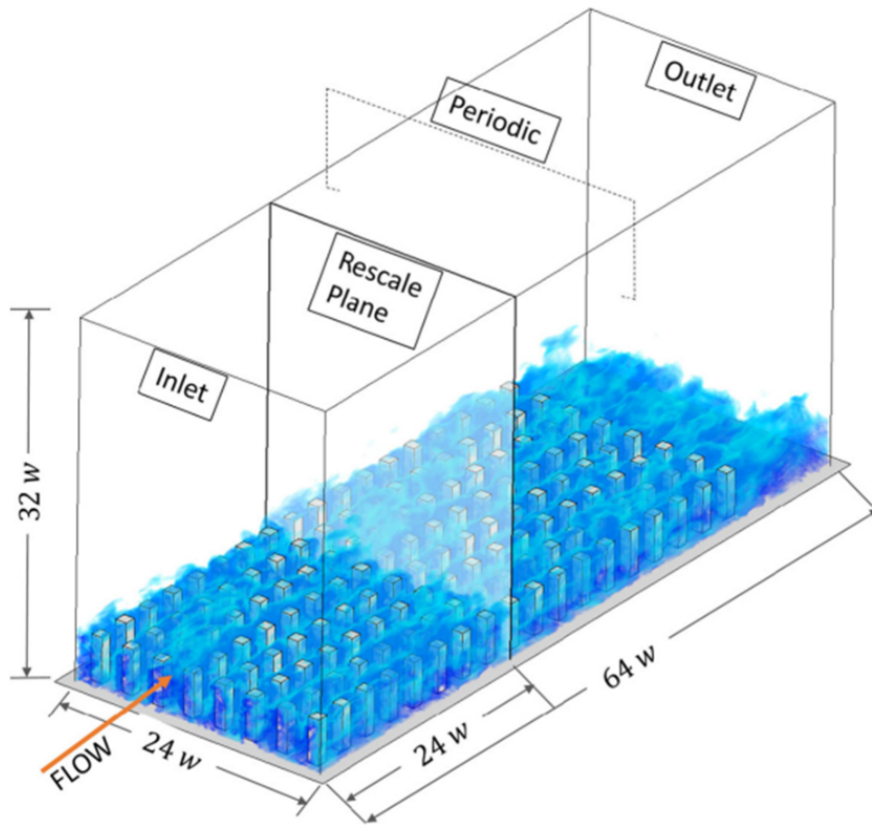


Figure 2.29: Aligned and staggered arrays of rectangular prism used in [143].

[144] conducted a DNS simulation over a transitionally rough wall with a sinusoidal surface. They used a solidity range from 0.05 to 0.54 with fixed Reynolds roughness based on $k^+ = 10$, where k is the sinusoidal semi-amplitude with varying sinusoidal wavelength. To this end, the minimal-span channel technique was adopted (introduced by [145]) to reduce the computational cost. Their simulation results were in good agreement with the literature regarding roughness solidity behaviour in three-dimensional geometry. Also, they proposed a model for the asymptotic behaviour of dense roughness ($\Lambda \rightarrow \infty$), which their simulation data provided good agreement with. They found that, in a sparse region, increasing density will lead to a decrease in the peak of stream-wise turbulent kinetic energy, while in a dense region, increasing density will lead to a decrease in the peak of stream-wise turbulent kinetic

energy. Their analysis of differences in integrated momentum balance between rough and smooth surfaces verified their simulation results on the effect of the solidity.

Over the past twenty years, turbulent high-fidelity methods have also been successfully used on riblet-like geometries to investigate the riblet effect. In [146] DNS method is used to make a distinction between thin longitudinal rectangular ribs with different spacing. They used $S^+ = 13$ to 41 spacing sizes in terms of wall units, which S^+ stands for transverse spacing of two consecutive ribs scaled with respected length scales. They found that using a spacing of $S^+ = 18$ can lead to a maximum drag reduction of 11%. Also, spacings larger than 30 were found to result in a drag increase.

[116] used DNS to analyze over-lying flow and riblet interaction. They found that the transverse groove section is a better length scale choice in larger riblets to characterize the riblet effect breakdown. They also attributed this breakdown to forming quasi-two-dimensional vortices below $y^+ = 30$. This structure had already been noticed in flows with transpiration.

Using high-resolution LES, [147] compared scalloped shape riblets results ranging from zero adverse pressure gradient to mild one (Fig. 2.30). They simulated different riblet sizes with different span-wise spacing and compared them with published experimental studies. According to their finding, there was only a slight increase in the performance of riblets with moderate adverse pressure gradient. They observed that stream-wise velocity and vorticity fluctuations and turbulent kinetic energy were scaled with riblet width, not drag reduction parameter. On the other hand, Reynolds stress was indeed scaled with drag reduction.

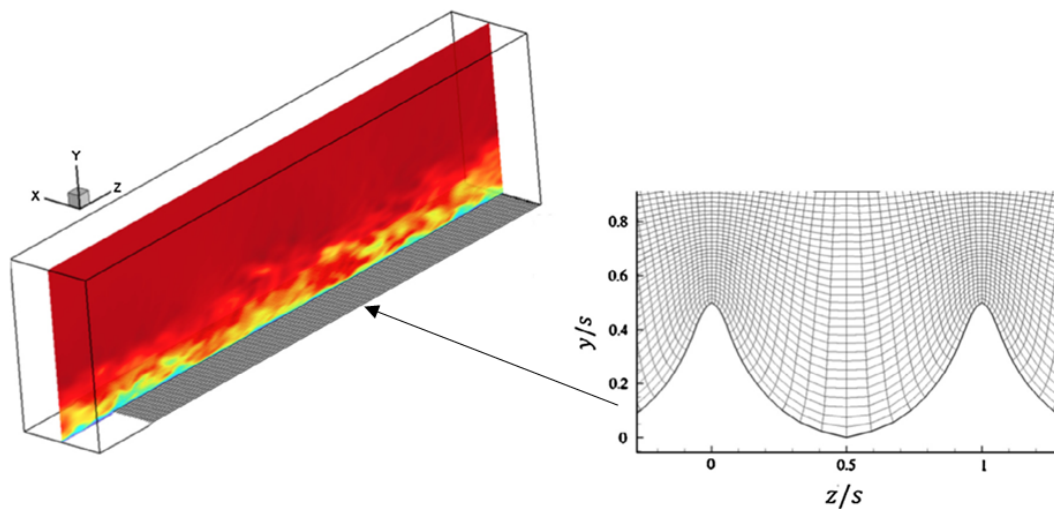


Figure 2.30: Scalloped shape used as riblet profile to cover the bottom wall [147].

2.4.2 Irregular geometries

Regular roughness comprises simple geometries in which only a few length scales participate in the over-lying flow characterization. A regular roughness is mainly designed to serve a particular purpose in engineering applications. riblet is one of the most well-known examples of such designs. Simple topology and clear roughness height identification are advantages of regular irregular roughness, making it easier to study. Such regular roughness is difficult to produce in reality. The regular well-designed surface modifications are typically somewhat irregular at least due to production errors. Generally speaking, due to the high number of length scales that play a role in an irregular roughness problem, results from the study of regular roughness are not directly applicable to irregular surfaces. At the same time, irregular roughened wall simulations are more difficult to simulate. The main issue relates to the meshing of more complex geometry and implications for mesh quality. Fully irregular roughness topologies are distributed randomly over space. Particular computational and statistical techniques must be used to define the roughness of geometrical shapes. Below is a summary of the past decade's successful high-fidelity simulations on irregular roughness.

[148], used LES approach on a 2D random roughness, investigating effective slope impact on roughness function. To generate the random boundary roughness, they used the superposition of the first three terms of the sinusoidal Fourier series with random amplitude and maximum wavelength (Fig. 2.31).

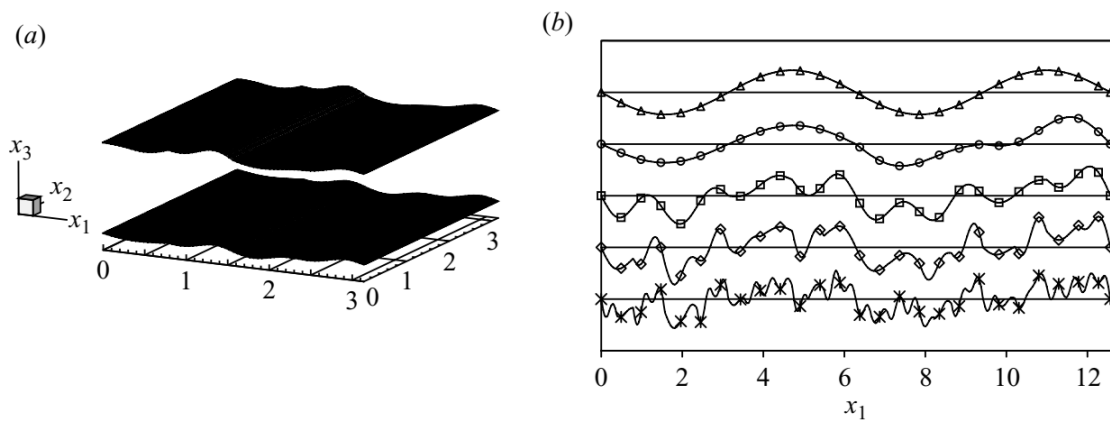


Figure 2.31: (a) clip from the layout of the channel flow. (b) random roughness profiles are generated in a stream-wise direction. [148].

[149] performed DNS simulation on zero pressure gradient boundary on a sand-paper roughness. Their results showed that random roughness highly impacts the shear and wall-normal Reynolds stresses. Also, they observed increased injection due to mixing effect enhancement.

[150] carried LES simulations in transitionally and rough regimes over sand-grain

roughness and five realistic roughness replicated from hydraulic turbine surfaces. They showed that roughness topography impacts the range of applicability of the equivalent roughness correlations as the critical value of the effective slope that determines the waviness of roughness changes.

[151] presented DNS simulations of 17 irregular surfaces at a Reynolds friction number of 180 while being transitionally rough (Fig. 2.32). They aimed to find the most important parameters suitable for incorporation in empirical correlations. They developed several models based on roughness parameters for the peak of turbulent kinetic energy and roughness function. They showed that the root mean square of roughness height and stream-wise correlation

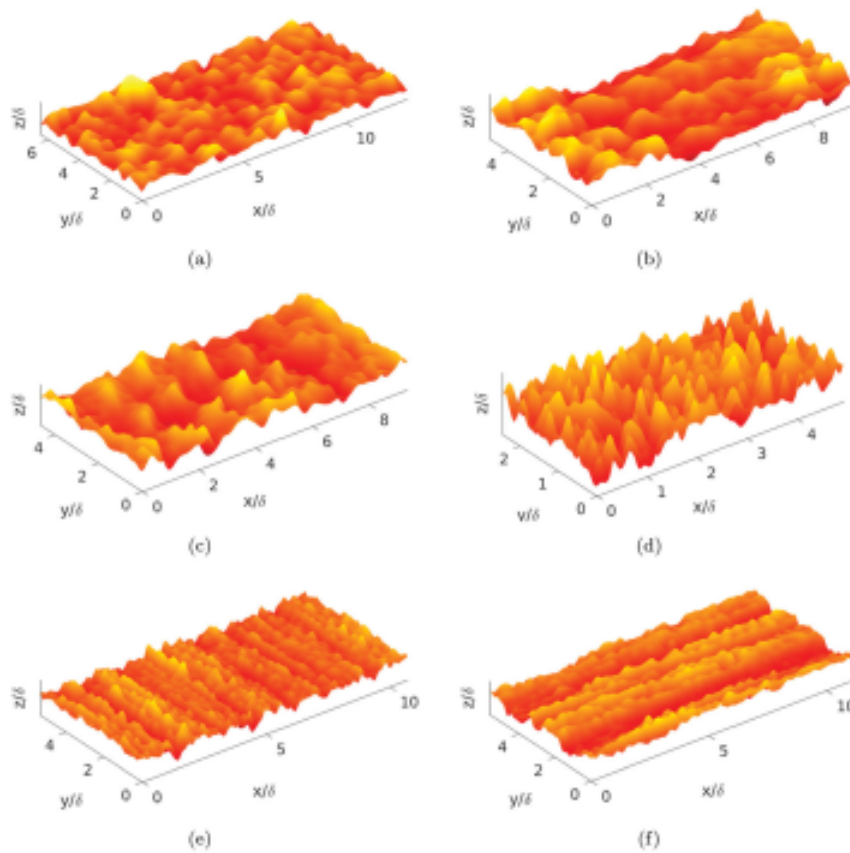


Figure 2.32: Six out of seventeen realistic roughness topologies produced and used in work of [151].

[152], investigated irregular roughness scanned from graphite surface. They used Fourier space filtering to remove small scales in the stream-wise and span-wise directions. The impact of the roughness was investigated through different sizes of filters. Using fine filters, variables such as Reynolds stress, mean velocity and dispersive stresses were in good agreement. With increasing filter size, those parameters began to deviate.

[153], carried out DNS simulations on fourteen randomly generated rough surfaces,

allowing varying roughness parameters. Their main goal was to investigate the possibility of characterizing surface roughness using wall normal turbulent fluctuations at the crest of irregular roughness based on [132]. [132] correlation was in good agreement when the roughness sizes were similar. By changing roughness element sizes, the correlation still holds somewhat but with less linearity. Depending on the location of the crest, their DNS results were over-predicted when compared with the correlation by a maximum of 15%. They argued that this is due to the dependency on wall-normal ejection to roughness heights. Also, they suggested that there is a linear correlation between roughness function and normal-to-wall velocity fluctuations exist when the crest location is between the mean wall distance of all roughness peaks and the statistical height of the highest roughness peaks.

[154], proposed an algorithm for generating a surface fouled with barnacles. [155] used LES methodology to investigate arrays of macro bio-fouling species (barnacle) on a developing turbulent boundary layer flow.

[156], used the high-resolution LES method on an open channel to resolve turbulent kinetic energy close to a naturally rough bed constituted from pebble layers (Fig. 2.33). They also suggested a new visualization method based on turbulent kinetic dissipation.

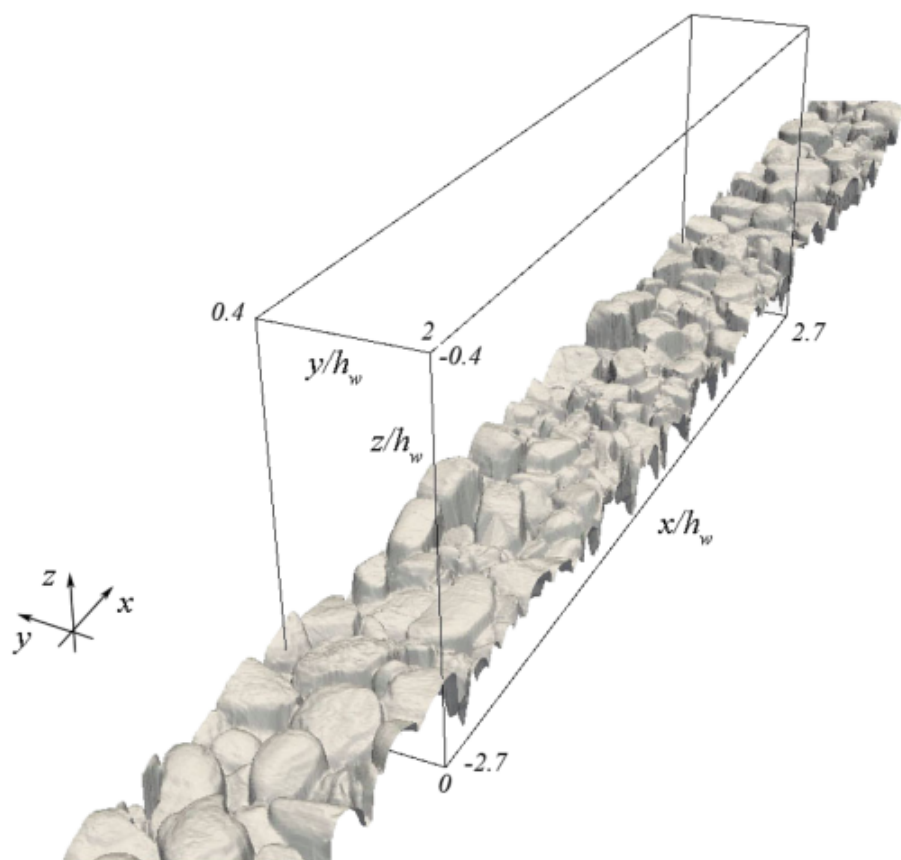


Figure 2.33: Open channel with pebble layer roughness [156].

[157] used LES to find a universal correlation for the roughness function. Their results suggested a correlation between effective slope (ES) and root mean square of roughness oscillation or ES and showed that mean absolute deviation of roughness height could successfully estimate the roughness function.

[158] used DNS to investigate the impact of effective slope in a span-wise direction ES_y , on the roughness function. Their findings showed that low ES_y could strongly affect skin friction. Furthermore, the low case study ES_y showed decreased outer layer similarity for mean velocity and turbulence statistics.

2.5 Summary and the contribution to the state of the art

The literature review is separated into two sections. The first section is dedicated to bio-fouling terminology and successful instances of biomimicry. The second part delves into pertinent literature on the interaction of turbulent flow and surface roughness. Regarding the interplay between turbulent flow and surface roughness and its application in anti-fouling, most of the prior research on anti-fouling has predominantly relied on experimental approaches conducted under laminar or static conditions. In this study, a high-fidelity Large Eddy Simulation (LES) method with no wall modelling is used to accurately capture turbulence effects within and above the surface textures. The contribution to the state of the art in this area of research is outlined as follows:

- Most of the turbulent flow simulations over rough surfaces have been presented in spatially averaged formats, which is suitable for engineering applications but does not provide any insight into local effects that influence bio-fouling at the early stage of their settlement. This study conducted analyses at specific locations where increased or reduced stresses were expected.
- The effect of various texture layout arrangements on the spatial distribution of Reynolds and dispersive stresses within each configuration and assessing their significance in the initial stages of fouling settlement has not been studied previously but its understanding aids in the selection of the optimal configuration to minimize fouling settlement.
- No prior attempts had been made to evaluate hydrodynamic forces acting on a settled organism. This has been the focus of the final LES simulation analysis, which considers four locations over a textured surface. The aim is to investigate the spatial variability of stresses acting on an organism at the early stages of its settlement.

Chapter 3

Turbulence modeling and the finite volume method

This chapter outlines the numerical formulation of the turbulent flow simulation performed. This includes a discussion of turbulence modelling, the finite volume method, numerical discretization schemes, and the Pimple Navier Stokes solution method.

3.1 Turbulence modeling

Turbulent flow is common in our daily lives, manifested in various phenomena. Examples include turbulent water currents in rivers and waterfalls and billowing smoke from a chimney. When we observe the currents of a waterfall more closely, we notice that they exhibit characteristics of chaos, instability, randomness, and unpredictability. In his drawings, Leonardo da Vinci was one of the early observers to highlight the intricate and unpredictable nature of turbulent flow, as depicted in Fig. 3.1. His sketches clearly illustrate the presence of swirling vortices known as eddies, which are integral parts of turbulent flows. Eddies are regions of swirling vorticity distributed across a range of length scales. Depending on the Reynolds number, turbulent flows can contain eddies spanning from microns to meters in size, existing simultaneously. Fig. 3.2 showcases a turbulent boundary layer that forms on a smooth surface at various angles. These images vividly demonstrate the presence of vortical structures of diverse scales saturating the flow layers.

The Navier-Stokes equations are a set of fundamental governing equations that are used to describe fluid flow motions. In the case of flow with a constant density, known as incompressible flow, these equations can be simplified to continuity and momentum transport equations described in Eq. (3.1) and (3.2).

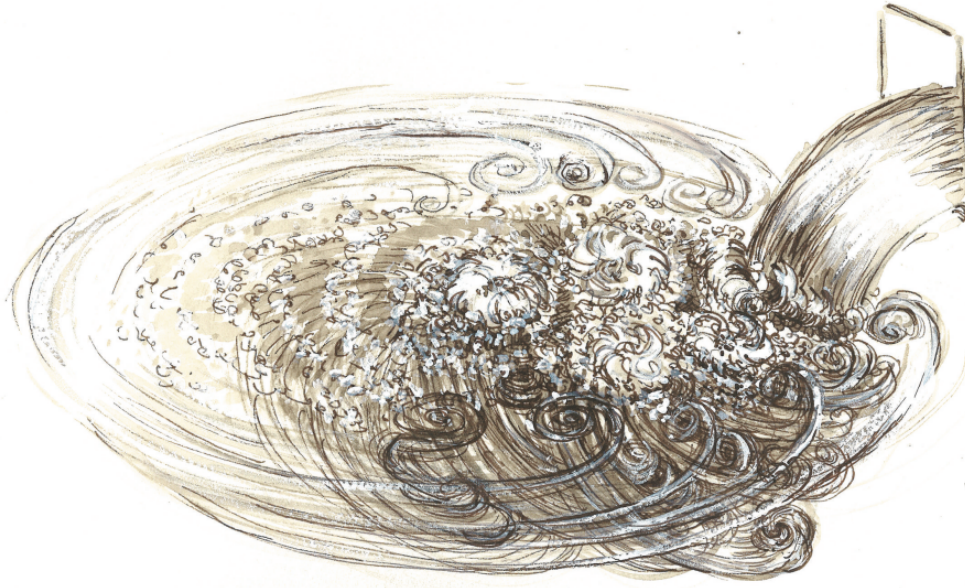


Figure 3.1: Leonardo Davinchi famous sketch of water falling into a pool [159].

$$\frac{\partial(\mathbf{u}_i)}{\partial x_i} = 0 \quad (3.1)$$

$$\frac{\partial(\mathbf{u}_i)}{\partial t} + \frac{\partial(\rho \mathbf{u}_i \mathbf{u}_j)}{\partial x_j} = -\frac{1}{\rho} \frac{\partial p}{\partial x_i} + \frac{1}{\rho} \frac{\partial \tau_{ij}}{\partial x_j} + f_i \quad (3.2)$$

Here \mathbf{u} denotes velocity (i and j are dummy indexes), ρ is density, p is pressure, τ_{ij} and f_i are tensor shear stress and body forces, respectively and x is the Cartesian coordinate.

To have a high-fidelity flow simulation, Eq. (3.1) and Eq. (3.2) should be solved directly. This means resolving the entire spatial and temporal, which is practically impossible for the simulations considered in this study due to the limitations of available computational resources. Another approach to circumvent this problem is to simulate larger eddies present in the flow, making it possible to use coarser computational meshes and time steps. This is known as the Large Eddy Simulation approach or LES. Mathematically, the LES method separates length scales and filters fine ones by applying convolution with a particular kernel on the Navier-stokes equations. The convolution operator is shown in Eq. (3.3).

$$\bar{\phi}(\mathbf{x}, t) = \iiint_{-\infty}^{+\infty} \phi(\mathbf{x}, t) G(\mathbf{x} - \xi, \Delta) d^3 \xi \quad (3.3)$$

G is the kernel function, and Δ is the cut-off filter parameter specifying the fine filtered-out scales. Applying the convolution operator on the Navier-stocks equations

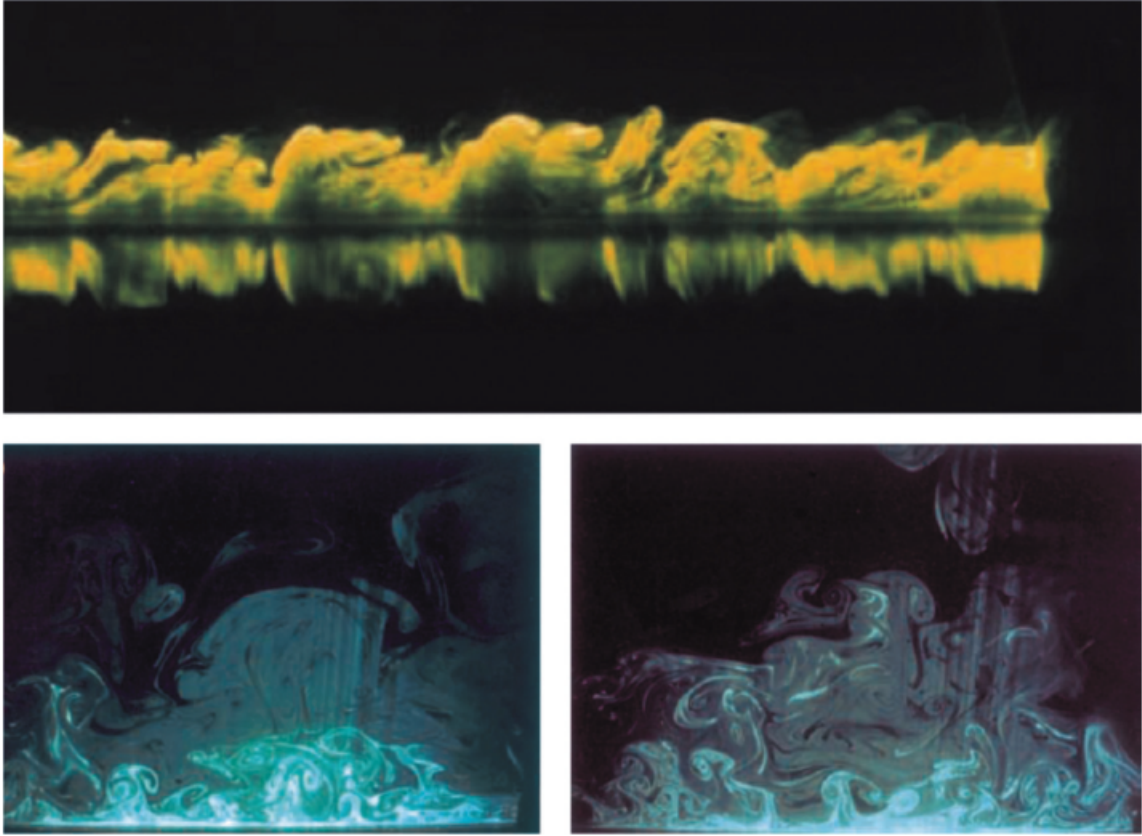


Figure 3.2: Different angles of a turbulent boundary layer formed on a smooth surface [159].

divides the flow variables into filtered and unfiltered terms:

$$\phi(\mathbf{x}, t) = \bar{\phi}(\mathbf{x}, t) + \phi''(\mathbf{x}, t) \quad (3.4)$$

which $\bar{\phi}(\mathbf{x}, t)$ is the resolved part and $\phi''(\mathbf{x}, t)$ is associated with the filtered part, which is known as sub-grid scales or SGS. Several filter functions, such as Gaussian, sharp spectral, and Box, have been proposed in [88] and [160]. In Fig. 3.3, a diagram of both instantaneous and filtered velocity are shown for illustration. Despite a large number of available filter functions, some can be challenging to implement in a general-purpose CFD code. The most popular filter function for finite volume CFD codes is the top hat filter, which uses mesh sizes as the filter cutoff width [161].

$$G(\mathbf{x} - \xi, \Delta) = \begin{cases} 1/\Delta^3 & , |\mathbf{x} - \xi| \leq \delta/2 \\ 0 & , otherwise \end{cases} \quad (3.5)$$

According to Eq. (3.5), filtering offers an average value over Δ^3 volume. Therefore,

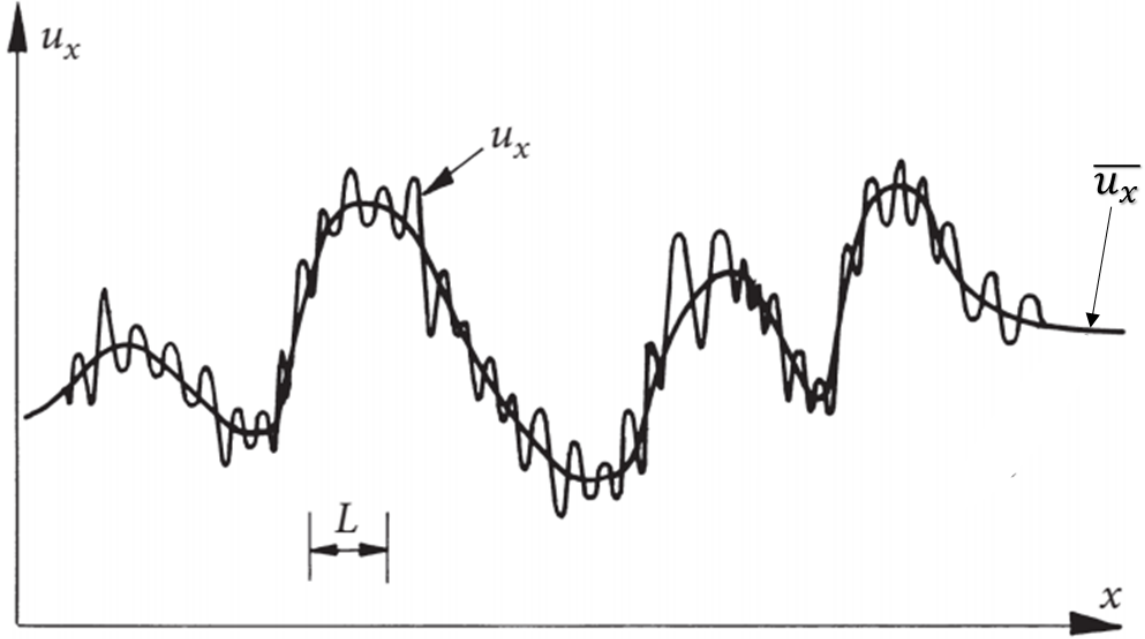


Figure 3.3: Instantaneous u_x and filtered velocity $\overline{u_x}$ [159].

Δ is naturally chosen as the cubic root of the computational mesh sizes.

$$\Delta = \sqrt[3]{\Delta x \Delta y \Delta z} \quad (3.6)$$

In which, $\Delta x, \Delta y, \Delta z$ are the computational mesh sizes in the respected coordinate system.

Applying the top-hat filter to the continuity and Navier stokes equations Eq. (3.1) and Eq. (3.2), we arrive at filtered Navier-stokes Eq. (3.7) and Eq. (3.8). It is worth noting that, unlike RANS turbulent models where variables are time-averaged, LES variables are functions of time and space.

$$\frac{\partial \overline{u}_i}{\partial x_i} = 0 \quad (3.7)$$

$$\frac{\partial \overline{u}_i}{\partial t} + \frac{\partial \overline{u}_i \overline{u}_j}{\partial x_j} = -\frac{1}{\rho} \frac{\partial \overline{p}}{\partial x_i} + \nu \frac{\partial^2 \overline{u}_i}{\partial x_i \partial x_j} \quad (3.8)$$

where $\nu = \mu/\rho$ is the kinematic viscosity of fluid and τ_{ij} is replaced by $2\nu S_{ij}$ which S_{ij} is the shear stress tensor [88].

The main issue with Eq. (3.8) is $\overline{u}_i \overline{u}_j$ term. SGS stress tensor $\overline{\tau}_{ij}$ is defined to address this issue.

$$\overline{\tau}_{ij} = \overline{u_i u_j} - \overline{u}_i \overline{u}_j \quad (3.9)$$

Inserting Eq. (3.9) in Eq. (2.8), the new governing equation for large scale is attain-

able.

$$\frac{\partial \bar{u}_i}{\partial t} + \frac{\partial \bar{u}_i \bar{u}_j}{\partial x_j} = -\frac{1}{\rho} \frac{\partial \bar{p}}{\partial x_i} + \frac{1}{\rho} \frac{\partial \bar{\tau}_{ij}}{\partial x_j} + \nu \frac{\partial^2 \bar{u}_i}{\partial x_i \partial x_j} \quad (3.10)$$

the Eq. (3.10) is not a closed equation, and SGS stress tensors, $\bar{\tau}_{ij}$, should be modelled.

3.1.1 SGS models

To have a closed-form equation in Eq. (3.10), SGS stresses should be modelled. Several sub-grid scale models or SGS have been developed, but only a few are suitable for general-purpose CFD codes. Analogous to RANS modelling, the most common way to model SGS stress is to employ the Boussinesq assumption [160]. This is the base assumption used in LES methods implemented in general-purpose CFD. This reads:

$$\bar{\tau}_{ij} = \frac{1}{3} Tr(\bar{\tau}_{ij}) \mathbf{I} + \nu_{sgs} (\nabla u + \nabla^T u) \quad (3.11)$$

where \mathbf{I} is the identity matrix, Tr represent the trace of tensor $\bar{\tau}_{ij}$ and ν_{sgs} is calculated turbulent viscosity.

The definition of ν_{sgs} , is justified on dimensional ground ν_{sgs} and is given by:

$$\nu_{sgs} = u_{sgs} l_{sgs} \quad (3.12)$$

According to Eq. (3.12), u_{sgs} and l_{sgs} are velocity and length scales used to define the sub-grid scales, respectively. An obvious choice for the SGS length scale is the cut-off mesh sizes. In this thesis, mesh size is used as the cut-off filter size (OpenFOAM). Regarding velocity SGS scales, numerous approaches have been proposed. [162] relied on an algebraic formula based on the mixing length theory [107]. In a 2D boundary layer this can be defined by:

$$\nu_t = l^2 \left| \frac{\partial \bar{v}_1}{\partial x_2} \right| \quad (3.13)$$

where ν_t is the eddy viscosity in the boundary layer, l and $\frac{\partial \bar{v}_1}{\partial x_2}$ are the mixing length scale and the velocity gradient normal to wall respectively.

Inspired by this definition, [162], correlated the SGS viscosity to the filter length scale and unresolved part of the velocity gradient. This model is used as a base model for other turbulence models.

$$\nu_{sgs} = (C_s \Delta)^2 |\bar{s}| \quad (3.14)$$

where $|\bar{s}|$ is the velocity gradient of the sub-filtered velocity, Δ is the filter length width and $C_s = 0.1$.

The Smagorinsky model assumes a local equilibrium between transferred turbulent kinetic energy at larger scales and dissipated kinetic energy at sub-filter scales.

The SGS part of turbulence equations could be modelled better if a transport equation for turbulent kinetic energy could be solved in the sub-filter region (k_{sgs}). This is known as a one-equation eddy viscosity model for LES. Similar to the LES Smagorinsky model, SGS stress tensors are written as:

$$\tau_{ij} = \frac{2}{3}k_{sgs} - 2\nu_{sgs}dev(\overline{D}_{ij}) \quad (3.15)$$

Where k_{sgs} is the SGS turbulent kinetic energy, $dev(\overline{D}_{ij})$ is the deviatoric part of the resolved velocity gradient (Eq. (3.16)) and δ_{ij} is the Kronecker delta.

$$\overline{D}_{ij} = \frac{1}{2}\left(\frac{\partial \overline{u}_i}{\partial x_j} + \frac{\partial \overline{u}_j}{\partial x_i}\right) \quad (3.16)$$

$$k_{sgs} = \frac{1}{2}(\overline{u_k u_k} - \overline{u}_k \overline{u}_k) \quad (3.17)$$

And finally, ν_{sgs} computes from:

$$\nu_{sgs} = C_k \Delta \sqrt{k_{sgs}} \quad (3.18)$$

where $C_k = 0.094$. It can be seen that the one-eddy equation model uses k_{sgs} instead of the filtered velocity gradient adopted by the Smagorinsky model. The main difference between the Smagorinsky and the one-equation model is in ν_{sgs} calculation. The Smagorinsky model assumes equilibrium turbulent kinetic energy transfer to estimate k_{sgs} . That might not be true in coarse meshes or high Reynolds numbers. On the contrary, one equation eddy viscosity model proposed by [163], solves a transport equation for k_{sgs} . This transport equation for k_{sgs} can take into account the historic effects of k_{sgs} production, dissipation and diffusion:

$$\frac{\partial k_{sgs}}{\partial t} + \frac{\partial(\overline{u}_i k_{sgs})}{\partial x_i} = 2\nu_{sgs}|\overline{D}_{ij}| - C_e \frac{k_{sgs}^{3/2}}{\Delta} + \frac{\partial(\nu_{sgs} \frac{\partial k_{sgs}}{\partial x_i})}{\partial x_i} + \nu_{sgs} \frac{\partial^2 k_{sgs}}{\partial^2 x_i} \quad (3.19)$$

Where \overline{D}_{ij} accounts for the filtered strain rate and $C_e = 1.048$. The four right-hand side terms in Eq. (3.19) are physically representative of production, turbulent dissipation and diffusion and finally viscose dissipation in k_{sgs} . The computed k_{sgs} from Eq. (3.19), substitutes in Eq. (3.18) to estimate ν_{sgs} .

3.2 Finite volume method

The Finite Volume Method (FVM) is one of the most widely used methods for solving Navier-stokes equations. It requires that spaces be discretised using discrete volumes that fully fill the physical space. The integral forms of the governing equations are solved to enforce conservation of transported quantities, including mass and momentum over each of these volumes and are intrinsically conservative in nature, making it particularly well adapted to Fluid Mechanics, in general, [161] and [164]. It owes its popularity to its ability to handle any polyhedral shape, making it easier to conform to complex geometries. The following section describes the process of domain discretization and then presents the semi-discretised form of a generic scalar transport equation before detailing the discretization schemes and an algorithm relevant to the study.

3.2.1 Solution domain discretization

To solve the Navier-stocks equations in a prescribed domain, space and time should be decomposed into finite volumes and steps, respectively. Space discretization serves to specify locations where variables are stored and define volumes where integration occurs on the Navier-stokes equations. These volumes are known as Control Volumes or CVs. The CVs do not overlap and fill the entire computational domain. In cell-centred FVMs, variables are stored at the centre of the CVs. Fig. 3.4 shows a typical CV where S_f is the surface normal to the face shared between two adjacent computational cells and P is the centre of the cell of volume V_P and N is the centre of the neighbour cell that share S_f . Fig. 3.4 shows a typical control volume.

3.2.2 Semi-discretised equations

The general transport equation for a scalar ϕ can be written in a conservative form as:

$$\underbrace{\frac{\partial \rho \phi}{\partial t}}_{\text{temporal term}} + \underbrace{\nabla \cdot (\rho \mathbf{v} \phi)}_{\text{convective term}} = \underbrace{\nabla \cdot (\Gamma_\phi \nabla \phi)}_{\text{diffusion term}} + \underbrace{S_\phi(\phi)}_{\text{source term}} \quad (3.20)$$

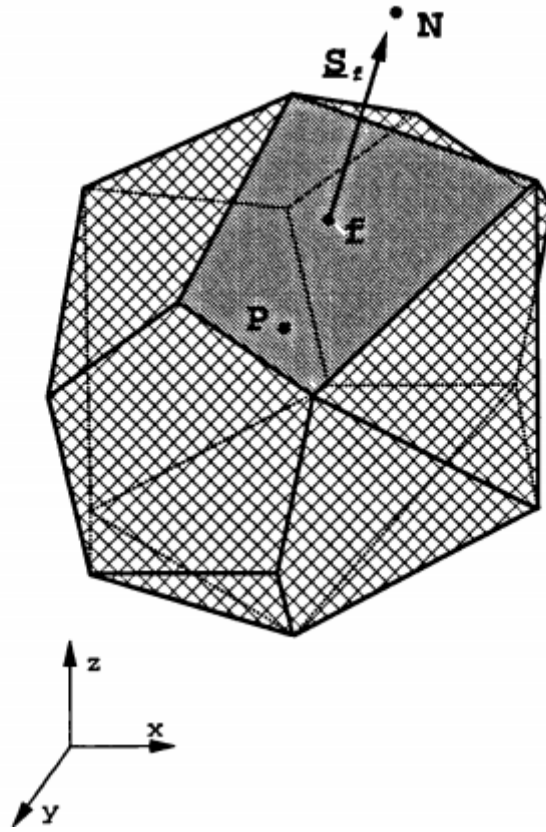


Figure 3.4: A typical control Volume [165].

Volume integration of Eq. (3.20) over a computational cell of volume V_p , gives the following semi-discretized form (Eq. (3.21)).

$$\int_t^{t+dt} \left[\frac{\partial}{\partial t} \int_{V_p} \rho \phi dV + \int_{V_p} \nabla \cdot (\rho \mathbf{v} \phi) - \int_{V_p} \nabla \cdot (\rho \Gamma_\phi \nabla \phi) dV \right] dt \quad (3.21)$$

$$= \int_t^{t+dt} \left(\int_{V_p} S_\phi(\phi) dV \right) dt$$

3.2.3 Spatial and temporal discretizational schemes

To solve Eq. (3.21), it should be cast into a set of algebraic equations through the discretisation of temporal and spatial terms. Spatial discretisation estimates the convective and diffusive fluxes at cell faces illustrated in Fig. 3.5. The schemes adopted in this research are presented in the following section.

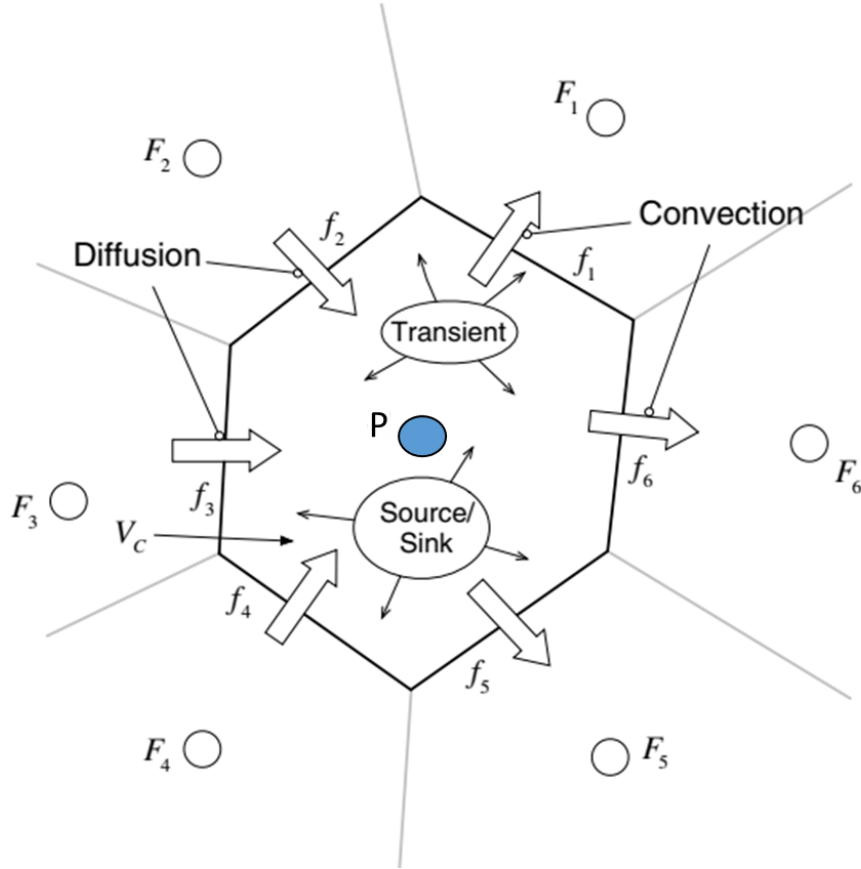


Figure 3.5: Conservative fluxes on CVs surfaces [164].

3.2.3.1 Spatial terms

The Gauss divergent theorem is used to cast volumetric integrals into surface integrals.

$$\int_{V_p} \nabla \cdot a \, dV_p = \oint_{\partial\Omega} dS \cdot a \quad (3.22)$$

$$\int_{V_p} \nabla \phi \, dV_p = \oint_{\partial\Omega} dS \phi \quad (3.23)$$

$$\int_{V_p} \nabla a \, dV_p = \oint_{\partial\Omega} dS a \quad (3.24)$$

Where $\partial\Omega$ is the closed surface bounding V_P and dS is an infinitesimal surface with a normal oriented outward cell centre P. The CV is bounded by a series of surfaces called faces. The Gauss theorem means that Eq. (3.22) can be expressed as a summation of integrals over these faces.

$$\int_{V_p} \nabla \cdot a \, dV_p = \oint_{\partial\Omega} dS \cdot a = \sum_f \int_f dS \cdot a \quad (3.25)$$

where the subscript f refers to the face number. Using a Taylor series and assuming a linear variation for a [165]:

$$\sum_f \int_f dS \cdot a = \sum_f S_f \cdot a_f \quad (3.26)$$

or:

$$\int_{V_p} \nabla \cdot a dV_p = \sum_f S_f \cdot a_f \quad (3.27)$$

In Eq. (3.27), S_f is the area vector normal to the face and pointing outward in the direction of the neighbouring cell.

Convective terms

Using Eq. (3.27) to discretise the convection term in Eq. (2.20), gives Eq. (3.28).

$$\begin{aligned} \int_{V_p} \nabla \cdot (\rho U \phi) &= \sum_f S_f \cdot (\rho U \phi)_f = \sum_f S_f \cdot (\rho U)_f \phi_f \\ &= \sum_f F_f \phi_f \end{aligned} \quad (3.28)$$

where F_f represents the mass flux rate through face f : $F = S_f \cdot (\rho U)_f$.

All fluxes and variables transported through a face f are approximated from its value at the centre of the face. The approximation can be shown to be second order. Generally, U and ρ on the interface of two cells are calculated through interpolation. However, special treatments must be adopted to calculate the variable ϕ to estimate its convective transport while ensuring stability. The Upwind and central differencing methods are the most commonly used.

Upwind differencing Scheme (UD)

In this method, ϕ_f the face value of ϕ is approximated by its value at the centroid of the upstream CV as illustrated in Fig. 3.6 for a 1D flow.

$$\phi_f = \begin{cases} \phi_P & \text{for } F \geq 0 \\ \phi_N & \text{for } F \leq 0 \end{cases} \quad (3.29)$$

The UD scheme is known for offering bounded solutions. This comes at the expense of accuracy since it is first order and introduces numerical diffusion [166].

Central differencing Scheme (CD)

The central differencing scheme assumes a linear variation of ϕ between two adjacent cells.

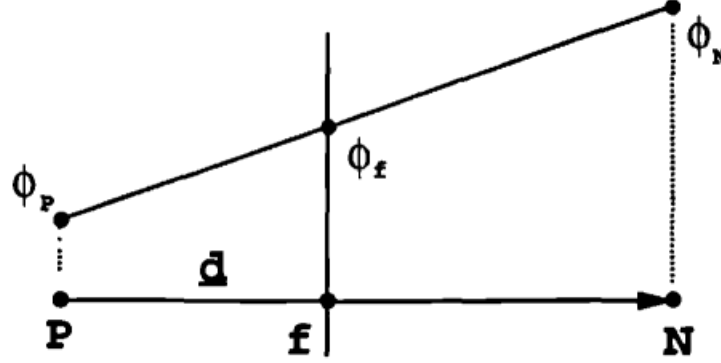


Figure 3.6: Linear interpolation between two straddling cell [165].

$$\phi_f = f_x \phi_P + (1 - f_x) \phi_N \quad (3.30)$$

where $f_x = \overline{fN}/\overline{Pf}$. According to [167], the CD scheme possesses second-order accuracy even for unstructured meshes. Unlike the UD scheme, the CD exhibits unboundedness behaviour in highly convective flows. The blended differencing scheme was introduced to benefit from both the boundedness of UD and the second-order accuracy of CD schemes. This uses a linear combination of UD and CD schemes [165].

Diffusion term

The diffusion term is discretised similarly to the convective term. Assuming a linear variation in ϕ , the diffusion term becomes:

$$\begin{aligned} \int_{V_p} \nabla \cdot (\rho \Gamma_\phi \nabla \phi) &= \sum_f S_f \cdot (\phi \Gamma_\phi \nabla \phi)_f \\ &= \sum_f (\rho \Gamma_\phi)_f S_f \cdot (\nabla \phi)_f \end{aligned} \quad (3.31)$$

If the meshes are orthogonal, i.e. \vec{PN} is in the direction of S_f , and $S_f \cdot (\nabla \phi)_f$ could be written as $S_f(\phi_N - \phi_P)/d$ where $d = |\vec{PN}|$. Since usually orthogonality is an exception rather than the norm in real flow problems (Fig. 3.7), a non-orthogonal correction term can be added (Eq. (3.32)).

$$S \cdot (\nabla \phi)_f = \underbrace{\Delta \cdot (\nabla \phi)_f}_{\text{orthogonal contribution}} + \underbrace{\mathbf{k} \cdot (\nabla \phi)_f}_{\text{non-orthogonal contribution}} \quad (3.32)$$

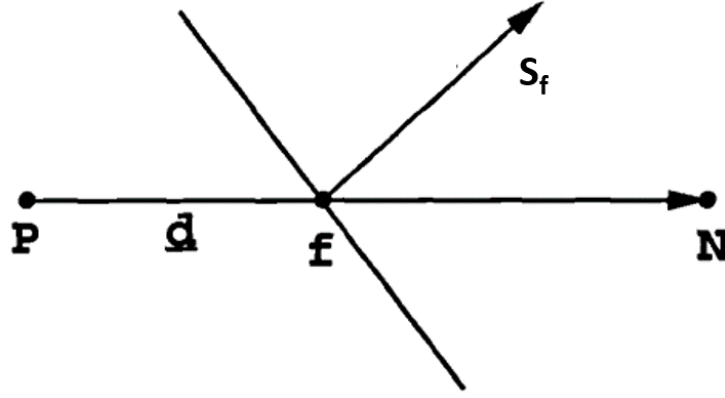


Figure 3.7: Mesh non-orthogonality [165].

where Δ is defined as $\Delta = S - k$. To improve boundedness of the solution (3.32), a deferred minimum correction approach with under-relaxation is adopted [165].

3.2.3.2 Source terms

All the terms that can not be treated as convection, diffusion or temporal are considered source terms, which could affect the boundedness of the solution. $S_\phi(\phi)$ is a general function of ϕ and should be linearized.

$$S_\phi(\phi) = S_u + S_p\phi \quad (3.33)$$

where S_u and S_p are functions of ϕ . The integral volume part of the source term in Eq. (3.21) takes the form of:

$$\int_{V_p} S_\phi(\phi) = S_u V_p + S_p V_p \phi_p \quad (3.34)$$

3.2.3.3 Temporal terms

Substituting the discrete approximations for the convective, diffusive and source terms in Eq. (3.21) gives:

$$\begin{aligned} \int_t^{t+dt} \left[\left(\frac{\partial \rho \phi}{\partial t} \right)_p V_p + \sum_f F \phi_f - \sum_f (\rho \Gamma_f)_f S.(\nabla \phi)_f \right] dt \\ = \int_t^{t+dt} (S_u V_p + S_p V_p \phi_p) dt \end{aligned} \quad (3.35)$$

Time derivative and integral in Eq. (3.35) can be written as:

$$\left(\frac{\partial \rho \phi}{\partial t}\right)_p = \frac{\rho_p^n \phi_p^n - \rho_p^0 \phi_p^0}{\Delta t} \quad (3.36)$$

$$\int_t^{t+dt} \phi dt = \frac{1}{2}(\phi^0 + \phi^n)\Delta t \quad (3.37)$$

Where ϕ^0 and ϕ^n are the values of ϕ values at t and $t + dt$ time, respectively. Assuming that ρ and Γ are constant in time, Eq. (3.35) gives:

$$\begin{aligned} \frac{\rho_p^n \phi_p^n - \rho_p^0 \phi_p^0}{\Delta t} V_p + \frac{1}{2} \sum_f F \phi_f^n - \frac{1}{2} \sum_f (\rho \Gamma)_f S \cdot (\nabla \phi)_f^n \\ + \frac{1}{2} \sum_f F \phi_f^0 - \frac{1}{2} \sum_f (\rho \Gamma)_f S (\nabla \phi)_f^0 \\ - S_u V_p + \frac{1}{2} S_p V_p \phi_f^n + \frac{1}{2} S_p V_p \phi_f^0 \end{aligned} \quad (3.38)$$

The discretization scheme used in Eq. (3.38) is called the Crank-Nicholson method, which is second-order accurate in time. The Crank-Nicholson method assumes an equal weighting average for both considered times. It calculates face values from cell values located at each side of the face. Since ϕ_f and $\nabla \phi_f$ values depend on cell values in surrounding cells, an algebraic Eq. (3.39), can be formed to calculate ϕ_p at cell centres.

$$a_p \phi_p^n + \sum_n a_N \phi_N^n = R_p \quad (3.39)$$

Since Eq. (3.39) can be written for every cell, an algebraic equation system should be solved to calculate ϕ_p at all cell centres.

$$[A][\phi_p] = [R] \quad (3.40)$$

Where $[A]$ is a sparse matrix in which its diagonal elements are a_p coefficient, and off-diagonals are comprised of a_N coefficients (neighbouring cells contribution) in Eq. (3.39), $[R]$ contains the source terms and $[\phi_p]$ is the vector of unknown values of ϕ_p . It is worth mentioning that The Crank-Nicholson method is unconditionally stable but does not guarantee boundedness [166].

Several temporal discretisation methods are proposed based on the assumption that ϕ and $\nabla \phi$ are constant in time. This allows for keeping temporal derivatives unchanged while considering the convection, diffusion and source terms at two different time levels (Eq. (3.41)). This approach is of the first order of accuracy, and choices

need to be made to calculate ϕ and $\nabla\phi$.

$$\begin{aligned} \frac{\rho_p\phi_p^n - \rho_p\phi_p^0}{\Delta t}V_p + \sum_f F\phi_f + \sum_f (\rho\Gamma)_f S \cdot (\nabla\phi)_f \\ = S_u V_p + S_p V_p \phi_p \end{aligned} \quad (3.41)$$

3.2.3.4 Explicit time discretization

In the explicit discretization method, the face values of ϕ and $\nabla\phi$ are calculated from their old-time values.

$$\phi_p^n = \phi_p^0 + \frac{\Delta t}{\rho_p V_p} \left[\sum_f F\phi_f - \sum_f (\rho\Gamma)_f S \cdot (\nabla\phi)_f \right] + S_u V_p + S_p V_p \phi_p^0 \quad (3.42)$$

Using old field values to calculate new ones obviates the necessity for solving a system of linear equations. However, it restricts the choice of time steps, as stability is conditional on the Courant number Co being less than 1.

$$Co = \frac{U_p d}{\Delta t} < 1 \quad (3.43)$$

In Eq. (3.43), U_p accounts for the velocity in the computational cells, and d is the characteristic cell size.

3.2.3.5 Euler implicit method

Unlike the Explicit method, the Euler implicit method uses new flow field values to estimate ϕ and $\nabla\phi$. The method is still first-order, but unconditionally stable and a system of equations needs to be solved. The face approximation of the transported variable and its gradient are defined by:

$$\phi_f = f_x \phi_p^n + (1 - f_x) \phi_N^n \quad (3.44)$$

$$S \cdot (\nabla\phi)_f = \Delta \frac{\phi_N^n - \phi_P^n}{d} + \underbrace{k \cdot (\nabla\phi)_f}_{\text{non-orthogonal contribution}} \quad (3.45)$$

3.2.3.6 Backward differencing in time

The Backward Time Differencing scheme time is a second-order accurate scheme where the temporal derivative is discretised assuming that ϕ and $\nabla\phi$ does not change with time in the approximation of fluxes. This scheme needs three time levels to be stored (n , 0 and 00 for times $\Delta t + 1$, Δt and $\Delta t - 1$) [165].

$$\begin{aligned} \frac{\frac{3}{2}\rho_p\phi_p^n - 2\rho_p\phi_p^0 + \frac{1}{2}\rho_p\phi_p^{00}}{\Delta t}V_p + \sum_f F\phi_f + \sum_f (\rho\Gamma)_f S \cdot (\nabla\phi)_f \\ = S_u V_p + S_p V_p \phi_p \end{aligned} \quad (3.46)$$

3.2.4 Navier-stokes solver

In a numerical simulation for incompressible Navier-stokes (N.S) equations, two problems need special attention: non-linearity and pressure-velocity coupling. The former is due to the convective term, i.e. $\nabla(UU)$, which means that the discretized equations are quadratic in velocity and the system is non-linear. The conventional way to address this issue is to linearize all non-linear terms. Part of the term is approximated from the previous time step or iteration and fluxes are corrected iteratively. The primary issue is that instability or errors can propagate exponentially in a poorly conditioned system, leading to a diverging solution. The pressure-velocity coupling, when an incompressible flow is solved using a segregated method to solve the conservation equations sequentially for the unknown variables of pressure and velocity. Since pressure is not present in the mass conservation equation, it is introduced by coupling the mass and momentum equations using a pressure-velocity coupling method.

3.2.4.1 Pressure equation

The pressure equation is expressed below in a semi-discretized form.

$$a_p U_p = H(U) - \nabla p \quad (3.47)$$

$H(U)$ in Eq. (3.47) includes fluxes with neighbouring cells and any source term except for contributions included in a_p . This may include contributions from transient terms or any deferred correction. In the absence of source terms other than the transient term, it is defined by

$$H(U) = - \sum_N a_N U_N + \frac{U^0}{\Delta t} \quad (3.48)$$

The pressure gradient in Eq. (3.48) is not yet discretized to incorporate the Rhie and Chow interpolation for co-located grids [168]. The discretized form of the incompressible continuity equation can be written as:

$$\nabla \cdot U = \sum_f S.U_f = 0 \quad (3.49)$$

Dividing Eq. (3.47) by a_p , provides an equation for U_p that can be interpolated at face centers Eq. (3.49).

$$U_f = \left(\frac{H(U)}{a_p} \right)_f - \left(\frac{1}{a_p} \right)_f (\nabla p)_f \quad (3.50)$$

Substituting Eq. (3.50) into Eq. (3.49), gives the following pressure equation:

$$\begin{aligned}\nabla \cdot \left(\frac{1}{a_p} \nabla p \right) &= \nabla \cdot \left(\frac{H(U)}{a_p} \right) \\ &= \sum_f S \cdot \left(\frac{H(U)}{a_p} \right)_f\end{aligned}\tag{3.51}$$

Discretizing Eq. (3.51), gives the final form of the discretised momentum and pressure equations:

$$a_p U_p = H(U) - \sum_f S p_f\tag{3.52}$$

$$\sum_f S \cdot \left[\left(\frac{1}{a_p} \right)_f \nabla p_f \right] = \sum_f S \cdot \left(\frac{H(U)}{a_p} \right)_f\tag{3.53}$$

Where the Flux calculated from Eq. (3.50) satisfy the discretized form of continuity Eq. (3.49).

3.2.4.2 Pressure-Velocity Algorithm

The pressure and velocity variables in the discretized form of the NS equations are strongly coupled. A number of solution procedures have been proposed to preserve this coupling. The SIMPLE ([166]) and PISO ([169]) algorithms were originally proposed for steady-state problems and transient flow problems, respectively. In this thesis, only the PISO algorithm is used.

3.2.4.3 The PISO Algorithm

The PISO (Pressure-implicit with the splitting of operators) algorithm was first introduced by [169] and was derived from the SIMPLE method (see [166]) for transient flow problems. It can be summarized as follows:

1. The first step is called **the momentum predictor**. The Eq. (3.52) is solved to update the velocity field. Since the pressure field is unknown at this stage, the old-time pressure field is adopted.
2. Using the updated velocity field, the vector $H(U)$ is assembled and substituted in Eq. (3.53) to calculate the new pressure field. This step is known as **the pressure solution** step.
3. The new pressure field is used to calculate new fluxes on faces Eq. (3.50). Since the pressure field is updated, new velocities can be calculated using Eq. (3.50) in an explicit manner [165]. This stage is called **The explicit**

velocity correction stage. Since the velocity correction term is being treated explicitly, a repeated PISO loop of momentum prediction and pressure solution is implemented to satisfy a target tolerance criteria ie a set Residual.

In this thesis, The Pimple algorithm, which is modified version of the PISO scheme, is adopted to increase the stability of the solution. The PIMPLE algorithm relies on an outer correction loop at each time-step which iterates over under-relaxed equations as outlined in Figure Fig. 3.8 (see [170]). In cases where only one outer corrector is employed, the PimpleFoam solver reverts back to the original PISO solver.

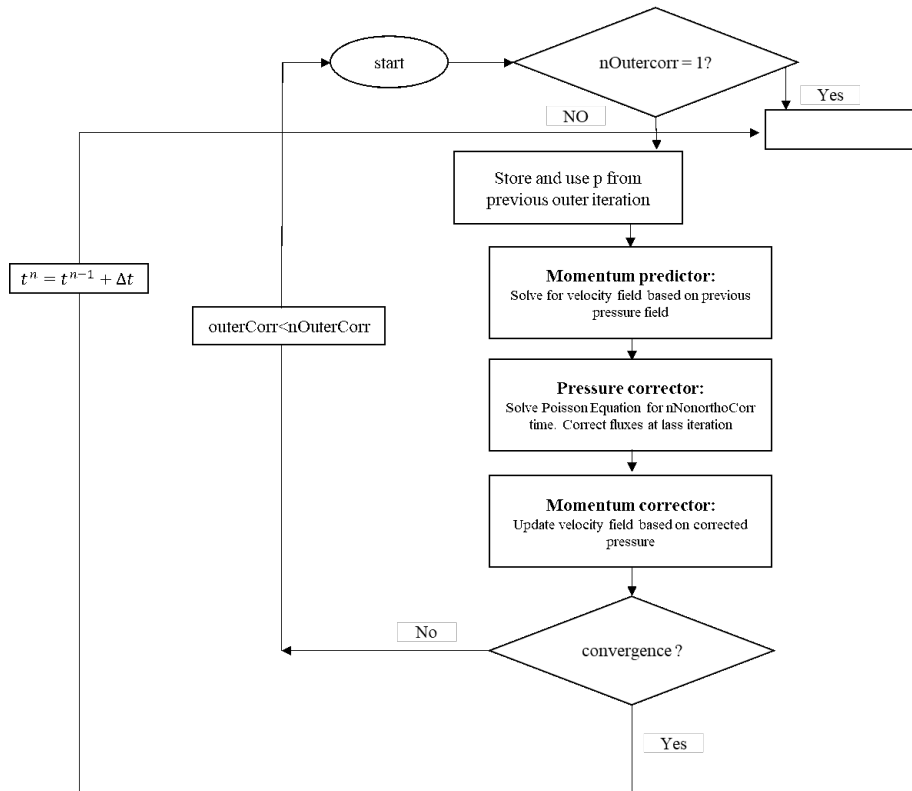


Figure 3.8: Flowchart of Pimple algorithm [170].

3.3 Summary and Conclusion

In this chapter, turbulence and finite volume schemes and algorithms for solving the Navier-Stokes equations were discussed. Given the need to resolve various time and spatial scales for the flow within textures, the high-fidelity Large Eddy Simulation (LES) method, specifically the k-equation, utilized in this thesis, was elaborated upon. Additionally, considering the nonlinearity of the Navier-Stokes equations, which can result in the divergence of discretized equations, special temporal and spatial schemes for achieving a robust solution were introduced and discussed in this chapter based on relevant literature.

Chapter 4

Numerical set-ups

This chapter outlines the numerical set-up for a fully developed turbulent channel flow covering both smooth, and textured walls. Also, it addresses the setup for situations where an organism is positioned at various locations on the textured surface. This includes the generation of meshes and the selection of numerical parameters for all simulation cases. Special attention is paid to flow simulation in channels with smooth walls, as it serves as an initial step to validate the results in channels with roughened walls.

4.1 Fully developed turbulent channel flow with smooth walls

A fully developed channel flow is a concept that represents a hypothetical geometry derived from a sufficiently large channel flow, where flow is driven by constant pressure. In this particular geometry, the turbulent flow is fully developed, where the viscous shear stresses at the walls and the effects of the pressure gradient are in equilibrium. It is customary to describe the fully developed channel flow using the coordinate system depicted in Fig. 4.2. In this coordinate system, the stream-wise direction of the flow is assigned to the variable x . The variable y represents the direction normal to the wall, extending from the lower wall to the upper wall, while the variable z corresponds to the span-wise direction perpendicular to the flow's main direction. These three variables form a right-hand Cartesian coordinate system (x, y, z) . In theory, the channel sizes along the stream-wise (x) and span-wise (z) directions are considered to be infinite. However, in order to conduct a numerical simulation, it is necessary to assign finite values to the stream-wise (l_x) and span-wise (l_z) channel lengths. These values should be large enough to accommodate the presence of large turbulent structures near the wall. Essentially, the computational domain should be adequately sized to include the self-sustaining

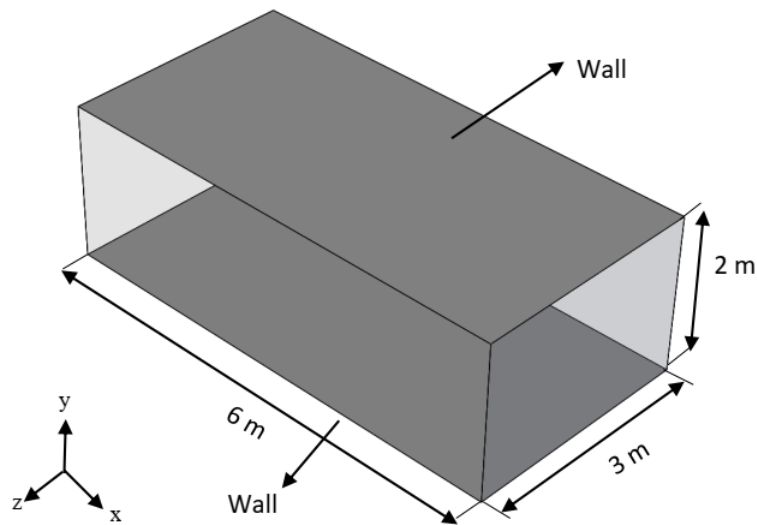


Figure 4.1: Computational domain used in smooth wall channel flow.

mechanism of turbulence regeneration in the near-wall region, as described by [171]. Failure to meet this requirement would result in failure to trigger the transition to turbulent flow. This study derives the specific channel length scale from previous works by [172]–[174]. Two-point correlations tested these length scales suitability, which showed that a stream-wise length $L_x^+ = 3000$ and span-wise length $L_z^+ = 1500$ were sufficient to guarantee that stable turbulent flow could develop and be maintained throughout the simulation. Here, L_x and L_z are scaled with the viscous length scale of a smooth wall, denoted as $\delta_v = \nu/u_\tau$. The two primary physical properties crucial to defining the problem are the pressure gradient, which drives the flow, and the fluid’s kinetic viscosity ν . Once these two values are determined, the problem is well-defined. An alternative to utilizing the pressure gradient is to use the bulk velocity U_b , which offers the advantage of specifying the bulk Reynolds number ($Re_b = U_b h/\nu$) to characterise the flow.

$$U_b = \frac{1}{h} \int_0^h \langle u \rangle dy \quad (4.1)$$

Where h is the half-channel height.

As mentioned in Chapter 2, friction velocity u_τ , is used to normalize turbulent statistics profiles in the wall region.

$$u_\tau = \sqrt{\frac{\tau_w}{\rho}} \quad (4.2)$$

Where ρ is the fluid density and τ_w is the wall mean shear stress. The Reynolds friction number is defined using the friction velocity scale instead of the bulk velocity.

$$Re_\tau = \frac{u_\tau h}{\nu} \quad (4.3)$$

It has been shown that the pressure gradient in a channel flow is correlated with wall shear stress [88].

$$\frac{d\langle p \rangle}{dx} = \frac{\tau_w}{2h} \quad (4.4)$$

Eq. (4.4) establishes a relationship between the pressure gradient and the Reynolds friction number, suggesting that either the bulk Reynolds number or the friction Reynolds number can be used to characterise the flow.

While most numerical benchmark cases present results based on Re_τ , practical considerations have led researchers to specify the flow conditions in terms of U_b (Re_b) instead and to evaluate Re_τ . This thesis uses an OpenFOAM solver to simulate the flow within the computational domain. The flow is defined in terms of the bulk velocity, and the pressure gradient is calculated to achieve the target flow rate through the channel and, hence, the bulk velocity. This is achieved by introducing an external force into the momentum Navier-Stokes equation [172].

Changes to the pressure gradient are needed to match changes to the shear stresses over the channel walls as the flow evolves towards its fully developed state. In this thesis, the geometric parameters and physical properties for the channel flow at $Re_\tau = 395$ are adopted from [172]–[174], and they are summarized in Table 4.1.

Parameters	Symbols	Value
stream-wise length scale	l_x	6(m)
span-wise length scale	l_z	3(m)
half-channel height	h	2(m)
bulk velocity	U_b	0.1335(m/s)
kinematic viscosity	ν	$2e^{-5}$ (m^2/s)
Reynolds bulk velocity	$U_b h / \nu$	13350

Table 4.1: Geometrical parameters and physical properties of the smooth wall fully developed turbulent channel flow at $Re_\tau = 395$.

4.1.1 Mesh generation

Because of the simple geometry of the channel flow, structured hexahedral meshes are used to build the computational domain. Three mesh sizes, namely coarse M1,

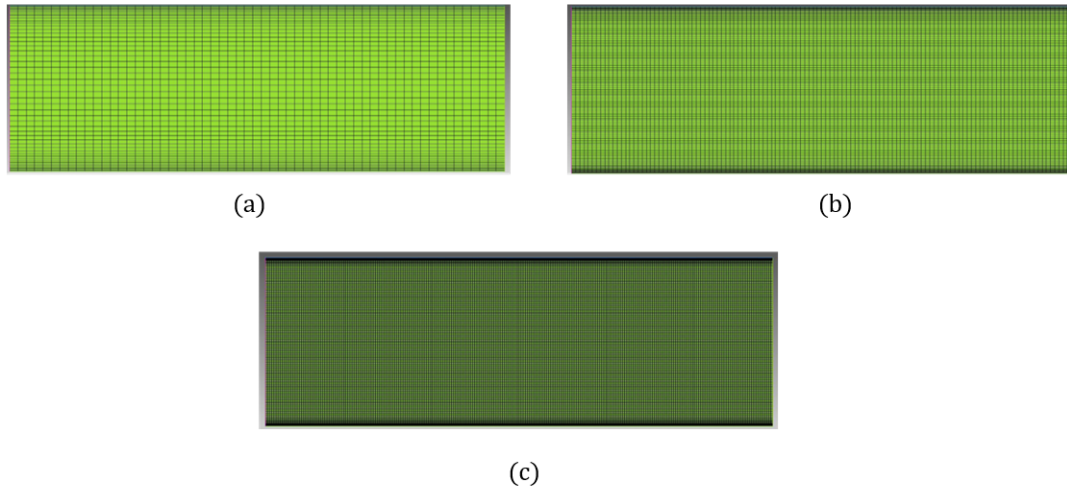


Figure 4.2: Computational mesh used in smooth wall channel flow. (a): coarse mesh, (b): medium mesh, (c): fine mesh.

medium M2, and fine M3, are employed in the present study to examine the impact of grid size on the LES solution. The details of these three meshes are provided in Table 4.2. In Table 4.1, Δx^+ and Δz^+ represent the mesh sizes scaled using viscous length scale δ_v , at $Re_\tau = 395$. It is evident that the mesh size of the M2 mesh (medium mesh) is half the size of the coarse mesh (M1), and similarly, the mesh size of the M3 mesh (fine mesh) is half that of M2 (Fig. 4.2). To enhance the resolution of turbulent structures in the vicinity of the wall and to accurately capture the associated gradients, a biased mesh was employed in the y -direction normal to the wall. This mesh stretches from the wall towards the centre of the channel, with a growth ratio of 1.1.

Mesh case	Number of nodes in $x \times y \times z$ directions	First cell height y^+	Δx^+	Δz^+	Total number of cells
M1	$60 \times 50 \times 45$	2.2	40	26	135,000
M2	$120 \times 100 \times 90$	1.05	20	13	1,080,000
M3	$240 \times 200 \times 180$	0.5	10	6.5	8,640,000

Table 4.2: The mesh properties employed to evaluate the LES methodology in a smooth channel flow at $Re_\tau = 395$.

4.1.2 Discretization schemes

The choice of suitable spatial and temporal discretization schemes is crucial for the stability and accuracy of the solution.

For time marching, a backward differencing scheme was used. This guarantees second-order accuracy in the temporal domain. Given that Large Eddy Simulation (LES) is employed for turbulence modelling, it is necessary to select time steps (Δt) which guarantee that the Courant number ($Co = U\Delta t/\Delta x$) remains smaller than 0.5 (see [172]). Given that the mesh refinement used between meshes M1, M2, and M3, this corresponds to a time step which reduces from 0.2s for mesh M1, to 0.1s for mesh M2, and 0.05s for mesh M3.

The linear schemes are recommended for the momentum convection terms for stable LES simulations. In the case of channel flow, where the mesh quality is excellent (with a mesh skewness quality of 1 due to the use of 90-degree hexahedral elements), a linear scheme was also adopted to compute the gradient terms at the cell centroids. In cases where the mesh quality was slightly diminished with more complex geometries (for example in the geometry of the organism within textures), the PIMPLE algorithm was used to correct for non-orthogonality using a deferred correction approach, as described in Chapter 3.

A high-resolution TVD scheme, known as the limitedLinear scheme in OpenFoam, was adopted to calculate face fluxes of sub-grid turbulent kinetic energy (k_{sgs}) at faces [170]. This method combines central differencing and first-order upwind schemes to estimate k_{sgs} .

$$\phi_f = \phi_{fUD} + \Psi(r)(\phi_{fHO} - \phi_{fUD}) \quad (4.5)$$

$$\Psi(r) = \max(\min(\frac{2}{K_D}r, 1), 0) \quad (4.6)$$

$$r = 2 \left(\frac{(\nabla\phi)_p \cdot d}{(\nabla\phi)_f \cdot d} \right) - 1 \quad (4.7)$$

Eq. (4.6) defines the flux limiter, denoted as $\Psi(r)$. This flux limiter is determined by the successive gradients (r) as indicated in Eq. 4.7, and depends on the parameter K_D , which is constrained within the range of $0 \leq K_D \leq 1$. In this thesis, a value of $K_D = 1$ was used. Further details can be found in the works by [164], [170].

4.1.3 Boundary conditions

To simulate channel flow, periodic boundary conditions were assigned to the inlet and outlet and to the walls in the span-wise direction. This is implemented to replicate an infinite computational domain in the span-wise and stream-wise directions.

The top and bottom walls are modelled with a no-slip condition. This means that the velocity components u_i and the sub-grid scale turbulent kinetic energy k_{sgs} are set to zero at the wall regions and a zero-gradient condition was imposed for the pressure field.

4.1.4 Solver algorithm

The PimpleFoam solver, implemented in OpenFOAM, is employed for solving the Navier-Stokes equations, as discussed in Chapter 3. Non-orthogonal loop correctors are activated in cases where the mesh is not perfectly orthogonal. To ensure a robust solution, two Pimple outer-corrector loops are utilized along with three non-orthogonal corrector iterations, as described by [172]. This combination has guaranteed stability for the tested simulations.

4.2 Fully developed turbulent channel Flow with roughened walls

As indicated in the literature review, marine animals employ surface features on their skin to prevent the settlement of fouling organisms. A simplified model of ridges, found on the skin of brill fish (*Scophthalmus rhombus*), was selected as a candidate for surface modification to disrupt biofouling organisms settlement [13](see Fig. 4.3). The candidate texture on the brill fish skin is characterized by arrays of individual separated micro-ridges of average length $l_x = 74.9\mu m$ and height $l_x = 11.7\mu m$. The mean peak-to-peak distance between neighbouring parallel ridges and intervals between successive features are $E = 16.6\mu m$ and $E = 16.6\mu m$, respectively. Textures similar to those considered in these simulations were successfully produced by micro-laser machining over flat samples made from a gel-coated composite material. Initial investigations have confirmed that current technology has the capacity to produce gaps as small as $10\mu m$ with good repeatability, albeit with some variation on the surface curvature over the prism edges. Currently, producing sharp edges would require an alternative approach but is possible by laser machining of thin films. A typical array viewed by SEM is shown along with the texture layout studied in this thesis in Fig. 4.3.

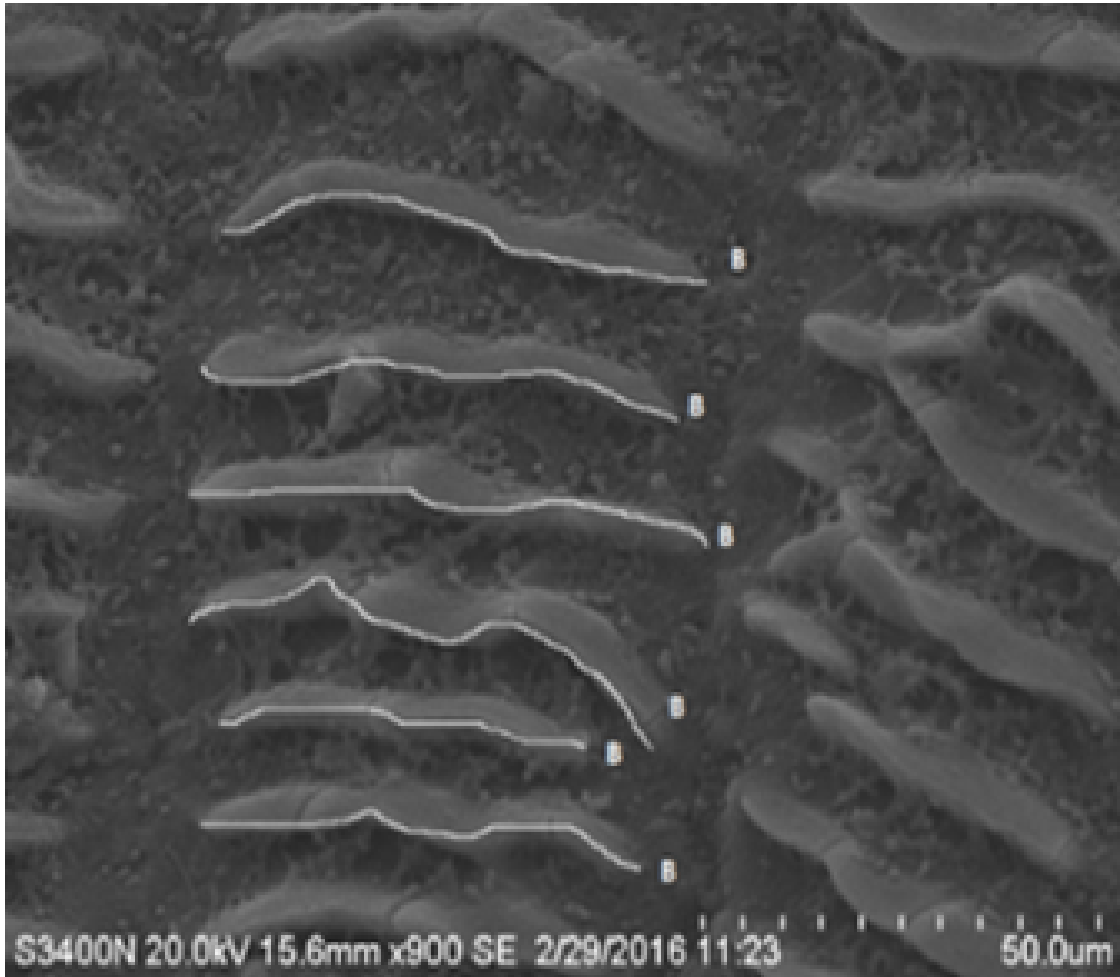


Figure 4.3: Image of Microridges from the growth rings of the brill fish, *Scophthalmus rhombus* [13].

A simplified model of textures was created to simulate their effects on the turbulent stresses. This model, depicted in Fig. 4.4, is made up of rectangular bars. The spacing between adjacent bars is chosen to cover the range of measurements taken from the brill fish ridge gap sizes and larger than that by scaling it with the smooth wall viscous length scale. A total of five texture configurations were chosen for the simulations. Four are based on rectangular bars, which are aligned in the stream-wise direction, while one is aligned in the span-wise direction. The study focuses on a parametric study of the gap size S separating adjacent bars. Results are reported in terms of the scaled parameter $S^+ = S/\delta_v$ in Chapter 6, where δ_v represents the viscous length scale and the plan area density λ_p in Chapters 7 and 8.

The five texture configurations can be observed in Fig. 4.5 where Images (a), (c) and (d) represent stream-wise textures with spacings of $S^+ = 10, 40,$ and 80 respectively. These textures have length, height, and width $l_x^+ = 316, h^+ = 40,$ and $l_z^+ = 105$ respectively. The case with spacing $S^+ = 20$ (Fig. 4.5, Image (b)) has a length scale which is twice that of other textures that is $l_x^+ = 632$. Fig. 4.5, Image (e) shows the

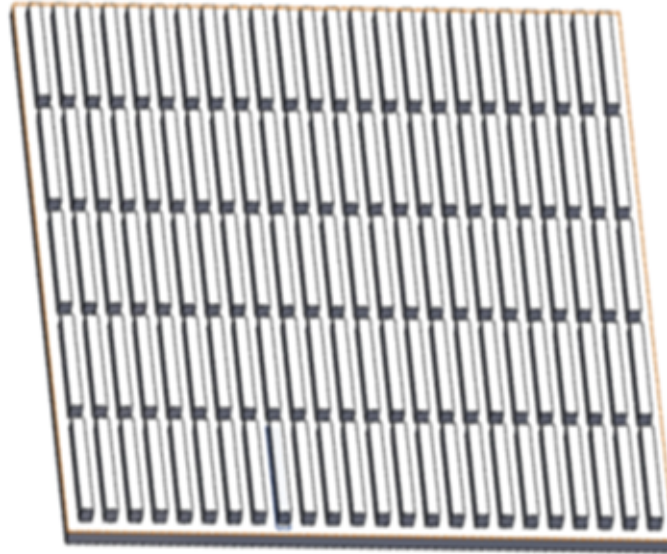


Figure 4.4: A simplified model of the candidate texture.

texture with a spacing of $S^+ = 80$, where the longer dimension ($l^+ = 316$) is in the span-wise direction. The mean gap observed on the growth ring of the brill fish is $10\mu m$, which corresponds to approximately 10 in viscous length scale if applied to the surface of the tidal turbine blade [175]. It should be noted that experimental observations showed evidence that a groove width as small as or smaller than $10\mu m$ (S gap) can effectively hinder access by bacteria and larger microalgae [13], but it may also prevent turbulent structures from penetrating within the gap between micro-textures with potentially undesirable effects on organism removal. The range of values of S considered in this study was chosen to explore the effects of the width of the groove on turbulent statistics and generated turbulent stresses.

Turbulent conditions generated by the rectangular shapes with sharp edges, as considered here are relatively Reynolds number independent [137], [176], [177], making it possible to consider a relatively small Reynolds number and rely on LES simulations to resolve most of the turbulent eddy spectrum without incurring excessive computational loads.

The roughness Reynolds number is defined by $k^+ = u_\tau l_y / \nu$ where l_y stands for roughness height and u_τ is calculated from the actual wall shear stress, taking account of the textures rather than the smooth wall equivalent. The roughness Reynolds number values tested are $k^+ = 38.5, 39, 5, 41.5, 48.5, 44.3$ for the four gaps $S^+ = 10, 20, 40, 80$ for the stream-wise textures and for $S^+ = 80$ for the span-wise texture, respectively. The flow can, therefore be considered transitionally rough in all cases. The geometry and computational meshes are illustrated for the cases shown in Fig. 4.5. The base mesh adopted is Mesh M3 from the validation study for smooth wall channels so the same block structure has been adopted for all cases.

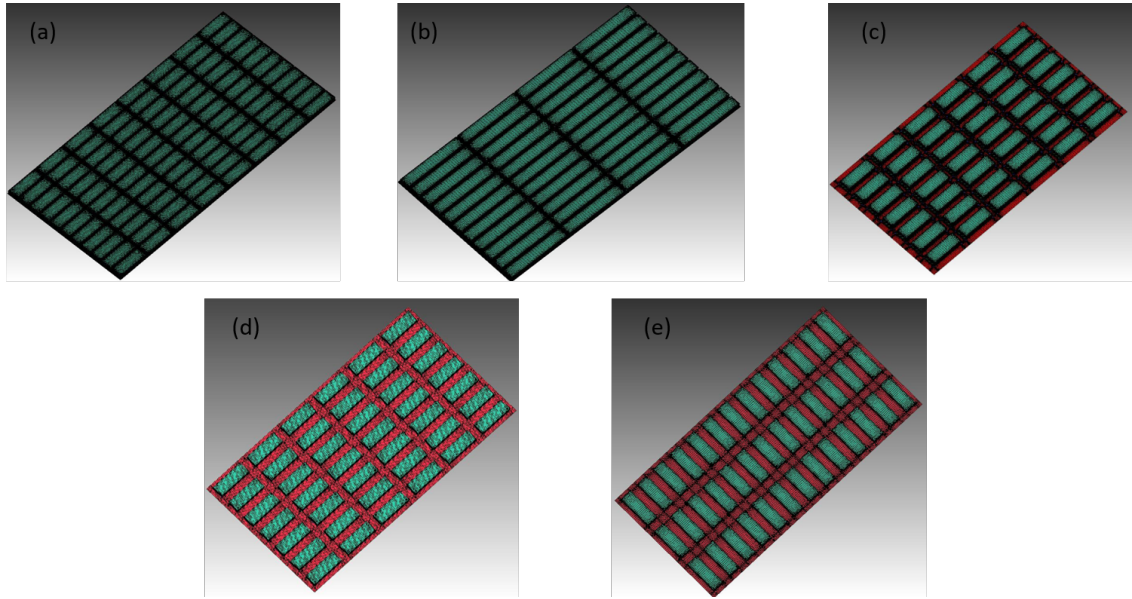


Figure 4.5: Five textures used in simulations: stream-wise textures separated by gaps (a) $S^+ = 10$, (b) $S^+ = 20$, (c) $S^+ = 40$, and (d) $S^+ = 80$ spacing, and span-wise textures with $S^+ = 80$.

Further refinement was needed to resolve the flow around the textures. The mesh resolution around the prisms was determined from the Kolmogorov length scale η , which was assumed for that purpose to be similar to values reported in [137] at $Re_\tau = 395$ as $\eta = 0.0075l_y$ and $\eta = 0.0039l_y$ within the roughness gap and in the shear layer over roughness textures, respectively. The three tested meshes were chosen so that the maximum cell length was 10 to 40 times the expected Kolmogorov length scales. The y^+ for the first cell height was chosen to be less than 1 for all cases. Biased non-uniform meshes with a growth ratio of 1.1, emphasizing walls within textures and rectangular sharp edges, are used to resolve fast gradients. The resulting mesh characteristics are given in Table 4.3.

Mesh case	Gap sizes based on wall units (S^+)	First cell height y^+	Δx^+	Δz^+	Number of cells	Number of Nodes in $x \times y \times z$ directions
1	10	0.8	10	6	17,088,435	$456 \times 108 \times 352$
2	20 elongated bars	1.05	10	6	11,340,000	$350 \times 108 \times 300$
3	40	1.3	10	6	7,358,390	$300 \times 108 \times 231$
4	80	1.5	10	6	7,358,390	$300 \times 108 \times 231$
5	80 span-wise	1.3	10	6	7,358,390	$300 \times 108 \times 231$

Table 4.3: Mesh characteristics used for the different textures at $Re_\tau = 395$.

4.2.1 Boundary conditions

A no-slip boundary condition was applied to all surfaces of the textures. Only one side of the channel is textured, and the top wall was model as a smooth wall. Periodic boundary conditions were applied to the computational domain's left, right, inlet, and outlet.

4.2.2 Discretization schemes and solver algorithm

The discretization scheme and algorithm that were successfully tested on a smooth channel wall have been adopted to solve the Navier-Stokes equations.

4.3 Fully developed turbulent channel flow with one-side textured wall and attached organism

This section describes the numerical set-up for a one-sided textured fully developed turbulent channel flow, with a single bio-fouling organism model placed at three different locations on and within the texture. The scenario where the organism is also positioned on the smooth wall of the channel flow was also investigated.

4.3.1 The candidate bio-organism geometry

The *Nitzschia* marine diatom species are predominantly found in cold water. This group of organisms are known to vary in length, from 1 to 100 μm or more, and in width, from 1 to 15 μm or more. The shape of the *Nitzschia* species is shown in Fig. 4.6 [178]. A less complex oval cylinder is recommended by the Baltic Marine Environment Commission suggested to represent the diatom's body for the purpose of evaluating its volume (Fig. 4.7) [179]. To avoid the extremely fine meshes that would be needed to capture the higher curvature at the tip of this shape, in the present study, a stadium cylinder was used instead. (Fig. 4.7). Also, to avoid dealing with fine organisms that would result in fine meshes that increase computational costs, larger *Nitzschia* species scales were chosen. These scales were selected based on the wall units calculated in [175] for the tip of the tidal turbine, with a viscous length scale of 1 μm . The diatom model length, width and height were chosen to represent a larger organism with $d_1^+ = 60$, $d_2^+ = 10$, and $h^+ = 5$, where the sizes are given in wall units. This corresponds to $d_1 = 60\mu m$, $d_2 = 10\mu m$ and $h = 5\mu m$ when related to the nominal viscous length scale used to represent flow over the turbine blade toward its tip or $d_1 = 145mm$, $d_2 = 23.7mm$ and $h = 12.5mm$ based on the smooth wall units at $Re_\tau = 395$, when the viscous length scale is 2.53mm.

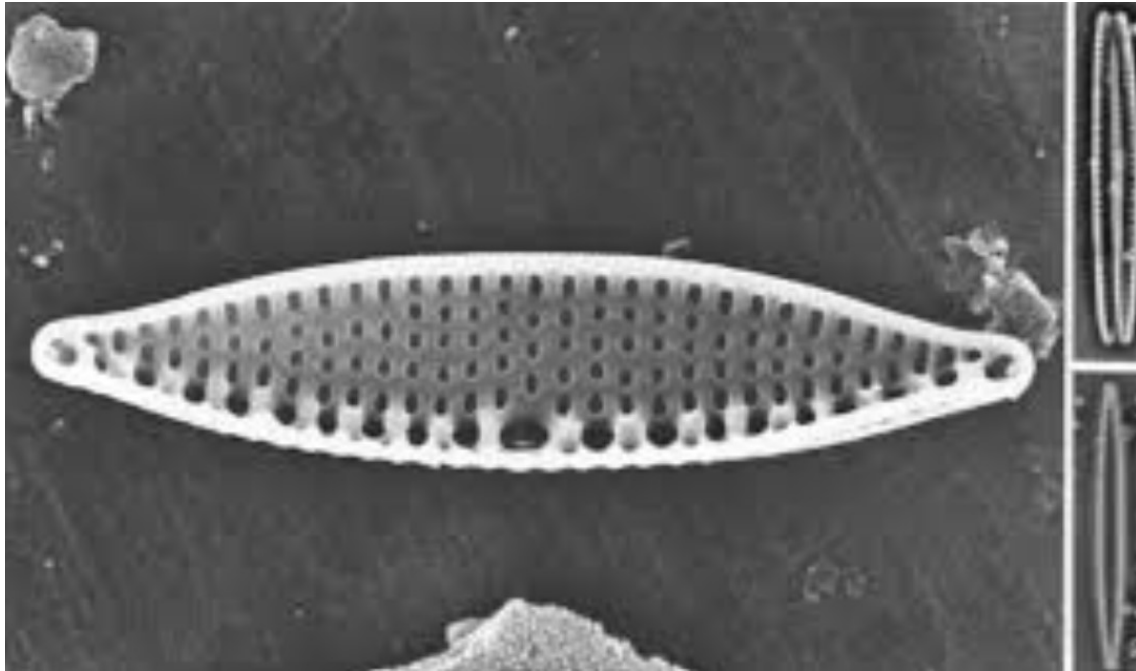


Figure 4.6: Image of a marine organism belonging to Nitzschia family taken from [178].

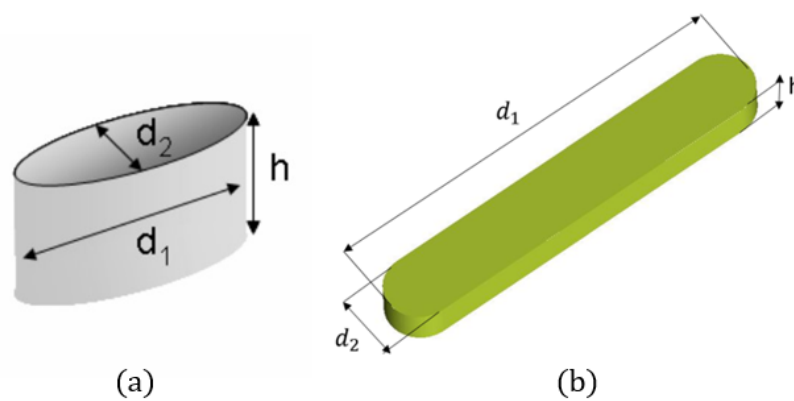


Figure 4.7: (a) The oval cylinder shape representing Nitzschia suggested by [179], (b) The stadium cylinder shape used in the present work to represent the Nitzschia.

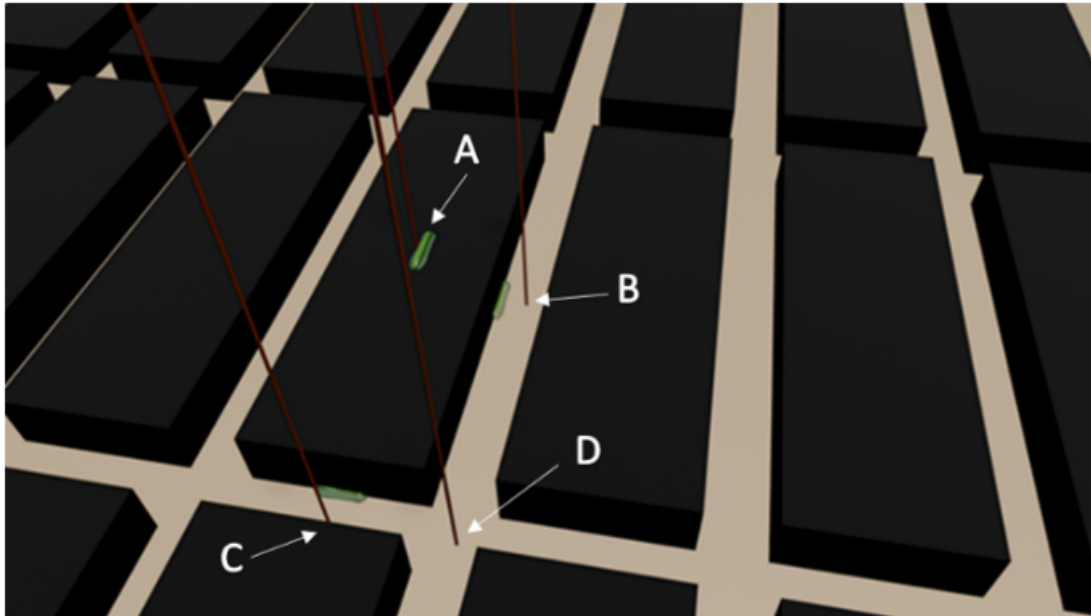


Figure 4.8: Illustration of the locations where the organism is placed [175].

4.3.2 Texture with the organism meshes

The candidate organisms were positioned in three distinct locations of the texture: A on the crest plane of texture, B in the bottom wall of the stream-wise gap, and C in the bottom wall of the span-wise gap of the texture $\lambda_p = 0.457$ stream-wise (see Chapter 7). The resulting forces are then compared with those obtained from an organism placed on the bottom wall of a smooth wall channel. A similar mesh with a similar cell count to the one-sided texture case was used to mesh this case away from the organisms. However, for the parts of the domain which include the organism, a higher mesh density is used to better resolve the flow interaction with the organism. A total of $16 \times 6 \times 9$ nodes were used to model the geometry of the organism. Once again the mesh was refined gradually toward the organism walls using a biased non-uniform mesh with a growth ratio of 1.07 (Fig. 4.9). Further details regarding the computational mesh in the vicinity of the organism for the four cases are given in Fig. 4.10 and Table 4.4. It is worth noting that the organism was oriented in the span-wise direction within the span-wise gap rather than in the stream-wise direction as for the stream-wise gaps. Similar attachment patterns have been observed in lab studies.

4.3.3 Boundary conditions

A no-slip boundary condition is used on all solid surfaces including on organisms. The remaining boundary conditions were set in the same way as for simulations without organisms.

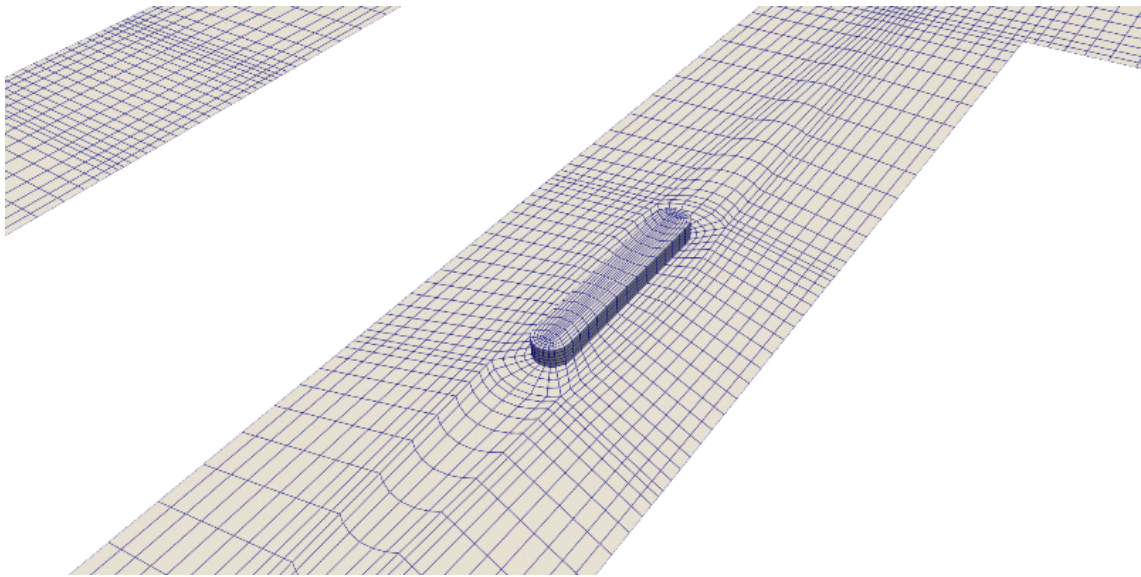


Figure 4.9: Surface meshes used on and around the organism.

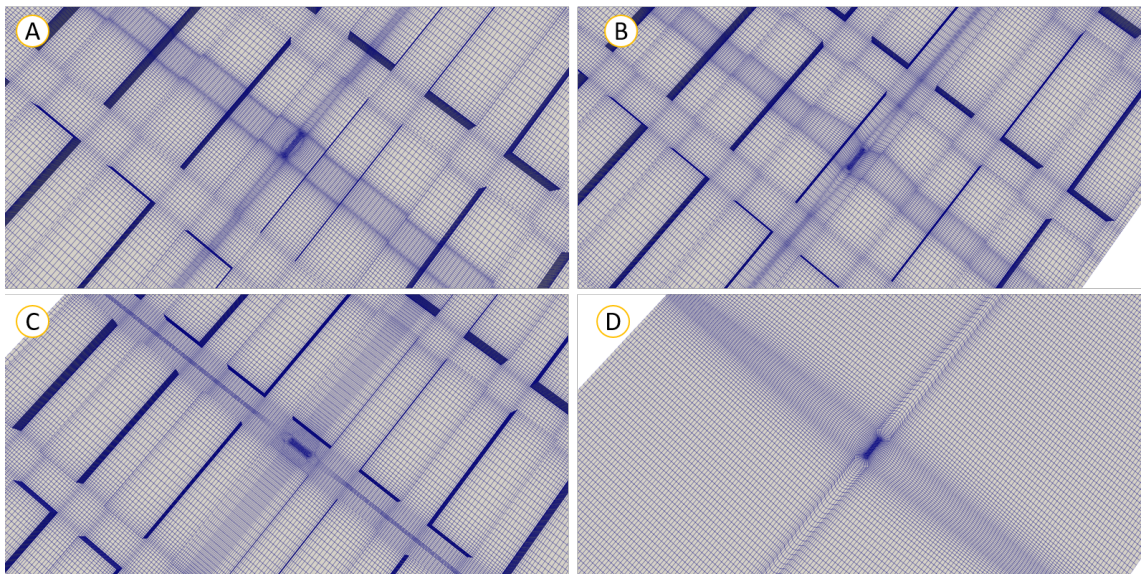


Figure 4.10: Overview of related geometry and mesh textures: (A) Organism placed at the texture crest, (B) Organism placed in the texture stream-wise gap, (C) Organism placed in the texture span-wise gap, (D) Organism placed at a smooth wall.

Cases	Organism Locations	Number of nodes in $x \times y \times z$ directions	Number of Cells
A	Texture Crest	$363 \times 140 \times 247$	12,552,540
B	Bottom of the stream-wise gap	$363 \times 140 \times 247$	12,552,540
C	Bottom of the span-wise gap	$317 \times 140 \times 247$	10,961,860
D	Smooth wall Organism	$260 \times 200 \times 247$	6,240,000

Table 4.4: Number of mesh nodes used for the $\lambda_p = 0.457$ stream-wise texture with the organism placed at different locations.

4.3.4 Discretization schemes and solver algorithm

The discretization scheme and algorithm validated on a smooth channel wall with textures have been employed to solve the Navier-Stokes equations. Two additional non-orthogonal correction iterations have been used with the pimpleFoam loop to account for the skewness of mesh in the vicinity of the organisms. The aim is to better control the diffusion errors that occur due to the mesh non-orthogonality in this part of the domain. All other aspects of the simulation setup were unchanged compared to the smooth wall case.

4.4 Simulation campaign and computational resources

In order to accurately resolve flow near surfaces, fine meshes are used to capture the velocity profile adjacent to the walls. A Courant number of less than 0.5 was used to maintain control over error propagation, necessitating small time steps for the cases involving textures (0.05 (s) for smooth walls and 0.01 (s) for textured walls). The introduction of organisms onto the textured surfaces further reduced the time step to 0.0025 seconds. For all cases, a preliminary transient simulation of duration $200T$ where $T = L_x/U_b$ was used before sampling of turbulent statistics, following the procedure adopted in [137]. After that, another $200T$ simulation time was used to probe turbulent statistics data. This duration was found to be necessary to converge the area averaged higher order statistics, to achieve the expected linear

slope in the reduction of turbulent shear stresses with the distance to the wall in the outer layer, and to reduce the large spatial variations linked to dispersive stresses in the outer layer. To enhance simulation efficiency, the computational domain was partitioned using the Scotch method, integrated into openFoam 6, and executed in parallel with a total of 640 processors. Overall, the simulations consumed over 2.5 million CPU hours. Table 4.5 summarizes how these computational resources were consumed based on their relevant plan area density λ_p .

cases	Number of meshes	Number of processors	Used CPU Hours
Smooth channel with coarse mesh	135,000	8	insignificant
Smooth channel with medium mesh	1,080,000	32	3k
Smooth channel with fine mesh	8,640,000	640	150k
$\lambda_p = 0.88$	17,088,435	640	400k
$\lambda_p = 0.77$	12,053,237	640	250k
$\lambda_p = 0.64$	7,358,390	640	120k
$\lambda_p = 0.457$ <i>stream - wise</i>	7,358,390	640	120k
$\lambda_p = 0.457$ <i>span - wise</i>	7,358,390	640	120k
organism on smooth wall	6,240,000	640	200k
organism at A location	12,552,540	640	350k
organism at B location	12,552,540	640	350k
organism at C location	10,961,860	640	350k

Table 4.5: Characteristics of carried out simulations.

4.5 Summary and Conclusion

In this chapter, the focus was on the geometrical configurations and the numerical setup for the high-fidelity simulations. Initially, the necessary geometrical length scales for a fully developed channel flow were introduced, and the corresponding mesh numbers were specified. Subsequently, the configurations of the textures and their respective mesh numbers were outlined. Additionally, it was noted that a stadium shape was employed to model the candidate organism. Towards the conclusion of the chapter, the numerical schemes and time steps utilized in the conducted simulations were presented. Finally, the computational costs for all simulations were detailed at the end of the chapter.

Chapter 5

LES solver validation on a smooth wall channel

This chapter presents the validation of the LES solver, performed on a smooth wall fully developed turbulent channel flow at a Reynolds number of $Re_\tau = 395$.

Simulation phases

Given the inherent unpredictability of turbulent flow, a common practice is to present turbulence results in an averaged form. For the case of fully developed turbulent channel flow, which is a statistically stationary problem, the simulation must be conducted in two phases (see Chapter 4). In the preliminary phase, each simulation is initiated with a precursor solution using a RANS $k - \omega SST$ model. The simulations were carried out for a duration of 10000 seconds with a prescribed time-step to achieve statistically stationary conditions. No data was sampled during this preliminary phase. The secondary phase involved time averaging, which starts at the beginning of this phase and continues for 20000 seconds, or until the statistical error becomes insignificant. This approach ensures that the turbulence results are obtained from a statistically stable and reliable state [172].

5.1 LES solutions on a smooth wall channel at $Re_\tau = 395$ (methodology validation)

This section presents the LES solutions for the smooth wall channel flow that were carried out to validate the mesh and simulation methodology. Results are compared with a DNS solution at $Re_\tau = 395$ [180].

5.1.1 Mean velocity profiles

This section presents the mean velocity in the stream-wise direction for the three meshes, shown in Fig. 5.1. Due to the statistically stationary state and boundary conditions, both mean velocities in the normal-to-wall and span-wise directions are zero everywhere.

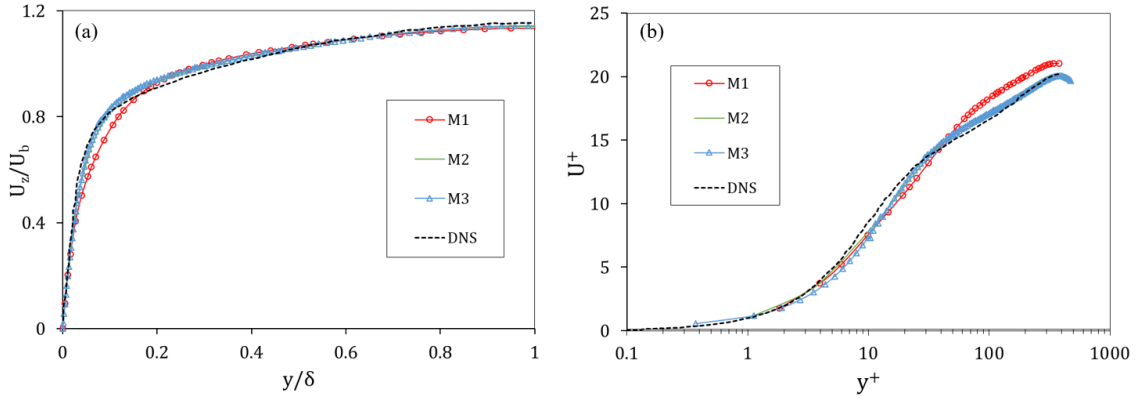


Figure 5.1: Comparison of the normalised stream-wise velocity profile predicted by mesh refinements with the LES turbulence model against DNS results from [180]. The plots are scaled against the wall distance, (a) in outer and (b) in inner units.

Fig. 5.1 (a) displays the mean stream-wise velocity scaled with the bulk velocity plotted against y/δ , where y represents the direction normal to the wall and δ denotes half of the channel height. It can be seen that there is no noticeable difference among the meshes when $y/\delta > 0.2$. However, below this range, within the inner layer, the coarser mesh (M1) lies well below the graphs for the other two meshes. Alone based on this diagram, it is hard to discuss the accuracy of the M2 and M3 results. An alternative diagram and scaling method involve scaling the velocity with the friction velocity from the smooth wall simulation and the wall distance with the viscous length scale δ_v . This is illustrated in Fig. 5.1 (b), where $U^+ = \langle U_z \rangle / u_\tau$ and $y^+ = y/\delta_v$, with y^+ represented on a logarithmic scale. The viscous length scale δ_v is computed in each simulation, and in the DNS simulation, it is reported to be 0.00253 [180]. When transitioning from the coarse mesh M1 to the finer M3, the computed value of u_τ increases from 0.00725 to 0.0077. The target value of u_τ from the DNS data is 0.0079. As observed in Fig. 5.1 (b), the coarse mesh fails to accurately capture the viscous sub-layer due to its larger mesh size near the wall. However, by increasing the number of cells near the walls in the M2 and M3 configurations, the captured viscous sub-layer aligns with the results of the DNS simulation ($0 \leq y^+ \leq 10$). Within the buffer layer ($10 \leq y^+ \leq 30$), all three meshes are shown to underestimate the velocity by comparison with the DNS results. However, as the value of y^+ approaches 30, the M1 mesh is shown to

improve prediction. Beyond $y^+ \geq 30$, the DNS data show a linear dependence on y^+ which is known as the log layer. In this log-layer region, all meshes overestimate DNS results. By increasing the mesh count, the results gradually converge towards the DNS results within the log-layer. The coarse mesh M1, exhibits a 20% error, while this error reduces to 2.5% with the fine mesh M3. This suggests that the M3 mesh achieves good accuracy for engineering applications, allowing the resolution of the wall velocity profile without the need for wall modelling.

5.1.2 Reynolds stress tensor (turbulence fluctuations)

Due to the random nature of turbulence, statistical methods are employed to describe the turbulent flow. Reynolds stresses are the parameters utilized to define fluctuations in turbulence. Fig. 5.2 to Fig. 5.4 display the scaled root mean square (RMS) values of the diagonal components of Reynolds stress tensors plotted against y/δ and y^+ . It has become customary in turbulence literature to employ the RMS values of the diagonal Reynolds stress tensors as indicators of turbulence fluctuations in the (x, y, z) directions. All the diagonal stresses are normalized with respect to u_τ . Fig 5.2 shows the stream-wise fluctuations plotted against the distance to the wall. It is evident that the coarser mesh M1, fails to capture the DNS results, while the finer meshes provide better resolution with convergence towards the DNS results. The differences between DNS and LES (large eddy simulation) results obtained with the finest mesh M3 are comparable to those reported in the study of [181], where an LES k-Equation model was used to simulate the same channel flow case at $Re\tau = 395$. In [181], the peak in stream-wise fluctuation was over-predicted by 8%, while the present results exhibit an over-prediction of 6%. Also, a similar trend is observed for the wall-normal and span-wise fluctuations, where the use of finer meshes enables better comparisons with DNS results.

Fig. 5.5 (a) and (b), show the off-diagonal term of the turbulent stress tensor, in the stream-wise direction, scaled in the outer and inner results as y/δ and y^+ , respectively. Due to the symmetrical geometry of the smooth wall channel flow, the shear stresses in the span-wise and normal-to-wall directions are both zero. Unlike the diagonal components of the Reynolds stress tensors, it is customary in the literature to normalize the shear stress using the square of u_τ . According to [88], the shear stress value is negative. Therefore, a minus sign is used to show the shear stress value.

The total stress is the sum of viscous and turbulent shear stresses [88]. Away from the wall, typically when $y^+ \geq 30$, the viscous stress becomes negligible compared to turbulent stresses, and it is expected that the turbulent stress takes on a linear dependence on y/δ . As observed, all three meshes can accurately reproduce the

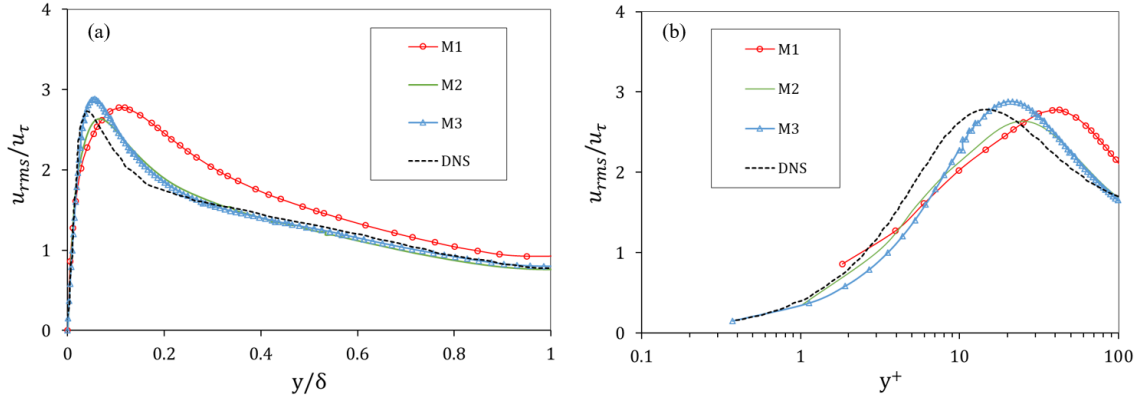


Figure 5.2: Comparison of the normalized stream-wise resolved Reynolds stress profile predicted by the successive mesh refinements with the LES turbulence model against DNS results from (citemoser1999direct). The plots are scaled against the wall distance, (a) in outer and (b) in inner units.

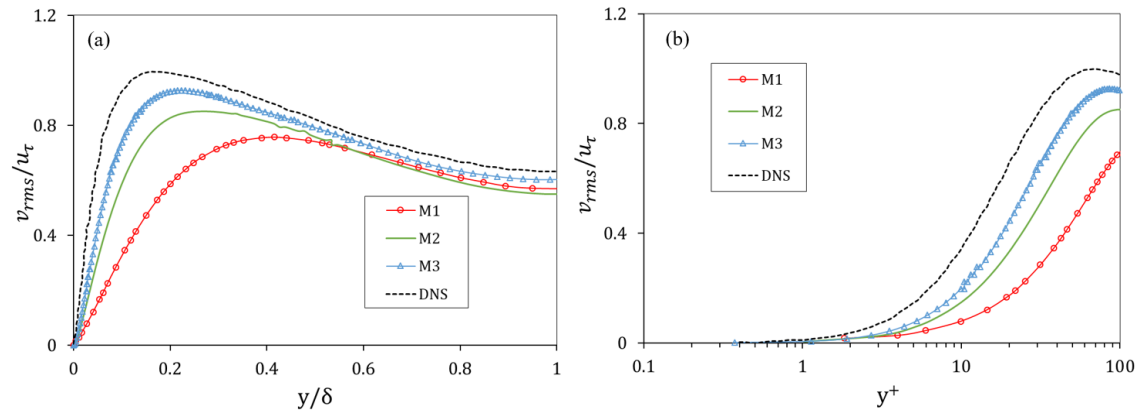


Figure 5.3: Comparison of the normalized normal-to-wall resolved Reynolds stress profile predicted by the successive mesh refinements with the LES turbulence model against DNS results from [180]. The plots are scaled against the wall distance, (a) in outer and (b) in inner units.

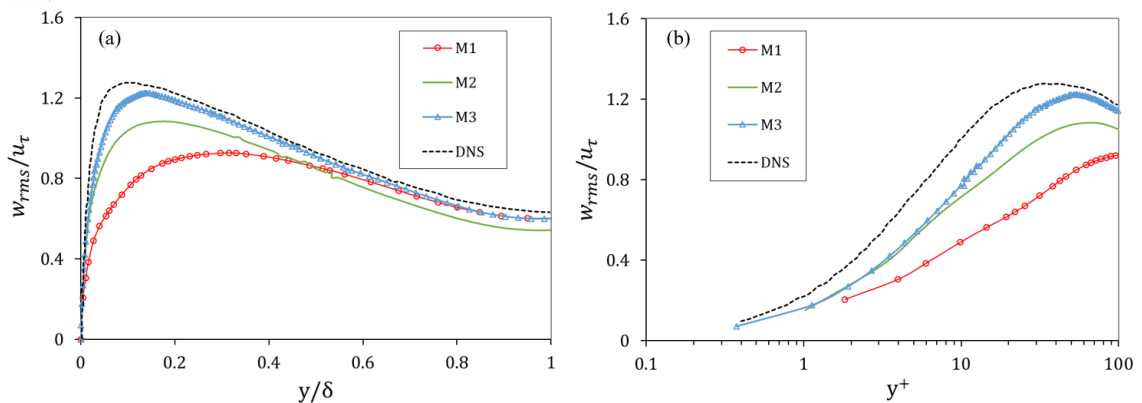


Figure 5.4: Comparison of the normalized span-wise resolved Reynolds stress profile predicted by the successive mesh refinements with the LES turbulence model against DNS results from [180]. The plots are scaled against the wall distance, (a) in outer and (b) in inner units.

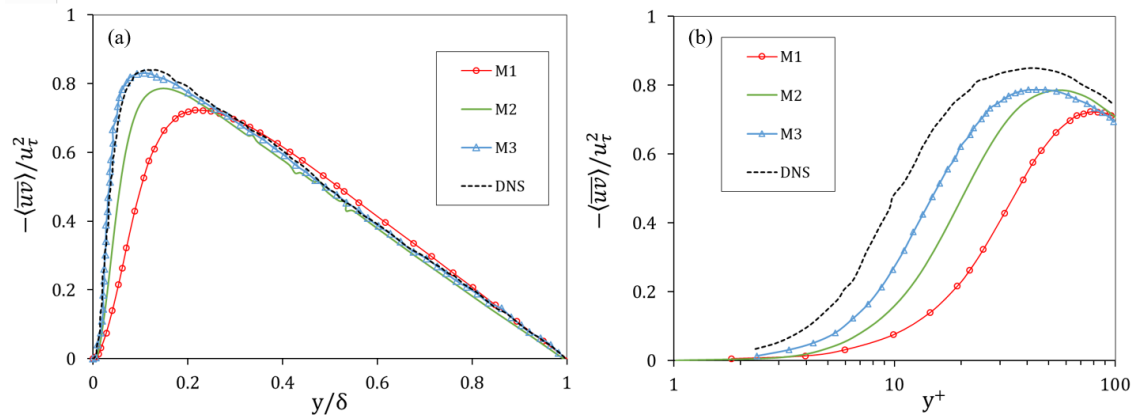


Figure 5.5: Comparison of the normalized resolved shear stress Reynolds stress profile predicted by the successive mesh refinements with the LES turbulence model against DNS results from [180]. The plots are scaled against the wall distance, (a) in outer and (b) in inner units.

linear portion of the DNS (direct numerical simulation) results. However, for $y/\delta \leq 0.2$, there are significant variations among the results produced by the three different meshes. In summary, as depicted in Fig. 5.5, the fine mesh results for the stream-wise stress exhibit good agreement with the DNS results.

5.1.3 Turbulent vortical structures

Based on the literature [87], [137], [171], vortical structures play a vital role in turbulent flows. When examining turbulent flow around a smooth wall, two types of vortical structures are identified based on their distance from the wall. Within the viscous sub-layer (where $0 \leq y^+ \leq 5$), elongated turbulent structures known as low and high-speed streaks begin to form, sometimes reaching a length scale of 1000 based on wall units. In the buffer layer (within $5 \leq y^+ \leq 30$), which contributes to the maximum production of the turbulent kinetic energy, the hairpin vortices emerge and generate turbulent kinetic energy through stretching. Also, hairpin vortices dominate the turbulent structures in the layer above the buffer layer, known as the logarithmic layer. The geometry of a hairpin vortex is illustrated in Fig. 5.6, as described by [159]. This vortex consists of two legs that are observed to rotate in opposite directions to one another. Fig. 5.8 displays numerically simulated stream-wise vortices located near the wall. It has been reported in the literature that these vortices, rotating in opposite directions, are associated with the legs of the hairpin vortex. The visualization of turbulent structures can be enhanced by examining flow over a series of surfaces parallel to the wall. Fig. 5.7 shows the vorticity contours at distances extending from the viscous sub-layer to the log-layer. At $y^+ = 5$, it is evident that elongated stream-wise structures with both high and low vorticity

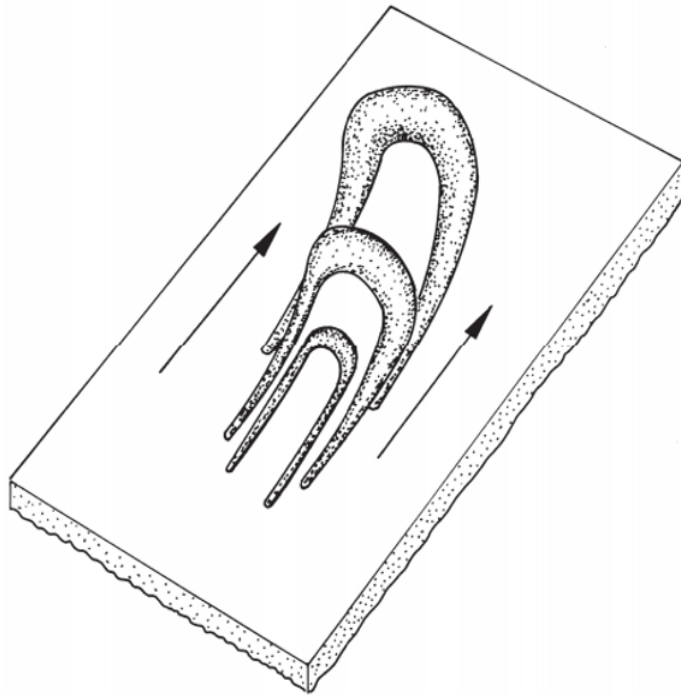


Figure 5.6: Hair-pin vortex shape [159].

values are positioned next to each other. As we move to $y^+ = 10$ and $y^+ = 15$, thicker streaks, which can be associated with the legs of the hairpin vortices, can be observed. As the distance from the wall increases further, the hairpin vortices become progressively thinner as they are stretched, which implies lower turbulent kinetic energy production.

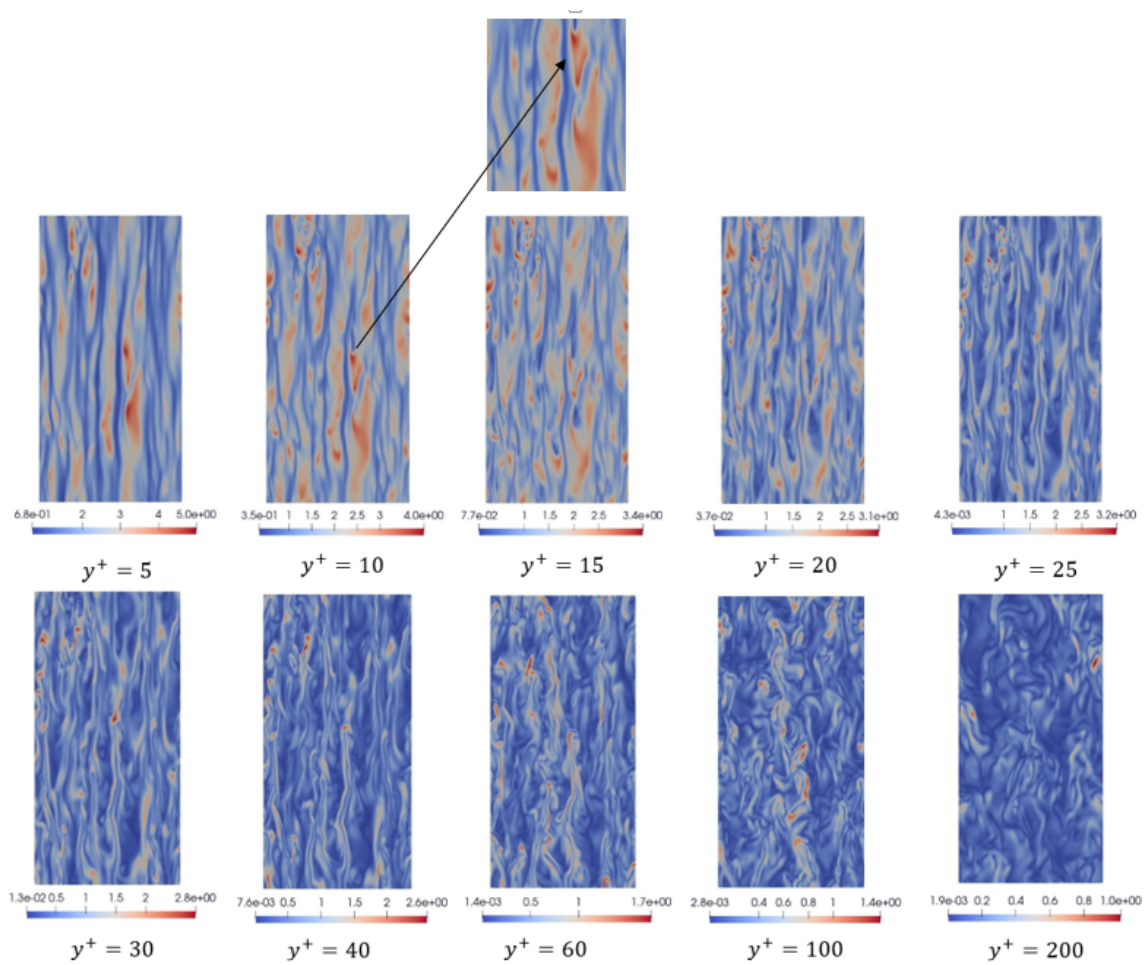


Figure 5.7: Vorticity contours at different y^+ normal to wall.

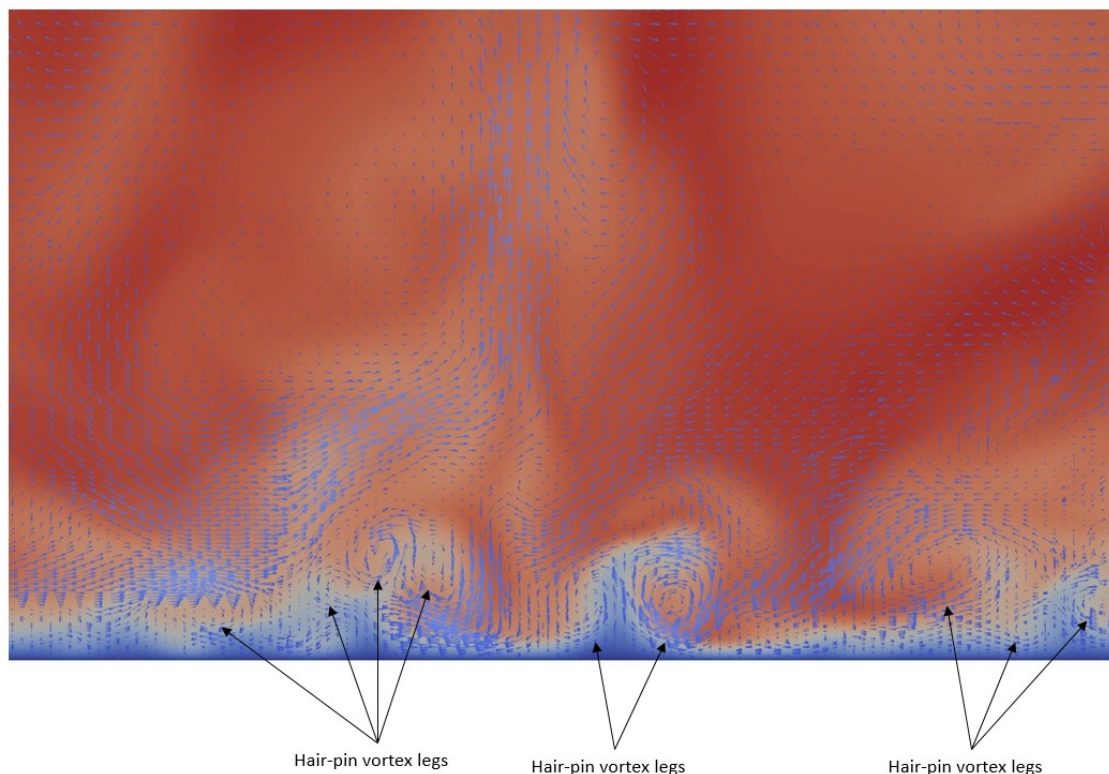


Figure 5.8: Stream-wise vortices next to wall (hair-pin legs).

5.2 Summary and Discussion

This chapter presents the results of LES simulations conducted on a fully turbulent channel flow. To evaluate the solver's accuracy, the Reynolds stresses tensor calculated from the LES solver is compared with the DNS solution. The results indicate that the LES estimation of the peak in the stream-wise fluctuation was over-predicted by 6% compared to the DNS solution. Additionally, it was noted that the LES results for stream-wise shear stress exhibited good agreement with the DNS results, especially for fine mesh configurations. Overall, transitioning from a coarse mesh to a fine mesh showed an improvement in accuracy, approaching the results obtained from DNS simulations. Therefore, for simulations involving textures in subsequent chapters, mesh sizes on the order of fine meshes or smaller are employed.

Chapter 6

LES results for the three stream-wise elongated textures at four different locations on and within textures

This chapter investigates the mean wall shear stress and local stream-wise fluctuations in second, third and fourth-order statistics (Reynolds stresses, skewness and flatness, respectively), for three distinct textures, namely $S^+ = 10, 40, 80$. Measurements are collected at four specified locations within and on the textures. Since all three mentioned cases involve rectangular textures aligned in the stream-wise direction, the focus is exclusively on these three textures. In the subsequent chapter, the other two textures ($S^+ = 20$ and $S^+ = 80$ in the span-wise direction) are included using plan area density [134], to distinguish between textures.

6.1 Mean wall shear stress within and on textures

Bio-fouling growth formation starts with the establishment and growth of a conditioning layer made of extracellular polymeric substances (EPS), which is typically thinner than the turbulent hydrodynamic layer over a hydro-turbine blade under nominal operating conditions. In highly turbulent flows, viscous and turbulent stresses can be expected to significantly impact early-stage foulers attaching to the surface and the subsequent growth of the EPS layer. While viscous shear forces are the only forces acting on the surface of smooth walls, textured surfaces can induce a combination of frictional and pressure drag components. In cases where the size of gaps between two consecutive roughness are larger than a certain threshold, the drag experienced by a texture is dominated by the pressure acting over the verti-

cal walls of the textures. For smaller distances between consecutive textures, the flow within the cavities formed by the gaps is characterized by weak vortices. The pressure acting on the vertical walls of the roughness elements becomes negligible in comparison with the frictional drag acting on the crest plane of roughness [127], [129], [132], [138].

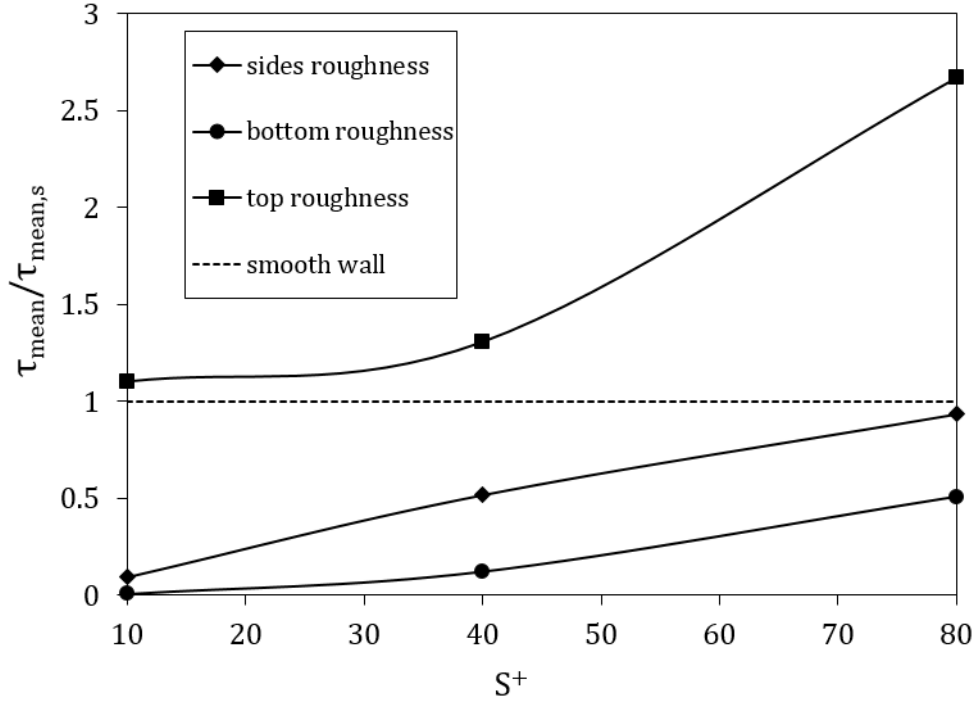


Figure 6.1: Mean wall shear stress on distinctive surfaces of rectangular cubes.

Since the present study’s largest pitch size (S^+) in all cases is at least twice the roughness height ($S^+ = 80$ is the largest gap size distance), frictional drag can be expected to remain the dominant force acting on surfaces. Fig. 6.1 summarizes the effect that surface texture has on the surface averaged wall shear stress compared with the smooth wall value. In this figure, τ_{mean} , the mean wall shear stress on rough surfaces, is scaled by $\tau_{mean,s}$, the mean wall shear stress on a smooth wall. It indicates that mean wall shear stress tends to reduce over the side walls of textures and over the surfaces at the bottom of gaps while increasing at the crest of the roughness compared to the smooth wall. The crest planes of $S^+ = 10, 40$ show nearly 10 to 30% increases in mean frictional stresses while showing a sharp rise from $S^+ = 40$ to 80 (170% increase). This can be attributed to an increase in the area-averaged velocity at the crest plane made possible by reducing the proportion of solid surface over the total area of the crest plane as S^+ increases [135]. It is also very clear that the mean shear stress over the lower surfaces within the grooves between prisms is much smaller than experienced over the smooth wall for all gaps considered except $S^+ = 80$.

6.2 Turbulent shear stresses within textures

The results presented in this section focus on the spatial distribution of turbulent shear stresses over horizontal inspection planes located at $y^+ = 12$ and $y^+ = 35$. The origin of the wall-normal coordinate y is placed at the crest plane of the textures, following the approach adopted in [135], [138]. The maximum zero wall displacement was calculated following the Jackson method [104] and was shown to be less than $\epsilon^+ = 2$ for $S^+ = 80$ at most and smaller for other gaps. In the case of the smooth wall, these locations are in the inner part of the boundary layer at either end of the buffer layer. With the textured surfaces considered, in this study, both inspection plane locations are below the crest plane of the textures and correspond to $y/l_y = 0.3$ and $y/l_y = 0.9$, where l_y is the roughness height. At flow conditions giving rise to a surface shear stress of 1000Pa and a viscous length scale of 1 μm (tip of the tidal turbine), The $y^+ = 12$ plane would be in close proximity to early stage micro-foulers settling over the bottom surface between roughness elements whereas the $y^+ = 35$ plane would be near organisms settling around the upper edge of the prisms. $y^+ = 12$ is also close to the location of peak production in turbulent kinetic energy for smooth walls. The shear stresses can be decomposed into two distinct terms: the viscous stresses and the Reynolds shear stress. The former stems from the viscosity of the fluid and the mean velocity gradients in the shear layer. Its contribution is important in the immediate vicinity of walls that are in the viscous sub-layer and in the buffer layer but becomes negligible fairly close to the walls. The viscous term contribution becomes small for flow over smooth surfaces at approximately $y^+ \sim 30$ [88]. Reynolds stresses are derived from the Navier-Stocks equations from Reynolds averaging and are representative of the turbulent mixing effect. For smooth wall boundary layers, they become the dominant stresses above $y^+ = 30$. The present analysis considers Reynolds shear stresses only. These refer to the three off-diagonal terms of the stress tensor $\overline{u_i u_j}$. Over smooth surfaces, the inner part of the turbulent boundary layer is dominated by stream-wise vortexes, characterised by one dominant shear stress \overline{uw} . The protrusion due to the surface texture can give rise to stronger span-wise fluctuations as stream-wise vortexes interact with eddies forming within the gap between textures. Results shown in Figs. 6.2 and 6.3 report the combined effects from the three shear stresses normalized with the square of the friction velocity from smooth wall boundary layer flow $u_{\tau,s}^2$ defined by Eq. (6.1):

$$\overline{\tau_{tot}} = (\sqrt{(\overline{uw})^2 + \overline{uw}^2 + \overline{vw}^2})/u_{\tau,s}^2 \quad (6.1)$$

The scaling with $u_{\tau,s}$ rather than the local friction velocity u_τ obtained with the appropriate textured surface is not customary but is intentional. The purpose is

to facilitate a comparison with stresses over smooth surfaces so that the impact of texturing as an anti-fouling strategy on the hydrodynamic stress can be assessed by reference to an untextured surface. Fig. 6.2 indicates that turbulent shear stresses cannot penetrate in any significant way into the lower part of the gaps when $S^+ = 10$. The $\overline{\tau_{tot}}$ in this case is less than 0.5% of the smooth wall mean kinematic shear stress ($u_{\tau,s}^2$). This increases to 18% and 40% when the gap size is changed to $S^+ = 40$ and 80, respectively. Closer to the crest plane at $y^+ = 35$, the contours, shown in Fig. 6.3, provide similar evidence that little turbulence penetrates within the gaps when it is reduced to $S^+ = 10$. For higher gap widths $S^+ = 40$ and 80, $\overline{\tau_{tot}}$ reaches 70% and 140% of the smooth wall mean shear stress. Taking a closer look at the $\overline{\tau_{tot}}$ contours over the stream-wise gaps, larger stresses can be seen in the gaps' core, away from the side walls at $y^+ = 12$. This is also true at $y^+ = 35$ for $S^+ = 10$ and 40, but increasing the gap to 80, shifts the stress concentrations toward the textures' side walls, where early-stage micro-organisms may seek to settle. The total stress is also clearly shown to be stronger at the junction between the stream-wise and span-wise gaps, where interactions between eddies from both directions and the textures are most likely to amplify fluctuations. So far, no attempt has

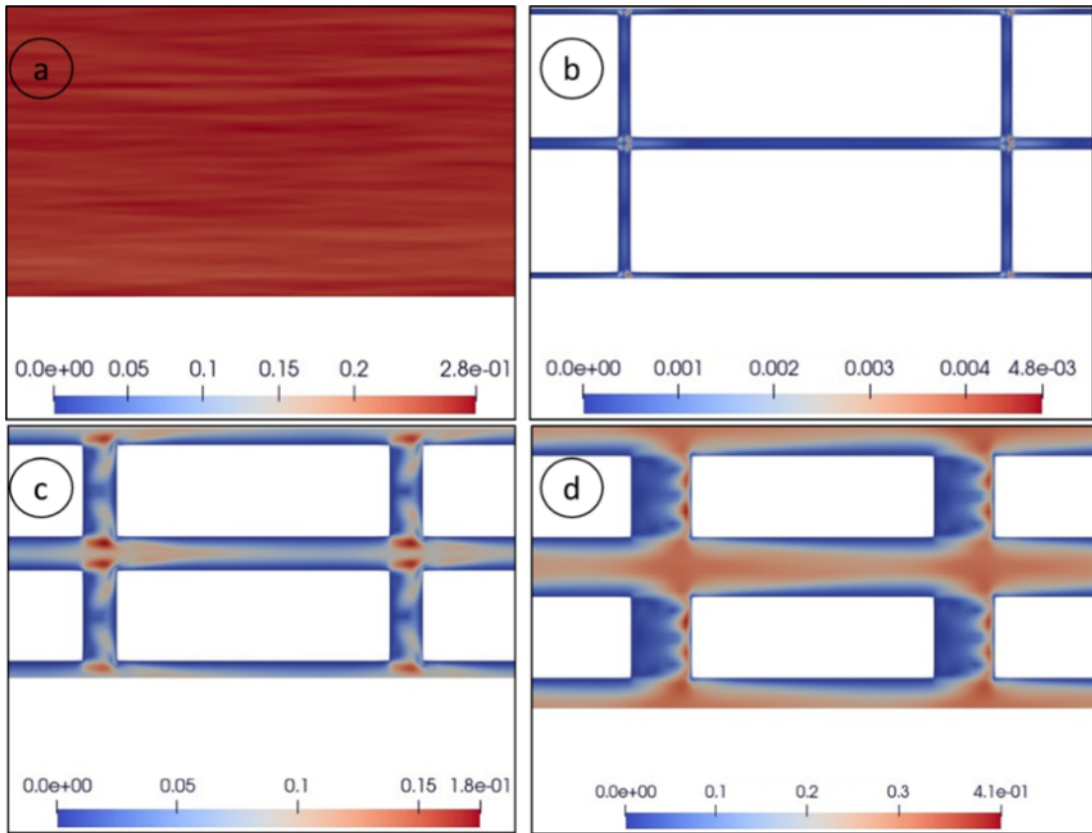


Figure 6.2: Contours of the normalized turbulent shear stress $\overline{\tau_{tot}}$ at $y^+ = 12$ or $y/l_y = 0.3$ for (a) Smooth wall , (b) $S^+ = 10$, (c) $S^+ = 40$ and (d) $S^+ = 80$.

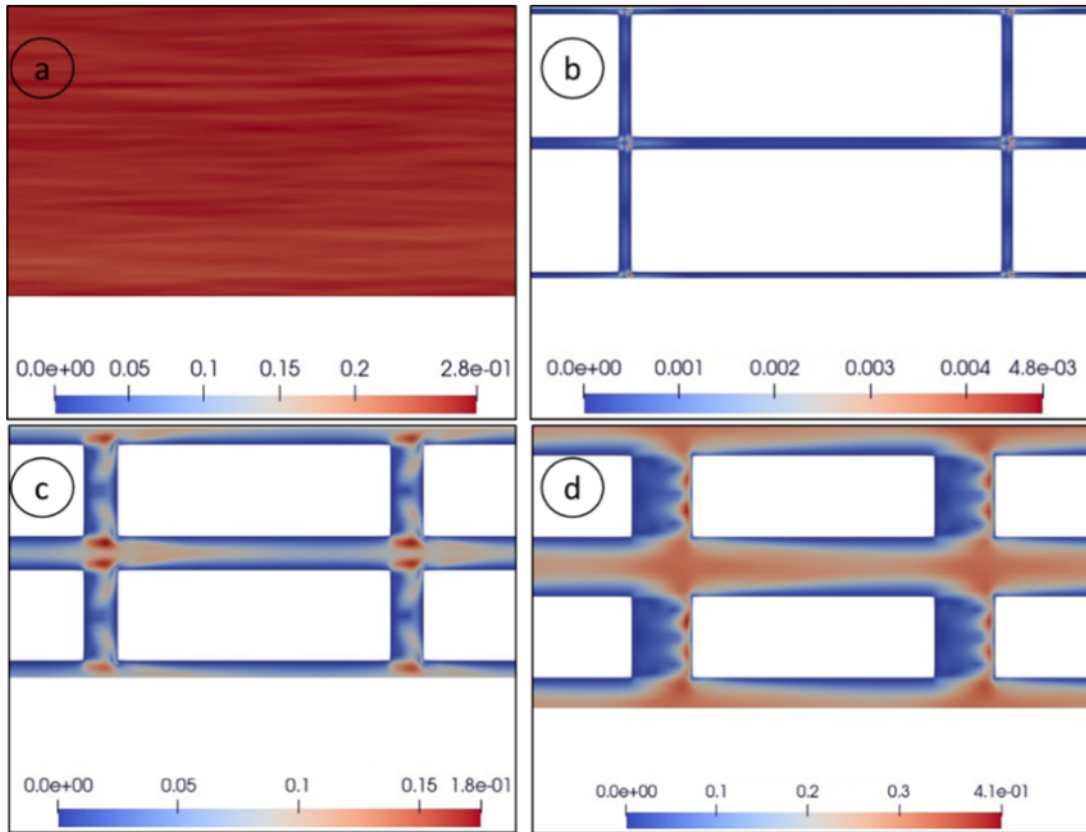


Figure 6.3: Contours of the normalized turbulent shear stress $\overline{\tau_{tot}}$ at $y^+ = 35$ or $y/l_y = 0.9$ for (a) Smooth wall, (b) $S^+ = 10$, (c) $S^+ = 40$ and (d) $S^+ = 80$.

been made to distinguish between the shear stress terms. It is, however, instructive to look at these individual stresses. This will be done in more detail in the next section but it is worth noting here that all three components of $\overline{\tau_{tot}}$ reach a maximum value (in the plane perpendicular to the stream-wise direction and containing the prism centroid) which is similar to the maximum reached by $\overline{\tau_{tot}}$. The contour plots of Fig. 6.4 show that all terms make a meaningful contribution to $\overline{\tau_{tot}}$ but with different distributions. $\overline{v\overline{w}}$ increases with y^+ but more so above the bar edges. There are elliptic areas of concentration of $\overline{v\overline{w}}$, which are centred almost directly on and slightly above the bar corners, while concentrations of $\overline{u\overline{w}}$ also appear near the bar corners, filling up most of the crest plane above the gaps. For $S^+ = 40$ and $S^+ = 80$, the $\overline{v\overline{w}}$ and $\overline{u\overline{w}}$, symmetric distributions with peaks of opposite signs can be observed and suggest that contra-rotating pairs of vortices form near the prism edges. This is consistent with the appearance of stream-wise vortices aligned with the gaps located in the upper part and above the gaps as illustrated by the $Q = 0.05$ field iso-surfaces shown in Fig. 6.5. The contours coloured by stream-wise vorticity, do show one instance of contra-rotating vortices penetrating well within the gap at $S^+ = 80$, while vortices appear to remain closer to the upper edges at $S^+ = 40$. This along with the stress contours suggests that as the gap widens,

vortexes penetrate further towards the bottom walls thereby concentrating stresses near the upper part of the vertical surfaces and the corners while also increasing stresses within the gaps. However, when the gap reduces to $S^+ = 10$, the vortexes can no longer penetrate the grooves reducing most of the Reynolds stresses.

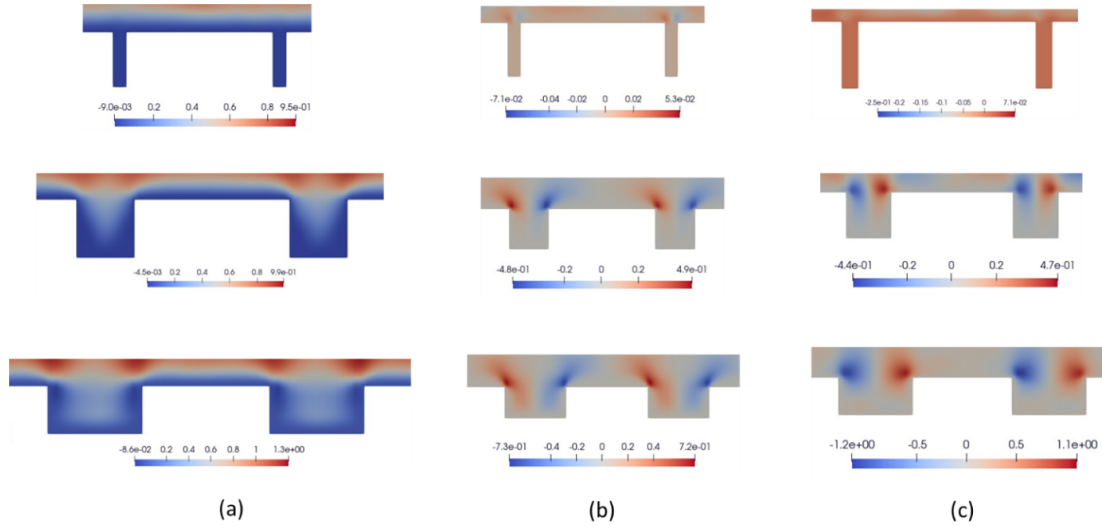


Figure 6.4: Contours of \overline{uv} (Left Column), \overline{vw} (middle column Column) and \overline{ww} (right column Column) stresses over the section plane centred over the textures. ((a) $S^+ = 10$, (b) $S^+ = 40$, (c) $S^+ = 80$). The cross-section shown is in the plane perpendicular to the stream-wise direction and contains the prism centroid.

6.3 Second to fourth order of statistics in four various regions

In this section, wall-normal profiles of second-order and higher order of turbulence statistics (stream-wise Reynolds shear stress, the transport of turbulent kinetic energy, and fourth-order moments) are studied over four sampling lines named A, B, C and D. A is located at the centre of the texture's crest plane, B and C are at the centre of the grooves between two textures in the stream-wise and span-wise respectively and D is at the centre of the junction of the stream-wise and span-wise grooves. The lines were chosen for their proximity to the location where higher levels of settlements of two diatoms *Amphora coffeaeformis* and *Nitzschia ovalis* were observed [13]. The four sampling lines are illustrated in Fig. 6.6.

6.3.1 Second order statistics

It is well documented that for the smooth channel flow, the Reynolds shear stresses $wv^+ = \overline{wv}/u_{\tau,s}^2$ reduce linearly with the wall distance up to the channel half height

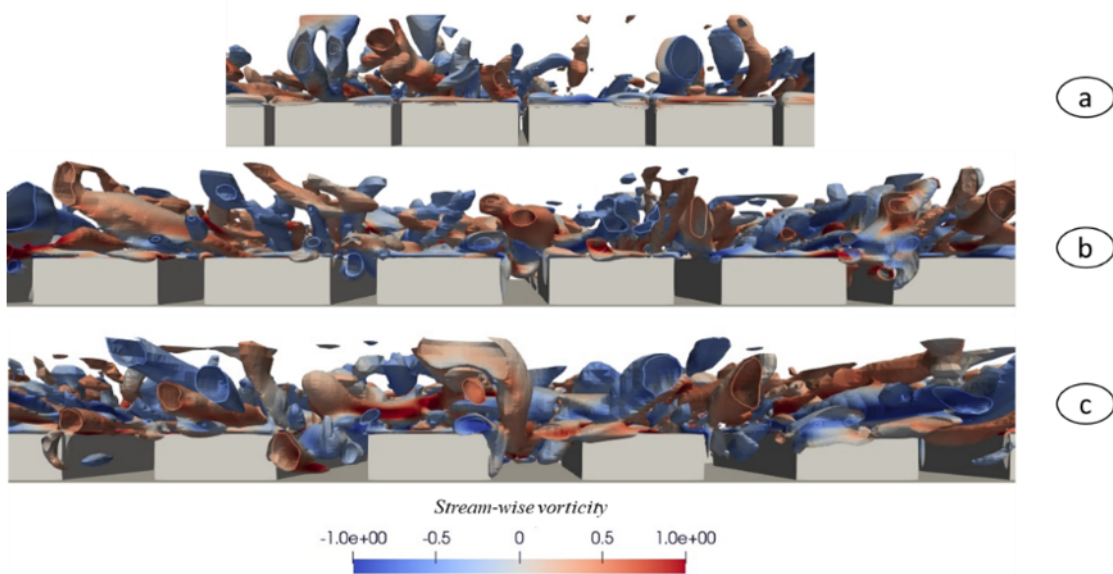


Figure 6.5: Vortical structures illustration with $Q=0.05$.

when scaled in outer units. This result is reproduced here by the LES simulations. Near the wall and in the vicinity of the roughness elements, significant changes are caused by local roughness effects. The gap between successive roughness elements transforms the wall into a porous boundary, reducing the velocity gradient and the viscous shear stress at the crest plane but allowing stronger vertical turbulent fluctuations through the gap. Resulting increases in the Reynolds shear stress by comparison with the smooth wall values strengthens the potential for passive transport of micro-organisms and nutrients towards solid surfaces but will also be felt as an increase in mechanical stresses acting on micro-organisms including organisms that have attached to surfaces near the edges of the roughness crest. As such, it is a good indicator of the effect of surface texturing on the turbulent mixing across the thickness of the roughness layer and, in turn on hydrodynamic conditions affecting early-stage bio-fouling. The impact of the roughness gap on the stress distributions is shown in Fig. 6.7 where the wall-normal profiles over the inner part of the boundary layer up to $y^+ = 120$ are compared against the corresponding smooth wall profile considering the four sampling locations in turn. For the smooth channel, uv^+ peaks to ~ 0.75 for $Re_\tau = 395$ is a value which is close to that reported by [174], from their DNS simulations at $Re_\tau = 180$ (which corresponds to a bulk Reynolds number $Re_b = \sim 3300$) or by [132] with a bulk Reynolds number $Re_b = \sim 4000$. Over the texture crest (sampling location A), this peak is increased by almost 50 % with the largest gap of $S^+ = 80$. It is interesting to contrast this with the 260% increase in the area averaged mean wall shear stress over the texture crests shown in Fig. 6.1. Over a smooth wall, an increase in the mean wall shear stress should translate into

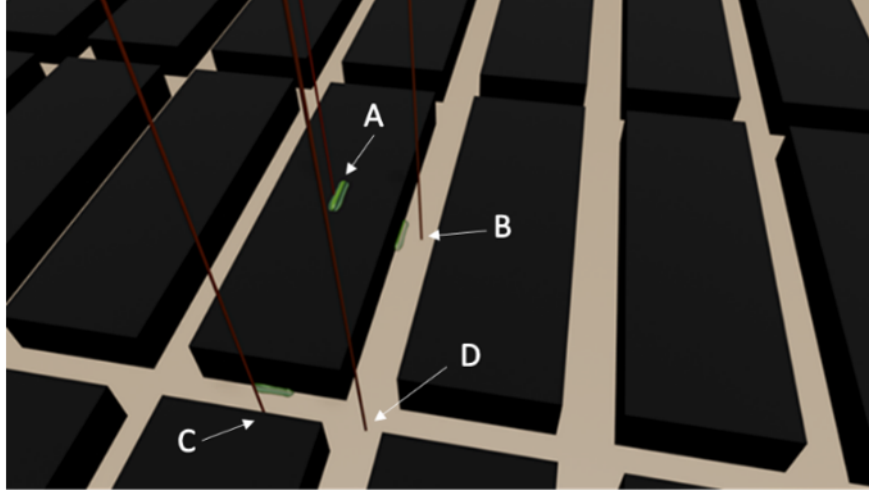


Figure 6.6: Illustration of the sampling wall normal lines A, B, C and D.

a similar increase in the Reynolds shear stress. The fact that the increase at location A is much smaller than 50% is due to local variations in wall stresses over the roughness crest. Wall stresses increase substantially towards the edges of the texture. The Reynolds shear stress peak in the wall-normal profile is at $y^+ \sim 80$, which is approximately 40 from the smooth wall or the crest plane for the textured surfaces. The textures are shown to shift the peak location gradually closer to the surface as the roughness gap S^+ increases. The stress curve for textured surfaces is also nearly flat for all gaps forming a near-constant stress region as reported by [182]. Within the gaps between textures, there is an obvious lack of turbulent activity in cases where the stream-wise vortexes are unable to penetrate the space between roughness. This is the case with $S^+ = 10$ for all orientations of the gap at locations B, C or D. For larger gaps, notable differences develop depending on the location. At location C, above the transverse gap and in front of the roughness, the profiles are similar to location A with some key distinctions. The peak values occur at lower y^+ values that are closer to potential organism settlement sites. There is also a notable increase with a stronger local peak at $y^+ \sim 55$ when $S^+ = 80$. Within the transverse gap, it is clear that very little stress develops as the roughness provides an effective shelter against turbulent-induced fluctuations. Profiles within the stream-wise gaps confirm earlier observations from Q field visualizations (Fig. 6.5) that vortexes can penetrate between textures once the gap reaches $S^+ = 40$. While the profile shows little difference between locations B and D, the gap size change from $S^+ = 40$ to $S^+ = 80$ is seen to have an effect. At $S^+ = 80$ a significant increase observed up to $y^+ \sim 20$ is followed by a local minima before a second increase to the near constant stress region. The evolution with $S^+ = 40$ on the other hand, shows a monotonic increase with y^+ to a maximum of 0.9 instead of 1.05 with $S^+ = 80$. The local minima with $S^+ = 80$ are located just below the crest plane at $y^+ \sim 40$

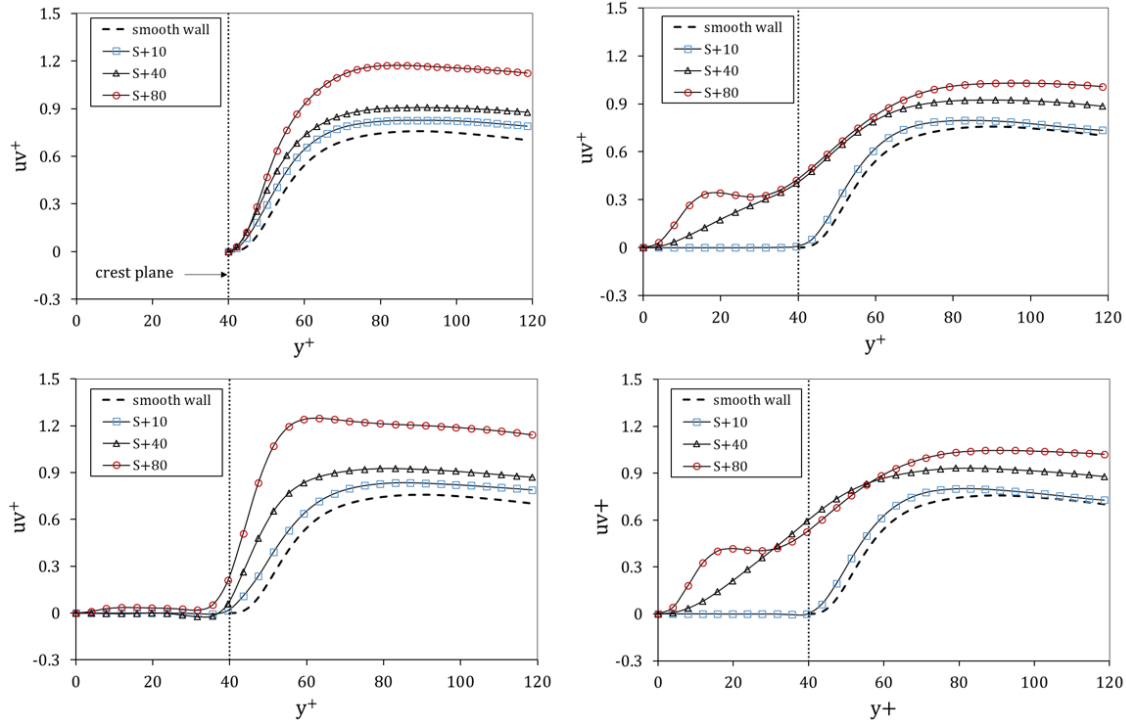


Figure 6.7: Comparison of uv^+ profiles at locations (a): A, (b): B, (c): C and (d): D against y^+ for three different textures.

so that locally Reynolds shear stresses are higher with $S^+ = 40$ than with $S^+ = 80$ in spite of a higher overall maximum in the latter case. This may be caused by the pair of contra-rotating vortices, which seem to evolve within the gap at $S^+ = 80$ instead of the single stream-wise vortices inferred from the Reynolds shear stresses and Q iso-contour plot at $S^+ = 40$.

The quadrant analysis adopted in [56] and [146] to study the roughness effect from mesh screens and longitudinal rectangular riblets, respectively, has been used here to explore the impact of the textures and gaps on the structure of turbulence at the four prescribed locations. The second and the fourth quadrants of the u - v sample space written Q_2 and Q_4 represent the strength of ejection and sweep events averaged over time. The analysis presented here considers both the strengths of Q_2 (Fig. 6.8) and Q_4 (Fig. 6.9) along the sampling lines. The comparisons of Q_2 relative to Q_4 are shown in Fig. 6.10. The ejections carry low-speed fluid to higher layers while sweeps bring down higher momentum fluid from upper fluid layers. Both contribute to increasing the Reynolds shear stress but the latter can be expected to have the greatest impact on settling or settled micro-organisms when present in close vicinity to the surface [57]. Previous studies [57], indicate that the contribution to the area-averaged Reynolds shear stress from ejection events is more than twice that of sweep events for most of the boundary layer except in the near vicinity to the surface. Whether the surface is smooth or rough, this is generally reported as being

the case. Closer to the wall, surface roughness is known to significantly increase the importance of sweeps relative to ejection. Results presented here indicate that important local effects need to be captured by a study of area-averaged Reynolds stresses alone. The first and most obvious observation is that the increase in gap width generally correlates with an increase in the strength of both ejections and sweeps. Interestingly, over the central part of the roughness crest surfaces at location A, sweeps and ejections are shown to increase at similar rates so that $Q_2 - Q_4$ is relatively unchanged up to $y^+ = 80$ for all gaps when compared with the smooth wall. The second clear result is that both Q_2 and Q_4 are dependent on the gap width for most sampling locations. There is an exception to this for sweep events (Q_4) which show very similar profiles for the two largest gaps through to $y^+ \sim 60$. Sweeps over the stream-wise gaps (locations B and D) are seen to strengthen much more as S^+ is increased from 10 to 40 than from 40 to 80. There are still benefits in increasing to $S^+ = 80$ when seeking to increase the strength of sweep events near the surface at the bottom of gaps. The local peak observed with the Reynolds shear stresses is clearly seen to correlate with increases in stresses associated with ejection and sweeps up to $y^+ \sim 20$. Finally, it is also interesting to note the strong effect that the smallest gaps $S^+ = 10$ have on both sweeps and ejection given the moderate impact it has on the total Reynolds shear stress. The local increase in sweeps and ejections with $S^+ = 40$ and $S^+ = 80$ towards the crest plane at locations B, C and D are consistent with earlier observations showing stress concentrations near the edges of the roughness crests. They indicate that turbulent structures will expose organisms to greater stresses in the upper part of the textures near the edges.

6.3.2 Higher-order statistics

Third-order moments provide a more sensitive indicator of the effect of surface texturing on turbulence [56]. All triple correlations presented in this section are scaled with the third power of the smooth wall friction velocity $u_{\tau,s}^3$. The correlation $(uuu)^+$ measures the time-averaged transport of stream-wise turbulent kinetic energy by stream-wise velocity fluctuations. In the literature, an increase in the peak value of the area-averaged correlation in the vicinity of the surface has been attributed to an increase in the frequency of sweep events over rough surfaces [182]. The profiles shown in Fig. 6.11 for the four sampling locations confirm again that there is a significant difference depending on the location relative to the texture. Over the roughness crest at location A and for all gaps, the trends are similar up to $y^+ \sim 55$. Compared to the smooth wall profile, a significant increase in peak can be observed at $y^+ \sim 50$. This more rapid increase in the flux with distance from the surface with the textured surfaces indicates that stream-wise turbulent fluctuations

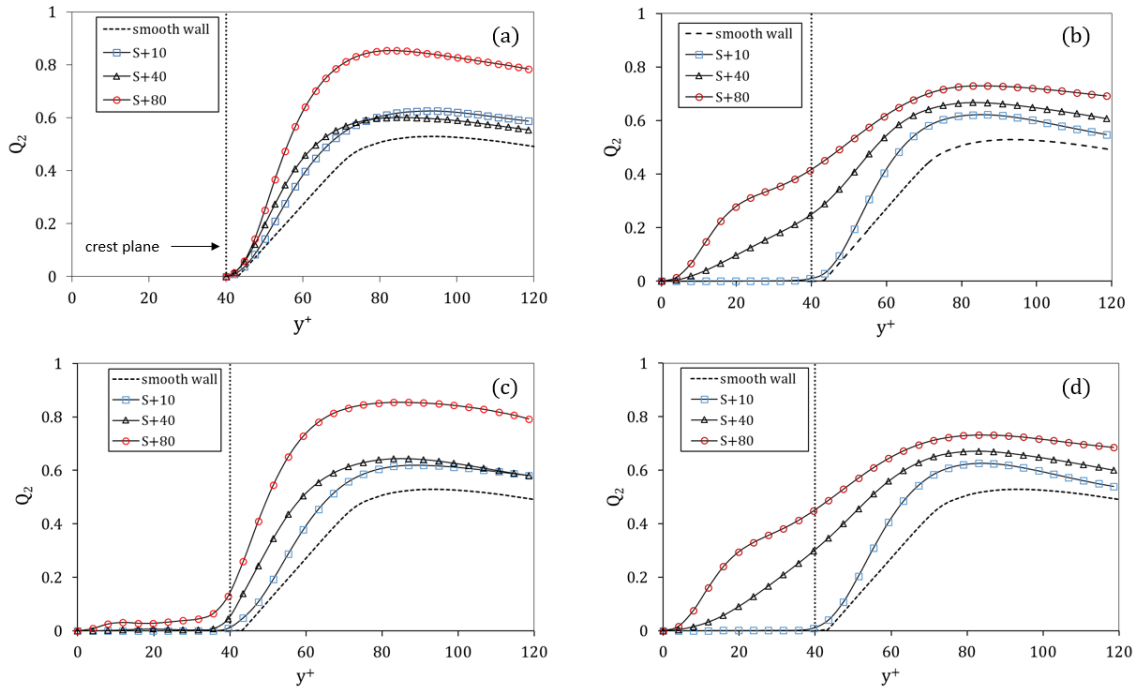


Figure 6.8: Comparison of wall-normal profiles of Q_2 as a measure of the strength of ejection events against y^+ at locations (a): A, (b): B, (c): C and (d): D for three different textures.

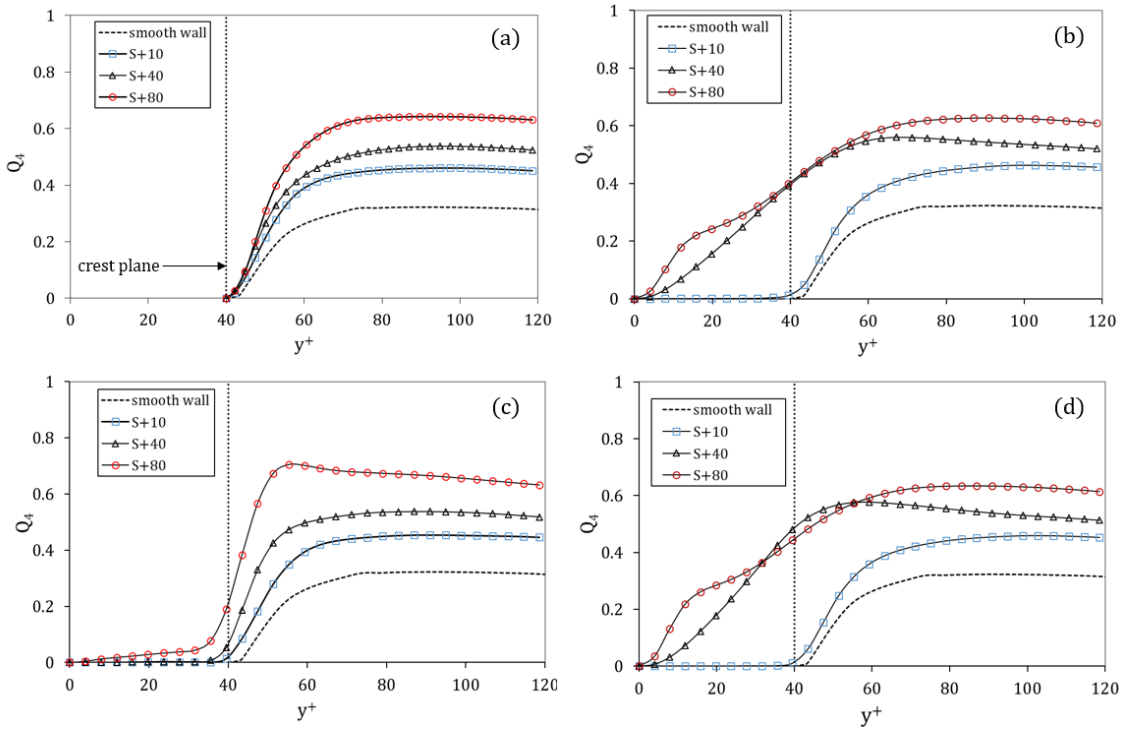


Figure 6.9: Comparison of wall-normal profiles of Q_4 as a measure of the strength of ejection events against y^+ at locations (a): A, (b): B, (c): C and (d): D for three different textures.

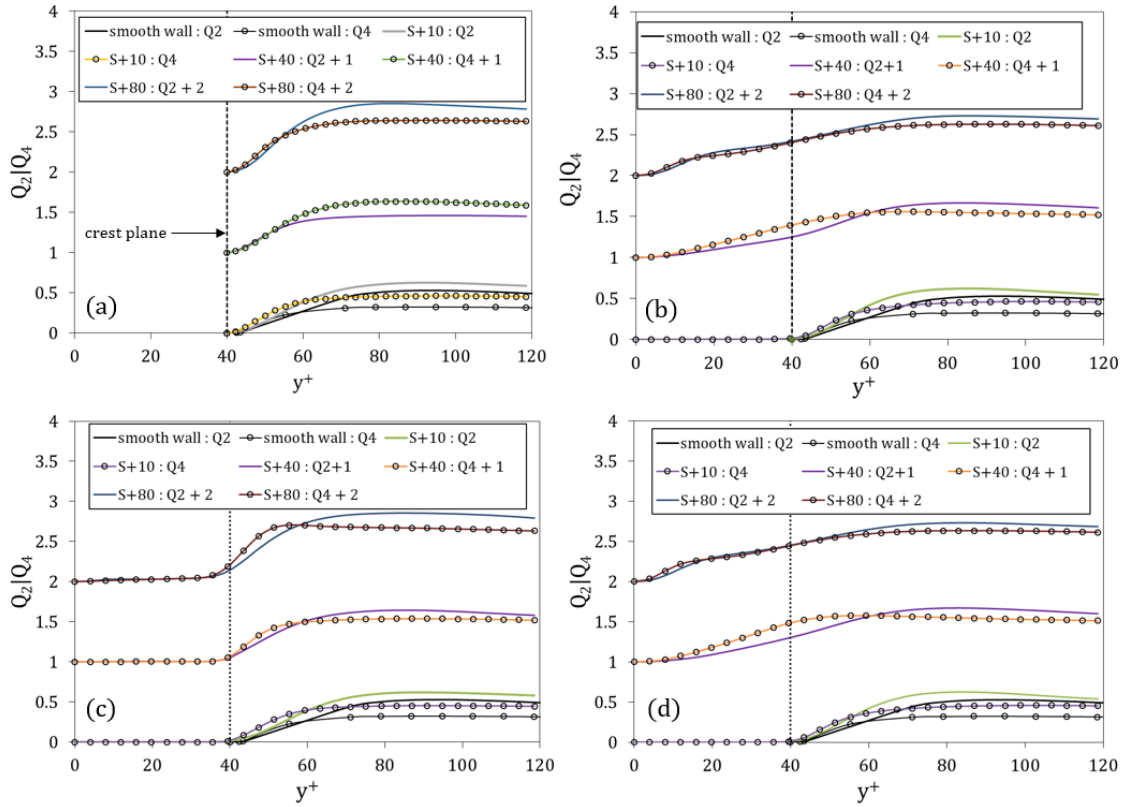


Figure 6.10: Comparison of wall-normal profiles of Q_2 and Q_4 against y^+ at locations (a): A, (b): B, (c): C and (d): D for three different textures.

close to the texture crests are much more pronounced than over a smooth surface and can indeed be linked to the increase in the frequency of sweep events predicted from area averaged profiles. This effect is even more amplified over the transverse gaps at location C. So, in this case, the transverse gaps are shown to increase both the strength (Fig. 6.9) and the frequency of sweeps. It is also interesting to note the deficit in turbulent kinetic energy further from the wall at locations $y^+ \sim [60 - 120]$ caused by the negative flux, which is clearly amplified by the surface texturing. The case $S^+ = 40$ is interesting in that it shows different trends from the increase in gap width. For all locations, it shows a much more moderate negative flux over this region of the flow and at the same time a higher positive flux near the crest plane and within the stream-wise gaps. This $S^+ = 40$ case is also distinctive in that it appears to spread out the positive peak in the stream-wise gap, suggesting a more pervasive impact of stream-wise turbulent fluctuations. For other gap sizes (i.e. below $y^+ = 40$) the flux is much reduced and virtually non-existent for $S^+ = 10$.

The transport of wall-normal turbulent kinetic energy by wall-normal velocity fluctuations (Fig. 6.12), written vvv^+ , is generally reported in the literature to remain positive for most of the boundary layer [183]. However, It has been shown in some cases to reduce with increases in the wall distance and reach a negative local min-

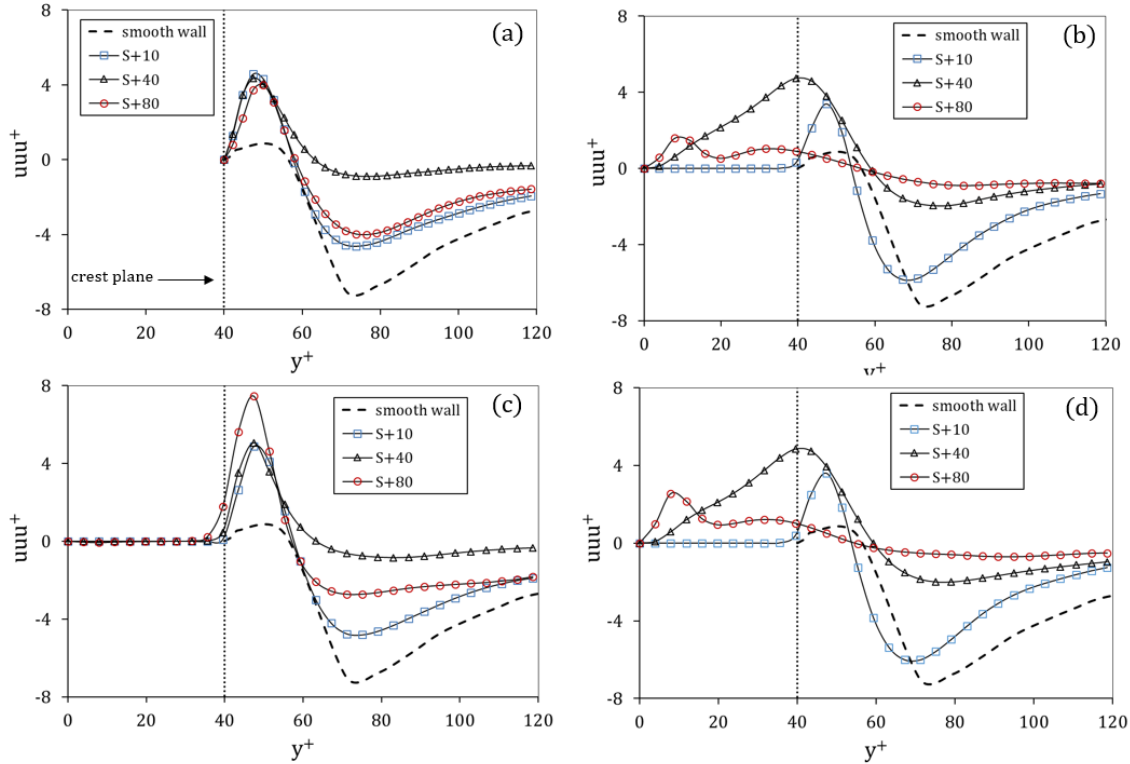


Figure 6.11: Comparison of $(uuu)^+$ profiles at locations (a): A, (b): B, (c): C and (d): D against y^+ for three different textures.

imum before increasing again [184]. Once again, this triple correlation is typically discussed in the literature as an area-averaged correlation. The local profiles reported do show that local negative minima can also occur depending on the location and gap size. The gap $S^+ = 40$ creates positive fluxes throughout at locations A and C but local negative minima are observed within the gaps at locations B and D. All other gaps show negative fluxes within the range $20 \leq y^+ \leq 80$. In general, these negative fluxes are much smaller than uuu^+ but as expected increase with the gap size due to the increase in the strength of sweeps and other downward flow fluctuations. The effect is strongest above the transverse gap at $S^+ = 80$ (location C) but also downstream of this at location A.

The transport of Reynolds shear stresses by stream-wise and wall-normal velocity fluctuations are written $(uuv)^+$ and $(uvv)^+$, respectively. The corresponding wall normal profiles in inner units are given in Fig. 6.13 and Fig. 6.14, respectively. Here again, it is clear that no meaningful shear stress flux occurs within the transverse grooves (location C) from either stream-wise or wall-normal fluctuations. The trends for both correlations and the smooth wall agree with those of the literature. For the smooth wall case, uvv^+ has a minor positive peak at a distance ~ 20 from the wall in inner units followed by a significant decrease to a negative local minimum at a distance ~ 95 . The trends are similar with all gaps from the crest plane up over

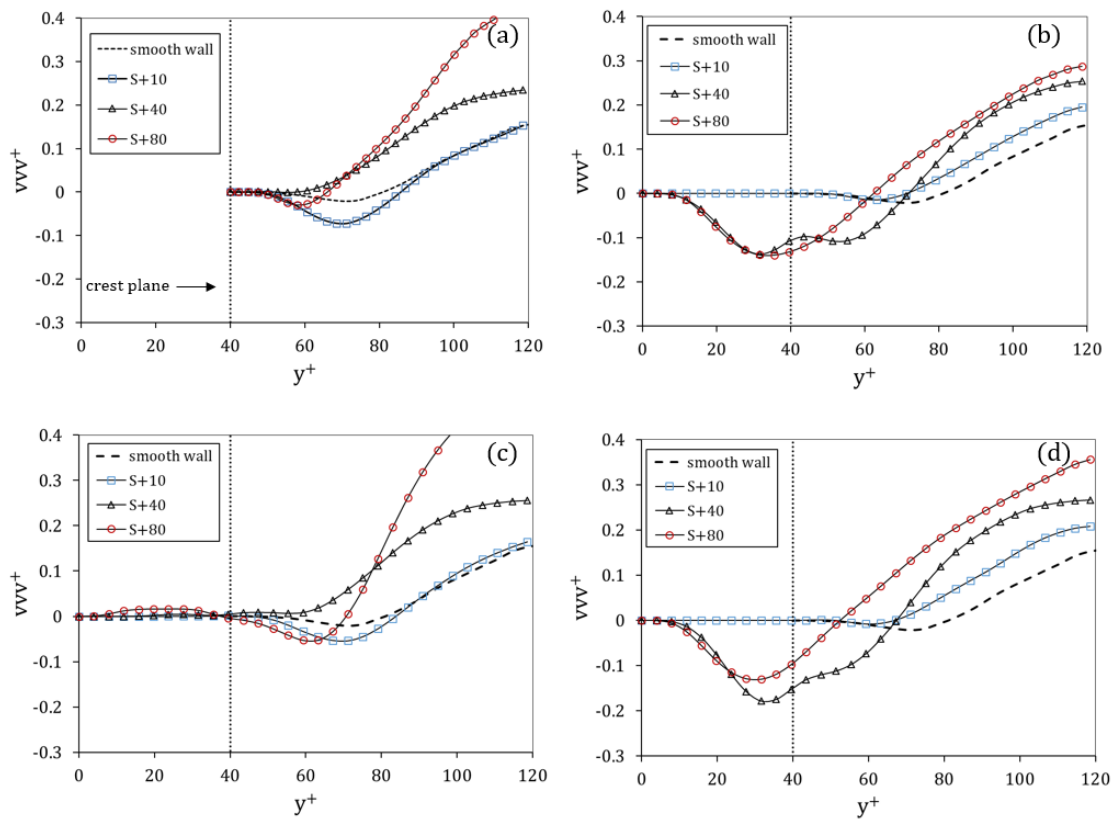


Figure 6.12: Comparison of $(vvv)^+$ profiles at locations (a): A, (b): B, (c): C and (d): D against y^+ for three different textures.

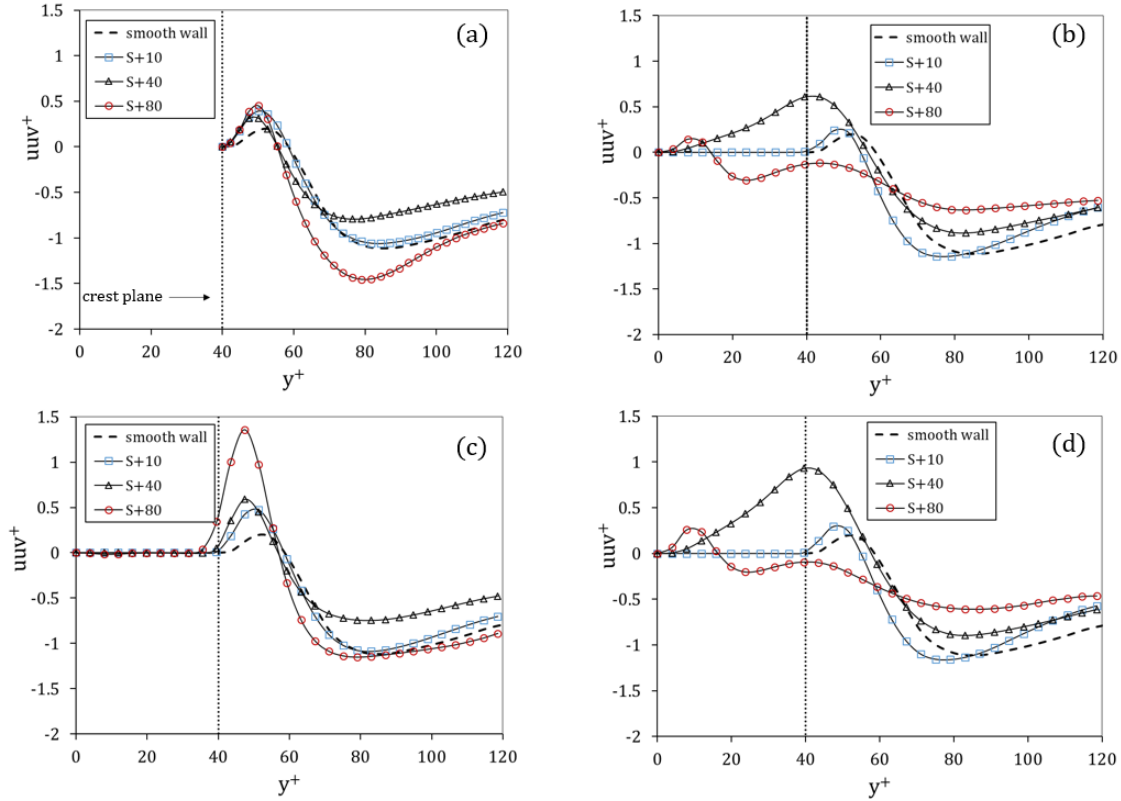


Figure 6.13: Comparison of $(uvv)^+$ profiles at locations (a): A, (b): B, (c): C and (d): D against y^+ for three different textures.

the roughness crest and upstream of the texture (location C) with one exception at $S^+ = 80$, which shows a significant increase in the positive peak value. Within the stream-wise grooves, there are significant sensitivities to the gap size and location. At locations B and D, $S^+ = 10$ and $S^+ = 80$ follow very similar trends to the smooth wall case, while with $S^+ = 40$, the profile changes significantly in the crest plane. In this case, $S^+ = 40$, the fluxes are largely positive throughout the grooves at both locations B and D, reaching a much larger peak value just above the crest plane. This matches earlier evidence showing a reduction in ejections relative to sweep events in the contribution to the Reynolds shear stresses. For uvv^+ over the smooth wall, a local maximum at $y^+ \sim 55$ is followed by a rapid drop to negative local minima at $y^+ \sim 105$. Over the roughness crest and transverse gap, the two smaller gaps are shown to reduce the intensity of fluxes, while the largest gaps increase the magnitude of the minimum peak. The much-reduced flux with $S^+ = 80$ over the upper half of gaps can be linked to the larger strengthening of sweeps relative to ejections for $S + 40$ compared to $S + 80$. The skewness factor for the stream-wise velocity fluctuations defined by $S_u = (u^3)/((u_{\tau,s}^2))^{3/2}$ provides additional information on the direction of flow through sweeps or ejections [174]. Of particular interest for the present study is the importance of the sweep events near the wall and this can be measured by the sign of the skewness. These results are

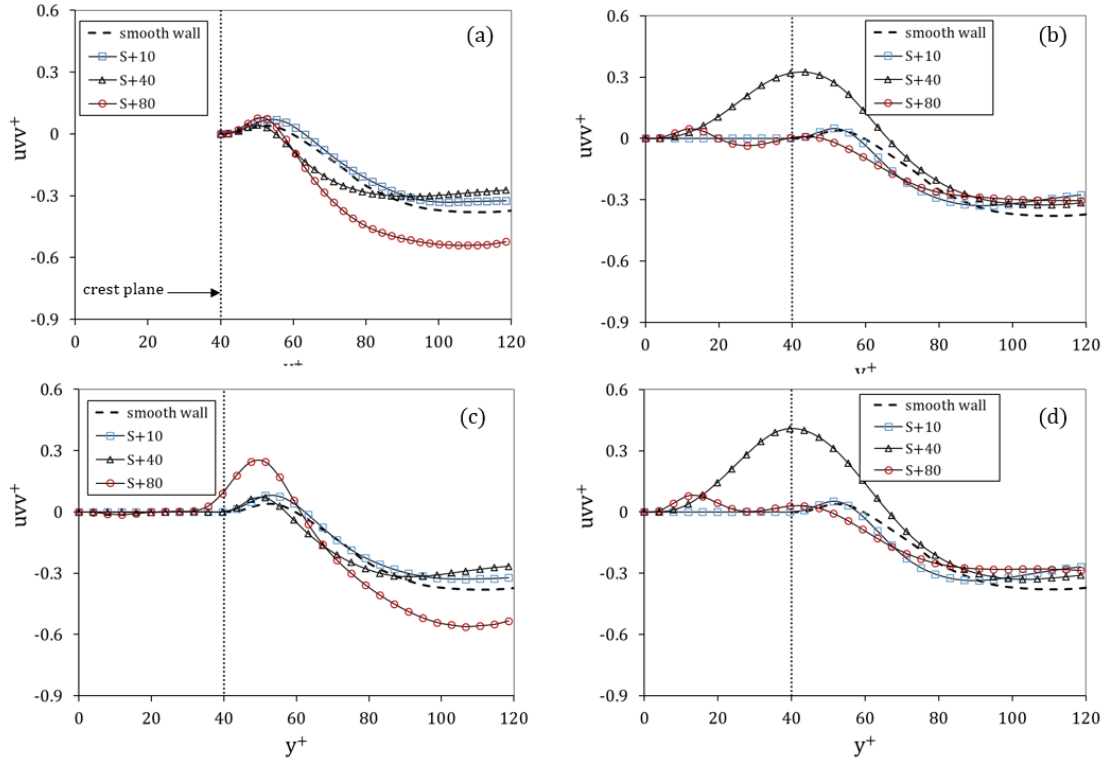


Figure 6.14: Comparison of $(uvv)^+$ profiles at locations (a): A, (b): B, (c): C and (d): D against y^+ for three different textures.

shown in Fig. 6.15. The positive skewness S_u over the crest planes indicates that there is a higher rate of energy flow from layers that are further from the surface and hence carry a higher momentum towards the surface. Over the roughness crest, the positive S_u changes moderately due to roughness, but a much higher sensitivity to the size of the gap is found within the gaps. A negative and reasonably uniform skewness is found within the stream-wise gaps except for a local increase near the crest plane with $S^+ = 10$ but significant variations are found in the transverse gap with both negative and positive values. Within the stream-wise gap, the skewness increases to values similar to the smooth surface case when approaching the bottom surface. Away from the surface towards $y^+ \sim 120$, the magnitude of the negative skewness reduces with the roughness. The reduction is consistent with the fact that roughened surfaces are known to break down larger stream-wise vortices, leading to more moderate transport of momentum. Interestingly, $S^+ = 40$ is again shown to amplify effects more than the larger gap $S^+ = 80$ increase. This means that higher momentum flow from the overlying layers is brought within the stream-wise gaps more effectively with $S^+ = 40$ than $S^+ = 80$.

A normalized fourth-order moment of stream-wise velocity fluctuations defined by the flatness factor $F_u = (u^4)/(u_{r,s}^2)$, where the scaling is with the fourth power of stream-wise root mean square velocity fluctuation from the smooth wall, is consid-

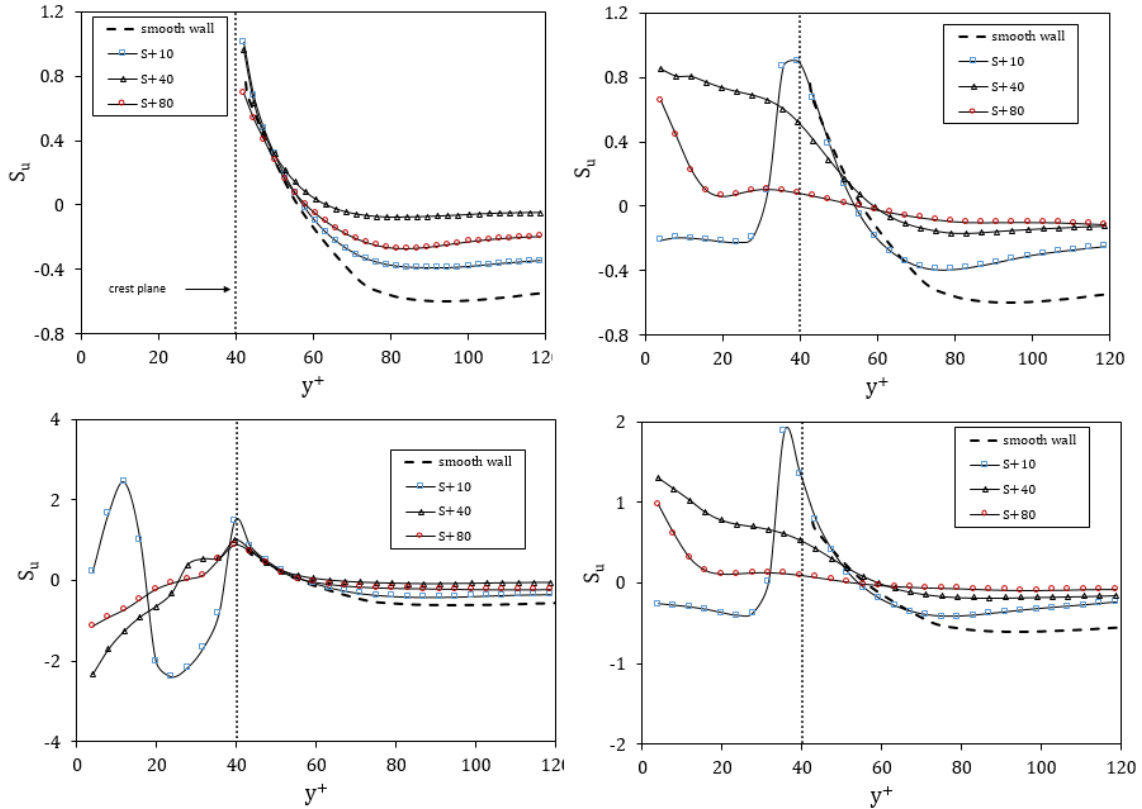


Figure 6.15: Comparison of S_u profiles at locations (a): A, (b): B, (c): C and (d): D against y^+ for three different textures.

ered to assess the effect of textures on the intermittency of fluctuations. If fluctuations follow a Gaussian distribution the flatness will be equal to 3, while larger values indicate an increase in the intermittency of fluctuations. This means that fewer fluctuations of higher intensity occur. These results are shown in Fig. 6.16. For all cases, including the smallest gap $S^+ = 10$, the flatness is shown to increase above the Gaussian value close to the walls and within the gaps. Such high intermittency has previously been linked to turbulent high-momentum fluctuations brought into roughness gaps by large-length-scale eddies [182]. It should be noted that these random impulses of higher momentum flow are the only turbulent statistics that suggest that bio-fouling organisms that manage to penetrate within the gaps may not be entirely sheltered from turbulence.

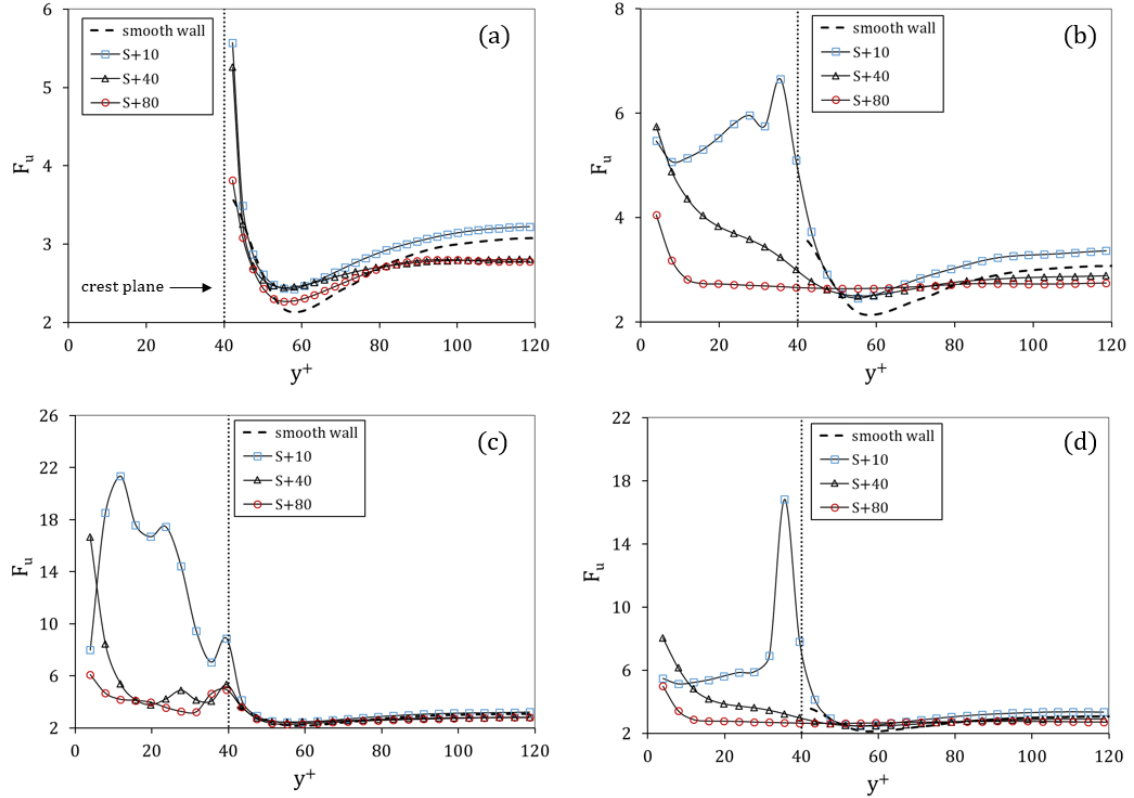


Figure 6.16: Comparison of F_u profiles at locations (a): A, (b): B, (c): C and (d): D against y^+ for three different textures.

6.4 Discussion and Conclusions

LES simulation results of fully developed channel flow in the smooth and transitionally rough regimes have been compared to characterise the effect of surface textures on turbulent statistics in the inner and overlap parts of the boundary layer. The ordered surface textures were inspired by the ridges of the growth rings of the brill fish, *Scophthalmus rhombus* and have been proposed as a strategy to control biofouling growth on marine surfaces exposed to hydrodynamic stresses due to water flow and specifically on the surface of marine hydro-turbine blades. The study has focused on the spatial variability of turbulent effects to explore whether early-stage fouling organisms may be exposed to varying turbulent stresses compared to smooth surfaces depending on their location around the textures. The simulations were performed at a friction Reynolds number $Re_\tau = 395$, characterized by an overlap region extending approximately to $y^+ \sim 300$. The roughness Reynolds number is $k^+ = 40$ while sensitivity to the three gap sizes $S^+ = 10, 40, 80$ have been studied. The focus on the lower part of the boundary layer is motivated by the study's aim to characterise the disruptive effect of textures on the early stage of settlement of micro-organisms. Organisms and their interaction with the flow are unresolved, so results should be interpreted in terms of the conditions to which settling organisms

are likely to be exposed. The sizes of marine micro-organisms can reach 100-200 viscous length scales in diameter or length but are more typically single-digit figures and comparable to the feature gaps and height considered in the study and smaller than the overlap part of the boundary layer. The conclusions of the analysis are the following:

- While there is evidence from a parallel study of immersion of textures in a stationary fluid [13] that the textures with the smallest gap $S^+ = 10$ do effectively hinder the settlement of micro-organisms within the gap between textures, these gaps are also shown in the present computational study to shelter surfaces against turbulent fluctuations in most cases. Iso-contour plots suggest that vortexes cannot penetrate the gaps, and as a result, Reynolds shear stresses as well as most other statistical measures of turbulence are significantly reduced below the smooth flat wall values. The only exceptions to this are increases in the skewness S_u and the flatness F_u above the smooth surface values. Values of F_u well in excess of 3 indicate that strong but infrequent stream-wise fluctuations can develop within all gaps including $S^+ = 10$. Although the data presented in this thesis is not conclusive, it is possible that these sporadic turbulent increases in stream-wise fluctuations could affect settlement within even the smallest gaps.
- Surface-averaged wall stresses are reduced over most parts of the textured surface compared to the smooth wall for all gaps considered, but there are areas where shear stresses are shown to increase. The shear stresses on the upper surface of the texture are higher than on the smooth surface by as much as 270% and increase locally near the edges. The upper parts of the vertical sides also experience higher stresses.
- The width and orientation of the texture gap have a significant impact on the stress distributions at the lower and upper parts of the gaps. At $y^+ \sim 12$, Reynolds shear stresses are lower than over the smooth surface except for the largest gap which shows local increases in maximum mean Reynolds shear stresses of up to 46% in the central part of the stream-wise gap and downstream of the textures in the transverse gap. Near the top edge of the texture at $y^+ \sim 35$, even higher increases occur with stress concentration shifting closer to the walls, particularly for the largest gap $S^+ = 80$.
- The Reynolds Shear Stress profiles in the wall-normal direction at the four sampling locations show an increase in the peak stress value in proportion to the gap width. Minimal Reynolds stresses developed within the transverse gap, but for the larger gaps $S^+ = 40$ and $S^+ = 80$, the profiles show similar

trends to the smooth plate but with increased magnitude. The quadrant analysis indicates that the importance of sweep events is increased by the surface textures. It is generally reported that from the start of the overlap region, the contribution from ejections can be twice that from sweeps. The difference is much smaller with the textures at all locations considered here and can even be higher (see $S^+ = 40$ at location A). Also while in the case of the smooth wall ejection and sweeps are of similar order below $y^+ \sim 60$, sweeps are shown to increase more rapidly above the crest plane over the transverse gap with $S^+ = 40$ and $S^+ = 80$ and over the stream-wise gap at $S^+ = 40$. This increase in turbulence-induced transport of higher stream-wise momentum can be expected to expose biofouling organisms that penetrate within the lower parts of the stream-wise gaps to higher intermittent stresses. The strength of sweep events over the stream-wise gaps is particularly strong with $S^+ = 40$ and contributes to much higher transport of Reynolds Shear stress by the stream-wise velocity fluctuations.

Chapter 7

Dispersive stress versus Reynolds stresses and its implication for bio-fouling prevention

This chapter compares and analyses stresses arising from temporal fluctuations (Reynolds stresses) and stresses originating from spatial fluctuation in velocity (dispersive stresses) to understand their potential impact on early-stage of bio-fouling settlement. Spatial averaging is applied to the time-averaged Navier-Stokes solutions [185] to analyze and calculate the stresses induced by spatial velocity fluctuations. The resulting dispersive stresses contribute to enhanced momentum transfer due to the spatial variation of the cross-flow.

7.1 Turbulent stresses in a textured Wall

It is well known that turbulent flows over rough surfaces generate much stronger turbulent intensity and inhomogeneity. As a result, the crests of the textures should experience greater viscous stresses compared to other parts of the textures [137], [175]. Turbulent stresses can be decomposed into Reynolds stresses and dispersive stresses, with the former representing enhanced momentum resulting from fluctuations in velocity over time and the latter representing increased momentum caused by spatial velocity fluctuations. Spatial averaging is needed to account for the spatial fluctuations of the velocity.

Spatial averaging provides a natural solution for addressing the issue of flow inhomogeneity, which commonly arises over and within roughened surfaces subjected to turbulent flow. Initially applied in the context of canopy flow problems, this approach has been particularly useful for analyzing flow scenarios involving urban structures or boundaries covered by vegetation [85], [185], [186]. To this end, spatial

averaging is performed within a thin horizontal plane volume perpendicular to the walls, while ensuring sufficient extent in the stream-wise and span-wise directions to exclude the effects of topological variations caused by obstacles. Consequently, prognostic variables such as the velocity components can be decomposed into three distinct terms: $u_i = \langle \bar{u}_i \rangle + \tilde{u}_i + u'_i$. Here, $\langle \bar{u}_i \rangle$ represents the spatial and temporal average of the velocity component u_i , while \tilde{u}_i and u'_i represent the spatial and temporal velocity fluctuations, respectively. The Navier-Stokes equations are initially averaged based on time, then averaged in space, to express turbulent shear stresses using these three different components.

$$\frac{\partial(\langle \bar{u}_i \rangle)}{\partial t} + \langle \bar{u}_j \rangle \frac{\partial(\langle \bar{u}_i \rangle)}{\partial x_j} = -\frac{\partial p}{\partial x_i} + \frac{\partial \tau_{ij}}{\partial x_j} + D_i \quad (7.1)$$

$$\frac{\tau_{i,j}}{\rho} = -\langle \bar{u}_i \bar{u}_j \rangle - \langle \tilde{u}_i \tilde{u}_j \rangle + \nu \frac{\partial \langle \bar{u}_i \rangle}{\partial x_j}$$

$$\frac{D_i}{\rho} = \frac{1}{V} \int \bar{P} n_i dS - \frac{\nu}{V} \int \frac{\partial \bar{u}_i}{\partial n} dS$$

where $\langle \bar{u}_i \bar{u}_j \rangle$, $\langle \tilde{u}_i \tilde{u}_j \rangle$ and $\nu \frac{\partial \langle \bar{u}_i \rangle}{\partial x_j}$ are spatially averaged Reynolds, dispersive and viscous stresses, respectively. D_i in Eq. (7.1) denotes the drag experienced by the roughness, which is the combined effect of the form drag (the first term on the right-hand side) and friction drag (the second term on the right-hand side). The term $\langle \bar{u}_i \bar{u}_j \rangle$ represents the averaged Reynolds stress across the entire prescribed horizontal plane and accounts for the transfer of momentum resulting from temporal fluctuations. Similar to the Reynolds stress, $\langle \tilde{u}_i \tilde{u}_j \rangle$ is referred to as dispersive stresses, which describes the transfer of momentum due to spatial variation. Based on the literature review, the viscous term $\nu \frac{\partial \langle \bar{u}_i \rangle}{\partial x_j}$ becomes negligible at a location just a few y^+ above the normal to the walls [137].

7.2 Spatially averaged stresses within and above textures

Spatial Reynolds and dispersive stresses are presented in this section and compared with smooth wall cases. Results for texture cases that have not been included in the previous chapter ($S^+ = 20$ and $S^+ = 80$ span-wise) are also presented. As these two cases differ geometrically from the earlier cases discussed in Chapter 6 (the $S^+ = 20$ case features longer prism elements aligned in the stream-wise direction, whereas the $S^+ = 80$ span-wise case concerns prism elements which are oriented

in the span-wise direction), the plan area density [134] is used rather than S^+ to present data. The plan area density is defined by Eq.(7.2).

$$\lambda_p = \frac{ab}{L_x L_z} \quad (7.2)$$

where b and a are the texture element sizes in the stream-wise and span-wise directions, respectively. L_x and L_z represent the length of area covered by the texture elements and half of the gap between adjacent elements in the stream-wise and span-wise directions respectively (Fig. 7.1).

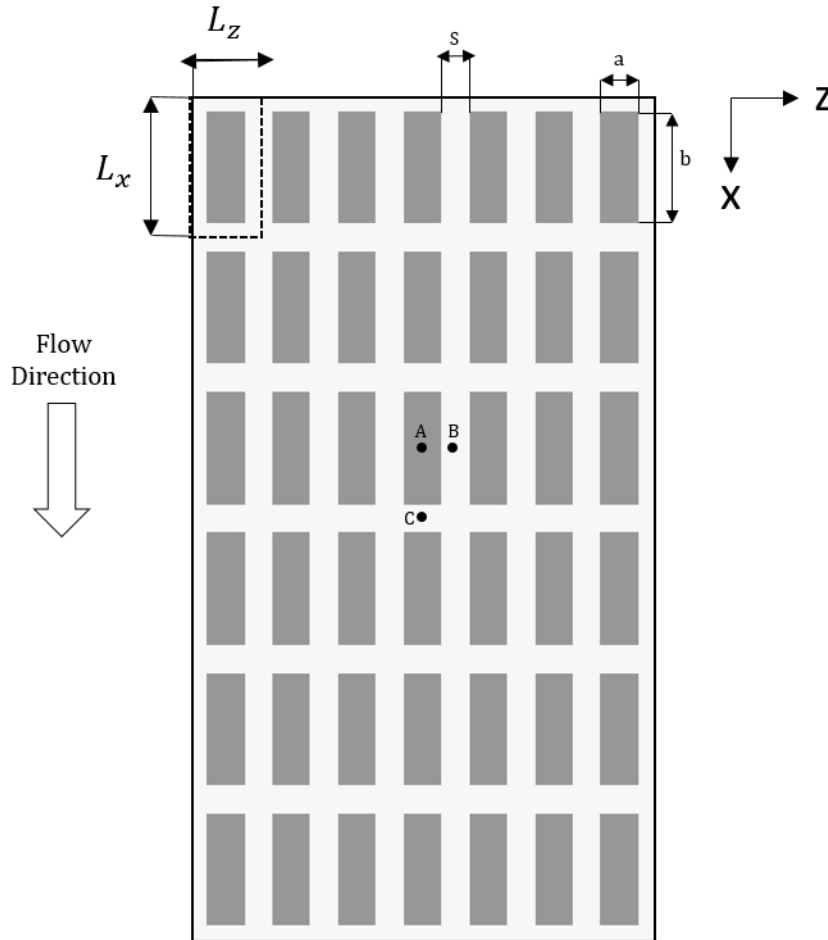


Figure 7.1: L_x , L_z , a and b lengths used in plan area density [134].

The cases plan area density and the corresponding element gap size S^+ are shown in Table 7.1.

7.2.1 Spatially averaged Reynolds and dispersive stresses

Due to the high inhomogeneity of turbulent flow above textures, it is customary to employ spatial averaging when presenting the data. It is also necessary to calculate

S^+	The plan area density (λ_p)
10	0.88
20 (Stream-wise length scale has doubled ($L_x^+ = 732$))	0.77
40	0.64
80	0.457
80 span-wise	0.457

Table 7.1: Plan area densities of the studied textures and their corresponding S^+ .

the zero-plane displacement ϵ^+ , which determines the origin for the vertical coordinate y [85]. ϵ^+ is calculated by scaling the displacement of the origin from the texture crest plane (ϵ) with the viscous length scale δ_ν of the roughened wall flow. According to Thom [103] and Jackson [104], ϵ^+ represents the momentum absorption by the textures. Alternatively, ϵ^+ can be viewed as the location where the total drag is exerted on the texture (centroid of the location of hydrodynamic forces acting on the texture). The values of ϵ^+ obtained for each test case are shown in Table 7.2. These results indicate that lower surface area density leads to higher momentum absorption by the textures. The stream-wise texture is also shown to decrease this momentum absorption effect by a factor of two approximately when compared with the span-wise texture which agrees with the observation from [135]. This aligns with the notion that span-wise textures have a greater impact on the overlying flow because of the intense flow ejections at the leading edges of the textures.

Textures λ_p (plan area density)	$\epsilon^+ = \epsilon/\delta_\nu$
0.88	~ 0.1
0.77	~ 0.1
0.64	0.9888
0.457 stream-wise	2.7668
0.457 span-wise	5.6126

Table 7.2: Zero-plane displacement calculated for each texture.

In Figs. 7.2 and 7.3, the resolved spatially averaged profiles of Reynolds and dispersive stresses respectively are plotted against the dimensionless wall distance $y^+ - \epsilon^+$. It is customary to present the averaged diagonal stresses $\overline{u_{ii}}$ as the root mean squared (RMS), represented as $u_{i,Rms} = \sqrt{\langle \overline{u_{ii}} \rangle}$. The subscript R denotes

Reynolds stresses while D refers to dispersive stresses. The calculated RMS are then scaled with the smooth wall mean friction velocity. The mean friction velocity $u_{\tau,s}$ at a Reynolds number of 395 is chosen as the scaling parameter. Also, the non-diagonal Reynolds shear stress is displayed as $uv_R^+ = -\langle \overline{uv} \rangle / u_{\tau,s}^2$. Similar scaling is used for dispersive stresses (Fig. 7.3).

Figs. 7.2 and 7.3 (a) show that the stream-wise dispersive stress is significantly higher than the Reynolds stress within the gap between textures, with a peak occurring near the surface of the crest. This stream-wise dispersive stress contributes to considerably increased dispersive shear stress compared to the Reynolds shear stress. For the span-wise and normal-to-wall stresses (Figs. 7.2 and 7.3 (b) and (c)), both stresses are of comparable magnitude within the gaps between the textures. In all cases, the dispersive stresses rapidly vanish as the profile approaches and exceeds the position of the texture crest plane. This observation aligns with the findings of [134], [137]. A closer look at the profiles shows that the texture with the highest area density ($\lambda_p = 0.88$), does not generate significant Reynolds and dispersive stresses within the textures. This indicates that stream-wise coherent structures are unable to penetrate these particular textures in any significant way [175]. However, the $\lambda_p = 0.457$ textures whether positioned in the stream-wise or span-wise exhibit notably elevated dispersive and Reynolds stresses within and above the gaps between the textures. This is also the case for $\lambda_p = 0.64$ although to a lesser extent. For $\lambda_p = 0.77$, Reynolds stresses within the gaps remain strong but not the dispersive stresses and finally as the gap size is reduced further with $\lambda_p = 0.88$, stresses almost vanish completely within the gaps.

Fig. 7.4 displays the total turbulent stresses ($(u_i u_j)_t^+ = \langle \overline{u_i u_j} \rangle + \langle \tilde{u}_i \tilde{u}_j \rangle$). As the viscous stresses become negligible only a few viscous lengths from the walls, this total stress becomes largely dominant. In particular, it can be observed that the presence of textures significantly enhances the stream-wise fluctuations compared to the smooth wall case, particularly for textures with low λ_p such as 0.457 cases. The observed maximum stream-wise fluctuations plateaus within the gaps with total stress that is approximately twice the maximum generated above the smooth wall. Transitioning from higher λ_p to lower texture densities is clearly shown to increase the transfer of turbulent fluctuations within the textures. A direct comparison of the Reynolds shear stresses (RSS) and dispersive shear stresses (DSS) for $\lambda_p = 0.457$ with the texture element oriented in both the span-wise and the stream-wise directions is shown in Fig. 7.5. Inside most of the gaps (except close to the bottom walls), the dispersive shear stresses are dominant and grow at a significantly higher rate with the distance from the wall. Approximately halfway up the gap (around ($\sim y^+ - \epsilon^+ = 30$ from the bottom wall)), the dispersive shear stress is nearly two to three times larger than the Reynolds shear stress. The trend is reversed from

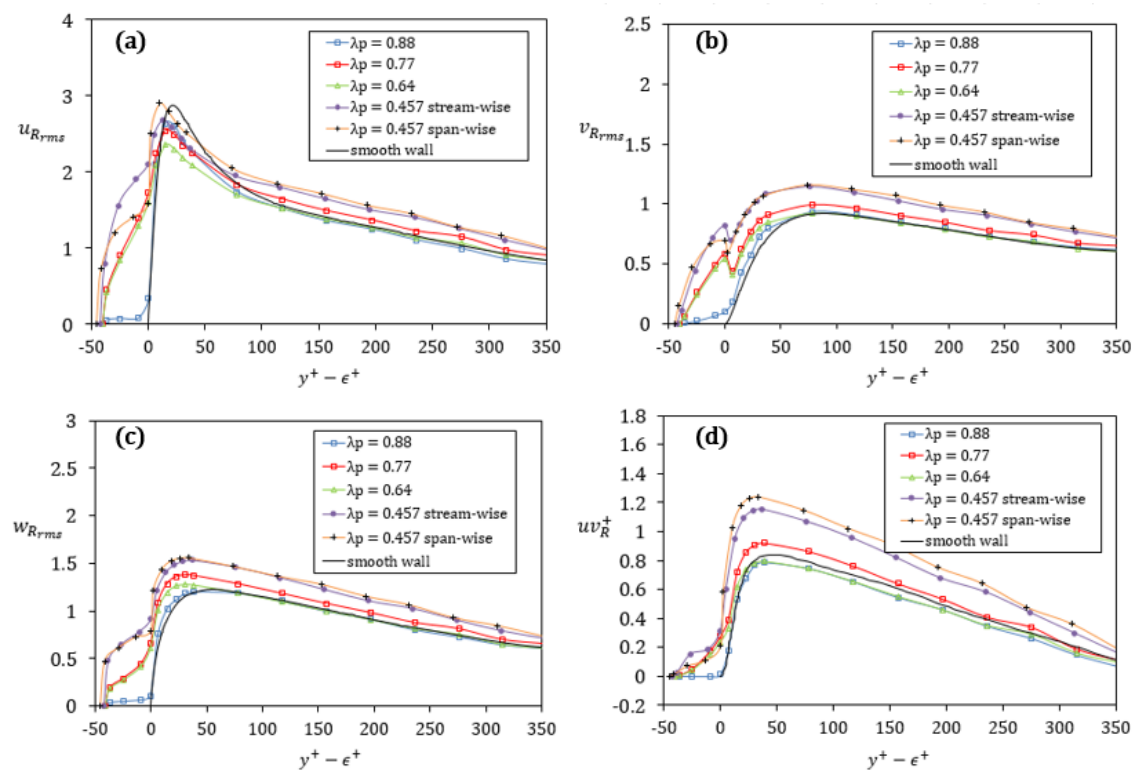


Figure 7.2: Spatially averaged Reynolds stresses for the textured surface plotted against the scaled wall distance $y^+ - \epsilon^+$ compared with smooth wall DNS results [174]. (a): scaled stream-wise Reynolds stresses, (b): scaled normal to wall Reynolds stresses, (c): scaled span-wise Reynolds stresses, (d): scaled Reynolds shear stress.

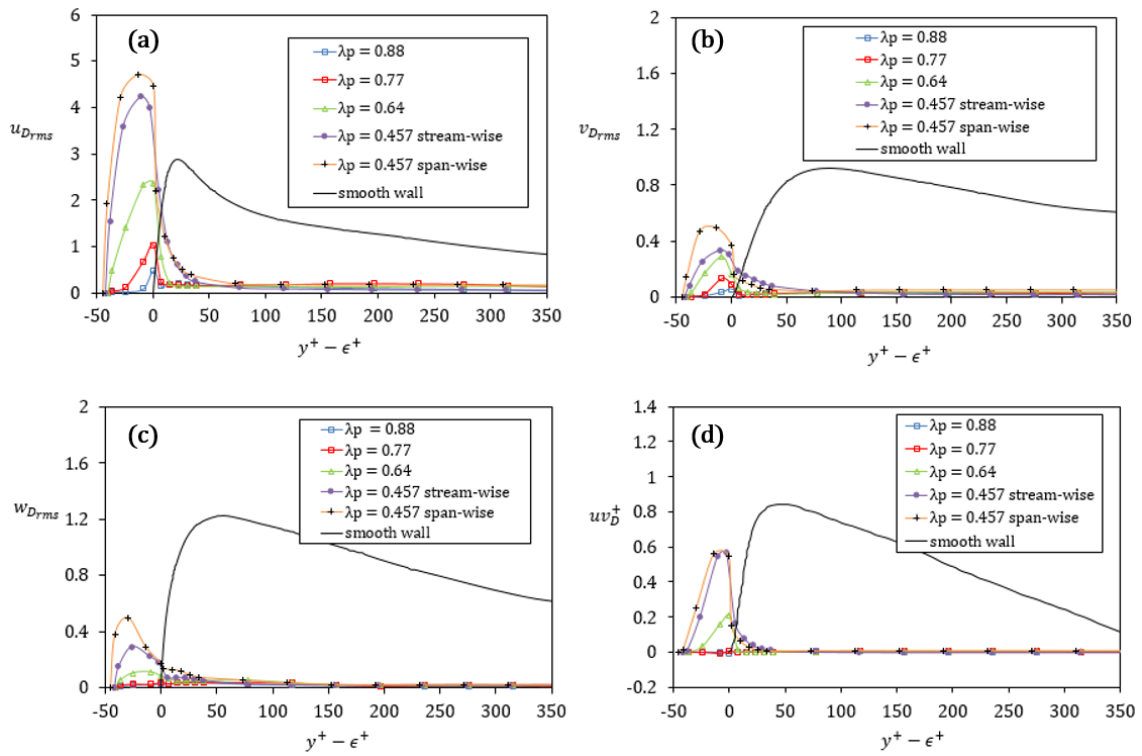


Figure 7.3: Spatially averaged dispersive stresses for the textured surface plotted against the scaled wall distance $y^+ - \epsilon^+$ compared with smooth wall DNS results [174]. (a): scaled stream-wise dispersive stresses, (b): scaled normal to wall dispersive stresses, (c): scaled span-wise dispersive stresses, (d): scaled dispersive shear stress.

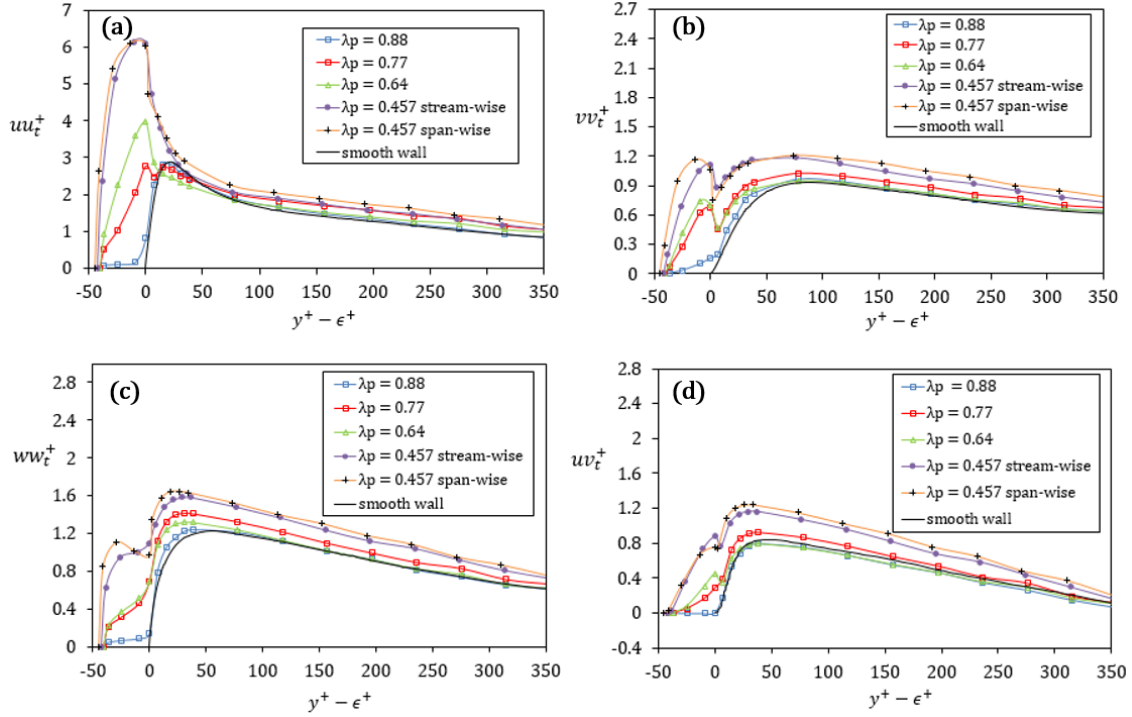


Figure 7.4: Normalized total stresses for the textured wall plotted against the scaled wall distance $y^+ - \epsilon^+$ compared with smooth wall DNS results [174]. (a): scaled total stream-wise stresses, (b): scaled total normal to wall stresses, (c): scaled total span-wise stresses, (d): scaled total turbulent shear stress.

$\sim y^+ - \epsilon^+ = 40 - 45$ from the bottom wall where the maximum dispersive stresses are reached so that the difference decreases gradually as the position approaches the crest plane where the two forms of stresses are approximately equal. Beyond this point the dispersive stresses rapidly become negligible.

7.2.2 Quadrant analysis and spatial average of higher order statistics of turbulent fluctuations

Chapter 6 includes a local Quadrant analysis at four locations positioned within the gap. This chapter presents a Quadrant analysis based on spatially averaged data for the five textures studied in the previous sub-section. Quadrant analysis [187] is used to identify the type of fluid motion responsible for Reynolds shear stress. Those turbulent structures can be characterized by observing the signs of velocity fluctuations in the stream-wise and wall-normal directions. They are assigned to the four quadrants defined in Chapter 6: $Q_1(+u, +v)$, $Q_2(-u, +v)$, $Q_3(-u, -v)$, and $Q_4(+u, -v)$. Q_2 and Q_4 refer to the ejection and sweep phenomena, respectively. The ejection phenomenon involves the expulsion of low-speed particles away from the wall, whereas the sweep phenomenon results in higher-speed fluids being swept down toward the wall. Q_1 and Q_3 are associated with inward and outward interactions of

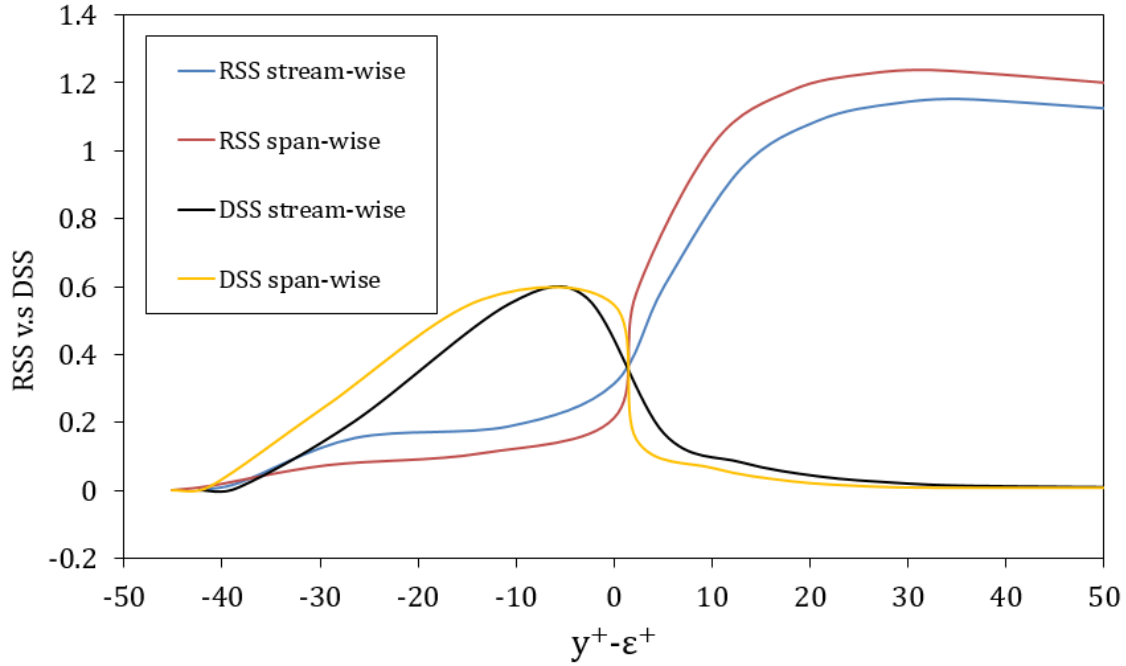


Figure 7.5: Comparison of spatially averaged Reynolds and dispersive shear stresses diagrams of $\lambda_p = 0.457$ textures drawn against $(y^+ - \epsilon^+)$.

the fluid close to the wall (as discussed in [188]). The total Reynolds shear stress can then be defined as the sum of the contributions from the four quadrants:

$$\underbrace{\langle \overline{uv} \rangle}_{Q_t} = \underbrace{\langle \overline{uv} \rangle}_1 + \underbrace{\langle \overline{uv} \rangle}_2 + \underbrace{\langle \overline{uv} \rangle}_3 + \underbrace{\langle \overline{uv} \rangle}_4 \quad (7.3)$$

where Angle brackets and overlines denote spatial and time averaging, respectively. Fig. 7.6 compares the contribution from each quadrant Q_i to the total Reynolds shear stress Q_t as a ratio. For $\lambda_p = 0.88$, Q_1 and Q_3 (representing inward and outward interactions) are the dominant motions within the texture gaps, while the flow exhibits minimal interaction with the overlying energetic flow (Figure 7.6) (a) and (c). According to the literature, [56], [85], Q_2 and Q_4 (associated with ejection and sweep) contribute the most to Reynolds shear stresses. This is evident from Figure 7.6 (b) and (d), where Q_2 and Q_4 whose contributions are shown to approach almost 50% for all textures except $\lambda_p = 0.88$.

Given that sweeps and ejections play significant roles in the production of Reynolds shear stresses, their profile is shown in Fig. 7.7 for all textures. Q_2 (ejection) exhibits greater strength than Q_4 (sweep) above the texture crest but the opposite is observed within the gaps. These findings are consistent with the experimental results of [189]. The results for Q_2 and Q_4 also appear to be relatively insensitive to the orientation of the texture (stream-wise or span-wise) except for part of the flow within the gaps where the stream-wise texture are shown to generate higher ejections and sweeps.

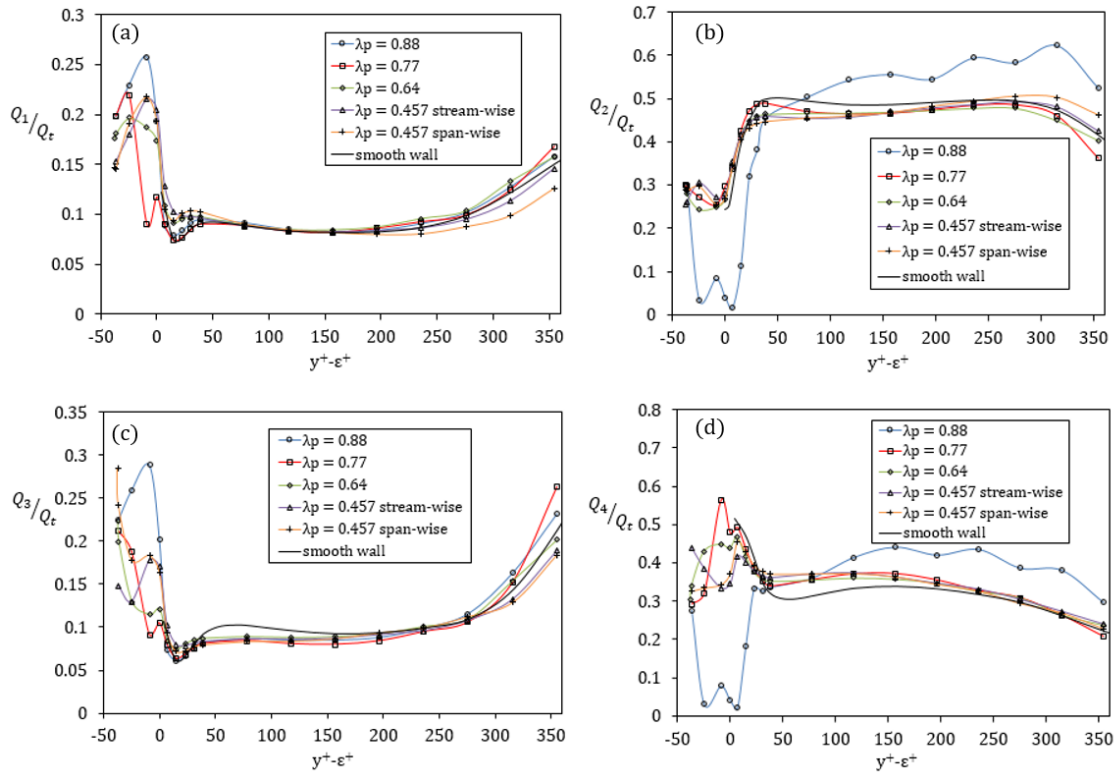


Figure 7.6: Comparison of the ratio of different Q_i on the total Q_t drawn against $y^+ - \epsilon^+$. (a): upward interaction (Q_1/Q_t), (b): ejection (Q_2/Q_t), (c): downward interaction (Q_3/Q_t) and (d): sweep (Q_4/Q_t).

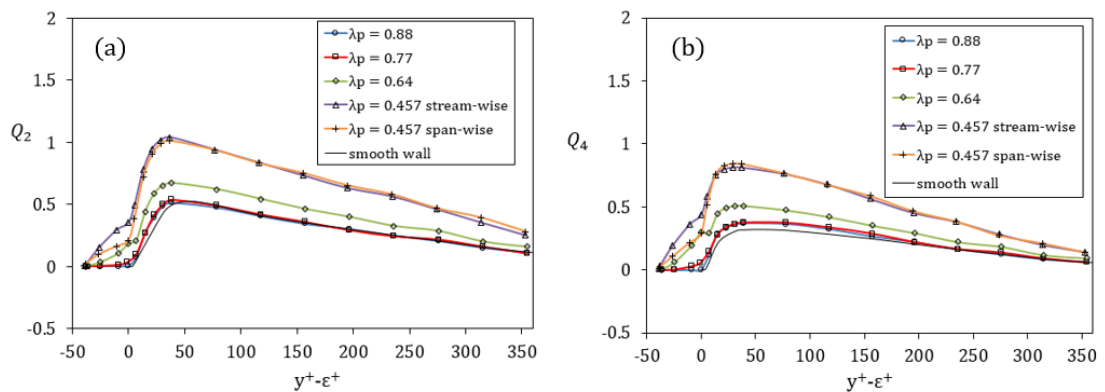


Figure 7.7: Profiles of (a) Q_2 (ejection) and (b) Q_4 (sweep) against $y^+ - \epsilon^+$.

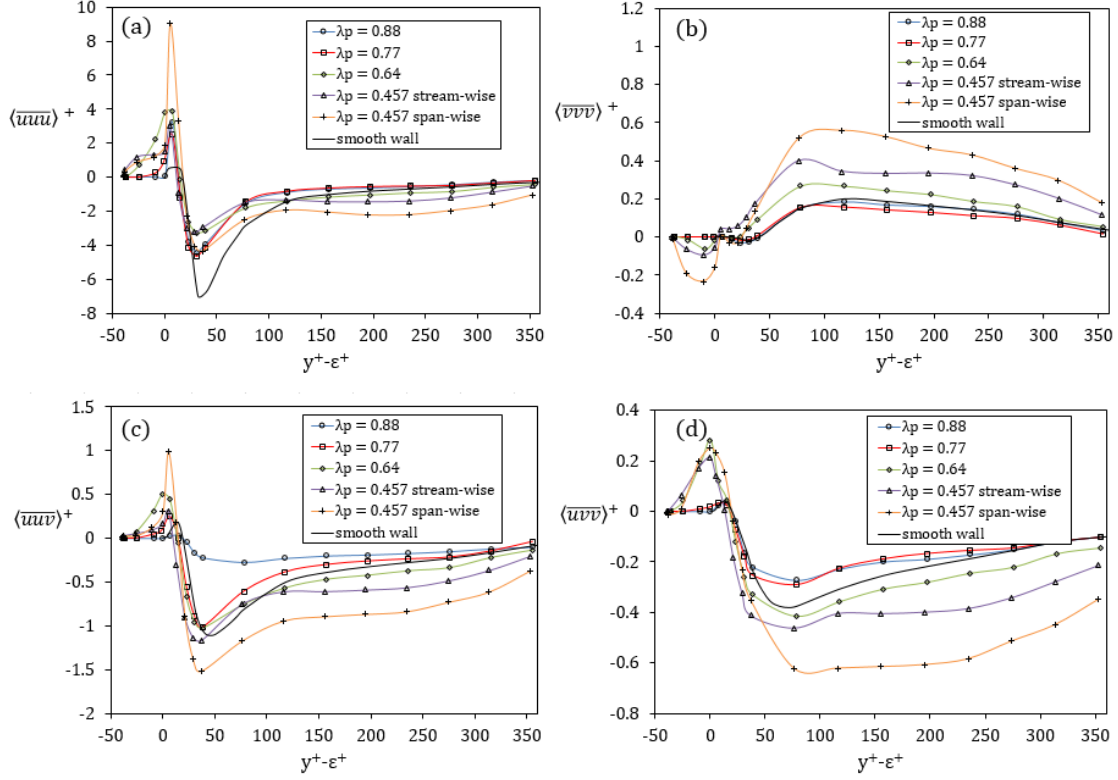


Figure 7.8: Comparison of the triple correlation profiles against $y^+ - \epsilon^+$ for flow over textured surfaces and the equivalent smooth surface for (a): $\langle \overline{uuu} \rangle^+$, (b): $\langle \overline{vvv} \rangle^+$, (c): $\langle \overline{uuv} \rangle^+$ and (d): $\langle \overline{uvv} \rangle^+$.

Spatially averaged higher-order statistics of turbulent fluctuations are presented here for the five textures. [190], [191] proposed that third-order moments serve as better indicators of the impact of textures on the flow above them. Fig. 7.8 presents these spatially averaged third-order moments for the stream-wise and normal-to-wall fluctuations in a horizontal plane, scaled with the cubic smooth wall friction velocity $u_{\tau,s}^3$. The correlation $\langle \overline{uuu} \rangle^+$ represents the average transport of turbulent kinetic energy caused by stream-wise velocity fluctuations. Fig. 7.8 (a), shows the distribution of $\langle \overline{uuu} \rangle^+$ against $y^+ - \epsilon^+$. The general features of the profile for $\langle \overline{uuu} \rangle^+$ are similar to key characteristics described in [183]. For all textures, $\langle \overline{uuu} \rangle^+$ shows a significant increase near and within the textures but a decrease in the overlying flow by comparison with flow over a smooth surface. [192] explains that these effects can be attributed to the reduced frequency of sweep events. This observation indicates that the presence of long span-wise gaps with $\lambda_p = 0.456$, reduces the sweep frequency much higher, resulting in an higher increase in $\langle \overline{uuu} \rangle^+$.

The correlation $\langle \overline{vvv} \rangle^+$ represents the spatially averaged turbulent transport of turbulent kinetic energy caused by velocity fluctuations in the direction normal to the wall. Its profile is plotted against $y^+ - \epsilon^+$ in Fig 7.8 (b) for all textures tested. The correlation is positive above the texture crest plane for all textures as observed in

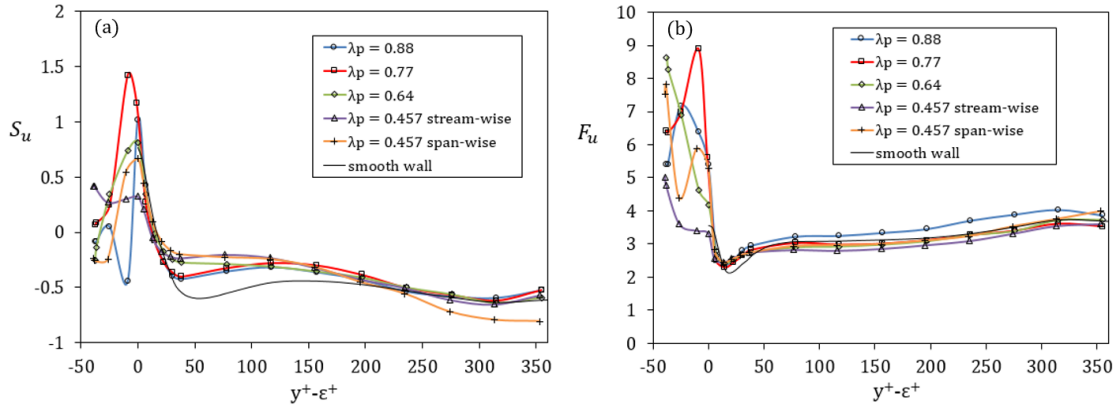


Figure 7.9: Comparison of the triple quadruple correlation profiles against $y^+ - \epsilon^+$ for flow over textured surfaces and the equivalent smooth surface for (a): Skewness, and (b): Flatness.

[183] and [192] but the value can decrease significantly within the textures. The wider the gap the more pronounced the reduction becomes producing the local minimum which is most noticeable with the span-wise texture. The correlations $\langle \overline{uuv} \rangle^+$ and $\langle \overline{uvv} \rangle^+$ represent the spatially averaged transport of turbulent kinetic energy and Reynolds shear stress caused by normal-to-wall velocity fluctuations (Fig.7.8) (c) and (d). According to [182], an increase in the gradients of \overline{uuv}^+ leads to higher \overline{u}^2 . This is evident in Figure (a), where the span-wise oriented $\lambda_p = 0.457$ produces the highest \overline{u}^2 and according to Fig.7.8 (c) exhibits the highest increase in \overline{uuv}^+ among other textures. This is due to the fact that $\frac{\partial(\overline{uuv})}{\partial y}$ represents turbulent diffusion in the transport equation of \overline{u}^2 [182]. Furthermore, it can be seen that the three textures with $\lambda_p = 0.64$ and $\lambda_p = 0.457$ show a significant increase in $\langle \overline{uuv} \rangle^+$ when compared to the smooth wall. [192] attributes this phenomenon to the strong sweeps that occur due to the presence of textures.

Fig. 7.9 presents the spatially averaged skewness (S_u) and flatness (F_u) of stream-wise velocity fluctuations. Skewness $S_u = \langle \overline{u^3} \rangle / (u_{\tau,s}^3)^2$, provides additional insight into the direction of the flow. Its sign is used to identify whether sweeps or ejections dominate the flow region. For all textures, S_u is either negative or close to zero near the bottom wall, changing the sign in the middle of gaps, except for the case of the $\lambda_p = 0.457$ stream-wise texture. This indicates that ejections dominate in the bottom regions of the textures. However, the $\lambda_p = 0.457$ stream-wise texture exhibits a consistently positive sign, indicating that high-momentum streaks penetrate from the overlying flow into gaps. Fig. 7.9 (b), shows the intermittency of fluctuations using the normalized spatially averaged fourth-order moment of stream-wise velocity fluctuations scaled by smooth wall mean shear stress to the power of four ($F_u = \langle \overline{u^4} \rangle / (u_{\tau,s}^2)^2$). F_u exhibits higher values than 3 within the texture gaps, suggesting greater intermittency in these regions. If fluctuations follow a Gaussian

distribution, the flatness factor will be equal to 3, while higher values indicate an increase in the intermittency of fluctuations.

7.2.3 Distribution of Reynolds and Dispersive stresses within textures

This section examines the spatial variations of stresses over planes parallel to the texture crest planes to identify regions with maximum and minimum stresses. Two positions between the bottom of the gaps and the crest plane at $y^+ = 10$ and $y^+ = 30$ measured from the bottom wall are considered.

The contours of the Reynolds stresses $\overline{u_i u_j}$ and the dispersive stresses ($\tilde{u}_i \tilde{u}_j$) on the two planes are shown in Figs 7.10 to 7.25. The $y^+ = 10$ contours provide insights into the turbulent conditions experienced by a fouling organism during initial settlement on the bottom surface while $y^+ = 30$ corresponds to the region where the dispersive stresses are at their highest.

Fig. 7.10 to Fig. 7.13 show the stream-wise Reynolds and dispersive stresses at $y^+ = 10$ and $y^+ = 30$. As λ_p decreases, the stream-wise Reynolds stresses are shown to increase rapidly in the stream-wise gaps but remain small in the span-wise gaps. The flow in the lee of the textures appears to remain largely sheltered from these stream-wise Reynolds stresses. The span-wise gaps, however, are not entirely sheltered from Reynolds stresses as wall-normal and more so span-wise Reynolds stresses $\overline{w w}$ are shown to concentrate on the forward facing vertical faces of textures (Fig. 7.18) (see Chapter 6).

Meanwhile, the strength of stream-wise dispersive stress $\tilde{u} \tilde{u}$ is clearly shown to fill most of the span-wise gaps whether it is in the lee of textures or at the intersection with the stream-wise gap. For example, in the case $\lambda_p = 0.457$ with the stream-wise textures, the stream-wise dispersive stress values reach nearly 5 at $y^+ = 10$ and 8 at $y^+ = 30$ which is much higher than the corresponding Reynolds stresses. This indicates that spatial variations can drive strong momentum transfer in the lee of the textures. Interestingly for the same texture density, $\lambda_p = 0.457$, but with textures aligned with the span-wise direction the stream-wise dispersive stress are seen to concentrate over the stream-wise gaps instead. This is likely due to the stronger interference from the textures when positioned perpendicular to the flow direction. A comparison between stream-wise stresses for the two textures of area density $\lambda_p = 0.457$ is shown in Figs. 7.10 to 7.13 (d) and (e), suggests that texture elements which extend further in the span-wise direction reduce the strength of dispersive stresses while providing a strong shelter against Reynolds stresses. As a results, much lower total stresses can be expected in the lee of textures that are aligned with the span-wise direction. Although this does not preclude using texture

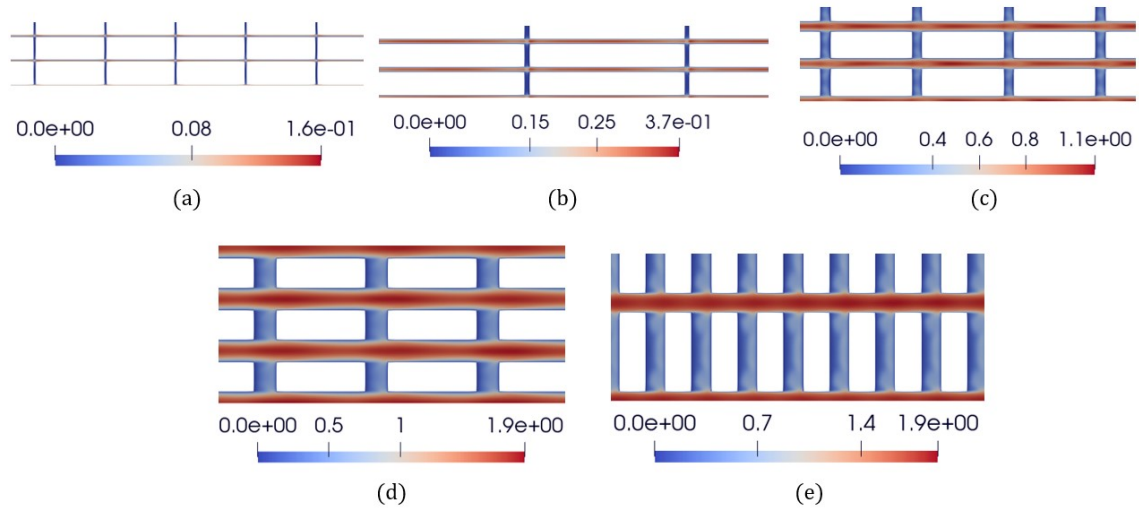


Figure 7.10: Contours of stream-wise Reynolds stress (\overline{uu}), at the height of $y^+ = 10$, above the bottom wall. (a): $\lambda_p = 0.88$, (b): $\lambda_p = 0.77$, (c): $\lambda_p = 0.64$, (d): $\lambda_p = 0.457$ stream-wise, (e): $\lambda_p = 0.457$ span-wise.

elements that are stretched in the flow direction, in practice it would be difficult to guarantee that the texture orientation is aligned with the flow direction. This suggest that shorter elements should be used to avoid creating shelters.

The span-wise Reynolds and dispersive stresses shown in Figs. 7.18 to 7.21 are of a similar order of magnitude as the stresses reported in the study conducted by [152]. In textures with higher area density λ_p , the Reynolds stresses in the span-wise direction (\overline{ww}) are larger in the span gaps, but as λ_p decreases, the Reynolds stresses in the span-wise direction also strengthen in the stream gaps. With $\lambda_p = 0.457$, Fig. 7.18 (d), these stresses are shown to concentrate in the wake of the texture elements near the forward-facing of the vertical face of the downstream texture element but only near the element vertical edge. For the elements aligned with the flow direction, this zone of higher span-wise Reynolds stresses covers most of the vertical face of the elements but for the span-wise element only a narrow region near the edges is affected. This is most likely due to time-varying flow separation along the vertical edge of the texture elements, as previously observed in the 2D C-type textures studied by ([124]). The span-wise dispersive stresses area is similarly concentrated near the edges of texture elements. The magnitude of these dispersive stresses increases as λ_p decreases.

Fig. 7.22 to 7.25 present a comparative analysis of Reynolds and dispersive shear stresses generated within textures at distances $y^+ = 10$ and $y^+ = 30$ measured from the bottom wall. In the case of textures with $\lambda_p = 0.77, 0.88$ and 0.64 , Reynolds shear stresses in $y^+ = 10$ are found to be negligible, but increase in $y^+ = 30$. On the contrary, for both textures with area density $\lambda_p = 0.457$ (stream-wise and span-wise), Reynolds shear stresses are mainly concentrated in stream-wise gaps. There

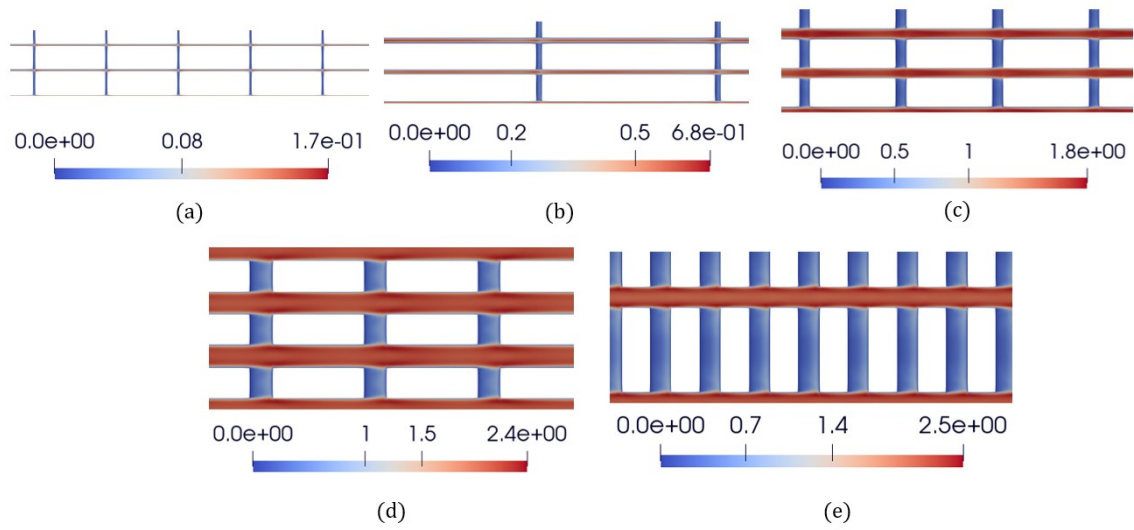


Figure 7.11: Contours of stream-wise Reynolds stress ($\overline{u'u'}$), at the height of $y^+ = 30$ above, the bottom wall. (a): $\lambda_p = 0.88$, (b): $\lambda_p = 0.77$, (c): $\lambda_p = 0.64$, (d): $\lambda_p = 0.457$ stream-wise, (e): $\lambda_p = 0.457$ span-wise.

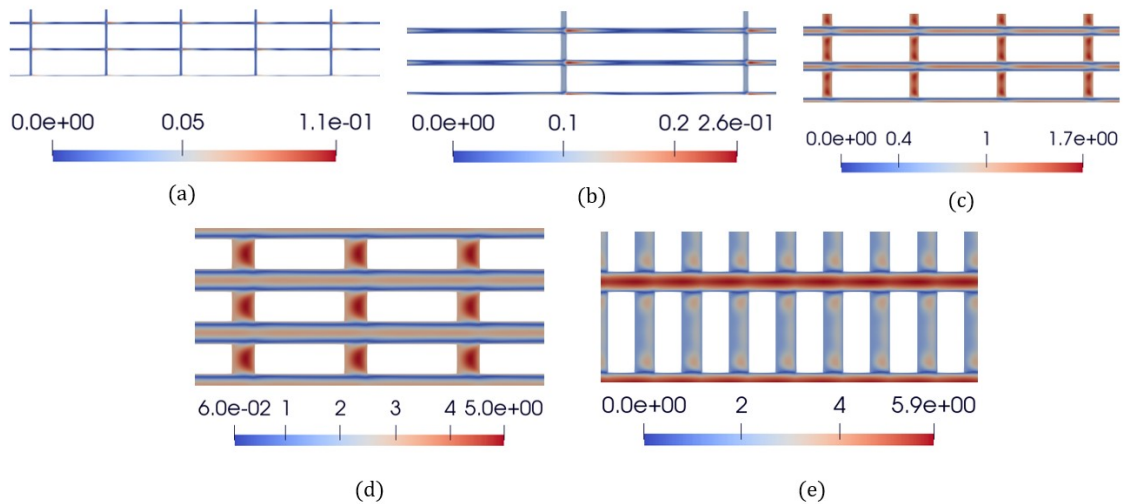


Figure 7.12: Contours of stream-wise dispersive stress ($\tilde{u}\tilde{u}$), at the height of $y^+ = 10$, above the bottom wall. (a): $\lambda_p = 0.88$, (b): $\lambda_p = 0.77$, (c): $\lambda_p = 0.64$, (d): $\lambda_p = 0.457$ stream-wise, (e): $\lambda_p = 0.457$ span-wise.

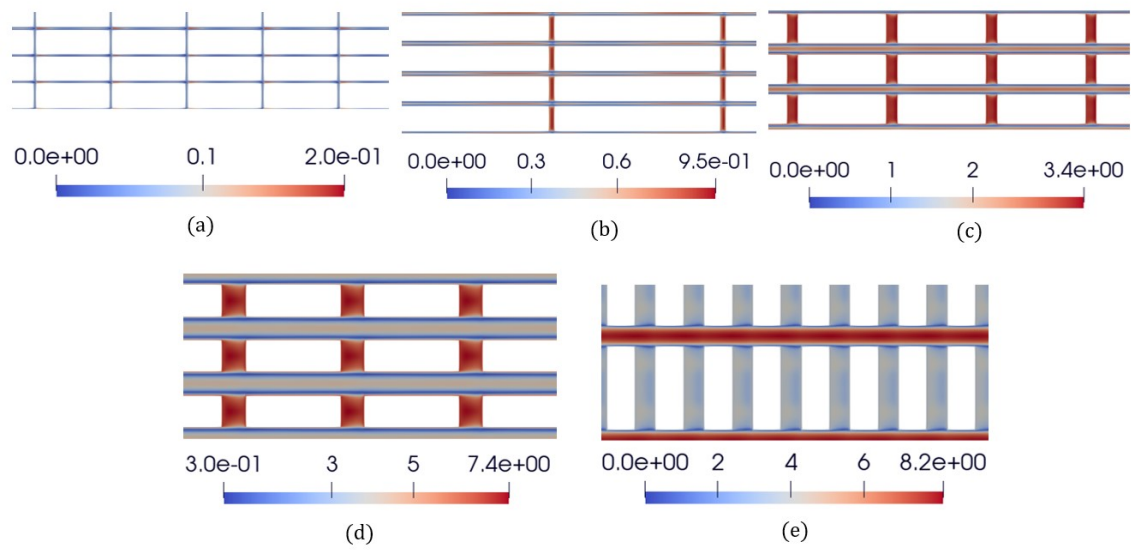


Figure 7.13: Contours of stream-wise dispersive stress $(\tilde{u}\tilde{u})$, at the height of $y^+ = 10$, above the bottom wall. (a): $\lambda_p = 0.88$, (b): $\lambda_p = 0.77$, (c): $\lambda_p = 0.64$, (d): $\lambda_p = 0.457$ stream-wise, (e): $\lambda_p = 0.457$ span-wise.

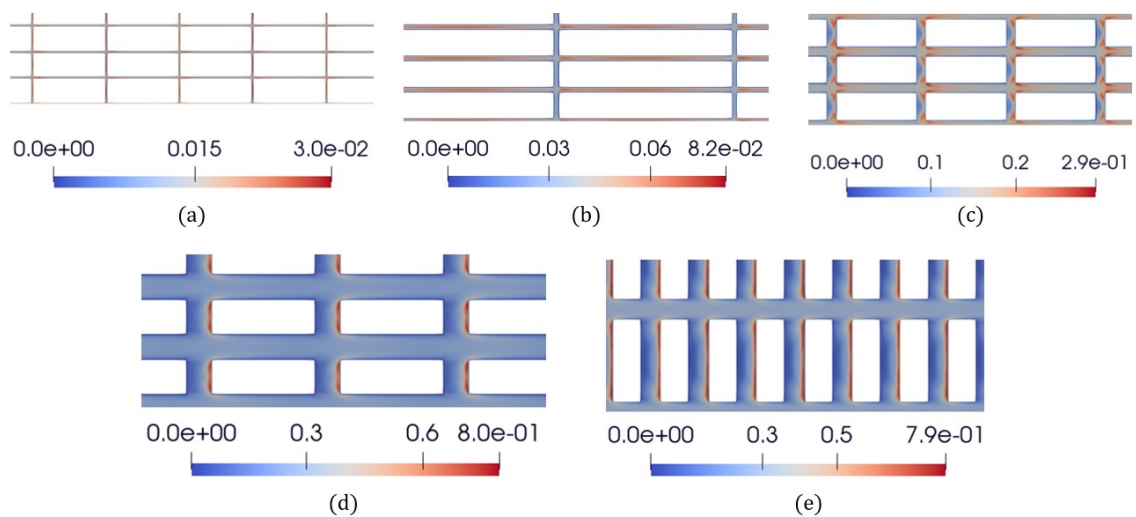


Figure 7.14: Contours of normal-to-wall Reynolds stress $(\tilde{v}\tilde{v})$, at the height of $y^+ = 10$, above the bottom wall. (a): $\lambda_p = 0.88$, (b): $\lambda_p = 0.77$, (c): $\lambda_p = 0.64$, (d): $\lambda_p = 0.457$ stream-wise, (e): $\lambda_p = 0.457$ span-wise.

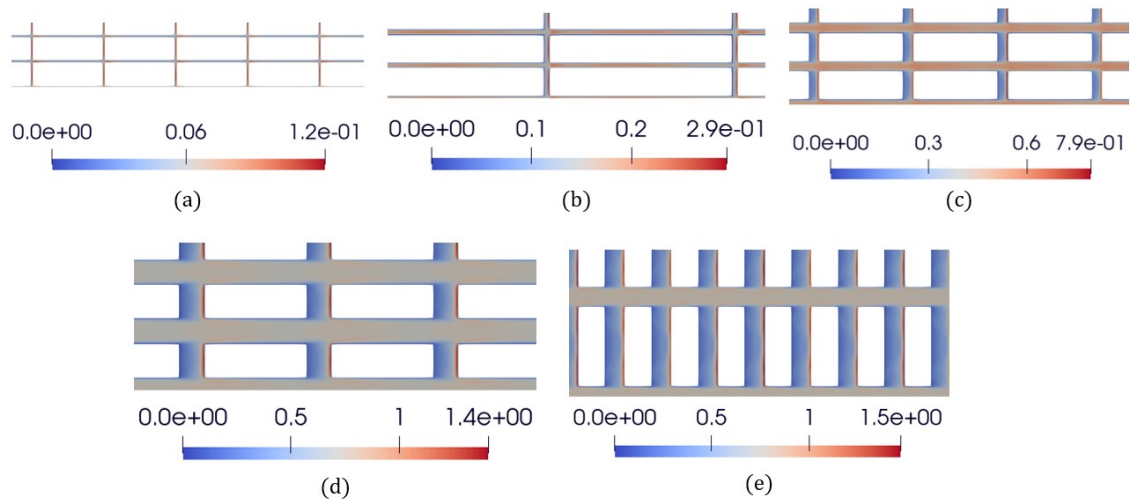


Figure 7.15: Contours of normal-to-wall Reynolds stress ($\overline{v\tilde{v}}$), at a height of $y^+ = 30$, above the bottom wall. (a): $\lambda_p = 0.88$, (b): $\lambda_p = 0.77$, (c): $\lambda_p = 0.64$, (d): $\lambda_p = 0.457$ stream-wise, (e): $\lambda_p = 0.457$ span-wise.

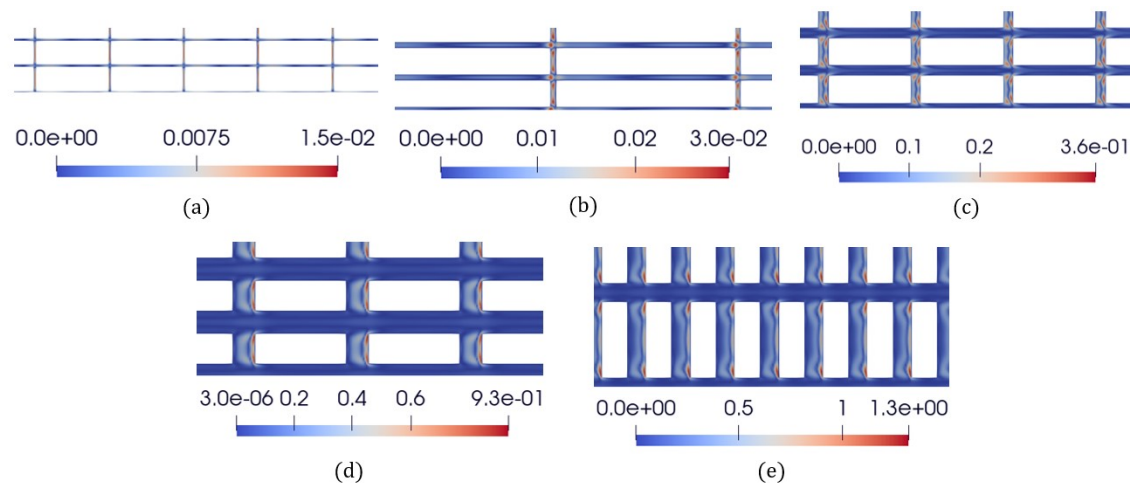


Figure 7.16: Contours of normal-to-wall dispersive stress ($\tilde{v}\tilde{v}$), at the height of $y^+ = 10$, above the bottom wall. (a): $\lambda_p = 0.88$, (b): $\lambda_p = 0.77$, (c): $\lambda_p = 0.64$, (d): $\lambda_p = 0.457$ stream-wise, (e): $\lambda_p = 0.457$ span-wise.

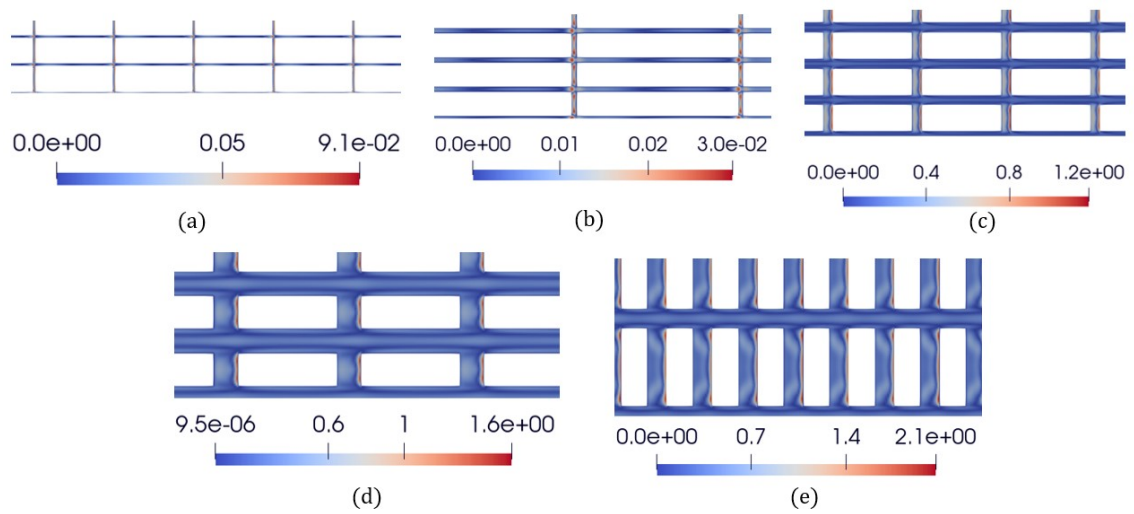


Figure 7.17: Contours of normal-to-wall dispersive stress $(\tilde{v}\tilde{v})$, at the height of $y^+ = 30$, above the bottom wall. (a): $\lambda_p = 0.88$, (b): $\lambda_p = 0.77$, (c): $\lambda_p = 0.64$, (d): $\lambda_p = 0.457$ stream-wise, (e): $\lambda_p = 0.457$ span-wise.

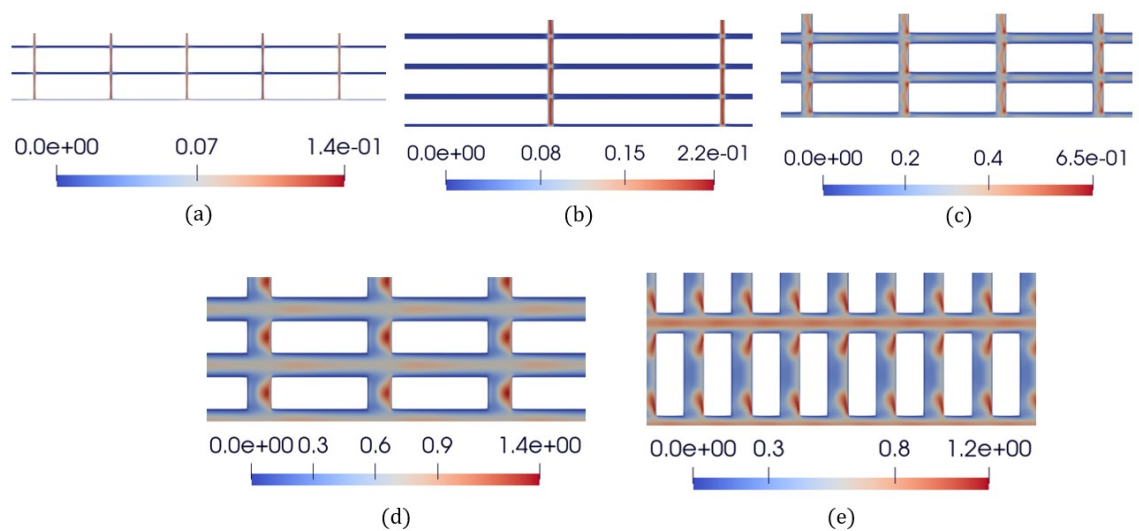


Figure 7.18: Contours of span-wise Reynolds stress $(\overline{w\overline{w}})$, at the height of $y^+ = 10$, above the bottom wall. (a): $\lambda_p = 0.88$, (b): $\lambda_p = 0.77$, (c): $\lambda_p = 0.64$, (d): $\lambda_p = 0.457$ stream-wise, (e): $\lambda_p = 0.457$ span-wise.

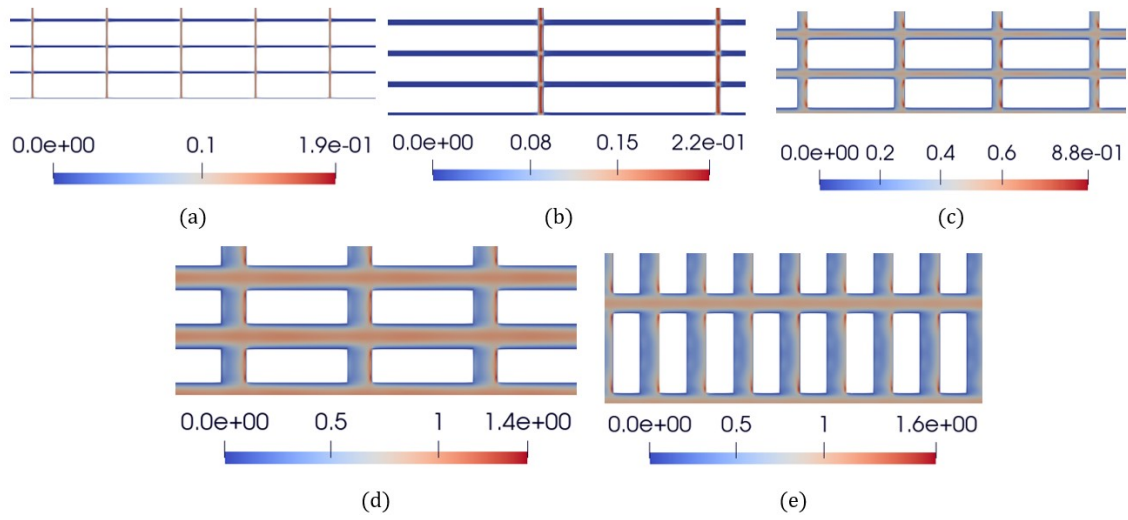


Figure 7.19: Contours of span-wise Reynolds stress $(\overline{w\tilde{w}})$, at the height of $y^+ = 30$, above the bottom wall. (a): $\lambda_p = 0.88$, (b): $\lambda_p = 0.77$, (c): $\lambda_p = 0.64$, (d): $\lambda_p = 0.457$ stream-wise, (e): $\lambda_p = 0.457$ span-wise.

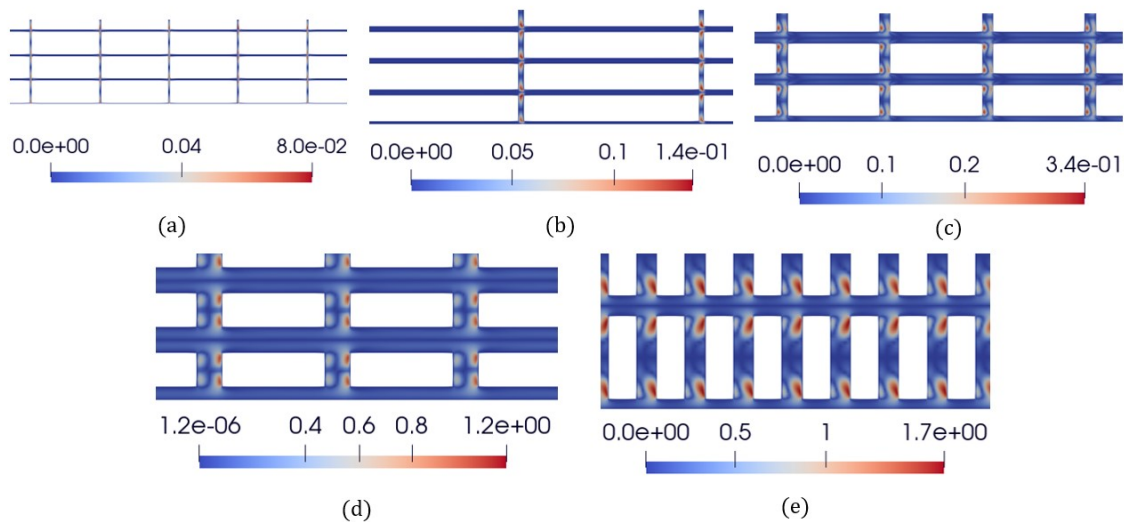


Figure 7.20: Contours of span-wise dispersive stress $(\tilde{w}\tilde{w})$, at the height of $y^+ = 10$, above the bottom wall. (a): $\lambda_p = 0.88$, (b): $\lambda_p = 0.77$, (c): $\lambda_p = 0.64$, (d): $\lambda_p = 0.457$ stream-wise, (e): $\lambda_p = 0.457$ span-wise.

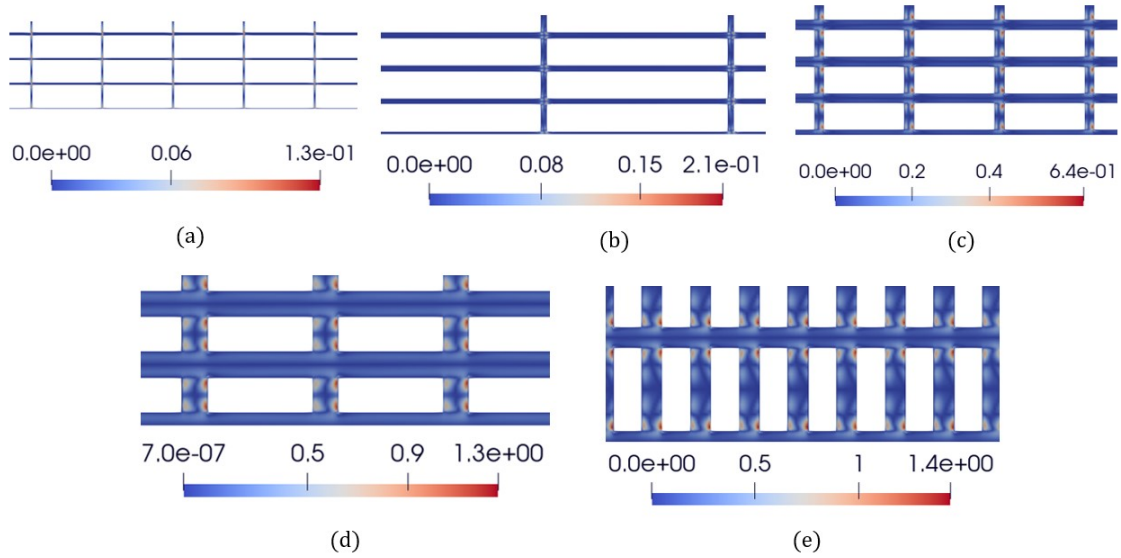


Figure 7.21: Contours of span-wise dispersive stress ($\tilde{u}\tilde{w}$), at the height of $y^+ = 30$, above the bottom wall. (a): $\lambda_p = 0.88$, (b): $\lambda_p = 0.77$, (c): $\lambda_p = 0.64$, (d): $\lambda_p = 0.457$ stream-wise, (e): $\lambda_p = 0.457$ span-wise.

is also a clear intensification in the Reynolds shear stresses at the junction between the span-wise and stream-wise gaps. This is most likely due to increased mixing as a result of the interaction between stream-wise and span-wise vortices. As is the case with Reynolds shear stresses, a high stream-wise dispersive stress region can generate a higher dispersive shear stress. This is observed in the span-wise gaps where stream-wise dispersive stress is high. At $y^+ = 10$ near the bottom wall, a thin layer of negative dispersive stress is observed in the span-wise gaps on the windward side of the textures. This negative layer increases in magnitude as λ_p is reduced. Further from the front side of texture elements, a region of positive dispersive stresses forms. For the stream-wise texture with $\lambda_p = 0.457$, this positive dispersive stress reaches a magnitude of 1.8 when scaled with smooth wall friction velocity. It concentrates on the lee of the texture element in an attached bubble. For the span-wise texture at the same area density, a similar increase forms near the vertical edges of the texture element but does not fill the backwards-facing vertical face of the elements. This confirms the earlier suggestion that the element size in the span-wise direction should be kept small to avoid creating relative shelters. Again, a reduction in the size of the gap is clearly seen to reduce the strength of the dispersive stresses. For example, with $\lambda_p = 0.62$, the maximum dispersive stress reaches 0.35 at $y^+ = 30$ instead of 1.8 for the lower area density.

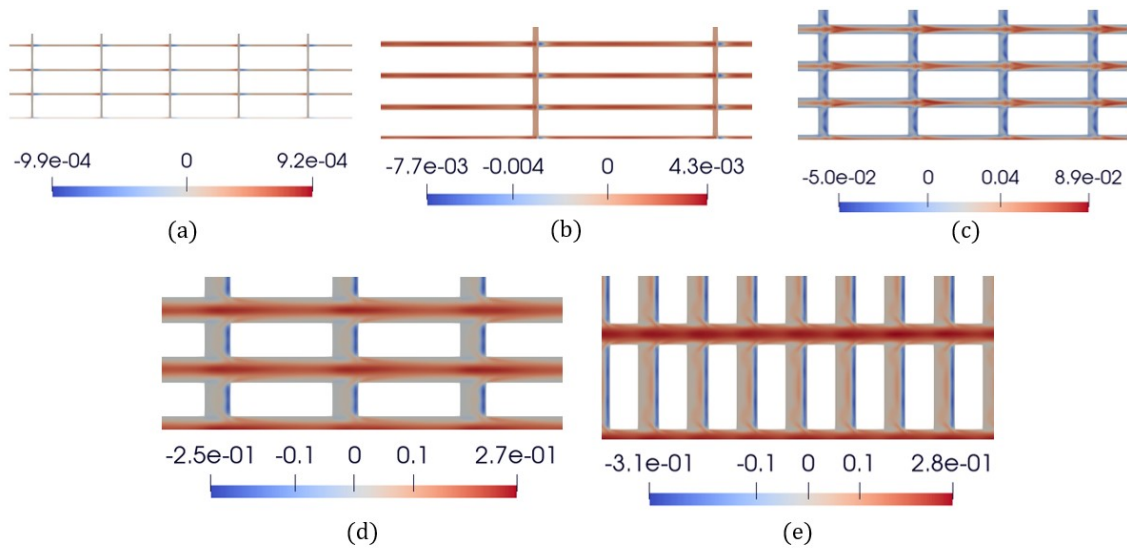


Figure 7.22: Contours of stream-wise Reynolds shear stress (\overline{uv}), at the height of $y^+ = 10$, above the bottom wall. (a): $\lambda_p = 0.88$, (b): $\lambda_p = 0.77$, (c): $\lambda_p = 0.64$, (d): $\lambda_p = 0.457$ stream-wise, (e): $\lambda_p = 0.457$ span-wise.

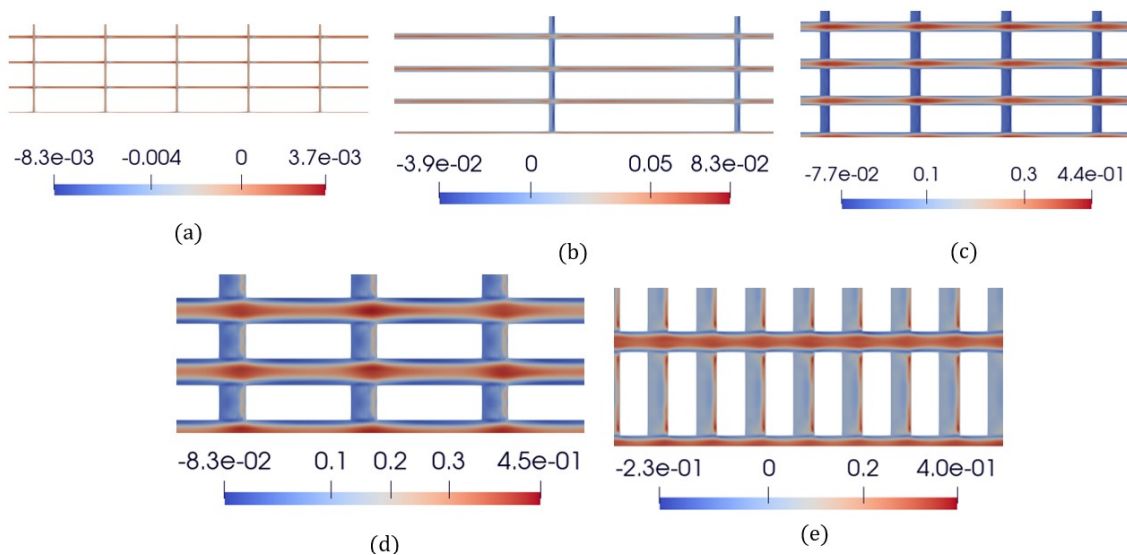


Figure 7.23: Contours of stream-wise Reynolds shear stress (\overline{uv}), at the height of $y^+ = 30$, above the bottom wall. (a): $\lambda_p = 0.88$, (b): $\lambda_p = 0.77$, (c): $\lambda_p = 0.64$, (d): $\lambda_p = 0.457$ stream-wise, (e): $\lambda_p = 0.457$ span-wise.

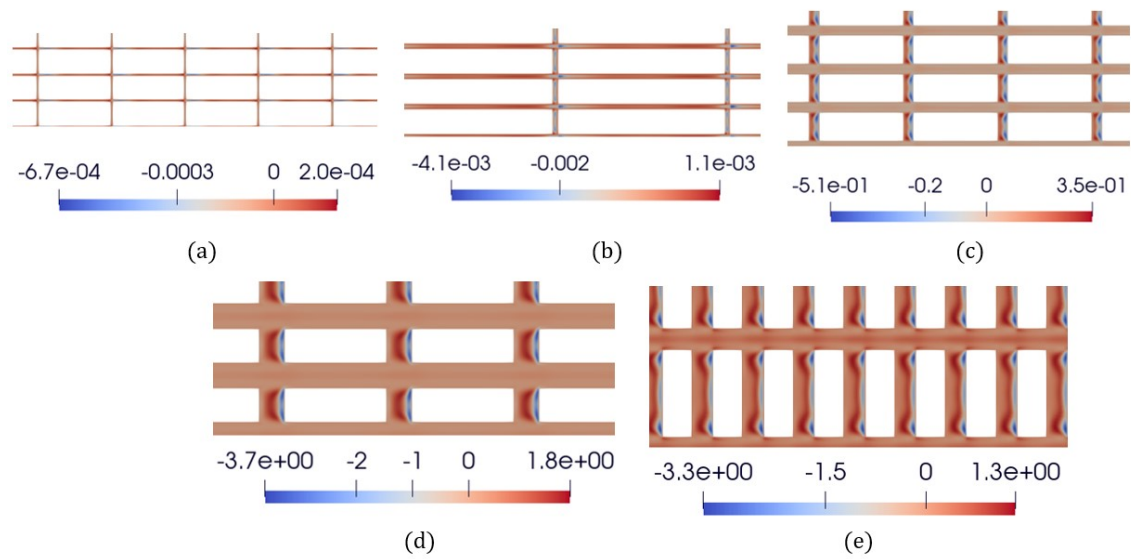


Figure 7.24: Contours of stream-wise dispersive shear stress $(\tilde{u}\tilde{v})$, at the height of $y^+ = 10$, above the bottom wall. (a): $\lambda_p = 0.88$, (b): $\lambda_p = 0.77$, (c): $\lambda_p = 0.64$, (d): $\lambda_p = 0.457$ stream-wise, (e): $\lambda_p = 0.457$ span-wise.

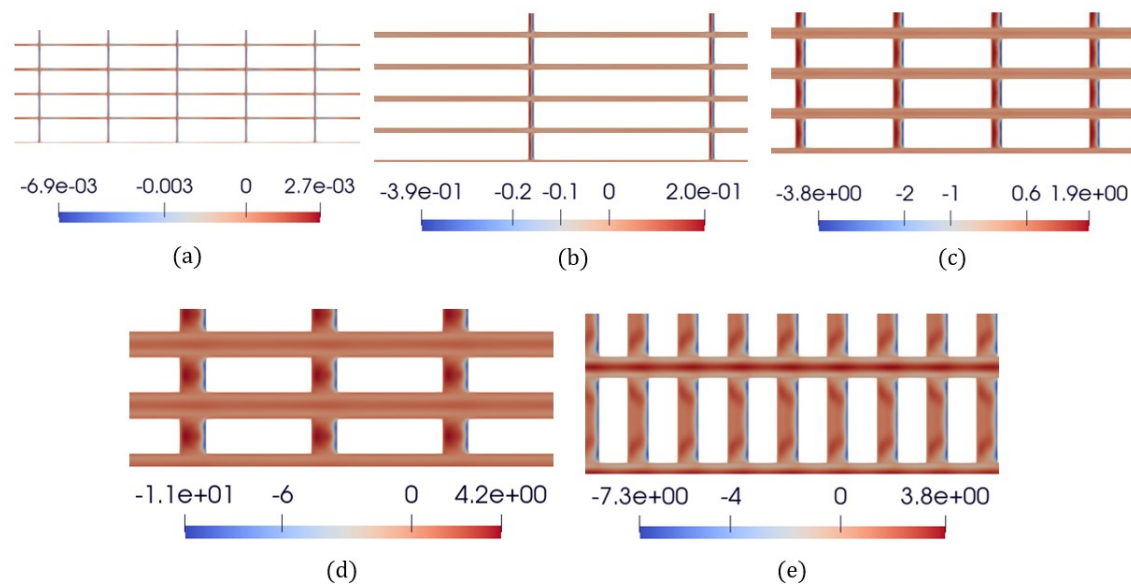


Figure 7.25: Contours of stream-wise dispersive shear stress $(\tilde{u}\tilde{v})$, at the height of $y^+ = 30$, above the bottom wall. (a): $\lambda_p = 0.88$, (b): $\lambda_p = 0.77$, (c): $\lambda_p = 0.64$, (d): $\lambda_p = 0.457$ stream-wise, (e): $\lambda_p = 0.457$ span-wise.

7.3 Discussion and Conclusions

This chapter analyzed two distinct turbulent stresses that a bio-fouling organism would experience at the initial stage of settlement, considering five different texture layouts. The organism was not modelled, so its effect on the flow is neglected. The primary objective was to assess the impact of the texture on turbulence within and above the texture, taking into account spatial variations. To this end, the average Reynolds and dispersive stresses are presented and analyzed in terms of the density of the texture area λ_p . The results reveal that in the case of a lower $\lambda_p = 0.457$, the spatially averaged stream-wise dispersive stresses are nearly twice as large as the Reynolds stream-wise stress close to the bottom wall within the gaps between textures. The dispersive shear stress is shown to dominate over the Reynolds shear stresses. On the other hand, higher λ_p , such as 0.88 and 0.77, do not produce significant turbulent stresses due to the absence of stream-wise turbulent structures. The turbulent stress distribution within the textures was then described in terms of the Reynolds and dispersive contours at distances of $y^+ = 10$ and $y^+ = 30$ from the bottom wall. It is observed that the Reynolds stresses are insignificant in the span-wise gaps for all textures, suggesting that the elements produce a stress-sheltered region. The results show however that dispersive stresses must also be considered. At lower density λ_p , very significant dispersive shear stresses develop both in the stream-wise and span-wise gaps. This can be expected to have an impact on the forces experienced by settling organisms and to prevent the formation of stress shelters in the lee of texture elements. There appears to be a limit to this effect as the element length in the span-wise direction is increased. Comparing dispersive shear stress contours for $\lambda_p = 0.457$ with the two orientations of the textures reveals that the dispersive shear stress is more pronounced in the span-wise gaps of stream-wise oriented texture. The Reynolds shear stresses are also shown to intensify at the junction between the stream-wise gaps met span-wise gaps. These observations suggest that textures should rely on thin prisms to maximize turbulent stresses within gaps and hence optimize the disruptive impact of turbulence on bio-fouling settlement. If elongated elements are used, for example, to minimize the processing steps needed to create the surface texture, these should be aligned with the flow direction. If the mean flow is intrinsically three-dimensional, elongated elements should be avoided and cubic elements would be preferable.

Chapter 8

Hydro-dynamical forces acting on a simplified organism model positioned on and within $\lambda_p = 0.457$ ($S^+ = 80$) stream-wise texture

This chapter reports simulations of hydrodynamic forces acting on a simplified organism model. The simulations were performed with the same Large Eddy Simulation (LES) approach as adopted previously. The primary objective is to compare forces acting on organisms at the early stage of settlement depending on its location around the texture and taking account of the effect of the organism on turbulence. A single texture is considered. The area density and orientation which maximized stresses is selected for this purpose that is the $\lambda_p = 0.457$ texture with elements aligned with the flow. The organism model is placed at three different positions on and around the texture. The three tested positions are:

- A, at the centre of the crest plane of a single texture element.
- B, at the bottom wall, in the middle of the stream-wise gap.
- C, at the bottom wall and in the middle of a span-wise gap.

A model micro bio-fouling organism based on the *Nitzschia Ovalis* marine diatom was selected for the tests and was modelled as a stadium cylinder. The geometry, meshing, and solution setup were described in Chapter 4. The results are compared with a scenario where the organism is placed on a smooth wall in a channel flow. The forces that act on the organism consist of pressure and viscous forces. OpenFOAM V6 function object "forces" is used to calculate viscous and pressure forces by applying the formula provided in the [193].

$$F_p = \sum_i \rho_i s_{f,i} (p_i - p_{ref}) \quad (8.1)$$

$$F_v = \sum_i s_{f,i} (\mu R_{dev}) \quad (8.2)$$

where the summation is performed over the discrete faces that represent the organism. ρ is the density, $s_{f,i}$ represents the face area vectors, p denotes pressure, μ is the dynamic viscosity, and R_{dev} represents the deviatoric stress tensor. To calculate pressure forces, the reference pressure p_{ref} is set to zero.

8.1 Time histories of forces acting on the organism

Figs. 8.1 to 8.3 present the time history of the hydrodynamic forces acting in the stream-wise (x), normal-to-wall (y), and span-wise (z) directions, for the respective cases. All force components are scaled by a notional force intended to represent the shear force that would be felt by an organism as it settles over the smooth untextured surface, assuming that the effect of the organism itself is negligible. The force is defined from the mean shear stress $\tau_{w,s}$ over the area covered by the footprint of the organism A_o as $F_{ref} = \tau_{w,s} A_o$. This reference force is calculated from the smooth wall simulation as $F_{ref} = 0.187 \text{ mN}$. Time is scaled in terms of the turnover time of eddies shed by textures $T_{ref} = h/u_\tau \sim 10(s)$. Here, h represents the texture heights, and u_τ corresponds to the friction velocity of the texture. The forces are sampled over time a period which is up to 12 times larger than T_{ref} , providing sufficient data for averaging. The difference between the mean values during the first and second half of the sampling period was less than 2% of the mean and maximum data values. Eq.(8.3) is used to calculate the intensity of forces acting on the organism.

$$I_i = \frac{(\frac{1}{T} \int_0^T \eta'^2 dt)^{0.5}}{\bar{\eta}} \quad (8.3)$$

T denotes a time sampling period, and η is the difference between the instantaneous value of η and the average value of η ($\bar{\eta}$).

Tables 8.1 and 8.2 provide a summary of the averaged forces acting on the organism model in x , y , and z directions and the corresponding intensities of the force fluctuations as defined by Eq. (8.3). The data, is given in Table. 8.1, shows an increase in the magnitude of the stream-wise force for points A and C by approximately 60% and 11% and a moderate decrease of 16% at B. These increases occur in spite of a substantial reduction in excess of 33% to 50% in the span-wise force component.

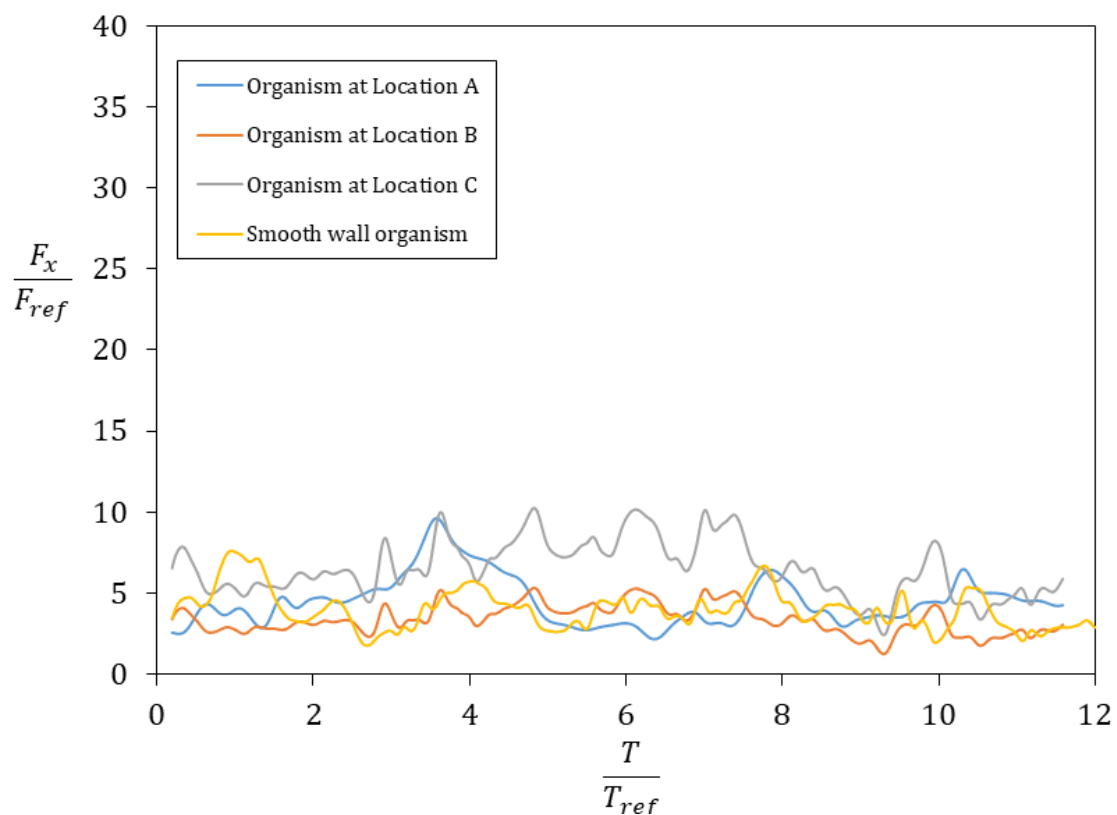


Figure 8.1: The time-history of hydrodynamic forces exerted on the organism model in the stream-wise direction.

organism location	$\overline{F_x}/F_{ref}$	$\overline{F_y}/F_{ref}$	$\overline{F_z}/F_{ref}$
Organism on the smooth wall	4.0659	1.2267	0.2922
A	4.5119	2.2795	0.1462
B	3.3954	1.5572	0.1542
C	6.5323	1.5102	0.1928

Table 8.1: Mean hydrodynamic forces acting on the organism in different directions.

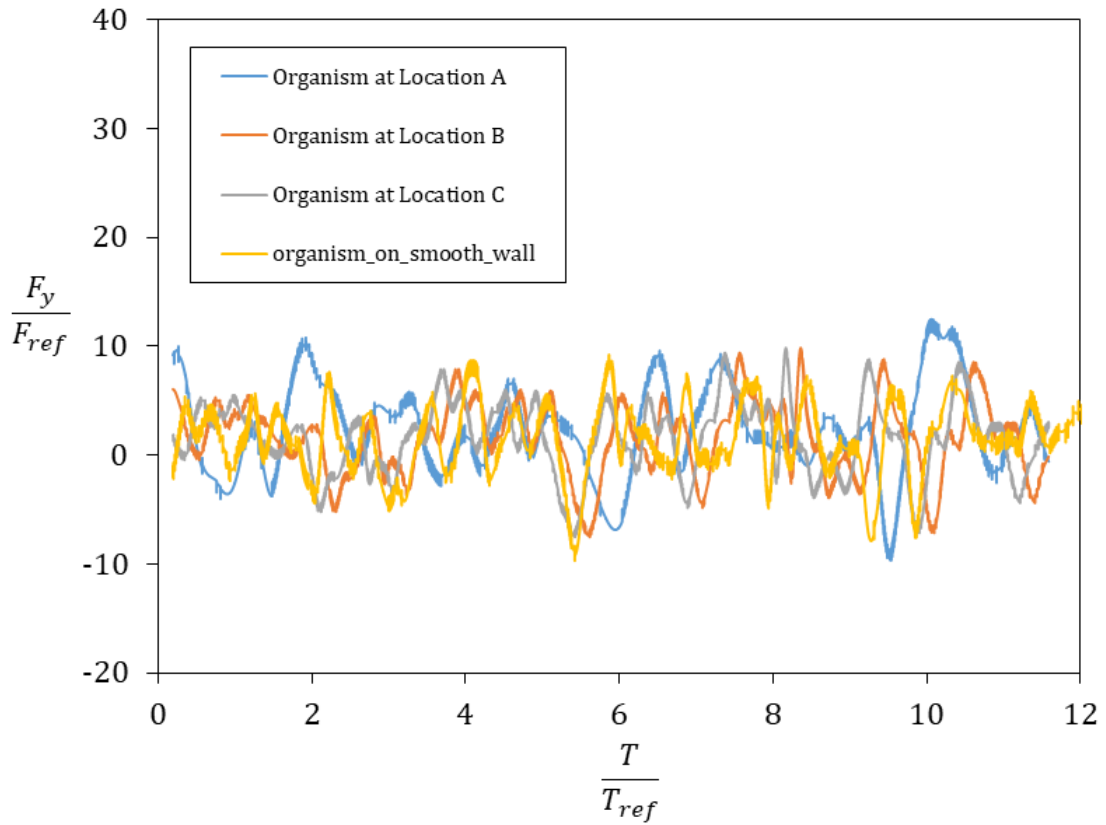


Figure 8.2: The time-history of hydrodynamic forces exerted on the organism model in the normal-to-wall direction.

organism location	I_x	I_y	I_z
Organism on the smooth wall	0.5457	2.7738	8.0212
A	0.3391	1.8099	20.5726
B	0.3732	3.0258	9.6579
C	0.3732	2.1920	10.6488

Table 8.2: Intensity of the hydrodynamic forces acting on the organism in different directions.

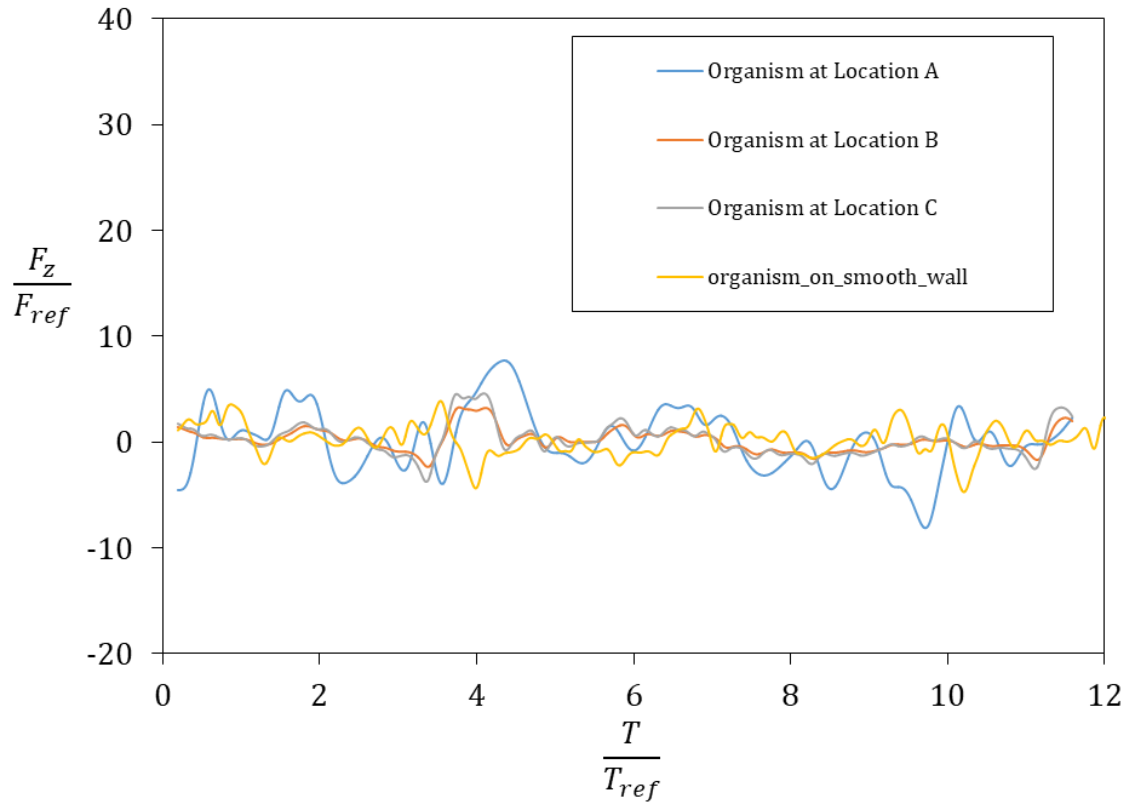


Figure 8.3: The time-history of hydrodynamic forces exerted on the organism model in the span-wise direction.

However, it is noted that this force component makes a minor contribution to the total hydrodynamic force. The increase at location C occurs in spite of what was interpreted as a sheltering effect from the texture when considering the Reynolds stress contours alone. The wall-normal component is also shown to increase by 23%, 27% and 86% for locations C, B and A, respectively. The intensity of fluctuations are also an important indicator of the effect of the textures as it reflects the strength of transient fluctuations that organisms are exposed to. A large departure from the mean can cause significant additional stresses. The texture is shown to induce a significant decrease in the stream-wise intensity at all locations and a more moderate one for the wall-normal intensity at locations A and C. Interestingly, although the increase in span-wise fluctuations is moderate at locations B and C, a very large increase of approximately 150% is observed at location A. This suggests that the textures have a strong impact on stream-wise vortexes over the crest plane, possibly due to the amplified eddy shedding in the span-wise and wall-normal directions caused by the sharp edges of the texture (see Chapter 6 Fig 6.4 (b) and (c)).

The height of the organism reaches $y^+ = 4.82$ at its apex. Reynolds and dispersive shear stresses contours from velocity fluctuations in the stream-wise direction below this level are given in Figs. 8.4, 8.6, and 8.6, for two planes at a distance $y^+ = 2$

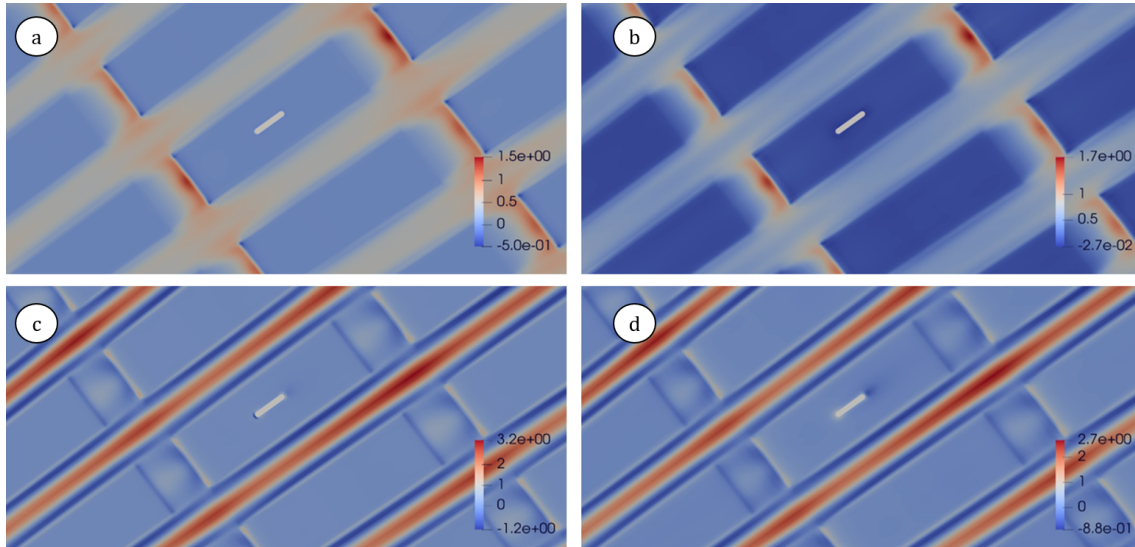


Figure 8.4: Contours of the stream-wise Reynolds and dispersive shear stresses around the organism model positioned at location A. (a): Reynolds shear stress at $y^+ = 2$, (b): Reynolds shear stress at $y^+ = 4$, (c): dispersive shear stress at $y^+ = 2$, (d): dispersive shear stress at $y^+ = 4$.

and $y^+ = 4$ from the base of the organism. The dispersive stresses can be seen to concentrate within the stream-wise gaps in the vicinity of the texture crest plane, while the Reynolds stresses are mainly significant in the span-wise gaps. Within the span-wise gaps, dispersive stresses are typically one order of magnitude larger than Reynolds stresses at $y^+ = 4$ and most likely a better measure of the effect of turbulence on forces experienced by the organisms settled within the gap. This can be explained by reference to the simplified equation Eqn. (7.1) which can simplify to Eqn. (8.4) in the case of statistically stationary flow.

$$\frac{\partial \langle \overline{uv} \rangle}{\partial y} = f_v + f_p \quad (8.4)$$

where f_v and f_p denote the viscous drag and the pressure drag. Increases in dispersive stresses normal to wall result in higher wall normal gradients in the span-wise gap and, hence, higher average stream-wise drag acting on the organism at location C.

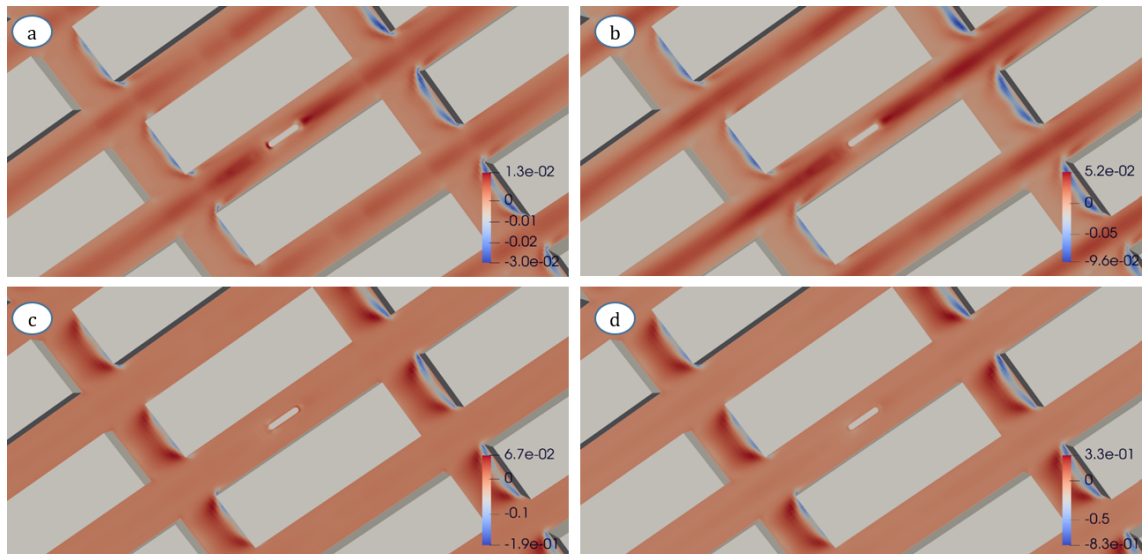


Figure 8.5: Contours of the stream-wise Reynolds and dispersive shear stresses around organism model positioned at location B. (a): Reynolds shear stress at $y^+ = 2$, (b): Reynolds shear stress at $y^+ = 4$, (c): dispersive shear stress at $y^+ = 2$, (d) dispersive shear stress at $y^+ = 4$.

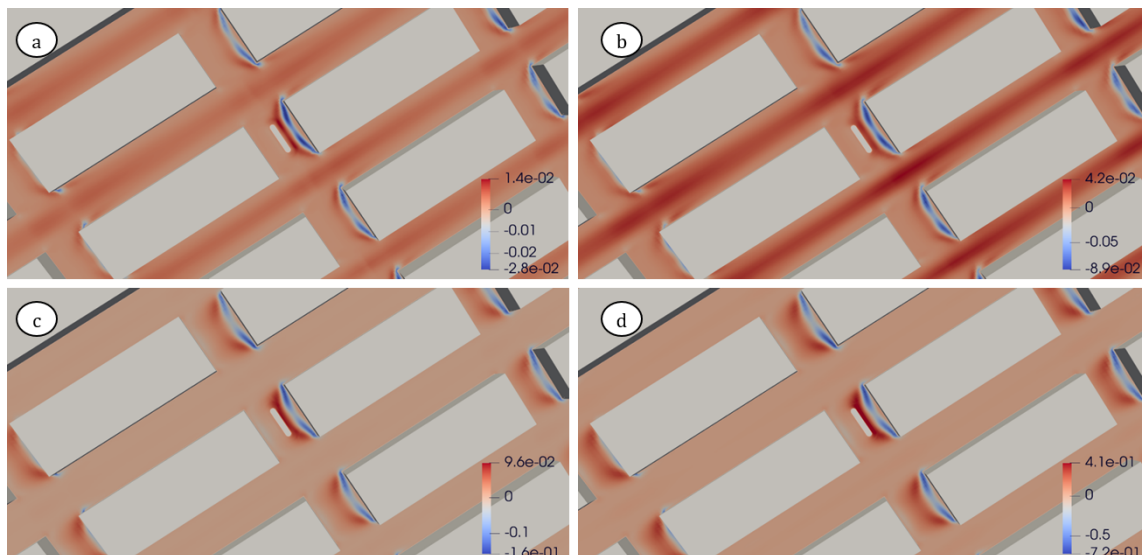


Figure 8.6: Contours of the stream-wise Reynolds and dispersive shear stresses around organism model positioned on C location. (a): Reynolds shear stress at $y^+ = 2$, (b): Reynolds shear stress at $y^+ = 4$, (c): dispersive shear stress at $y^+ = 2$, (d) dispersive shear stress at $y^+ = 4$.

	Pressure force ratios			Viscous force ratios		
	x	y	z	x	y	z
Force directions						
Organism on the smooth wall	1.37E-01	8.92E-01	6.04E-01	8.63E-01	1.08E-01	3.96E-01
A	1.46E-01	9.20E-01	6.33E-01	8.54E-01	8.01E-02	3.67E-01
B	1.36E-01	9.08E-01	5.98E-01	8.64E-01	9.17E-02	4.02E-01
C	1.36E-01	9.08E-01	5.98E-01	8.64E-01	9.17E-02	4.02E-01

Table 8.3: Pressure and viscous drag ratio acting on the organism.

Table 8.3 compares the forces exerted on the organism and scaled with the reference force. The positions around the texture appear to have only a moderate impact on the force which remains quite similar to that experienced over the smooth surface. Given that the organism's height is below $y^+ = 5$, the primary forces acting on it are mostly influenced by viscous effects.

Organism location	\overline{F}_t/F_{ref}	I_t	Max F_t/F_{ref}
Organism on the smooth wall	5.2574	0.6255	10.8212
A	6.9329	0.3514	13.4912
B	4.9424	0.4582	10.5037
C	7.5855	0.5134	13.6054

Table 8.4: Total hydrodynamic forces acting on the organism in different cases.

The effect of the location on the total hydrodynamic forces $F_t = \sqrt{F_x^2 + F_y^2 + F_z^2}$ experienced by the organism is illustrated and summarized in Figs. 8.7 and Tab. 8.4, where it is normalized by F_{ref} . The texture reduces the overall intensity of fluctuations compared to the smooth wall case but increases the mean total force and maximum force both at the crest and within the span-wise gaps (locations A and C). The increase in the mean total force is approximately 31% and 44%, respectively, compared to the smooth wall case, with a similar increase in the maximum forces. On the contrary, the organism at the base of the stream-wise gap (location B) experiences a slight decrease of 6% in the mean total forces with little change to the maximum. In terms of instantaneous maximum forces, locations A and C exhibit an approximate 25% increase compared to the smooth wall case, while point B does not show a significant change compared to the smooth wall pattern.

8.2 Dispersive and Reynolds shear stresses impact on the exerted forces

Results show that organisms within the groves experience larger forces when located in the lee of the texture rather than in the stream-wise groves. The comparison between forces at these two locations is shown in Fig. 8.8. This clearly shows that the only significant change comes from the shear dispersive stream-wise force. A similar observation was made with the stream-wise dispersive stresses, which were shown to concentrate around location C Fig. 8.6. This suggests that dispersive stresses have the strongest influence on the average force when organisms are located in the

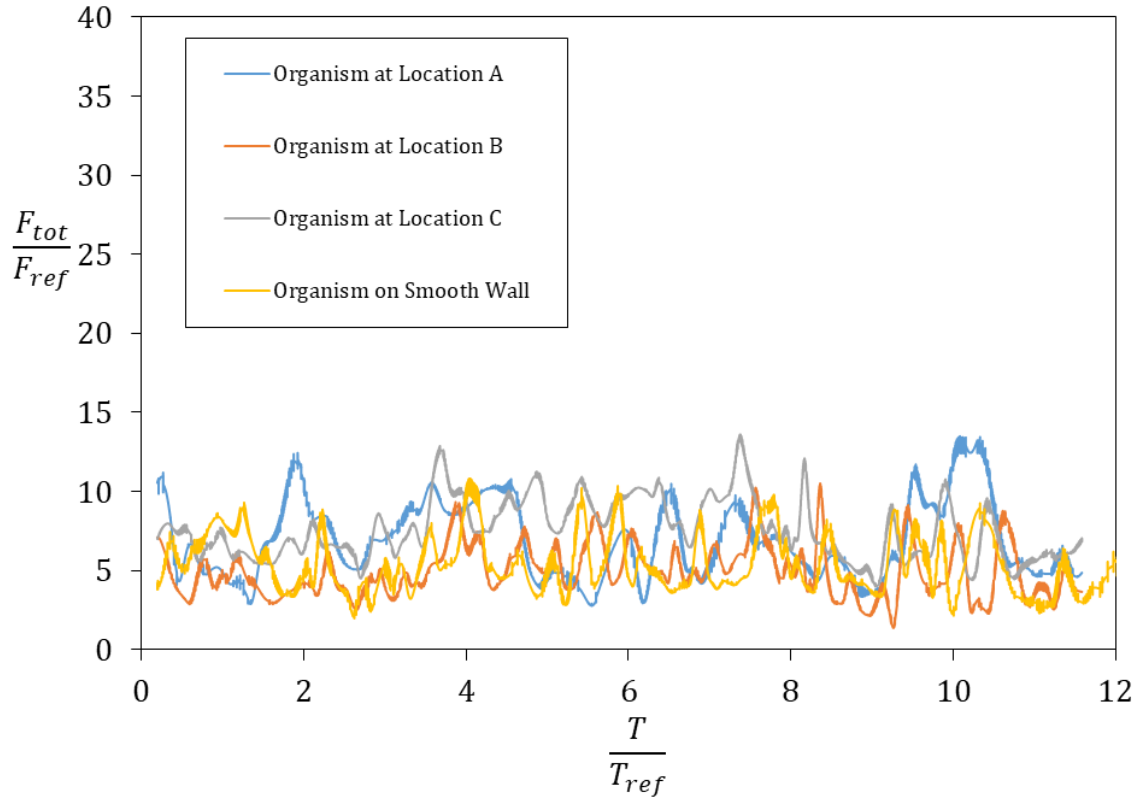


Figure 8.7: The time-history of total hydrodynamic forces exerted on the organism model.

lower parts of the gaps. Since the organism is almost entirely in the viscous sub-layer ($y^+ \leq 5$), viscous stresses can be expected to dominate compared to Reynolds stresses (normal to wall dispersive shear stress gradient has mostly influenced the viscous stresses). The comparison also shows how closely the time history of force fluctuation is irrespective of the location within the gaps (B or C), which explains the limited effects observed on the intensity of force fluctuations. This shows the same intensity of force acting on the organism placed at two different locations within the texture, indicating that Reynolds stresses are the dominant factor in the intensity of the forces. More variability is seen between forces acting on the organism located at A and C Fig. 8.9.

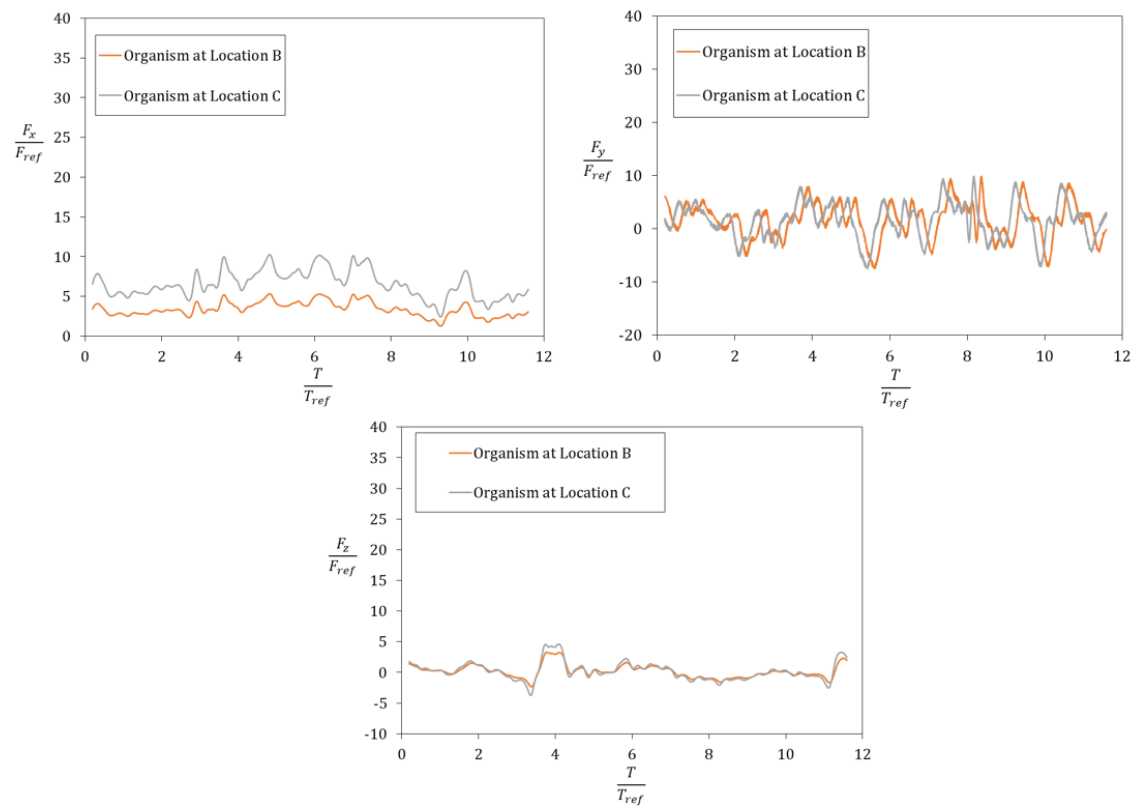


Figure 8.8: Forces applied to the organism at B and C locations within the texture, (a): stream-wise force (F_x/F_{ref}), (b): normal-to-wall force (F_y/F_{ref}), (c): span-wise force (F_z/F_{ref}).

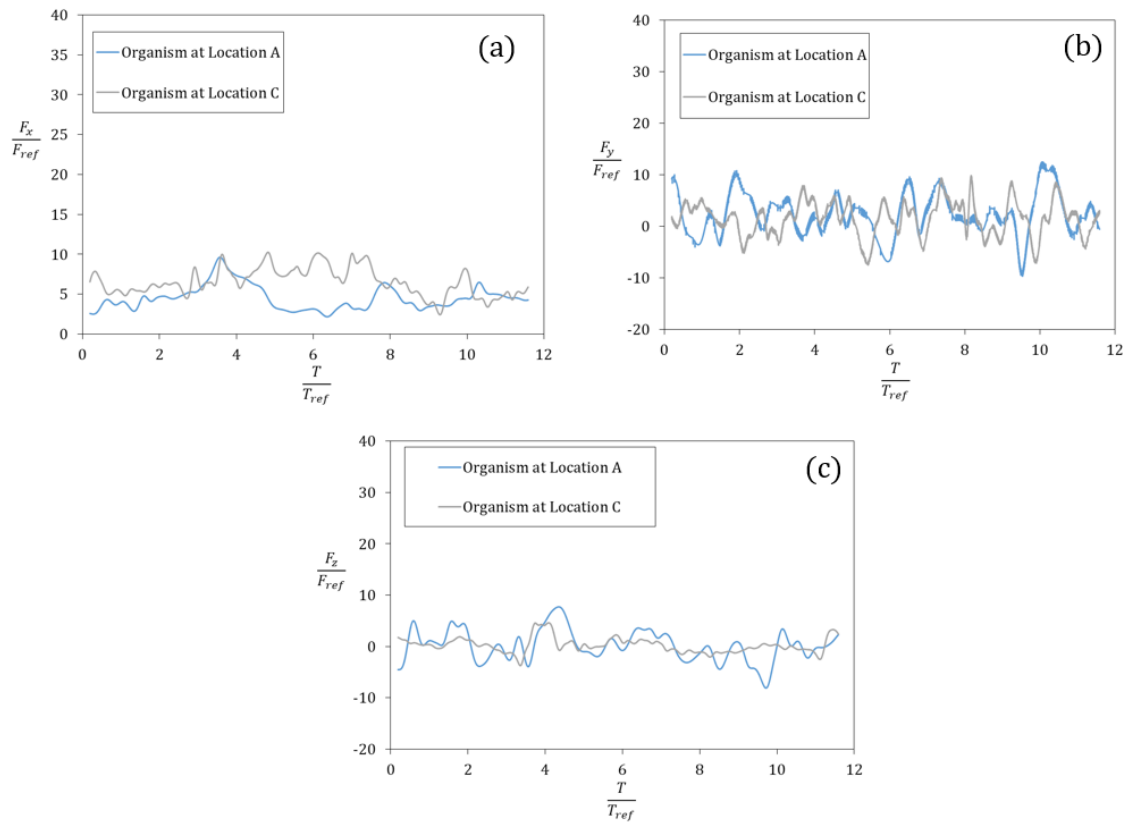


Figure 8.9: Forces applied to the organism at A and C locations, (a): stream-wise force (F_x/F_{ref}), (b): normal-to-wall force (F_y/F_{ref}), (c): span-wise force (F_z/F_{ref}).

8.3 Discussion and Conclusions

This chapter investigated hydrodynamic forces acting on an organism model at the early stage of its settlement, placed at three distinct positions within and above a candidate texture. The texture which generated the largest total stresses was selected. Its area density is $\lambda_p = 0.457$ and the elements are aligned with the flow direction. The results were compared with a scenario in which the organism model was placed on a smooth wall. The organism was placed at the centre of the texture crest plane, at the centre of the bottom wall in the stream-wise gap, and at the centre of the bottom wall in the span-wise gap. The height of the organism was set below $y^+ = 5$, when scaled with the smooth wall units. LES simulations have revealed that the texture elements led to a 44% increase in the mean flow-wise drag experienced by organisms located in the lee of the texture elements, where a large increase in dispersive stresses was also observed. Results suggest that dispersive stresses are predominantly impacting the mean component of hydrodynamic forces while Reynolds stresses play a role in controlling the fluctuation intensity of hydrodynamic forces. It was also observed that the stream-wise oriented sharp edges of the prism texture, induced span-wise eddy shedding, resulting in a nearly twofold enhancement in span-wise force intensity compared to the smooth wall scenario. The computation of total forces and their intensity shows that the texture reduces the intensity of hydrodynamic force fluctuations for organisms positioned on and around the texture when compared to a smooth wall position. Key results on the influence of the location include:

- organisms at positions C and A experience a mean hydrodynamic force which is approximately 60% and 11% higher than on a smooth surface,
- an organism at position B experienced a 6% reduction in the mean force,
- Organisms at positions A and C experience an increase of close to 25% in the maximum instantaneous forces, while position B exhibited no significant change.

Chapter 9

Overall thesis discussion

In this thesis, high-fidelity Large Eddy Simulation (LES) were conducted on five sets of textures inspired by the skin ridges of brill fish *Scophthalmus rhombus*. Due to the high computational demands of these simulations, a simplified elongated rectangular prism was employed to represent the texture elements. The primary focus of the simulations was to explore the influence of gap sizes on the resulting turbulent flow stresses and their implication for antifouling applications. Sharp edges were incorporated based on existing literature to mitigate the simulation's reliance on the Reynolds number. Five sets of different texture configurations were used in the simulations (with lateral spacings denoted as $S^+ = 10, 20, 40, 80, 80$ span-wise), where S^+ represents the lateral spacings of consecutive texture elements scaled with the smooth wall viscous length scale at $Re_\tau = 395$. The S^+10 spacing was designed to mimic the effect of ridges found on brill fish, while larger gaps simulated effects beyond $S^+ = 15$, which is a critical point for riblet effects.

Visualizing the turbulent flow structures around three stream-wise oriented textures ($S^+ = 10, 40, 80$), revealed that employing $S^+ = 10$ gap sizes (mimicking brill fish skin gap ridges) inhibits the penetration of stream-wise vortical structures crucial for turbulent stress propagation within the textures. Consequently, increasing the gap size to $S^+ = 80$ can lead to higher Reynolds stresses within the textures.

Recognizing that $S^+ = 10$ gaps result in negligible turbulent stresses within textures, it was noted that enlarging the spacing gap within textures gives rise to an additional category of turbulent stresses known as dispersive stresses. These dispersive stresses originate from the inhomogeneity of the flow within textures and intensify as the gap widens to $S^+ = 80$. Among the turbulent stresses, dispersive shear stresses were found to be dominant within the $S^+ = 80$ texture.

The turbulent flow around two distinct orientations of $S^+ = 80$ textures (stream-wise and span-wise) was analyzed, and the results were compared with the smooth wall case. It was observed that, in both stream-wise and span-wise scenarios, the concentration of Reynolds shear stresses is in the stream-wise gaps. Regarding dis-

persive stresses, for the $S^+ = 80$ stream-wise texture, dispersive stress becomes predominant in span-wise gaps. Upon closer examination of the dispersive stress distribution in the $S^+ = 80$ span-wise texture, it becomes apparent that dispersive stresses are more pronounced in stream-wise gaps due to a higher number of four-way conjunctions compared to the stream-wise texture case. This suggests that employing a greater quantity of texture elements with more equal-sided characteristics could potentially result in a more evenly distributed turbulent stress, thereby disrupting the initial settlement of biofoulings. Additionally, placing the organism model in various locations of the $S^+ = 80$ stream-wise texture confirmed the significance of dispersive stress in increasing hydrodynamical forces acting on an organism intending to settle on a surface.

Chapter 10

Conclusion and future works

This final section presents the conclusion drawn from the numerical simulations to explore bio-inspired surface textures impact on the overlying turbulent flow. The simulation was based on a high-resolution large eddy simulation (LES) technique without wall modelling.

The textures studied are based on simplified models inspired by the micro ridges found on the growth rings of the brill fish, *Scophthalmus rhombus*. The study aimed to analyze how variations in gap spacing sizes and texture layouts impact turbulent stresses and how this may be interpreted to impact the settlement of bio-fouling organisms.

The conclusions are presented in three main parts. Firstly, the discussion revolves around the local turbulent flow statistics from the second to the fourth order and their implications for fouling settlement carried out for three stream-wise textures. Secondly, a comparison between stresses generated by temporal fluctuations (Reynolds stresses) and spatial fluctuations (dispersive stresses) in velocity is drawn among five different configurations, including a span-wise configuration and a case with longer ridges. The goal was to understand how these stresses were related to the settlement of fouling. Lastly, an evaluation was conducted regarding the hydrodynamic forces exerted on a simplified model of an organism at the early stage of settlement. This organism model is positioned at three common regions that might occur within and above the texture.

Turbulent statistics ranging from the second to fourth order of stream-wise velocity fluctuation (Reynolds stresses, skewness and flatness) were calculated for four different locations within and above textures for three different stream-wise textures ($S^+ = 10, 40$ and 80). In addition, quadrant analysis was performed for those locations to compare sweep and ejection phenomena at the prescribed locations. In this study, it has been found that:

- While findings from a parallel study, involving the immersion of textures in

a stationary fluid [13], do suggest that textures with the smallest gap ($S^+ = 10$) effectively hinder the settlement of microorganisms within the gaps, the current computational investigation also unveils that these narrow gaps serve as effective shelters against turbulent fluctuations on surfaces. Iso-contour patterns indicate that stream-wise vortexes are unable to penetrate these gaps, leading to a significant reduction in Reynolds shear stresses and various other statistical turbulence measures, dropping well below the values observed on the smooth wall. The only exceptions are the skewness (S_u) and flatness (F_u) values of stream-wise velocity fluctuations, which exhibit an increase compared to the values of the smooth surface. Instances of F_u values exceeding 3 suggest the potential for strong yet infrequent stream-wise fluctuations to occur within all gaps, including the smallest $S^+ = 10$ gap. Although the data presented in this thesis is not conclusive, it is plausible that these sporadic turbulent increases in stream-wise fluctuations could impact settlement even within the smallest gaps.

- The averaged mean wall shear stresses are generally lower when compared to those observed on the smooth wall for all considered gap sizes. Nevertheless, certain regions demonstrate an increase in shear stresses. Notably, the upper surface of the texture (crest plane) displays elevated wall shear stresses for the stream-wise texture with a gap size of $S^+ = 80$ compared to the smooth surface, with increments reaching up to 270%. Moreover, localized increases are observed near the edges, accompanied by higher stresses along the upper portions of the vertical sides.
- The width and orientation of the texture gap have a substantial impact on stress distributions at both the lower and upper parts of the gaps. At a distance of $y^+ \sim 12$ from the bottom wall, Reynolds shear stresses are generally lower than those on the smooth surface, except for the stream-wise texture with a gap size of $S^+ = 80$. In this case, local increases in maximum mean Reynolds shear stresses of up to 46% are observed in the central part of the stream-wise gap and downstream of the textures in the transverse gap. Closer to the top edge of the texture at $y^+ \sim 35$, even higher increases occur, with stress concentration shifting closer to the walls, particularly for the largest gap, stream-wise $S^+ = 80$.
- The profiles of Reynolds shear stress in the normal-to-wall direction at the four sampling locations reveal an increase in the peak stress value corresponding to the gap width. Negligible Reynolds stresses are observed within the transverse gap; however, for the larger gaps, specifically $S^+ = 40$ and $S^+ = 80$, the profiles exhibit patterns akin to those of the smooth wall, albeit with heightened

intensity. The quadrant analysis indicates that surface textures amplify the significance of sweep events. Typically, it is reported that, at the onset of the overlap region, the contribution from ejections can be twice that of sweeps. However, with the presence of textures in all the examined locations, this distinction diminishes considerably and can even be reversed, as evidenced by the case of $S^+ = 40$ at location A. Furthermore, while for the smooth wall, ejections and sweeps exhibit magnitudes comparable to $y^+ \sim 60$, there is an accelerated increase in sweeps above the crest plane over the transverse gap with $S^+ = 40$ and $S^+ = 80$, as well as across the stream-wise gap at $S^+ = 40$. This heightened turbulence-induced transfer of increased stream-wise momentum is likely to subject biofouling organisms that infiltrate the lower portions of the stream-wise gaps to more intense intermittent stresses. In particular, the influence of sweep events is particularly pronounced across stream-wise gaps, especially in the case of $S^+ = 40$, significantly contributing to the elevated transport of Reynolds shear stress through stream-wise velocity fluctuations.

The temporally averaged turbulent fluctuations (Reynolds stresses) and spatially averaged turbulent fluctuations (dispersive stress) are assessed in five distinct texture configurations categorized by their plane area density λ_p . The utilization of plane area density (λ_p) serves as a distinguishing factor between textures, primarily due to differences in the configurations of the two new textures ($S^+ = 20, 80$ span-wise), that did not consider in local turbulence analysis. The primary objective is to assess how the arrangement of texture impacts the generation of Reynolds and dispersive stresses, aiming to minimize the likelihood of fouling settlement on and within the textured surface. The findings revealed that:

- In the case of the stream-wise texture with $\lambda_p = 0.457$ ($S^+ = 80$ stream-wise), the spatially averaged stream-wise dispersive stress was approximately double the magnitude of the Reynolds stress within the texture gap near the bottom walls. As a result, the dispersive shear stress prevailed over the Reynolds shear stresses, exerting a significant influence on the initial phase of bio-organism settlement.
- Observations revealed that Reynolds stresses were negligible in span-wise gaps across all textures, indicating areas sheltered from Reynolds stresses. Nevertheless, employing higher values of λ_p led to substantial dispersive shear stresses in span-wise gaps, which could potentially influence the settlement of bio-organisms.
- Considering the minimal presence of Reynolds stress behind texture elements (indicative of protected stress regions) and the increased dispersive shear stress

in span-wise gaps with higher λ_p values, two configurations of $\lambda_p = 0.475$ with stream and span-oriented elements were investigated. This investigation aimed to assess the impact of the size and orientation of the texture elements on stress generation. The results revealed that in stream-wise-oriented textures, dispersive shear stress concentrates predominantly in the span-wise gaps, while in span-wise-oriented textures, this concentration shifts to the stream-wise gaps. Furthermore, the distribution of Reynolds shear stresses within the textures exhibited heightened levels at four-way junctions where stream-wise gaps intersected with span-wise gaps. These observations suggest that employing more evenly sized, square-like prism textures may lead to a more uniform distribution of turbulent stresses, potentially enhancing their effectiveness in preventing fouling settlement.

Hydrodynamic forces acting on a simplified model of an organism placed in three distinct regions (within and above the texture) of a stream-wise texture with a plane area density of $\lambda_p = 0.457$ were examined. The primary goal was to analyze the forces exerted on an organism during the initial stage of settlement. The obtained results were then compared with the scenario where the organism was positioned on a smooth wall. The organism locations were as follows: A, positioned in the centre of a crest plane texture element. B, positioned at the bottom wall and in the middle of stream-wise gaps, and C, positioned at the bottom wall and in the middle of a span-wise gap. The height of the organism was maintained at a value lower than $y^+ = 5$, when scaled with the units of the smooth wall. It was found that:

- The presence of the prism-like texture leads to a significant increase of approximately 44% in stream-wise drag due to elevated dispersive stress behind the texture. It was observed that dispersive shear stress predominantly affected the mean component of the hydrodynamic forces. This underscored the pivotal role of Reynolds stress in governing the fluctuation intensity of hydrodynamic forces experienced by organisms situated near the bottom walls.
- The study showed that the stream-wise oriented sharp edges of the prism texture induced span-wise eddy shedding, resulting in a nearly two-fold enhancement in span-wise force intensity compared to the smooth wall scenario.
- The computation of the total forces and their intensity, acting on the organism, showed that the texture presence reduced the intensity of hydrodynamic forces exerted on the organism when compared with its position on a smooth wall.
- At positions C and A, the organism model displayed increments in mean hydrodynamic forces of around 60% and 11%, respectively, whereas position B experienced a 6% reduction. Moreover, positions A and C showed an almost

25% increase in instantaneous forces, while position B exhibited negligible discernible variation.

10.1 Future work

The following recommendations are proposed for additional research to improve the state-of-the-art understanding of the impact of surface textures on the flow of turbulence and their potential impact on biofouling organisms.

- This study focused on gaps that were aligned and perpendicular to the freestream direction. It remains to be determined how turbulent stresses are influenced by the angle formed between the textures and the flow direction.
- Investigate the impact of fully square-shaped roughness elements on the distribution of dispersive stresses within textures.
- Given that marine species have deformable skin features, it would be useful to explore whether fluid structure interactions can modify stress distributions in a significant way.
- Similarly, it would be useful to study both deformable and moving organisms to understand how the structure of the organism may respond to fluctuating stresses.
- Given that marine species enjoy curvy ridges rather than sharp edges, it would be useful to explore the impact of curvy ridge geometry on the distribution of dispersive stresses.

Appendix A

Celik LES Index Quality

Verifying the accuracy of a Large Eddy Simulation (LES) can be challenging due to the interdependence of both numerical diffusion errors and sub-grid scale modelling errors on the mesh resolution, as pointed out by Celik in their work [194]. The impact of large turbulent scales on turbulent activity in the vicinity of roughened walls has been established in studies by [134], [137]. To address this concern, Celik[194] introduced the quality of the Celik LES index in the same work of 2005. This index offers a metric that indicates the proportion of turbulent kinetic energy that the LES method can resolve. For practical engineering applications, a recommended index value greater than 0.8 is recommended. The equation used for calculating these index values is given as follows:

$$LESIQ = \frac{1}{1 + 0.05\left[\frac{(\nu + \nu_{sgs})}{\nu}\right]^{0.53}} \quad (\text{A.1})$$

Here, ν stands for the kinematic eddy viscosity of the flow, while ν_{sgs} represents the eddy viscosity associated with the sub-grid model.

The formula (A.1) is employed to compute LESIQ for the simulated textured flows. The LESIQ values across the simulated textures are illustrated in Figs. A.1 through A.5. It's evident that the range of LESIQ values falls between 0.93 to 0.95, which indicates a favourable outcome compared to the proposed minimum threshold of 0.8 by [194]. This range is narrower than the findings of [139], potentially attributed to the fact that a different LES method, the WALE method (WALE method [195]) has been used.

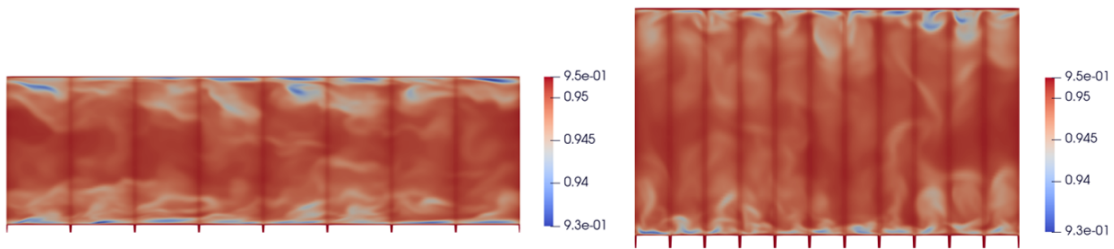


Figure A.1: LESIQ for $\lambda_p = 0.88$, [Left]: Stream-wise view, [Right]: Span-wise view.

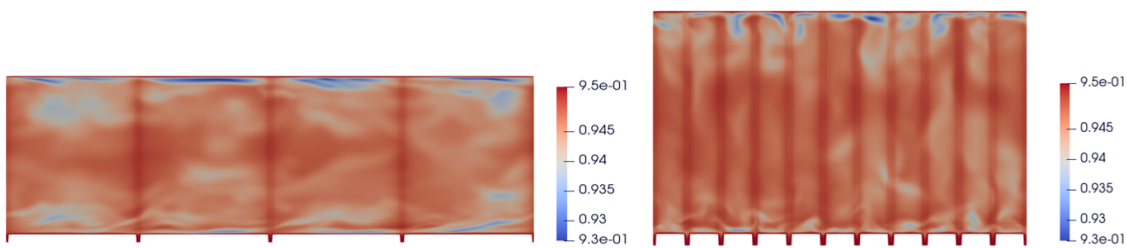


Figure A.2: LESIQ for $\lambda_p = 0.77$, [Left]: Stream-wise view, [Right]: Span-wise view.

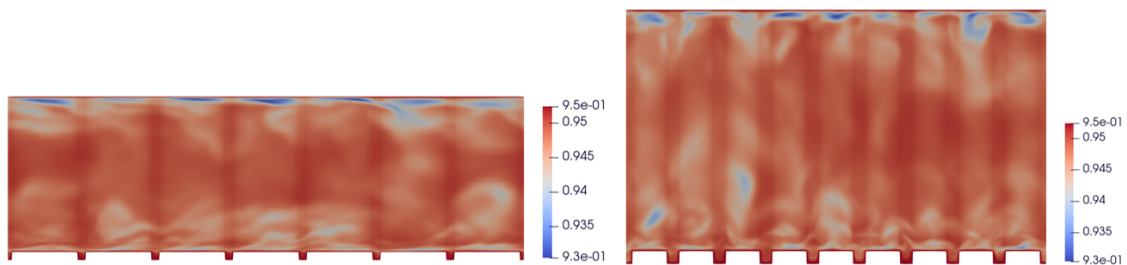


Figure A.3: LESIQ for $\lambda_p = 0.64$, [Left]: Stream-wise view, [Right]: Span-wise view.

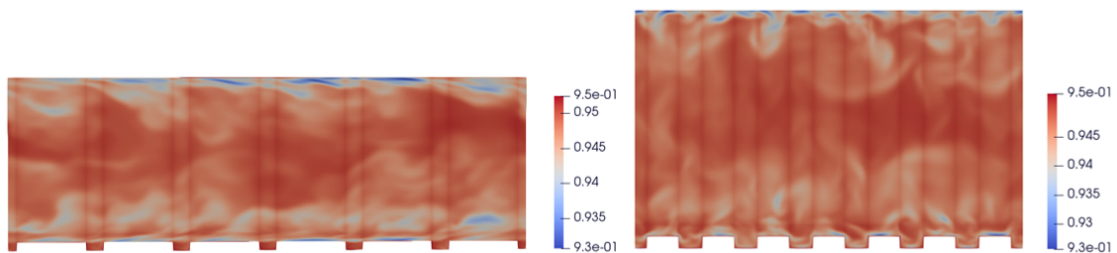


Figure A.4: LESIQ for $\lambda_p = 0.457$, [Left]: Stream-wise view, [Right]: Span-wise view.

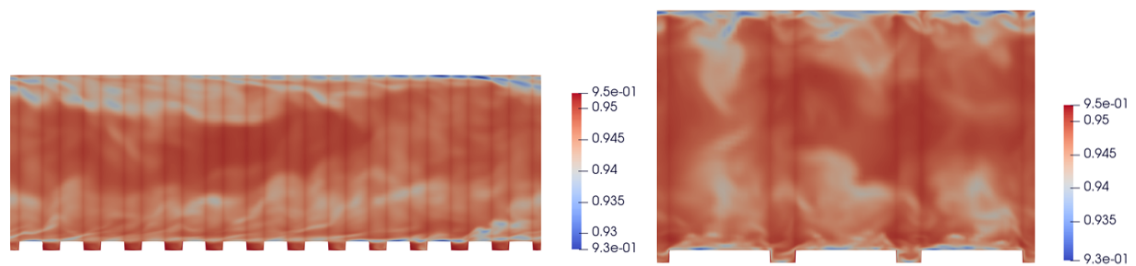


Figure A.5: LESIQ for $\lambda_p = 0.457$, [Left]: Stream-wise view, [Right]: Span-wise view.

Appendix B

Definition of the Statistical Quantities

This appendix contains definitions used for statistical measures employed in this thesis. Every quantity can be decomposed into a sum of its mean value, with the variations from this mean referred to as fluctuation. This concept is illustrated in Eq. (B.1).

$$\phi(x, t) = \langle \bar{\phi} \rangle + \phi' + \tilde{\phi} \quad (\text{B.1})$$

The symbols $\langle \phi \rangle$ and $\bar{\phi}$ represent spatial and temporal averages of ϕ , while ϕ' and $\tilde{\phi}$ denote fluctuations in both time and space, respectively. Temporal and spatial averaging procedures are described in the following sections.

B.1 Temporal averaging

Based on the definition, the time average of the quantity ϕ could be calculated as follows:

$$\overline{\phi(x, t)} = \lim_{T \rightarrow +\infty} \frac{1}{T} \int_0^T \phi(x, t) dt \quad (\text{B.2})$$

In Eq. (B.2), the time T used for averaging should significantly be larger than the largest time scale of the turbulent flow problem. For the textured turbulent flow cases examined in this study, the time averages were conducted over approximately 200-400 timescales of T , where T represents the necessary time for a flow particle to travel the stream-wise length of the channel. This amount of averaging time was crucial in establishing a linear correlation for the Reynolds stress diagram in the outer-layer flow.

For discrete time-step scenarios, the subsequent series can be employed to approxi-

mate the mean value.

$$\overline{\phi(x, t)} \approx \overline{\phi(x, t)}_N = \frac{1}{N} \sum_{n=0}^N \phi(x, t_n) \quad (\text{B.3})$$

Where N is the total number of time steps, $t_n = t_0 + n\Delta t$. Utilizing Eq. (B.3) to compute the mean value requires a substantial computational capacity to store data from N time steps. Alternatively, the average is progressively computed at each simulation time step by updating the ongoing estimate of the mean using the following equation.

$$\overline{\phi(x, t)}_{n+1} = \frac{\phi(x, t_{n+1}) + n\overline{\phi(x, t)}_n}{n+1} \quad (\text{B.4})$$

B.2 Spatial averaging

The spatial heterogeneity of turbulent flow around roughened walls remains significant even when considering time-averaging. This spatial heterogeneity gives rise to additional turbulent stress known as dispersive stress. To compute these stress effects, it is necessary to perform spatial averaging subsequent to time averaging. This spatial averaging is conducted within sufficiently large thin horizontal planes perpendicular to the wall in the $x \times z$ direction.

$$\langle \phi \rangle = \frac{1}{L_x L_z} \int_0^{L_x} \int_0^{L_z} \phi(x, t) dx dy \quad (\text{B.5})$$

Here, L_x and L_z represent the longitudinal and transverse length scales of the computational area. Employing spatial averaging for variables, when feasible, expedites the convergence of statistical results.

B.3 Higher order of statistics

In this thesis, skewness (S_u) and flatness (F_u) serve as indicators of the turbulent fluxes direction of the flow and turbulent intermittency, respectively. These metrics are derived from the second, third, and fourth statistical moments, and their expressions are as follows:

$$\mu_2(\phi) = \overline{\phi'^2} = \overline{(\phi - \bar{\phi})^2} = \overline{\phi^2} - \bar{\phi}^2 \quad (\text{B.6})$$

$$\mu_3(\phi) = \overline{\phi'^3} = \overline{(\phi - \bar{\phi})^3} = \overline{\phi^3} - 3\overline{\phi^2} \bar{\phi} + 2\bar{\phi}^3 \quad (\text{B.7})$$

$$\mu_4(\phi) = \overline{\phi'^4} = \overline{(\phi - \bar{\phi})^4} = \overline{\phi^4} - 4\overline{\phi^3} \bar{\phi} + 6\overline{\phi^2} \bar{\phi}^2 - 3\bar{\phi}^4 \quad (\text{B.8})$$

Here, ϕ and $\bar{\phi}$ represent the instantaneous and time-averaged magnitudes of ϕ , respectively. The aforementioned equations are employed to establish the definitions of skewness and flatness as depicted below:

$$S_{\phi} = \frac{\mu_3(\phi)}{\phi^2^{3/2}} \quad (\text{B.9})$$

$$F_{\phi} = \frac{\mu_4(\phi)}{\phi^2^2} \quad (\text{B.10})$$

Appendix C

Definition of Quadrant Analysis Variables and Higher Order Statistics in OpenFOAM

To calculate the quadrant analysis and higher-order statistics terms, codes are incorporated at the end of each Pimple loop in the PimpleFOAM solver. The added codes are shown as follows.

Listing C.1: PimpleFOAM solver with added snippet code for quadrant analysis and high-order statistics computation.

```
/*-----  
-----*\  
=====  
\\      /  F i e l d      | OpenFOAM: The Open Source CFD  
  Toolbox  
\\      /  O p e r a t i o n      | Website:  https://openfoam.org  
  \\    /    A n d      | Copyright (C) 2011-2018  
      OpenFOAM Foundation  
  \\/      M a n i p u l a t i o n      |  
-----  
-----  
License  
  This file is part of OpenFOAM.  
  
  OpenFOAM is free software: you can redistribute it and/or  
  modify it  
  under the terms of the GNU General Public License as  
  published by  
  the Free Software Foundation, either version 3 of the
```



```
License, or
(at your option) any later version.

OpenFOAM is distributed in the hope that it will be
useful, but WITHOUT
ANY WARRANTY; without even the implied warranty of
MERCHANTABILITY or
FITNESS FOR A PARTICULAR PURPOSE. See the GNU General
Public License
for more details.

You should have received a copy of the GNU General Public
License
along with OpenFOAM. If not, see <http://www.gnu.org/
licenses/>.
```

Application

```
pimpleFoam
```

Description

```
Transient solver for incompressible, turbulent flow of
Newtonian fluids,
with optional mesh motion and mesh topology changes.
```

```
Turbulence modelling is generic, i.e. laminar, RAS or LES
may be selected.
```

```
\*-----
-----*/
```

```
#include "fvCFD.H"
#include "dynamicFvMesh.H"
#include "singlePhaseTransportModel.H"
#include "turbulentTransportModel.H"
#include "pimpleControl.H"
#include "CorrectPhi.H"
#include "fvOptions.H"
```

```
// * * * * *
```

```
int main(int argc, char *argv[])
{
    #include "postProcess.H"

    #include "setRootCaseLists.H"
    #include "createTime.H"
    #include "createDynamicFvMesh.H"
    #include "initContinuityErrs.H"
    #include "createDyMControls.H"
    #include "createFields.H"
    #include "createUfIfPresent.H"
    #include "CourantNo.H"
    #include "setInitialDeltaT.H"

    turbulence->validate();

    // * * * * *

    Info<< "\nStarting time loop\n" << endl;

    while (runTime.run())
    {
        #include "readDyMControls.H"
        #include "CourantNo.H"
        #include "setDeltaT.H"

        runTime++;

        Info<< "Time = " << runTime.timeName() << nl << endl;

        // --- Pressure-velocity PIMPLE corrector loop
        while (pimple.loop())
        {
            if (pimple.firstIter() || moveMeshOuterCorrectors
                )
            {
                mesh.update();

                if (mesh.changing())
                {
```

```
MRF.update();

if (correctPhi)
{
    // Calculate absolute flux
    // from the mapped surface velocity
    phi = mesh.Sf() & Uf();

    #include "correctPhi.H"

    // Make the flux relative to the mesh
    // motion
    fvc::makeRelative(phi, U);
}

if (checkMeshCourantNo)
{
    #include "meshCourantNo.H"
}
}

#include "UEqn.H"

// --- Pressure corrector loop
while (pimple.correct())
{
    #include "pEqn.H"
}

if (pimple.turbCorr())
{
    laminarTransport.correct();
    turbulence->correct();
}

}

// higher order statistic computation codes

vort=fvc::curl(U);
```

```
mu3_u = (U.component(2)-UMean.component(2))* (U.  
    component(2)-UMean.component(2))*(U.component(2)-  
    UMean.component(2));  
mu3_v = (U.component(1)-UMean.component(1))* (U.  
    component(1)-UMean.component(1))*(U.component(1)-  
    UMean.component(1));  
mu3_w = (U.component(0)-UMean.component(0))* (U.  
    component(0)-UMean.component(0))*(U.component(0)-  
    UMean.component(0));  
mu4_u = (U.component(2)-UMean.component(2))* (U.  
    component(2)-UMean.component(2))*(U.component(2)-  
    UMean.component(2))*(U.component(2)-UMean.component  
    (2));  
mu4_v = ((U.component(1)-UMean.component(1))* (U.  
    component(1)-UMean.component(1))*(U.component(1)-  
    UMean.component(1))*(U.component(1)-UMean.component  
    (1)));  
mu4_w = ((U.component(0)-UMean.component(0))* (U.  
    component(0)-UMean.component(0))*(U.component(0)-  
    UMean.component(0))*(U.component(0)-UMean.component  
    (0)));  
u3 = (U.component(2)-UMean.component(2))*(U.component  
    (2)-UMean.component(2))*(U.component(2)-UMean.  
    component(2));  
v3 = (U.component(1)-UMean.component(1))*(U.component  
    (1)-UMean.component(1))*(U.component(1)-UMean.  
    component(1));  
u2v = (U.component(2)-UMean.component(2))*(U.component  
    (2)-UMean.component(2))*(U.component(1)-UMean.  
    component(1));  
uv2 = (U.component(1)-UMean.component(1))*(U.component  
    (2)-UMean.component(2))*(U.component(1)-UMean.  
    component(1));  
  
//Quadrant analysis terms computation codes  
  
forAll(U ,cellI)  
{  
  
    if ((U[cellI].component(2)-UMean[cellI].component(2))
```

```
>0 && (U[cellI].component(1)-UMean[cellI].component
(1))>0)
{
    Q_1 [cellI]= (U[cellI].component(2)-UMean[cellI].
        component(2)) * (U[cellI].component(1)-UMean[
        cellI].component(1));
    Q_2 [cellI] = 0;
    Q_3 [cellI] = 0;
    Q_4 [cellI] = 0;

}

else if ((U[cellI].component(2)-UMean[cellI].
    component(2))<0 && (U[cellI].component(1)-UMean[
    cellI].component(1))>0)
{
    Q_2 [cellI]= (U[cellI].component(2)-UMean[cellI].
        component(2)) * (U[cellI].component(1)-UMean[
        cellI].component(1));
    Q_1 [cellI] = 0;
    Q_3 [cellI] = 0;
    Q_4 [cellI] = 0;
}

else if ((U[cellI].component(2)-UMean[cellI].
    component(2))<0 && (U[cellI].component(1)-UMean[
    cellI].component(1))<0)
{
    Q_3 [cellI]= (U[cellI].component(2)-UMean[cellI].
        component(2)) * (U[cellI].component(1)-UMean[
        cellI].component(1));
    Q_2 [cellI] = 0;
    Q_1 [cellI] = 0;
    Q_4 [cellI] = 0;
}

else
{
    Q_4 [cellI]= (U[cellI].component(2)-UMean[cellI].
        component(2)) * (U[cellI].component(1)-UMean[
        cellI].component(1));
    Q_2 [cellI] = 0;
```

```
        Q_3 [cellI] = 0;
        Q_1 [cellI] = 0;
    }

}

runTime.write();

Info<< "ExecutionTime = " << runTime.elapsedCpuTime()
    << " s"
    << "   ClockTime = " << runTime.elapsedClockTime()
    << " s"
    << nl << endl;
}

Info<< "End\n" << endl;

return 0;
}

// *****
```

References

- [1] E. S. Poloczanska and A. J. Butler, “Biofouling and climate change,” *Biofouling*, pp. 333–347, 2010.
- [2] M. P. Schultz, “Effects of coating roughness and biofouling on ship resistance and powering,” *Biofouling*, vol. 23, no. 5, pp. 331–341, 2007.
- [3] C. C. Stringer and B. L. Polagye, “Implications of biofouling on cross-flow turbine performance,” *SN Applied Sciences*, vol. 2, pp. 1–13, 2020.
- [4] M. P. Schultz, J. Bendick, E. Holm, and W. Hertel, “Economic impact of biofouling on a naval surface ship,” *Biofouling*, vol. 27, no. 1, pp. 87–98, 2011.
- [5] C. M. Kirschner and A. B. Brennan, “Bio-inspired antifouling strategies,” *Annual review of materials research*, vol. 42, pp. 211–229, 2012.
- [6] A. Scardino, E. Harvey, and R. De Nys, “Testing attachment point theory: Diatom attachment on microtextured polyimide biomimics,” *Biofouling*, vol. 22, no. 1, pp. 55–60, 2006.
- [7] A. Scardino, J. Guenther, and R. De Nys, “Attachment point theory revisited: The fouling response to a microtextured matrix,” *Biofouling*, vol. 24, no. 1, pp. 45–53, 2008.
- [8] D. Bechert, M. Bruse, W. v. Hage, J. T. Van der Hoeven, and G. Hoppe, “Experiments on drag-reducing surfaces and their optimization with an adjustable geometry,” *Journal of fluid mechanics*, vol. 338, pp. 59–87, 1997.
- [9] D. Bechert, M. Bruse, and W. Hage, “Experiments with three-dimensional riblets as an idealized model of shark skin,” *Experiments in fluids*, vol. 28, no. 5, pp. 403–412, 2000.
- [10] Y. Huang, Y. Zheng, J. Li, *et al.*, “Enhancing microalgae biofilm formation and growth by fabricating microgrooves onto the substrate surface,” *Bioresource technology*, vol. 261, pp. 36–43, 2018.
- [11] G. Zilman, J. Novak, and Y. Benayahu, “How do larvae attach to a solid in a laminar flow?” *Marine biology*, vol. 154, pp. 1–26, 2008.

- [12] K. D. Esmerlyan, I. A. Avramova, C. E. Castano, *et al.*, “Early stage anti-bioadhesion behavior of superhydrophobic soot based coatings towards *Pseudomonas putida*,” *Materials & Design*, vol. 160, pp. 395–404, 2018.
- [13] C. Richards, “Marine inspired design for antifouling technology,” Ph.D. dissertation, Dublin City University, 2022.
- [14] C. Hellio and D. Yebra, *Advances in Marine Antifouling Coatings and Technologies*. May 2009, ISBN: Woodhead Publishing, Cambridge.
- [15] M. Otani, T. Oumi, S. Uwai, *et al.*, “Occurrence and diversity of barnacles on international ships visiting Osaka Bay, Japan, and the risk of their introduction,” *Biofouling*, vol. 23, no. 4, pp. 277–286, 2007.
- [16] S. Song, Y. K. Demirel, M. Atlar, and W. Shi, “Prediction of the fouling penalty on the tidal turbine performance and development of its mitigation measures,” *Applied Energy*, vol. 276, p. 115498, 2020.
- [17] M. D., “Ocean energy - technology development report 2020,” no. KJ-BK-21-007-EN-N (online), KJ-BK-21-007-EN-C (print), 2020, ISSN: 1831-9424 (online), 1018-5593 (print), 2600-0466 (online) 2600-0458 (print).
- [18] J. Loxton, A. Macleod, C. R. Nall, *et al.*, “Setting an agenda for biofouling research for the marine renewable energy industry,” *International journal of marine energy*, vol. 19, pp. 292–303, 2017.
- [19] E. Almeida, T. C. Diamantino, and O. de Sousa, “Marine paints: The particular case of antifouling paints,” *Progress in organic coatings*, vol. 59, no. 1, pp. 2–20, 2007.
- [20] A. M. Rouhi, “The squeeze on tributyltins,” *Chemical & Engineering News*, vol. 76, no. 17, pp. 41–42, 1998.
- [21] J. A. Callow and M. E. Callow, “Trends in the development of environmentally friendly fouling-resistant marine coatings,” *Nature communications*, vol. 2, no. 1, p. 244, 2011.
- [22] A. Jain and N. B. Bhosle, “Biochemical composition of the marine conditioning film: Implications for bacterial adhesion,” *Biofouling*, vol. 25, no. 1, pp. 13–19, 2009.
- [23] N. Aldred, A. Scardino, A. Cavaco, R. de Nys, and A. S. Clare, “Attachment strength is a key factor in the selection of surfaces by barnacle cyprids (*Balanus amphitrite*) during settlement,” *Biofouling*, vol. 26, no. 3, pp. 287–299, 2010.
- [24] B. T. Nedved and M. G. Hadfield, “*Hydroides elegans* (annelida: Polychaeta): A model for biofouling research,” in Springer, 2008.

- [25] A. J. Scardino and R. de Nys, “Mini review: Biomimetic models and bioinspired surfaces for fouling control,” *Biofouling*, vol. 27, no. 1, pp. 73–86, 2011.
- [26] F. E. Fish and C. A. Hui, “Dolphin swimming—a review,” *Mammal Review*, vol. 21, no. 4, pp. 181–195, 1991.
- [27] C. Baum, W. Meyer, R. Stelzer, L.-G. Fleischer, and D. Siebers, “Average nanorough skin surface of the pilot whale (*globicephala melas*, delphinidae): Considerations on the self-cleaning abilities based on nanoroughness,” *Marine Biology*, vol. 140, pp. 653–657, 2002.
- [28] X. Cao, “Interaction of zoospores of the green alga *ulva* with bioinspired micro- and nanostructured surfaces prepared by polyelectrolyte layer-by-layer self-assembly,” *Advanced Functional Materials*, 2010.
- [29] A. Lang, P. Motta, P. Hidalgo, and M. Westcott, “Bristled shark skin: A microgeometry for boundary layer control?” *Bioinspiration & biomimetics*, vol. 3, no. 4, p. 046 005, 2008.
- [30] J. F. Schumacher, M. L. Carman, T. G. Estes, *et al.*, “Engineered antifouling microtopographies—effect of feature size, geometry, and roughness on settlement of zoospores of the green alga *ulva*,” *Biofouling*, vol. 23, no. 1, pp. 55–62, 2007.
- [31] C. M. Magin, C. J. Long, S. P. Cooper, L. K. Ista, G. P. López, and A. B. Brennan, “Engineered antifouling microtopographies: The role of reynolds number in a model that predicts attachment of zoospores of *ulva* and cells of *cobetia marina*,” *Biofouling*, vol. 26, no. 6, pp. 719–727, 2010.
- [32] J. F. Schumacher, N. Aldred, M. E. Callow, *et al.*, “Species-specific engineered antifouling topographies: Correlations between the settlement of algal zoospores and barnacle cyprids,” *Biofouling*, vol. 23, no. 5, pp. 307–317, 2007.
- [33] M. L. Carman, T. G. Estes, A. W. Feinberg, *et al.*, “Engineered antifouling microtopographies—correlating wettability with cell attachment,” *Biofouling*, vol. 22, no. 1, pp. 11–21, 2006.
- [34] M. E. Callow, A. R. Jennings, A. Brennan, *et al.*, “Microtopographic cues for settlement of zoospores of the green fouling alga *enteromorpha*,” *Biofouling*, vol. 18, no. 3, pp. 229–236, 2002.
- [35] J. Köhler, P. Hansen, and M. Wahl, “Colonization patterns at the substratum-water interface: How does surface microtopography influence recruitment patterns of sessile organisms?” *Biofouling*, vol. 14, no. 3, pp. 237–248, 1999.

- [36] L. Hoipkemeier-Wilson, J. F. Schumacher, M. L. Carman, *et al.*, “Antifouling potential of lubricious, micro-engineered, pdms elastomers against zoospores of the green fouling alga ulva (enteromorpha),” *Biofouling*, vol. 20, no. 1, pp. 53–63, 2004.
- [37] A. Scardino and R. de Nys, “Fouling deterrence on the bivalve shell mytilus galloprovincialis: A physical phenomenon?” *Biofouling*, vol. 20, no. 4-5, pp. 249–257, 2004.
- [38] A. V. Bers and M. Wahl, “The influence of natural surface microtopographies on fouling,” *Biofouling*, vol. 20, no. 1, pp. 43–51, 2004.
- [39] L. Granhag, J. Finlay, P. Jonsson, J. Callow, and M. Callow, “Roughness-dependent removal of settled spores of the green alga ulva (syn. enteromorpha) exposed to hydrodynamic forces from a water jet,” *Biofouling*, vol. 20, no. 2, pp. 117–122, 2004.
- [40] Š. Petronis, K. Berntsson, J. Gold, and P. Gatenholm, “Design and microstructuring of pdms surfaces for improved marine biofouling resistance,” *Journal of biomaterials science, polymer edition*, vol. 11, no. 10, pp. 1051–1072, 2000.
- [41] C. J. Long, J. F. Schumacher, P. A. Robinson, *et al.*, “A model that predicts the attachment behavior of ulva linza zoospores on surface topography,” *Biofouling*, vol. 26, no. 4, pp. 411–419, 2010.
- [42] J. Bico, U. Thiele, and D. Quéré, “Wetting of textured surfaces,” *Colloids and Surfaces A: Physicochemical and Engineering Aspects*, vol. 206, no. 1-3, pp. 41–46, 2002.
- [43] D. Qu *et al.*, “Wetting and roughness,” *Annu. Rev. Mater. Res.*, vol. 38, p. 99, 2008.
- [44] R. E. Baier, “Surface behaviour of biomaterials: The theta surface for biocompatibility,” *Journal of Materials Science: Materials in Medicine*, vol. 17, no. 11, pp. 1057–1062, 2006.
- [45] R. N. Wenzel, “Resistance of solid surfaces to wetting by water,” *Industrial & Engineering Chemistry*, vol. 28, no. 8, pp. 988–994, 1936.
- [46] C. M. Magin, J. A. Finlay, G. Clay, M. E. Callow, J. A. Callow, and A. B. Brennan, “Antifouling performance of cross-linked hydrogels: Refinement of an attachment model,” *Biomacromolecules*, vol. 12, no. 4, pp. 915–922, 2011.
- [47] A. Cassie and S. Baxter, “Wettability of porous surfaces,” *Transactions of the Faraday society*, vol. 40, pp. 546–551, 1944.

- [48] S. P. Cooper, J. A. Finlay, G. Cone, M. E. Callow, J. A. Callow, and A. B. Brennan, “Engineered antifouling microtopographies: Kinetic analysis of the attachment of zoospores of the green alga *Ulva* to silicone elastomers,” *Biofouling*, vol. 27, no. 8, pp. 881–892, 2011.
- [49] J. A. Finlay, S. Krishnan, M. E. Callow, *et al.*, “Settlement of *Ulva* zoospores on patterned fluorinated and pegylated monolayer surfaces,” *Langmuir*, vol. 24, no. 2, pp. 503–510, 2008.
- [50] T. Kim, S. Kwon, J. Lee, J. S. Lee, and S. Kang, “A metallic anti-biofouling surface with a hierarchical topography containing nanostructures on curved micro-riblets,” *Microsystems & Nanoengineering*, vol. 8, no. 1, p. 6, 2022.
- [51] S. L. Pagliolico, V. R. L. Verso, F. Bosco, C. Mollea, and C. La Forgia, “A novel photo-bioreactor application for microalgae production as a shading system in buildings,” *Energy Procedia*, vol. 111, pp. 151–160, 2017.
- [52] M. Krsmanovic, D. Biswas, H. Ali, A. Kumar, R. Ghosh, and A. K. Dickerson, “Hydrodynamics and surface properties influence biofilm proliferation,” *Advances in Colloid and Interface Science*, vol. 288, p. 102336, 2021.
- [53] F. M. White and J. Majdalani, *Viscous fluid flow*. McGraw-Hill New York, 2006, vol. 3.
- [54] J. P. Crimaldi, J. K. Thompson, J. H. Rosman, R. J. Lowe, and J. R. Koseff, “Hydrodynamics of larval settlement: The influence of turbulent stress events at potential recruitment sites,” *Limnology and Oceanography*, vol. 47, no. 4, pp. 1137–1151, 2002.
- [55] J. E. Eckman, “A model of passive settlement by planktonic larvae onto bottoms of differing roughness,” *Limnology and oceanography*, vol. 35, no. 4, pp. 887–901, 1990.
- [56] P.-Å. Krogstad, R. Antonia, and L. Browne, “Comparison between rough- and smooth-wall turbulent boundary layers,” *Journal of Fluid Mechanics*, vol. 245, pp. 599–617, 1992.
- [57] M. Koehl, “Mini review: Hydrodynamics of larval settlement into fouling communities,” *Biofouling*, vol. 23, no. 5, pp. 357–368, 2007.
- [58] A. Abelson and M. Denny, “Settlement of marine organisms in flow,” *Annual Review of Ecology and Systematics*, vol. 28, no. 1, pp. 317–339, 1997.
- [59] P. R. Jonsson, C. André, and M. Lindegarh, “Swimming behaviour of marine bivalve larvae in a flume boundary-layer flow: Evidence for near-bottom confinement,” *Marine Ecology Progress Series*, pp. 67–76, 1991.

- [60] L. Mullineaux and E. Garland, “Larval recruitment in response to manipulated field flows,” *Marine Biology*, vol. 116, pp. 667–683, 1993.
- [61] M. L. Judge and S. F. Craig, “Positive flow dependence in the initial colonization of a fouling community: Results from in situ water current manipulations,” *Journal of Experimental Marine Biology and Ecology*, vol. 210, no. 2, pp. 209–222, 1997.
- [62] P.-Y. Qian, D. Rittschof, and B. Sreedhar, “Macrofouling in unidirectional flow: Miniature pipes as experimental models for studying the interaction of flow and surface characteristics on the attachment of barnacle, bryozoan and polychaete larvae,” *Marine Ecology Progress Series*, vol. 207, pp. 109–121, 2000.
- [63] M. Lindegarth, P. R. Jonsson, and C. André, “Physical and numerical modeling of the role of hydrodynamic processes on adult-larval interactions of a suspension-feeding bivalve,” *Journal of marine research*, vol. 60, no. 3, pp. 499–516, 2002.
- [64] S. A. Woodin, “Recruitment of infauna: Positive or negative cues?” *American Zoologist*, vol. 31, no. 6, pp. 797–807, 1991.
- [65] M. N. Tamburri, C. M. Finelli, D. S. Wethey, and R. K. Zimmer-Faust, “Chemical induction of larval settlement behavior in flow,” *The Biological Bulletin*, vol. 191, no. 3, pp. 367–373, 1996.
- [66] C. M. Finelli and D. S. Wethey, “Behavior of oyster (*crassostrea virginica*) larvae in flume boundary layer flows,” *Marine Biology*, vol. 143, pp. 703–711, 2003.
- [67] L. J. Walters and D. S. Wethey, “Settlement and early post-settlement survival of sessile marine invertebrates on topographically complex surfaces: The importance of refuge dimensions and adult morphology,” *Marine Ecology Progress Series*, vol. 137, pp. 161–171, 1996.
- [68] A. I. Larsson and P. R. Jonsson, “Barnacle larvae actively select flow environments supporting post-settlement growth and survival,” *Ecology*, vol. 87, no. 8, pp. 1960–1966, 2006.
- [69] M. Menesses, J. Belden, N. Dickenson, and J. Bird, “Measuring a critical stress for continuous prevention of marine biofouling accumulation with aeration,” *Biofouling*, vol. 33, no. 9, pp. 703–711, 2017.
- [70] T. R. Scheuerman, A. K. Camper, and M. A. Hamilton, “Effects of substratum topography on bacterial adhesion,” *Journal of colloid and interface science*, vol. 208, no. 1, pp. 23–33, 1998.

- [71] M. Armandei and A. C. Fernandes, “Marine current energy extraction through buffeting,” *International Journal of Marine Energy*, vol. 14, pp. 52–67, 2016.
- [72] J. Orme, I. Masters, and R. Griffiths, “Investigation of the effect of biofouling on the efficiency of marine current turbines,” in *Proc. MAREC*, vol. 2001, 2001, pp. 91–99.
- [73] J. M. Walker, K. A. Flack, E. E. Lust, M. P. Schultz, and L. Luznik, “Experimental and numerical studies of blade roughness and fouling on marine current turbine performance,” *Renewable Energy*, vol. 66, pp. 257–267, 2014.
- [74] A. Rivier, A.-C. Bennis, G. Jean, and J.-C. Dauvin, “Numerical simulations of biofouling effects on the tidal turbine hydrodynamic,” *International Marine Energy Journal*, vol. 1, no. 2, pp. 101–109, 2018.
- [75] R. Howell, N. Qin, J. Edwards, and N. Durrani, “Wind tunnel and numerical study of a small vertical axis wind turbine,” *Renewable energy*, vol. 35, no. 2, pp. 412–422, 2010.
- [76] P. Bachant and M. Wosnik, “Effects of reynolds number on the energy conversion and near-wake dynamics of a high solidity vertical-axis cross-flow turbine,” *Energies*, vol. 9, no. 2, p. 73, 2016.
- [77] Y. K. Demirel, M. Khorasanchi, O. Turan, A. Incecik, and M. P. Schultz, “A cfd model for the frictional resistance prediction of antifouling coatings,” *Ocean Engineering*, vol. 89, pp. 21–31, 2014.
- [78] Y. K. Demirel, O. Turan, and A. Incecik, “Predicting the effect of biofouling on ship resistance using cfd,” *Applied ocean research*, vol. 62, pp. 100–118, 2017.
- [79] A. Farkas, N. Degiuli, and I. Martić, “Towards the prediction of the effect of biofilm on the ship resistance using cfd,” *Ocean Engineering*, vol. 167, pp. 169–186, 2018.
- [80] S. Song, Y. K. Demirel, and M. Atlar, “An investigation into the effect of biofouling on the ship hydrodynamic characteristics using cfd,” *Ocean Engineering*, vol. 175, pp. 122–137, 2019.
- [81] D. Owen, Y. K. Demirel, E. Oguz, T. Tezdogan, and A. Incecik, “Investigating the effect of biofouling on propeller characteristics using cfd,” *Ocean Engineering*, vol. 159, pp. 505–516, 2018.
- [82] M. Acharya, J. Bornstein, and M. Escudier, “Turbulent boundary layers on rough surfaces,” *Experiments in Fluids*, vol. 4, pp. 33–47, 1986.

- [83] J. P. Bons, “St and cf augmentation for real turbine roughness with elevated freestream turbulence,” in *Turbo Expo: Power for Land, Sea, and Air*, vol. 36088, 2002, pp. 349–363.
- [84] P. M. Ligrani, M. M. Oliveira, and T. Blaskovich, “Comparison of heat transfer augmentation techniques,” *AIAA journal*, vol. 41, no. 3, pp. 337–362, 2003.
- [85] M. R. Raupach, R. A. Antonia, and S. Rajagopalan, “Rough-wall turbulent boundary layers,” 1991.
- [86] T. Ikeda and P. A. Durbin, “Direct simulations of a rough-wall channel flow,” *Journal of Fluid Mechanics*, vol. 571, pp. 235–263, 2007.
- [87] Z. Xie and I. P. Castro, “LES and RANS for turbulent flow over arrays of wall-mounted obstacles,” *Flow, Turbulence and Combustion*, vol. 76, no. 3, pp. 291–312, 2006.
- [88] S. B. Pope, *Turbulent flows*. Cambridge university press, 2000.
- [89] S. Kline, “The role of visualization in the study of the structure of the turbulent boundary layer,” *Coherent Structure of Turbulent Boundary Layers*, pp. 1–26, 1978.
- [90] K. A. Flack and M. P. Schultz, “Review of hydraulic roughness scales in the fully rough regime,” *Journal of fluids engineering*, vol. 132, no. 4, 2010.
- [91] J. Nikuradse, *Laws of flow in rough pipes, naca tech*, 1933.
- [92] C. F. Colebrook, T. Blench, H. Chatley, *et al.*, “Correspondence. turbulent flow in pipes, with particular reference to the transition region between the smooth and rough pipe laws.(includes plates).,” *Journal of the Institution of Civil engineers*, vol. 12, no. 8, pp. 393–422, 1939.
- [93] L. F. Moody, “Friction factors for pipe flow,” *Transactions of the American Society of Mechanical Engineers*, vol. 66, no. 8, pp. 671–678, 1944.
- [94] F. R. Hama, “Boundary layer characteristics for smooth and rough surfaces,” *Trans. Soc. Nav. Arch. Marine Engrs.*, vol. 62, pp. 333–358, 1954.
- [95] F. H. Clauser, “Turbulent boundary layers in adverse pressure gradients,” *Journal of the Aeronautical Sciences*, vol. 21, no. 2, pp. 91–108, 1954.
- [96] K. A. Flack and M. P. Schultz, “Roughness effects on wall-bounded turbulent flows,” *Physics of Fluids*, vol. 26, no. 10, p. 101305, 2014.
- [97] A. Townsend, *The structure of turbulent shear flow*. Cambridge university press, 1976.

- [98] M. Kadivar, D. Tormey, and G. McGranaghan, “A review on turbulent flow over rough surfaces: Fundamentals and theories,” *International Journal of Thermofluids*, vol. 10, p. 100 077, 2021.
- [99] A. E. Perry, W. H. Schofield, and P. N. Joubert, “Rough wall turbulent boundary layers,” *Journal of Fluid Mechanics*, vol. 37, no. 2, pp. 383–413, 1969.
- [100] R. Wooding, E. F. Bradley, and J. Marshall, “Drag due to regular arrays of roughness elements of varying geometry,” *Boundary-Layer Meteorology*, vol. 5, no. 3, pp. 285–308, 1973.
- [101] J. Jiménez, “Turbulent flows over rough walls,” *Annu. Rev. Fluid Mech.*, vol. 36, pp. 173–196, 2004.
- [102] P. M. Ligrani and R. J. Moffat, “Structure of transitionally rough and fully rough turbulent boundary layers,” *Journal of Fluid Mechanics*, vol. 162, pp. 69–98, 1986.
- [103] A. Thom, “Momentum absorption by vegetation,” *Quarterly Journal of the Royal Meteorological Society*, vol. 97, no. 414, pp. 414–428, 1971.
- [104] P. Jackson, “On the displacement height in the logarithmic velocity profile,” *Journal of fluid mechanics*, vol. 111, pp. 15–25, 1981.
- [105] M. Placidi and B. Ganapathisubramani, “Effects of frontal and plan solidities on aerodynamic parameters and the roughness sublayer in turbulent boundary layers,” *Journal of Fluid Mechanics*, vol. 782, pp. 541–566, 2015.
- [106] H. J. Koloseus and J. Davidian, *Free-surface Instability Correlations: And Roughness-concentration Effects on Flow Over Hydrodynamically Rough Surfaces*. US Government Printing Office, 1966.
- [107] H. Schlichting, *Experimental investigation of the problem of surface roughness*. National Advisory Committee for Aeronautics, 1937.
- [108] F. Dvorak, “Calculation of turbulent boundary layers on rough surfaces in pressure gradient.,” *AIAA journal*, vol. 7, no. 9, pp. 1752–1759, 1969.
- [109] D. Bettermann, “Contribution a l’etude de la convection forcee turbulente le long de plaques rugueuses,” *International Journal of Heat and Mass Transfer*, vol. 9, no. 3, pp. 153–164, 1966.
- [110] J. E. Danberg and A. Sigal, “Analysis of turbulent boundary-layer over rough surfaces with application to projectile aerodynamics,” Army Ballistic Research Lab Aberdeen Proving Ground MD, Tech. Rep., 1988.

- [111] A. Sigal and J. E. Danberg, “New correlation of roughness density effect on the turbulent boundary layer,” *AIAA journal*, vol. 28, no. 3, pp. 554–556, 1990.
- [112] J. A. Van Rij, B. Belnap, and P. Ligrani, “Analysis and experiments on three-dimensional, irregular surface roughness,” *J. Fluids Eng.*, vol. 124, no. 3, pp. 671–677, 2002.
- [113] D. Waigh and R. Kind, “Improved aerodynamic characterization of regular three-dimensional roughness,” *AIAA journal*, vol. 36, no. 6, pp. 1117–1119, 1998.
- [114] R. L. Simpson, “A generalized correlation of roughness density effects on the turbulent boundary layer.,” *AIAA Journal*, vol. 11, no. 2, pp. 242–244, 1973.
- [115] A. Musker, “Universal roughness functions for naturally-occurring surfaces,” *Transactions of the Canadian Society for Mechanical Engineering*, vol. 6, no. 1, pp. 1–6, 1980.
- [116] R. Garcia-Mayoral and J. Jiménez, “Drag reduction by riblets,” *Philosophical transactions of the Royal society A: Mathematical, physical and engineering Sciences*, vol. 369, no. 1940, pp. 1412–1427, 2011.
- [117] W. Reif and A. Dinkelacker, “Hydrodynamics of the squamation in fast swimming sharks,” *Neues Jahrbuch für Geologie und Paläontologie-Abhandlungen*, pp. 184–187, 1982.
- [118] F. Hama, “Some current problems in turbulent shear flows,” *Naval Hydrodynamics*, 1957.
- [119] S. J. Kline, W. C. Reynolds, F. Schraub, and P. Runstadler, “The structure of turbulent boundary layers,” *Journal of Fluid Mechanics*, vol. 30, no. 4, pp. 741–773, 1967.
- [120] M. Walsh and A. Lindemann, “Optimization and application of riblets for turbulent drag reduction,” in *22nd aerospace sciences meeting*, 1984, p. 347.
- [121] A. Ashrafian, H. I. Andersson, and M. Manhart, “Dns of turbulent flow in a rod-roughened channel,” *International Journal of Heat and Fluid Flow*, vol. 25, no. 3, pp. 373–383, 2004.
- [122] Y. Nagano, H. Hattori, and T. Houra, “Dns of velocity and thermal fields in turbulent channel flow with transverse-rib roughness,” *International Journal of Heat and Fluid Flow*, vol. 25, no. 3, pp. 393–403, 2004.
- [123] Y. Miyake, K. Tsujimoto, and N. Nagai, “Numerical simulation of channel flow with a rib-roughened wall,” *Journal of Turbulence*, vol. 3, no. 1, p. 035, 2002.

- [124] S. Leonardi, P. Orlandi, R. Smalley, L. Djenidi, and R. Antonia, “Direct numerical simulations of turbulent channel flow with transverse square bars on one wall,” *Journal of Fluid Mechanics*, vol. 491, pp. 229–238, 2003.
- [125] A. Grass, R. Stuart, and M. Mansour-Tehrani, “Common vortical structure of turbulent flows over smooth and rough boundaries,” *AIAA journal*, vol. 31, no. 5, pp. 837–847, 1993.
- [126] P.-Å. Krogstad and R. Antonia, “Structure of turbulent boundary layers on smooth and rough walls,” *Journal of Fluid Mechanics*, vol. 277, pp. 1–21, 1994.
- [127] J. Cui, V. C. Patel, and C.-L. Lin, “Large-eddy simulation of turbulent flow in a channel with rib roughness,” *International Journal of Heat and Fluid Flow*, vol. 24, no. 3, pp. 372–388, 2003.
- [128] L. Djenidi, R. Elavarasan, and R. Antonia, “The turbulent boundary layer over transverse square cavities,” *Journal of Fluid Mechanics*, vol. 395, pp. 271–294, 1999.
- [129] S. Leonardi, P. Orlandi, and R. A. Antonia, “Properties of d-and k-type roughness in a turbulent channel flow,” *Physics of fluids*, vol. 19, no. 12, p. 125 101, 2007.
- [130] S. Leonardi, E. Mostarda, P. Orlandi, and R. Antonia, “Budgets of reynolds stress in a rough wall channel flow,” in *Direct and Large-Eddy Simulation V: Proceedings of the fifth international ERCOFTAC Workshop on direct and large-eddy simulation held at the Munich University of Technology, August 27–29, 2003*, Springer, 2004, pp. 509–516.
- [131] P. Orlandi, S. Leonardi, R. Tuzi, and R. Antonia, “Direct numerical simulation of turbulent channel flow with wall velocity disturbances,” *Physics of Fluids*, vol. 15, no. 12, pp. 3587–3601, 2003.
- [132] P. Orlandi, S. Leonardi, and R. Antonia, “Turbulent channel flow with either transverse or longitudinal roughness elements on one wall,” *Journal of Fluid Mechanics*, vol. 561, pp. 279–305, 2006.
- [133] C. S. B. Grimmond and T. R. Oke, “Aerodynamic properties of urban areas derived from analysis of surface form,” *Journal of Applied Meteorology and Climatology*, vol. 38, no. 9, pp. 1262–1292, 1999.
- [134] M. Kanda, R. Moriwaki, and F. Kasamatsu, “Large-eddy simulation of turbulent organized structures within and above explicitly resolved cube arrays,” *Boundary-Layer Meteorology*, vol. 112, pp. 343–368, 2004.

- [135] P. Orlandi and S. Leonardi, “Dns of turbulent channel flows with two-and three-dimensional roughness,” *Journal of Turbulence*, no. 7, N73, 2006.
- [136] K. Bhaganagar, J. Kim, and G. Coleman, “Effect of roughness on wall-bounded turbulence,” *Flow, turbulence and combustion*, vol. 72, no. 2-4, pp. 463–492, 2004.
- [137] O. Coceal, T. G. Thomas, I. P. Castro, and S. E. Belcher, “Mean flow and turbulence statistics over groups of urban-like cubical obstacles,” *Boundary-Layer Meteorology*, vol. 121, pp. 491–519, 2006.
- [138] S. Leonardi and I. P. Castro, “Channel flow over large cube roughness: A direct numerical simulation study,” *Journal of Fluid Mechanics*, vol. 651, pp. 519–539, 2010.
- [139] D. Chatzikyriakou, J. Buongiorno, D. Caviezel, and D. Lakehal, “Dns and les of turbulent flow in a closed channel featuring a pattern of hemispherical roughness elements,” *International Journal of Heat and Fluid Flow*, vol. 53, pp. 29–43, 2015.
- [140] L. Chan, M. MacDonald, D. Chung, N. Hutchins, and A. Ooi, “A systematic investigation of roughness height and wavelength in turbulent pipe flow in the transitionally rough regime,” *Journal of Fluid Mechanics*, vol. 771, pp. 743–777, 2015.
- [141] X. I. Yang, J. Sadique, R. Mittal, and C. Meneveau, “Exponential roughness layer and analytical model for turbulent boundary layer flow over rectangular-prism roughness elements,” *Journal of Fluid Mechanics*, vol. 789, pp. 127–165, 2016.
- [142] R. M. Cionco, “A mathematical model for air flow in a vegetative canopy,” *Journal of Applied Meteorology and Climatology*, vol. 4, no. 4, pp. 517–522, 1965.
- [143] J. Sadique, X. I. Yang, C. Meneveau, and R. Mittal, “Aerodynamic properties of rough surfaces with high aspect-ratio roughness elements: Effect of aspect ratio and arrangements,” *Boundary-layer meteorology*, vol. 163, pp. 203–224, 2017.
- [144] M. MacDonald, L. Chan, D. Chung, N. Hutchins, and A. Ooi, “Turbulent flow over transitionally rough surfaces with varying roughness densities,” *Journal of Fluid Mechanics*, vol. 804, pp. 130–161, 2016.
- [145] D. Chung, L. Chan, M. MacDonald, N. Hutchins, and A. Ooi, “A fast direct numerical simulation method for characterising hydraulic roughness,” *Journal of Fluid Mechanics*, vol. 773, pp. 418–431, 2015.

- [146] O. El-Samni, H. Chun, and H. Yoon, “Drag reduction of turbulent flow over thin rectangular riblets,” *International Journal of Engineering Science*, vol. 45, no. 2-8, pp. 436–454, 2007.
- [147] A. Boomsma and F. Sotiropoulos, “Riblet drag reduction in mild adverse pressure gradients: A numerical investigation,” *International Journal of Heat and Fluid Flow*, vol. 56, pp. 251–260, 2015.
- [148] E. Napoli, V. Armenio, and M. De Marchis, “The effect of the slope of irregularly distributed roughness elements on turbulent wall-bounded flows,” *Journal of Fluid Mechanics*, vol. 613, pp. 385–394, 2008.
- [149] J. Cardillo, Y. Chen, G. Araya, J. Newman, K. Jansen, and L. Castillo, “Dns of a turbulent boundary layer with surface roughness,” *Journal of Fluid Mechanics*, vol. 729, pp. 603–637, 2013.
- [150] J. Yuan and U. Piomelli, “Estimation and prediction of the roughness function on realistic surfaces,” *Journal of Turbulence*, vol. 15, no. 6, pp. 350–365, 2014.
- [151] M. Thakkar, A. Busse, and N. Sandham, “Surface correlations of hydrodynamic drag for transitionally rough engineering surfaces,” *Journal of Turbulence*, vol. 18, no. 2, pp. 138–169, 2017.
- [152] A. Busse, M. Lützner, and N. D. Sandham, “Direct numerical simulation of turbulent flow over a rough surface based on a surface scan,” *Computers & Fluids*, vol. 116, pp. 129–147, 2015.
- [153] P. Forooghi, A. Stroh, P. Schlatter, and B. Frohnäpfel, “Direct numerical simulation of flow over dissimilar, randomly distributed roughness elements: A systematic study on the effect of surface morphology on turbulence,” *Physical Review Fluids*, vol. 3, no. 4, p. 044605, 2018.
- [154] S. Sarakinos and A. Busse, “An algorithm for the generation of biofouled surfaces for applications in marine hydrodynamics,” *Recent Advances in CFD for Wind and Tidal Offshore Turbines*, pp. 61–71, 2019.
- [155] J. Sadique, X. I. Yang, C. Meneveau, and R. Mittal, “Simulation of boundary layer flows over biofouled surfaces,” in *22nd AIAA Computational Fluid Dynamics Conference*, 2015, p. 2616.
- [156] G. Alfonsi, D. Ferraro, A. Lauria, and R. Gaudio, “Large-eddy simulation of turbulent natural-bed flow,” *Physics of Fluids*, vol. 31, no. 8, p. 085105, 2019.

- [157] M. De Marchis, D. Saccone, B. Milici, and E. Napoli, “Large eddy simulations of rough turbulent channel flows bounded by irregular roughness: Advances toward a universal roughness correlation,” *Flow, Turbulence and Combustion*, vol. 105, pp. 627–648, 2020.
- [158] T. Jelly, A. Ramani, B. Nugroho, N. Hutchins, and A. Busse, “Impact of spanwise effective slope upon rough-wall turbulent channel flow,” *Journal of Fluid Mechanics*, vol. 951, A1, 2022.
- [159] P. A. Davidson, *Turbulence: an introduction for scientists and engineers*. Oxford university press, 2015.
- [160] P. Sagaut, *Large eddy simulation for incompressible flows: an introduction*. Springer Science & Business Media, 2005.
- [161] H. K. Versteeg and W. Malalasekera, *An introduction to computational fluid dynamics: the finite volume method*. Pearson education, 2007.
- [162] J. Smagorinsky, “General circulation experiments with the primitive equations: I. the basic experiment,” *Monthly weather review*, vol. 91, no. 3, pp. 99–164, 1963.
- [163] A. Yoshizawa, “A statistically-derived subgrid model for the large-eddy simulation of turbulence,” *The Physics of Fluids*, vol. 25, no. 9, pp. 1532–1538, 1982.
- [164] F. Moukalled, L. Mangani, and M. Darwish, *Fluid mechanics and its applications the finite volume method in computational fluid dynamics*, 2016.
- [165] H. Jasak, “Error analysis and estimation for the finite volume method with applications to fluid flows,” 1996.
- [166] S. V. Patankar and D. B. Spalding, “A calculation procedure for heat, mass and momentum transfer in three-dimensional parabolic flows,” in *Numerical prediction of flow, heat transfer, turbulence and combustion*, Elsevier, 1983, pp. 54–73.
- [167] J. H. Ferziger, M. Perić, and R. L. Street, *Computational methods for fluid dynamics*. Springer, 2002, vol. 3.
- [168] C. M. Rhie and W.-L. Chow, “Numerical study of the turbulent flow past an airfoil with trailing edge separation,” *AIAA journal*, vol. 21, no. 11, pp. 1525–1532, 1983.
- [169] R. I. Issa, “Solution of the implicitly discretised fluid flow equations by operator-splitting,” *Journal of computational physics*, vol. 62, no. 1, pp. 40–65, 1986.

- [170] E. Robertson, V. Choudhury, S. Bhushan, and D. K. Walters, “Validation of openfoam numerical methods and turbulence models for incompressible bluff body flows,” *Computers & Fluids*, vol. 123, pp. 122–145, 2015.
- [171] J. Jiménez and A. Pinelli, “The autonomous cycle of near-wall turbulence,” *Journal of Fluid Mechanics*, vol. 389, pp. 335–359, 1999.
- [172] T. Mukha and M. Liefvendahl, “Large-eddy simulation of turbulent channel flow,” Technical Report, Tech. Rep., 2015.
- [173] P. Moin and J. Kim, “Numerical investigation of turbulent channel flow,” *Journal of fluid mechanics*, vol. 118, pp. 341–377, 1982.
- [174] J. Kim, P. Moin, and R. Moser, “Turbulence statistics in fully developed channel flow at low reynolds number,” *Journal of fluid mechanics*, vol. 177, pp. 133–166, 1987.
- [175] A. Peyvastehnejad, R. Fiona, C. Richards, *et al.*, “The impact of bio-inspired micro-textures on turbulence and implications for bio-fouling settlement,” Available at SSRN 4379639,
- [176] W. H. Snyder and I. P. Castro, “The critical reynolds number for rough-wall boundary layers,” *Journal of Wind Engineering and Industrial Aerodynamics*, vol. 90, no. 1, pp. 41–54, 2002.
- [177] I. Castro and A. Robins, “The flow around a surface-mounted cube in uniform and turbulent streams,” *Journal of fluid Mechanics*, vol. 79, no. 2, pp. 307–335, 1977.
- [178] “Nitzschia image.” (), [Online]. Available: <https://diatoms.org/species/nitzschia-inconspicua>.
- [179] I. Olenina, “Biovolumes and size-classes of phytoplankton in the baltic sea,” 2006.
- [180] R. D. Moser, J. Kim, and N. N. Mansour, “Direct numerical simulation of turbulent channel flow up to re $\tau = 590$,” *Physics of fluids*, vol. 11, no. 4, pp. 943–945, 1999.
- [181] C. Fureby, A. Gosman, G. Tabor, H. Weller, N. Sandham, and M. Wolfshtein, “Large eddy simulation of turbulent channel flows,” *Turbulent shear flows*, vol. 11, pp. 28–13, 1997.
- [182] B. Erbaş and M. Atlar, “Boundary layer turbulence statistics over transitionally rough marine fouling control coatings,” *Ocean Engineering*, vol. 217, p. 108 032, 2020.

- [183] K. Flack, M. Schultz, and J. Connelly, “Examination of a critical roughness height for outer layer similarity,” *Physics of Fluids*, vol. 19, no. 9, p. 095 104, 2007.
- [184] R. Antonia and P. Krogstad, “Effect of different surface roughnesses on a turbulent boundary layer,” *Journal of the Brazilian Society of Mechanical Sciences*, vol. 22, pp. 1–15, 2000.
- [185] M. R. Raupach and R. H. Shaw, “Averaging procedures for flow within vegetation canopies,” *Boundary-layer meteorology*, vol. 22, no. 1, pp. 79–90, 1982.
- [186] J. Finnigan, “Turbulence in plant canopies,” *Annual review of fluid mechanics*, vol. 32, no. 1, pp. 519–571, 2000.
- [187] J. M. Wallace, H. Eckelmann, and R. S. Brodkey, “The wall region in turbulent shear flow,” *Journal of Fluid Mechanics*, vol. 54, no. 1, pp. 39–48, 1972.
- [188] J. M. Wallace, “Quadrant analysis in turbulence research: History and evolution,” *Annual Review of Fluid Mechanics*, vol. 48, pp. 131–158, 2016.
- [189] H. Nakagawa and I. Nezu, “Prediction of the contributions to the reynolds stress from bursting events in open-channel flows,” *Journal of fluid mechanics*, vol. 80, no. 1, pp. 99–128, 1977.
- [190] R. Antonia and P.-Å. Krogstad, “Turbulence structure in boundary layers over different types of surface roughness,” *Fluid Dynamics Research*, vol. 28, no. 2, p. 139, 2001.
- [191] J. Andreopoulos and P. Bradshaw, “Measurements of turbulence structure in the boundary layer on a rough surface,” *Boundary-Layer Meteorology*, vol. 20, pp. 201–213, 1981.
- [192] O. G. Akinlade, “Effects of surface roughness on the flow characteristics in a turbulent boundary layer,” *PhD in Department of Mechanical Engineering, University of Saskatchewan*, 2005.
- [193] “Forces object function embeded in openfoam.” (), [Online]. Available: <https://www.openfoam.com/documentation/guides/latest/doc/guide-fos-forces-forces.html>.
- [194] I. Celik, Z. Cehreli, and I. Yavuz, “Index of resolution quality for large eddy simulations,” 2005.
- [195] F. Nicoud and F. Ducros, “Subgrid-scale stress modelling based on the square of the velocity gradient tensor,” *Flow, turbulence and Combustion*, vol. 62, no. 3, pp. 183–200, 1999.

Publications

- A. Peyvastehnejad, F. Regan, C. Richards, A. Delgado, P. Daly, J. Grande, and Y. Delauré, “The impact of bio-inspired micro-textures on turbulence and implications for bio-fouling settlement,” *Ocean Engineering* 285, 115223 (2023).